Modelling of solar energetic particles by stochastic processes

JP van den Berg

orcid.org/0000-0003-1170-1470

Dissertation submitted in partial fulfilment of the requirements for the degree *Master of Science in Astrophysical Sciences* at the North-West University

Supervisor: Prof RDT Strauss

Graduation May 2019

24182869

sto-chas'ties *b.nw.* ook **stogasties** Vermoedelik, waarskynlik; bepaal deur 'n willekeurige verspreiding van moontlikhede; beheer deur die wette van moontlikhede [G. *stochastikos* gissend].
- HAT: Verklarende Handwoordeboek van die Afrikaanse Taal, 2005, 5de uitg., Kaapstad: Pearson Education

To my late grandparents, Koos and Rita van den Berg, and Faan and Clasie van Zyl.

Abstract

The focused transport of solar energetic particles has received increasingly more interest in the last couple of years due to upcoming missions to the Sun. Stochastic differential equations offer a numerically robust way to model solar energetic particle events, but very few models exist which utilize the full capability of this approach. This dissertation summarises the fundamental physics underlying the propagation of solar energetic particles and develops a numerical code to model a solar energetic particle event. In order to understand the microphysics involved in the propagation of solar energetic particles, wave-particle interactions are investigated and charged particles propagating in model slab turbulence are simulated to build a conceptual understanding of the influence of magnetic turbulence on the propagation of charged particles. It is shown that the classical idea of hard-sphere collisions should not be naively applied to charged particles interacting with turbulence due to the unique nature of the wave-particle interactions. These insights motivate the terms in the focused transport equation, which is derived from physical arguments and processes. Stochastic differential equations are used to solve the focused transport equation in one spatial dimension with energy losses. The developed model is extensively benchmarked and is shown to correctly model solar energetic particle events. It is found that different numerical integration schemes, of increasing accuracy, do not yield any improvement in the model solutions as the results are governed by stochastic behaviour. The effects of solar wind advection and energy losses upon observable characteristics of solar energetic particle events are explored and it is shown that the neglect of these processes would predict incorrect event onset times and peak intensities. The somewhat unexplored topics of propagation times and energy losses are also investigated and it is shown that high energy particles have short propagation times and experience little energy losses. It is found that the average propagation time can be described by the diffusion approximation for cosmic rays, while an improved expression is derived for the average energy loss.

Keywords: *solar energetic particles, focused transport equation, stochastic differential equations, wave-particle interactions, magnetic turbulence, propagation times, energy losses*

Acronyms and Abbreviations

Listed below are the acronyms and abbreviations used in the text. For the purpose of clarity, any such usages are written out in full when they first appear in a chapter and the abbreviation is given in brackets.

2D	Two-dimensional
AU	Astronomical Unit[1]
CME	Coronal Mass Ejection
CR	Cosmic Ray
EUV	Energetic Ultra-violet
eV	Electron Volt[2]
FD	Finite Difference
FLRW	Field Line Random Walk
FPE	Fokker-Planck Equation
FTPE	Focused Transport Equation
GC	Guiding Centre
GCR	Galactic Cosmic Ray
HMF	Heliospheric Magnetic Field
MFP	Mean Free Path
PAD	Pitch-angle Distribution
PADC	Pitch-angle Diffusion Coefficient
PRN	Pseudo-random Number
PRNG	Pseudo-random Number Generator
QLT	Quasi-linear Theory
SDE	Stochastic Differential Equation
SEP	Solar Energetic Particle
SN	Sunspot Number
SW	Solar Wind
TPE	Transport Equation

[1] Defined to be the average distance between the Sun and Earth; $1\ \mathrm{AU} = 1.496 \times 10^{11}\ \mathrm{m}$.

[2] Defined to be the energy gained by a particle with the elemental charge when accelerated by a potential difference of $1\ \mathrm{V}$; $1\ \mathrm{eV} = 1.602 \times 10^{-19}\ \mathrm{J}$.

Contents

1 Introduction **1**

2 The Active Sun and Solar Energetic Particles **4**

2.1 The Active Sun 4

2.1.1 The Sun and the Solar Cycle 5

2.1.2 The Solar Wind 7

2.1.3 The Heliospheric Magnetic Field 9

2.2 Solar Energetic Particles 11

2.2.1 In Situ and Remote-sensing Observations of Solar Energetic Particles . . . 11

2.2.2 Two Types of Solar Energetic Particles 14

2.2.3 Characteristics of Impulsive Solar Energetic Particle Events 15

2.3 Summary 18

3 The Micro-physics of Charged Particles Propagating in Slab Turbulence **19**

3.1 The Newton-Lorentz Equation and Some Analytical Solutions 19

3.1.1 Magnetic Focusing 22

3.2 Turbulence, Scattering, and Diffusion 23

3.2.1 Turbulence in the Heliosphere 24

3.2.2 Wave-particle Interactions 26

3.2.3 Slab Turbulence and Pitch-angle Scattering 38

3.3 Summary 48

4 The One-dimensional Focused Transport Equation for Solar Energetic Particles 50

4.1 Concepts in Momentum Space . . . 50

4.2 The Distribution Function and Fokker-Planck Equation . . . 52

4.2.1 The Distribution Function . . . 52

4.2.2 The Fokker-Planck Equation . . . 54

4.2.3 The Transport Equation for Focused Transport in One Dimension . . . 57

4.3 The One-dimensional Focused Transport Equation of Ruffolo . . . 58

4.3.1 The Co-rotating Solar Wind Frame . . . 58

4.3.2 Energy Changes . . . 59

4.3.3 Field-parallel Transport . . . 63

4.3.4 Pitch-cosine Transport . . . 63

4.3.5 The Focused Transport Equation . . . 64

4.4 Summary . . . 65

5 Stochastic Differential Equations 66

5.1 Stochastic Differential Equations . . . 66

5.1.1 The Definition of a Stochastic Differential Equation . . . 67

5.1.2 Constructing the Distribution Function and Boundary Conditions . . . 70

5.2 Brownian Motion . . . 72

5.3 The Stochastic Transport Model for Solar Energetic Particles . . . 77

5.3.1 The Stochastic Differential Equations for Focused Transport . . . 78

5.3.2 Numerical Solution of the Stochastic Transport Model . . . 78

5.3.3 The Pitch-angle Diffusion Coefficient and Some Aspects of the Stochastic Transport Model . . . 79

5.4 Summary . . . 82

6 The Focused Transport of Solar Energetic Particles 83

6.1 The Diffusion Approximation and Telegraph Equation . . . 84

6.1.1 Isotropic Scattering . . . 86

6.1.2 Anisotropic Scattering . . . 90

6.2 The Effect of Advection and Energy Losses 94
6.3 Energy Losses, Propagation Times, and Other Observational Features 100
6.3.1 Energy Losses 103
6.3.2 Propagation Times 106
6.3.3 Observational Features 109
6.4 Summary 112

7 Summary and Conclusions **114**

A Analytical and Numerical Solutions of the Newton-Lorentz Equation **118**
A.1 Some Analytical Solutions of the Newton-Lorentz Equation 118
A.1.1 A Constant and Uniform Electric and Magnetic Field 118
A.1.2 Magnetic Mirroring 121
A.2 Numerical Solutions of the Newton-Lorentz Equation 123
A.2.1 The Boris Method 124
A.2.2 The Vay Method 126
A.2.3 The Runge-Kutta Method 126
A.2.4 Analysing the Numerical Results 128
A.2.5 Visualising Electric and Magnetic Field Lines 129
A.2.6 Stability and Convergence of the Numerical Methods 129

B Numerical Solutions of Stochastic Differential Equations and Specifics of the Stochastic Transport Model **134**
B.1 Numerical Solutions of Stochastic Differential Equations 134
B.1.1 The Advantage and Conditions of Numerical Schemes 134
B.1.2 The Euler-Maruyama Scheme 136
B.1.3 The Milstein Scheme 137
B.1.4 The Order 1.5 Strong / 2 Weak Taylor Scheme 138
B.1.5 A Variable Time Step 138
B.2 Specifics of the Stochastic Transport Model 139
B.2.1 Derivatives of the Drift and Diffusion Coefficients 139

B.2.2 Derivatives of the Pitch-angle Diffusion Coefficient 140
B.2.3 Arc and Focusing Length 142
B.2.4 Initial and Boundary Conditions 143
B.2.5 Constructing the Distribution Function 145
B.2.6 Observable Quantities 145

Bibliography **148**

Acknowledgements **158**

Chapter 1

Introduction

The current Parker Solar Probe (`http://parkersolarprobe.jhuapl.edu/index.php`) and upcoming Solar Orbiter (`http://sci.esa.int/solar-orbiter`) missions are expected to provide a wealth of new information regarding the acceleration and propagation of solar energetic particles close to the Sun. Solar energetic particles (SEPs) are defined here to include all energetic particles, but mostly protons and electrons, of solar origin, whether originating from a solar flare, a coronal mass ejection, or a combination of both processes. In order to understand these future observations, the data will be compared to theoretical models, for which sophisticated numerical modelling are needed to solve the relevant transport equations. Additionally, with the planned missions to the Moon and Mars by various space agencies, SEP events pose a huge radiation hazard to astronauts outside of the Earth's protective magnetosphere. Large SEP events can also cripple communication, GPS, and Earth observing satellites within the magnetosphere, induce currents in ground based transmission lines, leading to power outages, and even pose serious health risks to passengers and crew of high altitude aircraft on trans-polar routes, whom are already exposed to enhanced levels of radiation from galactic cosmic rays. SEPs are therefore not just of academic interest, but need to be understood in order to predict the radiation levels of a remote-sensed solar event before it reaches Earth or other locations of interest [*Mewaldt*, 2006; *Reames*, 2013, 2017; *Klein and Dalla*, 2017].

The study of SEPs has previously been dominated by cosmic ray research in the nearly isotropic limit [*Parker*, 1965; *Webb and Gleeson*, 1979], with the result that the underlying micro-physical processes governing, and the focused transport equation (FTPE) describing the propagation of SEPs are not well documented, with the exception of perhaps *Ruffolo* [1995] and *Zank* [2014]. Since almost all of the observations are in the ecliptic plane, most of the numerical models only have two spatial dimensions (see e.g. *Lampa* [2011] or *Strauss and Fichtner* [2015]). Ideally, additional computational dimensions are needed to study the full spatial distribution, time evolution, and energy changes of SEPs. The addition of these dimensions, however, would make the traditional finite difference-based numerical schemes unstable.

The question then arises if it is possible to develop a time dependent model with three spatial dimensions and energy losses for the propagation of SEPs, which is numerically stable and

capable of handling complicated physical processes?

This is indeed possible by casting the FTPE into a set of stochastic differential equations (SDEs) and constructing the SEP distribution function from the computed solutions [*Gardiner*, 1985; *Strauss and Effenberger*, 2017]. This creates the possibility of solving the FTPE in a greater number of computational dimensions (e.g. three spatial dimensions, time, momentum, and pitch-angle) with unconditional numerical stability, allowing complicated and detailed physical structures and processes to be incorporated. This also allows execution on parallel computing platforms to reduce runtime, as the computed solutions are independent of each other. The number of studies which utilize SDE-type numerical methods to construct three-dimensional models are few and the numerical aspects are not documented extensively (see e.g. *Dröge et al.* [2010], with *Qin et al.* [2006] and *Zhang et al.* [2009] seemingly the best documented thus far).

This research will summarise the fundamental physics underlying the propagation of SEPs and aims to develop a numerical code which will solve the FTPE in terms of time, one spatial dimension, momentum, and pitch-angle by using its equivalent set of SDEs. As the ultimate aim of the research is to lay a solid foundation on which a sophisticated three-dimensional model can be developed in the future using SDEs, special attention will be given to the numerical implementation and benchmarking of the model.

The structure of the dissertation is as follows:

Chapter 2 introduces the basic concepts related to SEPs and their origin on the Sun, giving the backdrop within which the current study applies. Solar activity is discussed first, including sunspots, solar flares, the solar wind, and the heliospheric magnetic field. The chapter is concluded with the origin, observation, and characteristics of SEP events.

Chapter 3 will attempt to build a conceptual understanding of the micro-physics of charged particles propagating in turbulent electric and magnetic fields. This chapter will start with a discussion of the analytical solutions of the Newton-Lorentz equation, during which the solution for a uniform and constant electric and magnetic field will be discussed, drifts will be introduced, and a discussion of magnetic focusing will be given. An introduction into the basics of turbulence and wave-particle interactions will then be given, after which an investigation of the interaction of charged particles with model slab turbulence will be performed. **Appendix A** gives the analytical solution of the Newton-Lorentz equation in the case of constant and uniform electric and magnetic fields and magnetic mirroring, as well as a discussion on how the Newton-Lorentz equation can be solved numerically to allow the incorporation of complex electric and magnetic fields.

In **Chapter 4**, a one-dimensional FTPE, describing the evolution of the anisotropic SEP distribution function, will be derived from physical grounds following the derivation of *Ruffolo* [1995]. The derivation will begin by deriving the Fokker-Planck equation and writing it in a convenient set of coordinates, after which expressions will be derived for the various terms as applicable to the transport of SEPs.

In order to solve the FTPE, **Chapter 5** introduces SDEs. The chapter will begin with a discussion on SDEs and the usage thereof in solving Fokker-Planck type equations, covering a broad range of topics starting with the definition of an SDE, the link between an SDE and a Fokker-Planck equation, the interpretation of an SDE based solution, constructing the distribution function from these solutions, and some boundary conditions. All of the introduced concepts will then be explained using Brownian motion in one dimension. The chapter will be concluded with a discussion of the stochastic transport model used in solving the one-dimensional FTPE for SEP propagation derived in Chapter 4. **Appendix B** deals with the numerical solutions of SDEs and some specifics of the stochastic transport model.

The aim of **Chapter 6** is to verify the stochastic transport model by benchmarking against published numerical models and comparing with analytical approximations, as well as to investigate different characteristics of the focused transport of SEPs. The model results will first be compared to the diffusion approximation and telegraph equation for the simplified FTPE of *Roelof* [1969]. The model results will then be compared to a few published numerical models, of both finite difference and SDE types. This discussion will also investigate the effect of the different physical processes and how different numerical integration schemes compare to one another, as well as the usage of a variable time step. The energy losses and propagation times of SEPs will then be investigated as an application of the model. These results will be compared with the predictions of the diffusion approximation used for cosmic rays, while an attempt will be made at deriving improved predictions from the terms in the FTPE. Lastly, a few observational features of SEP events will be discussed.

The last chapter presents a summary of the main results and conclusions drawn from these results, as well as possible avenues of future research.

Aspects of this work were presented at the following conferences:

- The 11^{th} National Conference of the Centre for High Performance Computing (CHPC) in Pretoria, South Africa (December 2017).
- The 63^{rd} Annual Conference of the South African Institute of Physics (SAIP) in Bloemfontein, South Africa (June 2018).

Chapter 2

The Active Sun and Solar Energetic Particles

In this chapter the basic concepts related to solar energetic particles and their origin on the Sun are introduced. Solar activity is discussed first, including sunspots, solar flares, the solar wind, and the heliospheric magnetic field. The chapter is concluded with the origin, observation, and characteristics of solar energetic particles. The basic concepts introduced here will form the backdrop within which the current study applies.

2.1 The Active Sun

In the 17^{th} century the idea began to surface that the Sun is a dynamic structure which changes over time. The periodic activity of the Sun was later confirmed and is an important aspect in space physics as it influences all of the structures and processes associated with the Sun and thus also the Earth. The Sun's main influence sphere is called the *heliosphere* and is the result of the interaction between the solar and interstellar plasmas. In this section, aspects important to the inner heliosphere will be discussed and the influence of solar activity on the inner heliosphere will also be highlighted. These aspects include sunspots, solar flares, the solar wind, and the heliospheric magnetic field. For a general overview of solar activity, see *Hathaway* [2010] and for a review of solar activity over millennia, see *Usoskin* [2013]. For an interesting review on how the Ulysses mission has shaped and improved our understanding of the heliosphere and its various structures, see *Balogh et al.* [2008]. *Tandberg-Hanssen and Emslie* [1988], *Benz* [2008], *Chen* [2011], *Shibata and Magara* [2011], and *Webb and Howard* [2012] give extensive reviews on the observations and theory of solar flares and coronal mass ejections, as well as the intricate connection between them. For a review on the origin of the solar wind, see *Marsch* [2006] and **?**. *Owens and Forsyth* [2013] give a review on the heliospheric magnetic field and the influence of solar activity thereupon.

2.1.1 The Sun and the Solar Cycle

When the Sun is observed in white light, irregularly shaped black spots can be seen on the photosphere, the Sun's visible surface. These spots are called *sunspots* and records have been kept of the number of sunspots since the 1600s. *Parker* [1955] showed that sunspots are caused by magnetic flux tubes (regions of concentrated magnetic fields surrounded by weak magnetic fields) piercing the photosphere by the process of magnetic buoyancy: the flux tubes are formed due to convection in the plasma and becomes buoyant if the plasma in the flux tube is less dense than the surrounding plasma, with the magnetic field being carried by the plasma since the magnetic field is frozen into the plasma. A pair of sunspots can be created in this way, with the pair of spots having opposite polarity, and sunspots appear darker because the plasma in the flux tube has a lower temperature than the surrounding plasma. The convection of plasma, together with the differential rotation of the Sun in its outer layers, is the general mechanism responsible for the Sun's magnetic field: the plasma is set into motion by these movements and since plasma is charged, the motion can be seen as currents which induce magnetic fields. The Sun's magnetic field is therefore the net effect of these small scale magnetic fields, this process being called the *solar dynamo* [*Parker*, 1955; *Choudhuri*, 1998; *Reames*, 2017].

The top panel of Fig. 2.1 shows the average sunspot number (SN) from 1980 to 2017, and a clear variation with time can be distinguished. Since sunspots are produced by the Sun's magnetic field, the SN is therefore an indication of the Sun's magnetic activity. Every ~ 11 years the Sun goes through a period of intense magnetic activity, called *solar maximum*, during which the polarity of the Sun's magnetic field switches. This period is marked by an increase in the SN, the Sun's magnetic field strength (bottom panel of Fig. 2.1), and the occurrence of more transient events, such as solar flares and coronal mass ejections. The dashed lines in Fig. 2.1 show approximate times of solar maximum. Solar maximum is followed by a decrease in solar activity towards *solar minimum*, a period marked by a low SN and magnetically quiet conditions on the Sun. This 11-year cycle is called the *Schwabe cycle* and the solar cycle has an influence on the whole heliosphere and the structures therein. The area of the Sun covered by sunspots increases towards solar maximum and the position of sunspots follow *Spörer's law of zones*, where sunspots appear in a range at latitudes above $\sim 20^\circ - 25^\circ$ at solar minimum and then slowly broaden while the central latitudes drift towards the equator when approaching solar maximum [*Hathaway*, 2010; *Usoskin*, 2013].

The ~ 22 year cycle during which the Sun's magnetic polarity has reversed twice, is called the *Hale cycle*, and other cycles can also be observed. A ~ 27 day cycle is associated with the rotation of the Sun and a ~ 154 day cycle is also observed. The $\sim 60 - 120$ year change in the amplitude of the Schwabe cycle is known as the *Gleissberg cycle* and is characterised by grand minima and maxima. Other periodicities include $\sim 205 - 210$ (the *de Vries* or *Suess cycle*), $\sim 600 - 700$, $\sim 1000 - 1200$, and $\sim 2000 - 2400$ years. The short temporal variations, which are in the order of days, are caused by transient events. The causes of the long-term varia-

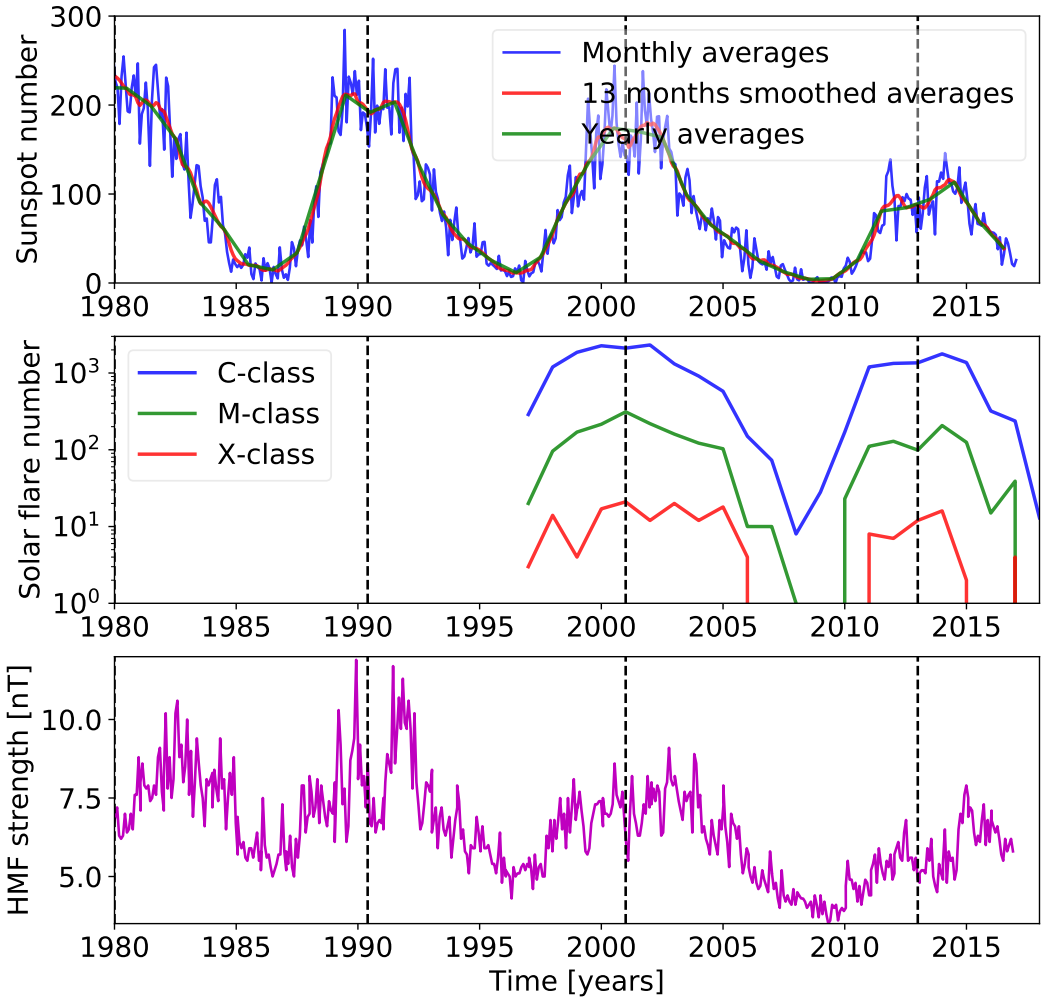

Figure 2.1: Temporal variations of the averaged sunspot number (*top*), the yearly number of solar flares (*middle*), and the heliospheric magnetic field strength at Earth (*bottom*). The vertical dashed lines indicate times of approximate solar maximum activity. Notice that a logarithmic scale was used for the number of solar flares per year. Sunspot number data obtained from `http://sidc.be/silso/`, yearly number of solar flares obtained from `https://www.spaceweatherlive.com/en/solar-activity/solar-cycle`, and heliospheric magnetic field strength data obtained from `http://cohoweb.gsfc.nasa.gov`.

tions, which are in the order of a few hundred to thousands of years, are still uncertain. The influence of the solar cycle can be seen on various observable quantities, as is evident from Fig. 2.1. Some observable quantities in which the solar cycle is also evident, but which are not indicated, include sunspot areas and sunspot positions, the 10.7 cm radio flux and the total solar irradiance, transient events and geomagnetic activity. Both the 10.7 cm radio flux and total solar irradiance (the energy emitted by the Sun at all wavelengths crossing a unit area outside the Earth's atmosphere per unit time) increase towards solar maximum. Solar maximum is also accompanied by an increase in the geomagnetic activity of the Earth's magnetic field due to an increase of transient events [*Hathaway*, 2010; *Usoskin*, 2013].

While observing a group of sunspots, *Carrington* [1859] and *Hodgson* [1859] independently made the first observations of a *solar flare* in white light, lasting for ~ 5 minutes. The flare

seemed to occur above the sunspots, as it did not change the sunspot group's structure, and geomagnetic activity commenced ~ 16 hours later. Flares are caused by the magnetic reconfiguration of magnetic flux tubes in the solar corona to lower energy states. This magnetic reconfiguration between magnetic fields of opposite directions, forms a current sheet in which magnetic reconnection between the opposing fields dissipate the associated electric current. During the reconnection, magnetic energy is transferred to the plasma as kinetic energy. This leads to the emission of soft and hard X-rays, synchrotron radiation, Hα-lines, and even white light, together with radio waves and energetic particles. Flares are classified according to their soft X-ray emissions: the classification letter (B, C, M, or X) represents the order of magnitude of the soft X-ray flux (10^{-4}, 10^{-3}, 10^{-2}, or 10^{-1} $\mathrm{ergs \cdot cm^{-2} \cdot s^{-1}}$, respectively for the classes) and a subsequent numerical value indicates the multiple of the order of magnitude (i.e. a C2.1 flare indicates a soft X-ray flux of 2.1×10^{-3} $\mathrm{ergs \cdot cm^{-2} \cdot s^{-1}}$). The middle panel of Fig. 2.1 shows the yearly number of C-, M-, and X-class flares from 1997 to 2018. The solar cycle is also evident in the number of flares, with a ~ 3 months lag which cannot be clearly seen, and it can be seen that the average number of flares are much more numerous for B- or C-classes than for M- or X-classes. Flares can have spatial extends of $\sim 10^4 - 10^5$ km, lasting $\sim 60 - 10^5$ s, and releasing $\sim 10^{19} - 10^{25}$ J of energy in various forms. About one flare occurs per day during solar minimum on average, while this increases to an average of ~ 20 per day during solar maximum [*Tandberg-Hanssen and Emslie*, 1988; *Miller et al.*, 1997; *Benz*, 2008; *Hathaway*, 2010; *Shibata and Magara*, 2011].

Another process which often accompanies a solar flare, is a *coronal mass ejection* (CME), although the two events can be mutually exclusive. CMEs were discovered 112 years after solar flares in 1971 in a coronagraph taken by the seventh Orbiting Solar Observatory (OSO-7). CMEs are caused by erupting magnetic flux tubes ejecting between $\sim 10^{11} - 10^{13}$ kg of mass from the Sun with inferred speeds between $\sim 200 - 3500$ $\mathrm{km \cdot s^{-1}}$. Just as solar flares follow the solar cycle, so do CMEs, with less than 2 CMEs occurring per day on average during solar minimum, while this increases to an average of ~ 8 per day during solar maximum, where the maximum of the occurrence rate is delayed by $6-12$ months in comparison to solar maximum. On average $\sim 30\%$ of C-class, $\sim 56\%$ of M-class, and $\sim 90\%$ of X-class flares are accompanied by CMEs. CMEs are massive events with angular widths of $\sim 2^\circ - 360^\circ$, with a significant fraction having $\lesssim 20^\circ$ and only a small fraction having $\gtrsim 120^\circ$, and a volume of $\sim 10^{24}$ $\mathrm{m^3}$. The average mass released by a CME is $\sim 3 \times 10^{12}$ kg and $\sim 15\%$ of CMEs have a mass less than 10^{11} kg. CMEs have an average speed of ~ 300 $\mathrm{km \cdot s^{-1}}$ and ~ 500 $\mathrm{km \cdot s^{-1}}$ during solar minimum and maximum, respectively. The energy of a CME is comparable to that of a solar flare, ranging between $\sim 10^{22} - 10^{25}$ J [*Chen*, 2011; *Webb and Howard*, 2012].

2.1.2 The Solar Wind

The *solar wind* (SW) is due to the outflow of matter from the Sun. It was first proposed by *Biermann* [1957] to explain the direction of a comet's tail which is always pointing radially

away from the Sun and which could not be explained by radiation pressure. Building on Biermann's so called "solar corpuscular radiation", *Parker* [1958] used hydrodynamic equations to prove that the corona, the Sun's atmosphere, cannot be in static equilibrium and that there must be a supersonic outflow of matter from the Sun with a speed of $\sim 500\ \mathrm{km \cdot s^{-1}}$. Parker used the term "solar wind" to distinguish this concept from other concepts of slow moving or stationary interplanetary gas. The SW was observed the first time by spacecrafts in the early 1960s and Ulysses was the first spacecraft measuring the SW out of the ecliptic regions. The SW is observed at Earth as a supersonic, radially outwards moving plasma with an average proton speed of $\sim 400 - 800\ \mathrm{km \cdot s^{-1}}$ and an average density of $\sim 7\ \mathrm{particles \cdot cm^{-3}}$ at Earth. Since the SW originates from the Sun, its composition is representative of the corona, being composed primarily of protons, electrons, and alpha particles, with small amounts of other elements [*Balogh and Lanzerotti*, 2008; *Smith*, 2008; *von Steiger*, 2008; *Cranmer et al.*, 2017].

Sheeley et al. [1997] found that the SW accelerates, across all latitudes, within $\sim 30\ r_\odot$ from the Sun and approaches a constant radial flow at about ~ 0.3 AU, where $r_\odot \approx 0.005$ AU is the Sun's radius. Ulysses observed that the SW is not always uniform over all solar latitudes, but that its speed is influenced close to the Sun by the solar magnetic field. When the field lines are closed, they form loops perpendicular to the radial SW and inhibits the outflow. These regions give rise to the so called *slow SW streams* and are generally found near the equator where the SW has typical speeds of $\sim 400\ \mathrm{km \cdot s^{-1}}$. Regions containing open magnetic field lines, found towards the poles, are less inhibiting to the radial SW outflow and give rise to the *fast SW streams* having typical speeds of $\sim 800\ \mathrm{km \cdot s^{-1}}$ and lower densities than the slow SW (notice that all magnetic field lines must be closed and that 'open magnetic field lines' refer here to magnetic field lines which stretch to distances of $\gtrsim 100$ AU such that they seem to be open in the heliosphere). During solar minimum conditions, large polar coronal holes develop at high latitudes and the presence of the coronal holes result in fast SW streams with speeds decreasing again near the equatorial regions where the closed magnetic fields are found. During solar maximum conditions, when the well-defined coronal holes disappear, the SW is a mixture of both slow and fast SW, so that there is no discernible speed profile and the latitudinal dependence disappears [*von Steiger*, 2008; *Cranmer et al.*, 2017].

SW models for this observed radial and latitudinal dependencies can be found in *Langner* [2004] or *Moeketsi et al.* [2005]. For the current discussion, where observations of solar energetic particles are confined to latitudes around the equatorial plane, the SW in the inner heliosphere will be assumed to be slow and constant over the spatial and temporal scales under consideration. Neglecting the regions close to the Sun where the SW is accelerating, the SW will be modelled by

$$\vec{v}_{\mathrm{sw}} = v_{\mathrm{sw}} \hat{r}, \tag{2.1}$$

where $v_{\mathrm{sw}} = 400\ \mathrm{km \cdot s^{-1}}$ is the magnitude of the SW and $\hat{r}$ is a unit vector in the radial direction.

2.1.3 The Heliospheric Magnetic Field

As a consequence of the SW, *Parker* [1958] realized that since the entire corona is threaded by magnetic fields, the SW will drag these magnetic fields with it into the heliosphere. Even though the Sun's magnetic field dominates the SW outflow in the corona, the SW flow becomes radial and dominates the magnetic field at a radial distance of $\sim 10 - 20\ r_{\odot}$, assuming a uniform corona without the complications of active regions or coronal holes [*Chhiber et al.*, 2018]. This is the *Alfvén radius*, where the hydrodynamic ram pressure of the SW becomes greater than the magnetic pressure. Due to the SW plasma's high conductivity, the SW kinetic energy dominates the magnetic energy contained in the magnetic fields, such that the Sun's magnetic field gets 'frozen into' or embedded in the SW and is carried off into interplanetary space, forming the *heliospheric magnetic field* (HMF; also referred to as the 'interplanetary magnetic field'). During solar minimum conditions, the Sun's magnetic field takes on its simplest form with two different types of distinguishable structures: firstly, regions containing open magnetic field lines, having opposite polarity in the two hemispheres, are caused by the large coronal holes near the poles; secondly, regions containing closed magnetic field lines are found in the equatorial regions with most sunspots also found within $\sim 20^{\circ}$ North and South of the equator. During solar maximum, however, the Sun's global magnetic field structure changes drastically: the coronal holes are smaller and more or less uniformly distributed in the corona, the magnetic field strength increases (as can be seen in the bottom panel of Fig. 2.1) and the strong opposite polarities of the open magnetic fields are not present any more, with both polarities present in both hemispheres [*Hathaway and Suess*, 2008; *Owens and Forsyth*, 2013].

The HMF, as derived by *Parker* [1958], is the most basic view of the HMF and has been shown to hold quite well on average. Parker used magnetohydrodynamics, ignoring all electric fields and currents, and focusing only on the magnetic fields and SW plasma. By assuming that the magnetic field is frozen into the SW plasma, any relative motion between the plasma and the field can be eliminated, with the effect that the magnetic field is parallel to the SW velocity, electric fields vanish, and large currents are avoided. The electric field $\vec{E}_{\mathrm{HMF}}$ can be computed afterwards from the SW velocity and magnetic field $\vec{B}_{\mathrm{HMF}}$ by $\vec{E}_{\mathrm{HMF}} \approx -\vec{v}_{\mathrm{sw}} \times \vec{B}_{\mathrm{HMF}}$, while currents $\vec{J}$ can be computed by $\mu_0 \vec{J} = \vec{\nabla} \times \vec{B}_{\mathrm{HMF}}$, where μ_0 is the permeability of vacuum (notice that *Jokipii and Levy* [1979] do not expect that the electric field would have a significant effect on particles propagating diffusively in the heliosphere). Since the SW is expanding radially away from the Sun, the magnetic field will also be directed radially, but since the field lines are anchored to the Sun and the Sun is rotating, the field lines will be wound up into a spiral. The Parker HMF thus has a radial and longitudinal component, but no latitudinal component if it is assumed that the Sun rotates as a rigid body, causing a magnetic field line that originates from a polar angle θ to stay on a cone of constant half opening angle θ [*Parker*, 1958; *Smith*, 2008; *Owens and Forsyth*, 2013]. Fig. 2.2 illustrates the Parker HMF for a constant SW speed.

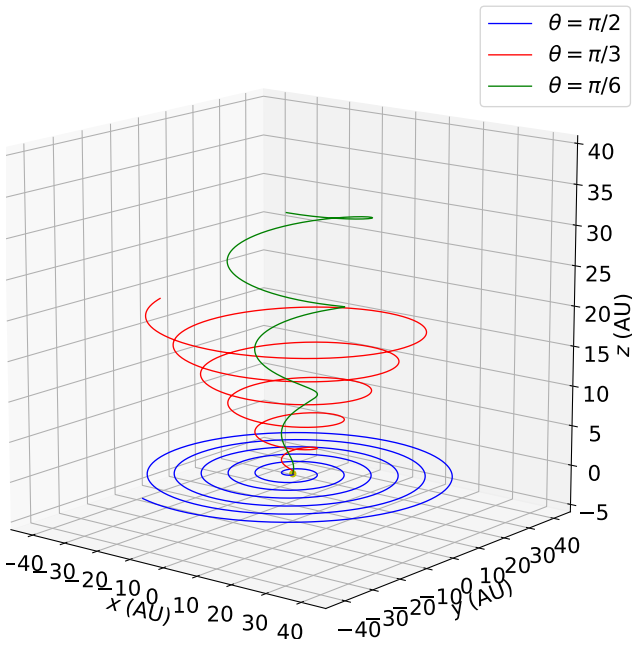

Figure 2.2: A representation of the Parker heliospheric magnetic field lines at polar angles of $\theta = \pi/2$ (in the equatorial plane), $\theta = \pi/3$, and $\theta = \pi/6$ for a constant solar wind speed of $v_{\rm sw} = 400\ {\rm km \cdot s^{-1}}$. The Sun is at the origin represented by a yellow dot.

The Parker HMF can be written as

$$\vec{B}_{\rm HMF} = AB_0 \left(\frac{r_0}{r}\right)^2 \left(\hat{r} - \tan\psi\hat{\phi}\right), \tag{2.2}$$

where $\hat{\phi}$ is a unit vector in the azimuthal direction and B_0 is a normalization value, usually related to the HMF magnitude as observed at Earth, $B_\oplus = 5\ {\rm nT}$ (for solar minimum conditions) at $r_0 = 1\ {\rm AU}$, such that

$$B_0 = \frac{B_\oplus}{\sqrt{1 + (\omega_\odot r_0/v_{\rm sw})^2}}, \tag{2.3}$$

with $\omega_\odot \approx 2\pi/25\ {\rm days} = 2.66 \times 10^{-6}\ {\rm rad \cdot s^{-1}}$ the solar rotation rate. The HMF *spiral angle* ψ is defined as the angle between the HMF line and the radial direction and is given by

$$\tan\psi = \frac{\omega_\odot (r - r_\odot)}{v_{\rm sw}} \sin\theta, \tag{2.4}$$

if it is assumed that the SW is immediately constant when leaving the solar surface. In the equatorial regions, the spiral angle at Earth is $\psi \approx 45°$ and increases to $\psi \approx 90°$ when $r > 10$ AU. The HMF polarity is determined by

$$A = \pm H(\theta - \theta'), \tag{2.5}$$

where ± 1 refers to the different HMF polarity cycles (positive if the field is pointing outwards in the northern hemisphere) and

$$H(\theta - \theta') = \begin{cases} 1 & \text{for } \theta < \theta' \\ 0 & \text{for } \theta = \theta' \\ -1 & \text{for } \theta > \theta' \end{cases}, \tag{2.6}$$

with θ' the angular extent of the heliospheric current sheet (the boundary separating regions of opposite polarity in the HMF, acting therefore as the heliospheric magnetic equator). The magnitude of the HMF is given by

$$B_{\mathrm{HMF}} = B_0 \left(\frac{r_0}{r}\right)^2 \sqrt{1 + \tan^2 \psi}, \tag{2.7}$$

from which it is evident that B_{HMF} decreases as $1/r^2$ in the polar regions and $1/r$ in the equatorial regions [*Parker*, 1958; *Smith*, 2008; *Owens and Forsyth*, 2013].

2.2 Solar Energetic Particles

Although Carrington and Hodgson did not know it at the time they discovered solar flares, they were looking at an extreme process on the Sun which accelerates particles from the background plasma to relativistic energies. *Forbush* [1946] was the first to report an observation of these energetic particles as a *ground level enhancement*, an increase above the background galactic cosmic ray (GCR; highly energetic charged particles originating outside the heliosphere) fluxes observed on Earth by neutron monitors and muon telescopes due to GeV protons presumably accelerated by shock waves. In this section aspects important to solar energetic particles will be discussed. This discussion will begin with how these events are observed, followed by highlighting the two different categories of solar energetic particles, and concludes with the characteristics of impulsive events. General reviews on solar energetic particles are given by *Reames* [1999, 2013, 2017], *Mewaldt* [2006], and *Klein and Dalla* [2017]. See *Ryan et al.* [2000] for a reconstruction of a solar energetic particle event and the onset times of the different observable features of the source region. *Miller et al.* [1997] gives a review on the acceleration of charged particles in solar flares.

2.2.1 In Situ and Remote-sensing Observations of Solar Energetic Particles

Instruments on various spacecraft directly measure energetic particles, supplying not only temporal intensity profiles of the various energy ranges and energy spectra of the various particles, but also the compositions and charge states, as well as the arrival directions. These measurements are called *in situ observations* as the particles are directly measured in their environment. In situ measurements also include important information about the SW and HMF, which are used in determining the magnetic connection of the spacecraft to the source surface of the Sun, the amount of turbulence in the HMF, and the identification of various transient structures. The parameters of and the various structures present in the SW and HMF, influence the propagation of the energetic particles and is used in models trying to explain the observations [*Dresing*, 2014]. Ground based neutron monitors can also detect large scale events connected to energetic particles. It was already stated that a solar energetic particle event with sufficient energetic particles, will be registered as a ground level enhancement [*Ryan et al.*, 2000].

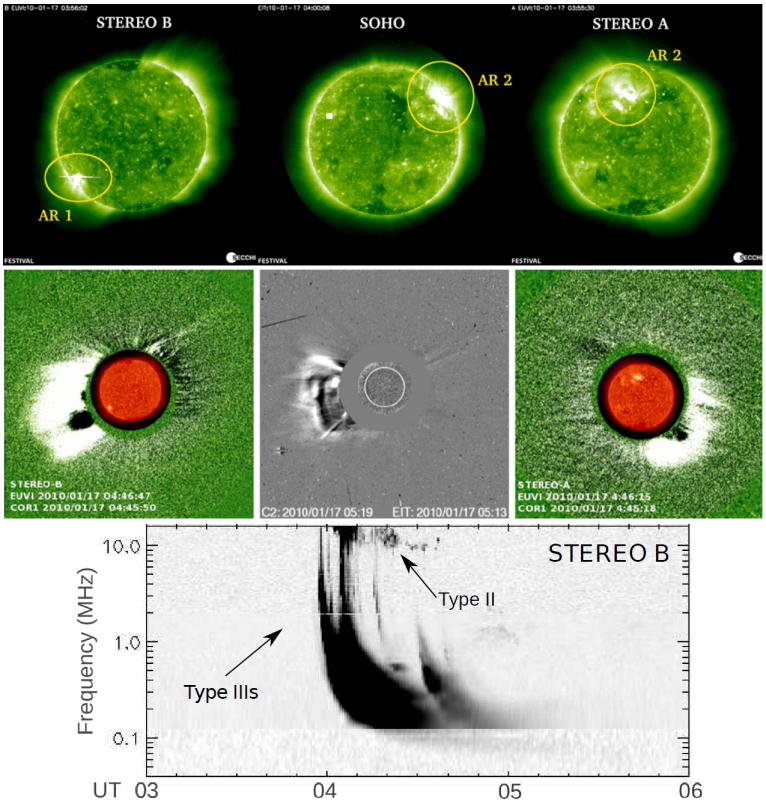

Figure 2.3: Different remote-sensing observations of a solar energetic particle event on 17 January 2010 with STEREO and SOHO. *Top panels:* Energetic ultra-violet images by STEREO B (left), SOHO (middle), and STEREO A (right) during the flare time. Two different active regions were observed on the Sun, labelled "AR 1" and "AR 2", but the flare was only seen by STEREO B in AR 1. *Middle panels:* Energetic ultra-violet images, surrounded by coronagraphs, by STEREO B (left) and STEREO A (right), as well as a coronagraph by SOHO (middle). Difference images of the coronagraph observations are shown to increase the visibility of the coronal mass ejection. *Bottom panel:* Radio spectrogram as observed by STEREO B. Both type II and type III radio bursts were observed. These figures were taken from *Dresing et al.* [2012].

In situ observations are complimented by other observations regarding the Sun. These observations, which are done by instruments on Earth and various spacecraft, are called *remote-sensing observations* as signatures of the sources of these energetic particles are observed. Fig. 2.3 show examples of remote-sensing observations of a solar energetic particle event. A few of these remote-sensing observations include:

- Type III radio bursts drift fast from high to low frequencies and is caused by energetic charged particles moving through plasma, with varying density, and inducing plasma waves at the plasma frequency or harmonics thereof. Type III bursts are associated in the corona with electron beams in solar flares, with these electron beams moving out towards $\sim 10\ r_\odot$ without any noticeable deceleration, at an average inferred speed of $\sim 0.33\ c$, varying between speeds of $\sim 0.25\ c$ and $\gtrsim 0.6\ c$, and corresponding to electron energies of $\sim 10 - 100\ \mathrm{keV}$, where $c = 2.998 \times 10^8\ \mathrm{m \cdot s^{-1}}$ is the speed of light in vacuum. It should however be noted that radio traps can occur in the flare, and such a flare might be radio

quiet [*Krüger*, 1979; *Benz*, 2008; *Shibata and Magara*, 2011; *Dresing*, 2014].

- Type II radio bursts are slow-drift bursts and are associated in the corona and beyond with charged particles accelerated by shock waves, with these disturbances moving at inferred speeds varying between $\sim 200 - 2000\,\mathrm{km \cdot s^{-1}}$. The type II burst from CMEs are caused by electrons accelerated at the shock front, but which do not cause type III bursts as they are transported downstream from the shock and cannot stream away [*Krüger*, 1979; *Chen*, 2011; *Webb and Howard*, 2012; *Dresing*, 2014].

- Line emissions, especially of the Hα-line, can be seen in different phases and parts of a solar flare [*Krüger*, 1979; *Benz*, 2008; *Shibata and Magara*, 2011; *Dresing*, 2014].

- Some solar flares are also visible in the visible light range. However, visible light is mostly used in coronagraphs, where the solar disk is masked out to reveal the white light from the solar corona. CMEs can be observed in coronagraphs by the Thompson-scattered light of particles in the CME [*Krüger*, 1979; *Tandberg-Hanssen and Emslie*, 1988; *Benz*, 2008; *Chen*, 2011; *Shibata and Magara*, 2011; *Dresing*, 2014].

- Energetic ultra-violet (EUV) images of the chromosphere and corona represent different temperatures. Coronal holes, which are the source of fast SW, can be seen as dark regions in EUV images as they are cold and less dense. Active regions, which are the regions where flares and CMEs originate, appear as bright spots in EUV images as they are hotter and denser [*Chen*, 2011; *Webb and Howard*, 2012; *Dresing*, 2014].

- The difference between two EUV images or coronagraphs (called 'difference images') show the changes from one image to the other and enhances the appearance of moving disturbances [*Dresing*, 2014].

- Different phases and parts of a solar flare can be seen in both soft and hard X-rays and it was already stated that X-rays are used to classify flares [*Krüger*, 1979; *Benz*, 2008; *Shibata and Magara*, 2011; *Dresing*, 2014].

- Gamma-rays can be produced in a solar flare by various nucleic processes, like capturing, inelastic scattering, spallation, particle decay, and annihilation [*Tandberg-Hanssen and Emslie*, 1988; *Ryan et al.*, 2000; *Benz*, 2008; *Shibata and Magara*, 2011].

The following most prominent spacecraft, which are used in studying energetic particles in the heliosphere, supply both in situ and remote-sensing observations: particle, SW, and HMF measurements are performed by the Interplanetary Monitoring Platforms (IMP) series of Earth-orbiting spacecraft, the Geostationary Operational Environment Satellites (GOES) orbiting the Earth, the International Sun-Earth Explorer (ISEE) near Earth's orbit, the MErcury Surface Space ENvironment GEochemistry and Ranging (MESSENGER) which began to orbit Mercury in March 2011, the Advanced Composition Explorer (ACE) at the Sun-Earth Lagrange point

(L1), and the two HELIOS spacecraft orbiting between 0.29 and 0.98 AU. The SOlar and Heliospheric Observatory (SOHO), also at L1, does not have magnetic field instruments, but provides coronagraphs and EUV images. The Solar TErrestrial RElations Observatory (STEREO) spacecraft consist of two satellites, one in a slightly smaller orbit than the Earth and hence ahead of Earth (STEREO A) and the other in a slightly larger orbit than the Earth and hence behind Earth (STEREO B). This leads to a $\sim 22^\circ$ increase in longitude per year between Earth and the two STEREO spacecrafts, giving STEREO the opportunity to observe the Sun from two distinct longitudes which are centred with respect to Earth. STEREO provides particle, SW, and HMF measurements, radio spectrograms, coronagraphs, and EUV images. Solar radio bursts are also observed by various ground-based stations and the WIND spacecraft, which cover lower frequencies. GOES, Yohkoh, and RHESSI provide X-ray observations, while the Fermi Large Area Telescope (Fermi-LAT) provides gamma-ray observations [*Dresing*, 2014]. The Parker Solar Probe (`www.nasa.gov/content/goddard/parker-solar-probe`), launched on the 12^{th} of August 2018, will collect in situ data during its seven year mission when passing 24 times through the upper corona at a distance of $\sim 8.2\, r_\odot \approx 0.0409$ AU from the Sun's surface. The Solar Orbiter (`http://sci.esa.int/solar-orbiter/`), scheduled to be launched in 2020, will only come within ~ 0.28 AU from the Sun during its seven year mission, but will supply in situ and remote sensing observations out of the ecliptic plane up to latitudes of $\sim 25^\circ$ and later $\sim 34^\circ$ during its extended mission.

2.2.2 Two Types of Solar Energetic Particles

As the name suggests, *solar energetic particles* (SEPs; also referred to as 'solar cosmic rays') are charged particles with energies ranging from a few keV to a few GeV, which are accelerated in solar flares and the shock waves associated with CMEs, and observed as an increase in fluxes lasting a few hours to a few days. SEP events become numerous during solar maximum (see Fig 1.8 in *Reames* [2017] for a comparison between SEP and GCR intensities and the SN). SEP events were originally connected to solar flares since CMEs were not yet discovered, but the exact acceleration mechanism was unknown. In subsequent years, the scientific community tried to explain all the properties of SEP events by the transport of energetic charged particles injected as a point source at the Sun, as would be suggested by a flare. This, which were termed the *Solar Flare Myth* by *Gosling* [1993], somewhat hindered the development and understanding of SEPs as it led to unphysical conclusions about the transport mechanisms. Today it is accepted that there are two distinct categories of SEPs, which will be discussed in this section, although it seems that the solar flare myth might still be deeply rooted [*Reames*, 1999, 2013, 2017].

SEP events were initially classified by *Pallavicini et al.* [1977] as *impulsive* or *gradual* events, connected to either impulsive or long-duration soft X-ray events at flares, respectively, with the latter also associated with CMEs inferred from coronagraphs. This classification was supported by *Cane et al.* [1986] which found that SEPs associated with the two classes of X-ray

events had different proton to electron ratios, but these authors also suggested different particle acceleration mechanisms for the two classes of events. The first evidence of two distinct acceleration mechanisms for SEPs came from radio observations when *Wild et al.* [1963] suggested that electrons were accelerated in flares to produce type III radio bursts and that accelerated protons in shock waves lead to the production of type II radio bursts. Meanwhile, various researchers found different characteristics between these two types of events, with the significant discovery by *Cliver et al.* [1983] that the intensity of X-ray flares is irrelevant in the intensity of large SEP events [*Reames*, 1999, 2013, 2017].

Gosling [1993] finally argued against the relationship between large SEP events and gradual flares and stressed the importance of shock acceleration of particles by CME associated shock waves. Gosling's arguments were based on the fact that there are magnetically well-connected flares with no associated SEP events and large gradual SEP events with no associated flares, that there is a strong correlation between large gradual SEP events and fast CMEs, and that ^{3}He-rich SEP events are associated with impulsive flares. This led *Hudson* [1995] to argue that the term "flare" should include not only the flare itself, but also the CME, shock, and any other related physics, *Miller* [1995] to argue that flares were a better subject for acceleration studies as they are more numerous, and *Reames* [1995] to argue that both flare and shock acceleration by CMEs should be studied separately. The argument of Reames for two distinct acceleration mechanisms and classifications was further supported by different elemental abundances and charge states of ions between impulsive and gradual events which could not be explained by the physics involved in flares and which indicated that the particles originate in two distinct plasmas, respectively. Today SEP events are still classified as impulsive or gradual events, but based on the temporal intensity profiles of the observed energetic particles (see e.g. Fig. 2.4), where the impulsive events are considered to be caused by flares and the gradual events by CME associated shocks. This clear cut separation of events are of course blurred if a CME accompanies a flare or if there are remnant flare particles accelerated by a CME [*Reames*, 1999, 2013, 2017].

2.2.3 Characteristics of Impulsive Solar Energetic Particle Events

Impulsive SEP events, which will be the focus of this study, are caused by solar flares and dominated by electrons streaming along the HMF away from the Sun. The temporal intensity profile of impulsive SEP events are characterized by a quick increase to the peak intensity, being $\sim 10 - 10^3$ times higher than background levels, followed by a slow decrease to background levels, as illustrated in the right panel of Fig. 2.4. The peak intensity is determined by the particle acceleration at the flare and the magnetic connection between the observer and the source, with the highest intensities seen by an observer directly connected to the source: due to the spiral pattern of the Parker HMF, an observer will see most impulsive SEPs originating from $\sim 40^\circ - 60^\circ$ west, with respect to an observer on Earth looking upwards to the Sun. A spread in the source longitude result from changes in connection longitude due to variations

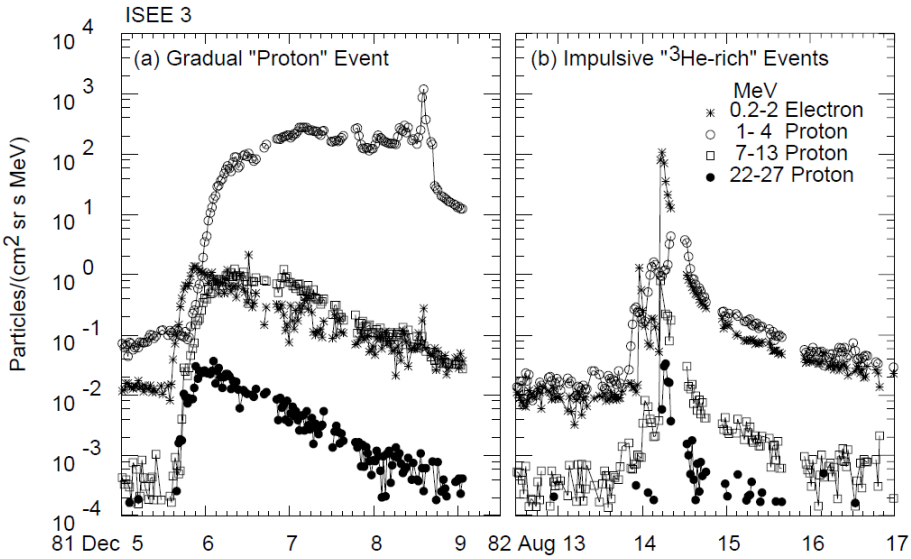

Figure 2.4: Temporal intensity profiles of electrons and protons measured in situ by ISEE 3 during a 'pure' gradual (*left*) and impulsive (*right*) solar energetic particle event in December 1981 and August 1982, respectively. The gradual event had a coronal mass ejection but no flare and the impulsive event had a series of flares but no coronal mass ejection. This figure was taken from *Reames* [1999].

in the SW speed and perhaps the random walk of magnetic fields (see e.g. the path of solar energetic electrons reconstructed by *Reames and Stone* [1986] from type III radio bursts). The duration of the temporal intensity profiles, normally lasting several hours, is determined by the acceleration of particles in the flare and scattering of the particles as they propagate from the Sun to the observer [*Reames*, 1999, 2013, 2017; *Lario et al.*, 2013; *Klein and Dalla*, 2017].

The elemental abundances of impulsive SEPs are close to the coronal and SW abundances, due to their origin in the corona. The most prominent differences are an increase in electrons, as electrons are easier accelerated by flares than ions, up to a $\sim$ 1000-fold enhancement in the $^3\mathrm{He}/^4\mathrm{He}$ ratio (first discovered by *Hsieh and Simpson* [1970]), and a $\sim$ 10-fold enhancement in the $\mathrm{Fe/O}$ ratio. Enhancements in heavy elements are also seen, with enhancements which are more pronounced for heavier elements. The event-to-event variations in the abundances of different elements are uncorrelated and the abundances are also independent of the energy and charge state of the particles. The charge state of impulsive SEPs are indicative of typical flare-heated material with a temperature of $\sim 10^6$ K. All elements up to silicon are fully ionized, the average ionization of iron is found to be ~ 20, and ionization increases with energy. The energy spectra (that is the flux per energy, normally assumed to have some sort of inverse power law dependence upon energy) of the various particles in impulsive SEP events seem to have no correlation between events or the various particles. Acceleration theories, however, predict a power law dependence between the spectral index and the charge-to-mass-ratio, which is observed. It is also predicted that self-generating turbulence or acceleration due to magnetic reconnection, could cause a break in the spectrum, especially for electrons. Very steep spectra (in terms of the spectral index or the slope of the spectrum on a log-log scale), steeper than

diffusive shock acceleration, are predicted and also observed, meaning that there are numerous low energy particles and very few very high energy particles (also called a 'soft spectrum'). Spectral indexes of various ions can range between $\sim 1.1 - 4.4$. The protons' spectral index in impulsive X-ray flares seems to lie between $\sim 1.5 - 4.5$, with most events having a spectral index of $\sim 2.7 - 3.0$, while the electrons' spectral index lie between $\sim 2.1 - 3.9$, with most events having a spectral index of $\sim 2.4 - 2.7$ and $\sim 3.3 - 3.6$ [*Hsieh and Simpson*, 1970; *Cook et al.*, 1984; *Cane et al.*, 1986; *Luhn et al.*, 1987; *Reames et al.*, 1994; *Miller and Roberts*, 1995; *Miller et al.*, 1996, 1997; *Reames*, 1999, 2013, 2017; *Tylka*, 2001; *Kontar and Reid*, 2009; *Tan*, 2018].

The $^3\mathrm{He}/^4\mathrm{He}$ ratio in the SW fluctuate significantly, but rarely exceed 1%, whereas this ratio is typically unity for impulsive events. It is estimated that more than 10% of the $^3\mathrm{He}$ in the flare volume is accelerated, that this acceleration must be in the lower corona as there is not enough $^3\mathrm{He}$ in the upper corona, and that the decrease in the $^3\mathrm{He}/^4\mathrm{He}$ ratio in large events is due to the depletion of $^3\mathrm{He}$ in the flare volume. The average abundance ratio of various elements to carbon seems to be grouped into three distinct groups based on the ratios: the first group consists of helium, nitrogen, and oxygen with ratios of ~ 1; the second group consists of neon, magnesium, and silicon with ratios of $\sim 2 - 4$; the last group consists of iron with a ratio of ~ 6.7. *Reames et al.* [1994] found that species in each group have a different charge-to-mass-ratio and suggested that these elements would resonate with turbulence in a given frequency range, where the frequency and the intensity of the resonant turbulence varies from group to group. For this preferential acceleration to be consistent with the observation that all elements up to silicon are fully ionized, the particles must be accelerated before they are ionized [*Reames*, 1999, 2013, 2017].

It seems that the enhancements in abundance ratios are due to resonant wave-particle interactions in the flare acceleration mechanism: magnetic reconnection in a flare could generate long wavelength turbulence, assuming the turbulence to be comparable to Alfvén waves; the large amplitude, long wavelength turbulence would then cascade to higher frequencies until the dissipation range is reached where they can interact with low energy particles through stochastic acceleration; near the end of the cascade, the turbulence would first resonate with ambient ions of the lowest cyclotron frequency, which is iron; the turbulence not absorbed by iron will continue to cascade and resonate with silicon, then magnesium, neon, oxygen, carbon, $^4\mathrm{He}$, and eventually hydrogen, leading to a declining pattern of enhancements. Electrons can also be accelerated in this way, but $^3\mathrm{He}$, however, is not accelerated in this way. The streaming electrons in flares, as suggested by type III radio bursts, generate oblique electromagnetic ion cyclotron waves having frequencies below that of hydrogen's cyclotron frequency where they can resonate directly with and accelerate $^3\mathrm{He}$ to MeV energies since these waves are not damped by any other wave-particle interactions. Heavier ions can also be accelerated by this mechanism as they interact with the waves through the second harmonic of their cyclotron frequency or through shear Alfvén waves produced at the same time [*Temerin and Roth*, 1992; *Miller and Viñas*, 1993; *Miller and Roberts*, 1995; *Miller et al.*, 1996, 1997; *Reames*, 1999, 2013, 2017].

2.3 Summary

In this chapter it was seen that the Sun is not a static object, but has a very dynamic nature. Periodicities in various observables of the Sun show both short term trends of a few hours to a few days, which are caused by the rotation of the Sun and transient events, and long term trends of a few hundred to a few thousand years, of which the origin is not yet known. The most important cycle is the ~ 11 year Schwabe cycle, which is driven by the Sun's magnetic field, and which is characterized by periods of maximum and minimum activity. The Sun's magnetic field changes polarity every ~ 11 years during solar maximum and this then leads to the ~ 22 year Hale cycle, during which the polarity of the Sun's magnetic field is restored. This dynamic nature of the Sun leads to the violent and energetic events of solar flares and coronal mass ejections (CMEs). The number of flares and CMEs follow the solar cycle with a slight delay between solar maximum and the maximum rate of flares and CMEs.

Parker [1958] proposed that there is a constant supersonic outflow of matter from the Sun, as its corona cannot be in hydrodynamic equilibrium. This solar wind (SW) is accelerated close to the Sun and then becomes a constant radially outflowing plasma with speeds varying between $\sim 400 - 800\ \mathrm{km \cdot s^{-1}}$. During solar minimum, slow SW are observed around the equatorial plane with a transition to fast SW towards the poles. During solar maximum, this latitudinal dependence disappears and a mixture of both slow and fast SW is observed over all latitudes. At the radial distance where the hydrodynamic ram pressure of the SW becomes greater than the magnetic field pressure, the Sun's magnetic field gets frozen into the SW and is carried away from the Sun to form the heliospheric magnetic field (HMF). In the Parker model, the HMF forms Archimedean spirals which lie on cones of constant latitude. The Sun's magnetic field has an approximate dipole structure during solar minimum, but a much more complex structure during solar maximum as the polarity of the field is reversed. The solar cycle is also evident in the HMF strength, with the field being stronger during solar maximum than solar minimum.

It was seen that solar energetic particles (SEPs), being energetic charged particles originating from solar flares and CMEs, can be observed in situ by spacecraft and that these observations are supplemented by in situ observations of the SW and HMF, as well as remote-sensing of the source regions of the energetic particles. SEP events can be classified as either impulsive or gradual, with the focus of this study falling on the former. Impulsive events are observed as a quick increase in energetic particle fluxes followed by a slow decrease in fluxes, lasting several hours, and is caused by solar flares. Impulsive events are characterized by elemental abundances typical of the corona, with enhancements in $^3\mathrm{He}$, highly ionized heavy ions, and electrons. The elemental abundances are caused by turbulent energy dissipation in the flare. Impulsive events also have steep spectra and directional particles streaming away from the Sun.

Chapter 3

The Micro-physics of Charged Particles Propagating in Slab Turbulence

To better understand the transport of solar energetic particles, a conceptual understanding of the micro-physics of charged particles propagating in electric and magnetic fields is needed. The movement of charged particles is governed by the Newton-Lorentz equation and this chapter starts with a discussion of results of its analytical solution to illustrate the basic effects which a charged particle is expected to experience. During this discussion, the solution for a uniform and constant electric and magnetic field will be discussed, drifts will be introduced, and a discussion of magnetic focusing will be given as a special application to solar energetic particles. Appendix A gives the analytical solution in the case of constant and uniform electric and magnetic fields and magnetic mirroring, as well as a discussion on how the Newton-Lorentz equation can be solved numerically to allow the incorporation of complex electric and magnetic fields. These numerical methods are used to investigate the interaction of charged particles with turbulent electric and magnetic fields. This discussion will start with an introduction into the basics of turbulence and wave-particle interactions, after which an investigation of the interaction of charged particles with model slab turbulence will be done.

Section 3.2.3 was presented as a presentation at the 2018 South African Institute of Physics' (SAIP) National Conference in Bloemfontein, South Africa.

3.1 The Newton-Lorentz Equation and Some Analytical Solutions

To understand the processes involved in the propagation of solar energetic particles (SEPs), the movement of a single charged particle in an electric and magnetic field must be studied. The motion of a particle, with mass m and charge q, moving with a velocity $\vec{v}$ in an electric field $\vec{E}$ and magnetic field $\vec{B}$, is governed by the *Newton-Lorentz* equation

$$m\frac{d(\gamma\vec{v})}{dt} = q\left(\vec{E} + \vec{v}\times\vec{B}\right), \tag{3.1}$$

where

$$\gamma = \frac{1}{\sqrt{1-(v/c)^2}} \tag{3.2}$$

is the relativistic Lorentz factor [*Chen*, 1984; *Choudhuri*, 1998; *Griffiths*, 1999]. The electrons of interest in SEP events mostly have energies $\lesssim 100$ keV while the protons of interest have energies $\lesssim 300$ MeV [*Reames*, 1999, 2013, 2017]. The Lorentz factor for a 100 keV electron is $\gamma_e = 1.1992$, while this is $\gamma_p = 1.3198$ for a 300 MeV proton. A non-relativistic description of SEPs is therefore not a bad approximation and this simplification will be used throughout this chapter. The most basic and important analytical solutions of the Newton-Lorentz equation can be found in any plasma physics textbook (see e.g. *Chen* [1984] or *Choudhuri* [1998]).

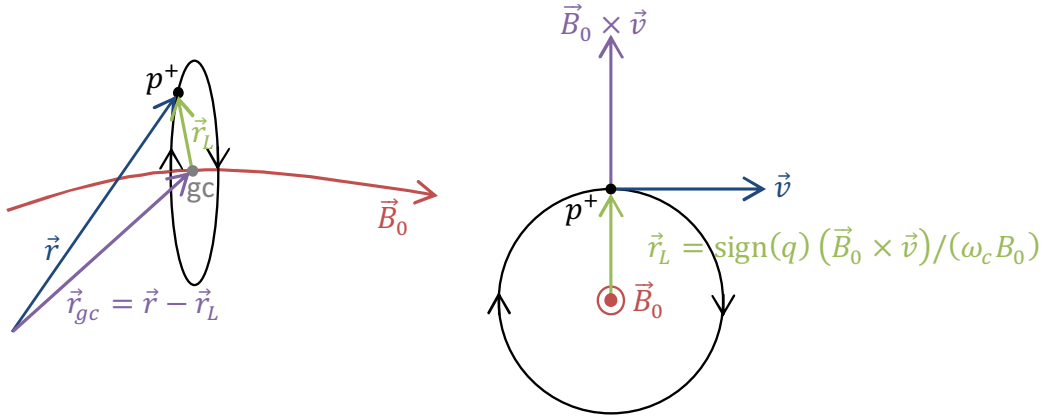

Figure 3.1: *Left:* Illustration of a proton's position (blue vector), guiding centre (purple vector), and directional Larmor radius (green vector) during its gyration (black circle, with the arrows indicating the rotation direction) around the background magnetic field line (red vector). This figure was adapted from *Northrop* [1961]. *Right:* A face-on illustration of the proton's orbit with the various terms in the calculation of the directional Larmor radius (Eq. 3.5) in the absence of an electric field.

Consider a particle moving perpendicular to a constant and uniform magnetic field, with strength B_0, in the absence of electric fields. The vector product in Eq. 3.1 implies that the particle experiences a centripetal acceleration and will therefore gyrate around the magnetic field, with positive and negative particles gyrating in a left- and right-hand manner, respectively (meaning that the direction in which one's fingers curl, if one's thumb is directed along the magnetic field, indicates the direction of gyration). The particle will gyrate around the magnetic field at an angular frequency

$$\omega_c = \frac{|q|B_0}{m}, \tag{3.3}$$

called the *cyclotron frequency*, while tracing a circle of radius

$$r_L = \frac{v_\perp}{\omega_c} = \frac{m v_\perp}{|q|B_0}, \tag{3.4}$$

called the *Larmor radius*, where $v_\perp$ is the speed of the particle perpendicular to the magnetic field. The imaginary point around which the particle gyrates, is called the *guiding centre* (GC) and its position can be found by subtracting a directional Larmor radius, which is essentially a

vector perpendicular to both the velocity and magnetic field pointing from the GC to the particle and having the Larmor radius as magnitude, from the particle's position. This is illustrated in Fig. 3.1 and can be written as

$$\vec{r}_{\rm gc} = \vec{r} - \frac{{\rm sign}(q)\vec{B}_0}{\omega_c B_0} \times \left(\vec{v} - \frac{\vec{E}_0 \times \vec{B}_0}{B_0^2} \right), \tag{3.5}$$

where $\vec{E}_0$ is the constant and uniform electric field, if present. If the particle had a velocity component parallel to the magnetic field $v_\parallel$, the particle would still gyrate around the magnetic field while moving along the magnetic field at this speed. The particle will therefore follow a helical path which can be decomposed into a gyration around the GC and the movement of the GC along the magnetic field (the GC will move along the magnetic field in the same way as the particle would; see Appendix A.1.1). This is illustrated in the left panel of Fig. 3.2. Notice that since the magnetic force is perpendicular to the direction of motion, the magnetic field does no work on the particle and cannot change its energy [*Northrop*, 1961; *Chen*, 1984; *Burger et al.*, 1985; *Choudhuri*, 1998].

It is convenient to introduce the particle's *pitch-angle*, defined as the angle between the particle's velocity vector and the magnetic field vector. An expression for the pitch-angle can be defined either by using the scalar product between the velocity and the magnetic field or by using the perpendicular and parallel speeds,

$$\alpha = \arccos\left(\frac{\vec{v} \cdot \vec{B}_0}{v B_0} \right) = \arcsin\left(\frac{v_\perp}{v} \right) = \arccos\left(\frac{v_\parallel}{v} \right) = \arctan\left(\frac{v_\perp}{v_\parallel} \right). \tag{3.6}$$

The parallel and perpendicular speeds can be calculated from the pitch-angle by

$$v_\parallel = v\cos\alpha = v\mu \tag{3.7}$$

and

$$v_\perp = v\sin\alpha = v\sqrt{1-\mu^2}, \tag{3.8}$$

respectively, where the so called *pitch-cosine*

$$\mu = \cos\alpha \tag{3.9}$$

is a quantity which is normally used in transport equations instead of the pitch-angle itself. Since the parallel and perpendicular speed is constant in a constant and uniform magnetic field, the pitch-angle will also be constant in such a field [*Northrop*, 1961; *Chen*, 1984; *Burger et al.*, 1985; *Choudhuri*, 1998].

If there is only a constant and uniform electric field, it will accelerate the particle in the (opposite) direction of the electric field if the particle is (negatively) positively charged. If both an electric and magnetic field exist, the particle will be accelerated along the magnetic field if the electric field has a component along the magnetic field. In addition to the gyration of the particle around the magnetic field, the particle can now also have motion perpendicular to

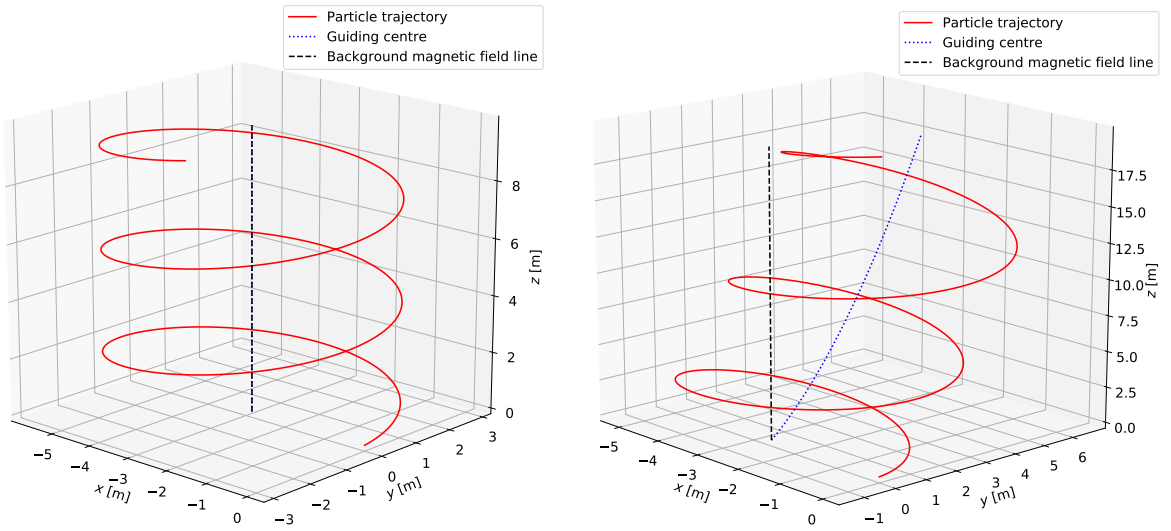

Figure 3.2: Simulation of an electron in a constant and uniform magnetic field (*left*) and magnetic with electric field (*right*) performed with the fourth-order Runge-Kutta scheme discussed in Appendix A. The trajectories of the particle (solid red) and its guiding centre (dotted blue; Eq. 3.5) are shown, together with a single magnetic field line (dashed black). The electron was initialized at $t_0 = 0$ s at the origin with an initial velocity $\vec{v}_0 = (0.5\hat{y} + 0.1\hat{z})$ m $\cdot$ s^{-1}. A time step of $\Delta t = 1 \times 10^{-3}$ s was used and $N_t = 10^5$ iterations was performed. The constant and uniform magnetic field was $\vec{B}_0 = 1 \times 10^{-12}\hat{z}$ T and $\vec{E}_0 = -(5\hat{x} + 1\hat{z}) \times 10^{-14}$ N $\cdot$ C^{-1} was used for the electric field. When the electric field is added, the spiral trajectory of the particle is stretched along the z-direction, due to the electric field acceleration, and the guiding centre moves away from the central magnetic field line along the y-axis, due to the electric field drift.

the magnetic field if the electric field has a component perpendicular to the magnetic field, as illustrated in the right panel of Fig. 3.2. The GC will have a constant velocity perpendicular to both the electric and magnetic field and the need of the $\vec{E}_0 \times \vec{B}_0$ term in its definition (Eq. 3.5) is recognised to account for this electric field drift. When including a gravitational force or a non-uniform or varying electric or magnetic field, various types of drifts will arise: in these cases, the GC will *drift* away from the magnetic field line on which it started [*Northrop*, 1961; *Chen*, 1984; *Burger et al.*, 1985; *Choudhuri*, 1998]. In the heliosphere, the most prominent drifts for SEPs will be due to the curvature and gradient of the heliospheric magnetic field (HMF). Although drifts will not be considered in this study, the interested reader is referred to *Dalla et al.* [2013] for analytical expressions of the drift velocities of SEPs in a Parker HMF.

3.1.1 Magnetic Focusing

A derivation of magnetic mirroring and the invariance of the magnetic moment is given in Appendix A.1.2. An interesting effect occurs when the magnetic field has a gradient along it: the particle will experience a force parallel to the magnetic field (Eq. A.12) which will be in the opposite direction of the gradient. Due to the invariance of the magnetic moment (Eq. A.11) and the conservation of kinetic energy, this force is accompanied by an interchange between parallel and perpendicular energy: as the particle moves into a region of larger magnetic field strength, its perpendicular speed increases, with the effect that its parallel speed decreases

[*Chen*, 1984; *Choudhuri*, 1998]. The *mirroring condition* of Eq. A.13 (see its discussion for details) in terms of the pitch-cosine, is given by

$$\mu_m = \sqrt{1 - \frac{B}{B_m}}. \tag{3.10}$$

Due to the decrease of the HMF strength with heliocentric radius, SEPs will experience the opposite of magnetic mirroring, called *magnetic focusing*. As a particle moves into regions of weaker parallel magnetic fields, the particle's perpendicular speed will decrease while its parallel speed will increase, causing the particle's motion to become increasingly ballistic [*Roelof*, 1969]. Since focusing causes the perpendicular speed to decrease, it might be incorrectly expected that the Larmor radius (which is dependent on the perpendicular speed) would also decrease. The Larmor radius, however, is inversely proportional to the magnetic field strength, which decreases as $1/r$ for the Parker HMF in the equatorial plane. From the definition of the magnetic moment (Eq. A.11) and its invariance, it can be seen that the perpendicular speed does not change at the same rate as the magnetic field, since the magnetic moment is dependent on the square of the perpendicular speed. The HMF strength therefore decreases faster than the perpendicular speed close to the Sun and this would causes the Larmor radius to increase as SEPs move away from the Sun.

3.2 Turbulence, Scattering, and Diffusion

Due to the low density of the solar wind (SW), the Coulomb collision rate between particles is much smaller than the cyclotron frequency. The SW and other low density plasmas within the SW, such as cosmic rays or SEPs, are therefore approximated as collisionless plasmas and the charged particles in these plasmas would have followed the smooth motions described in the previous section, were it not for turbulence. The invariance of the magnetic moment will be violated by varying electric and magnetic fields with a characteristic frequency equal to or larger than the cyclotron frequency. This will cause the particle to lose or gain energy and its GC to jump between magnetic field lines in a random manner, compared to normal drifts [*Chen*, 1984; *Tsurutani and Lakhina*, 1997]. In this section, the influence of turbulence on the propagation of charged particles will be investigated and illustrated, starting with a general background discussion on magnetic turbulence. In order to better understand the possible influence of turbulence, the interactions between electromagnetic plasma waves and particles will then be discussed. Finally, a toy model for slab turbulence will be constructed and the numerical methods of Appendix A will be used to simulate the motion of a test particle in this slab model. These discussions and simulations aim to illustrate the concepts of pitch-angle scattering, momentum diffusion, and perpendicular diffusion.

3.2.1 Turbulence in the Heliosphere

Parker [1958] warned that the HMF will not be smooth, but will be perturbed due to instabilities in the SW. Magnetic fields contain *turbulence*, which can be described as seemingly random fluctuations containing some level of correlations/structures. The total magnetic field can be written as the sum of a large-scale average/background $\vec{B}_0$ and fluctuating $\delta\vec{B}$ magnetic field,

$$\vec{B}(s_{\parallel};\vec{s}_{\perp}) = B_0(s_{\parallel})\hat{e}_{\parallel} + \delta B(s_{\parallel};\vec{s}_{\perp})\hat{e}_{\perp}, \tag{3.11}$$

where $s_{\parallel}$ and $\vec{s}_{\perp}$ are the position along and perpendicular to the background magnetic field, respectively, and $\hat{e}_{\parallel}$ and $\hat{e}_{\perp}$ are unit vectors in the direction parallel and perpendicular to the background magnetic field, respectively. It is assumed, for simplicity, that the fluctuations are perpendicular to the background magnetic field, such that $\vec{B}_0 \cdot \delta\vec{B} = 0$, although it is possible for the decomposition to have a turbulent magnetic field along the background magnetic field if longitudinal fluctuations are also present. It is furthermore assumed that the fluctuations are random, such that $\langle \delta\vec{B} \rangle = \vec{0}$ and $\langle \vec{B} \rangle = \vec{B}_0$, where $\langle \cdots \rangle$ indicates a suitable average. The variance of the fluctuations, δB^2, is related to the energy contained in the turbulence [*Goldstein et al.*, 1995; *Choudhuri*, 1998; *Shalchi*, 2009].

Two viewpoints exist in turbulence theory: firstly the *turbulence viewpoint* assumes a dynamical interaction between fluctuations with a statistical description of turbulence; secondly the *wave viewpoint* assumes a superposition of different types of small-amplitude waves of different wave numbers and phases with frequencies which are deterministically governed by the dispersion relations of these waves, and that there is little interaction between the waves themselves. Although a consistent theory of turbulence would probably require a mixture of both these viewpoints, it is conceptually appealing to think of turbulence as waves. *Kolmogorov* [1941] (see *Kolmogorov* [1991] for a translation) developed the first dynamical theory of fully developed homogeneous and isotropic hydrodynamic turbulence in a steady state, meaning that the generation of the turbulence is assumed to be constant, that the generation mechanism has no influence on the evolution of the turbulence, and that the turbulence is independent of translations, rotations, or reflections. The turbulence can be thought of as being added to the fluid at large scales, that is, at long wavelengths or small wave numbers. The energy is then transferred from these large scales to smaller scales via a cascade process, up to small length scales where the fluid is heated by the viscous dissipation of the turbulence. Kolmogorov showed on dimensional grounds that the energy contained in the turbulence as a function of the wave number k, called the *energy spectrum* $E(k)$, must be proportional to the wave number by

$$E(k) \propto k^{-5/3}, \tag{3.12}$$

during the cascade process. This range in the energy spectrum where the energy cascade occurs, is called the *inertial range*. *Iroshnikov* [1964] and *Kraichnan* [1965] extended this theory to plasmas and showed that the energy spectrum should scale as

$$E(k) \propto k^{-3/2} \tag{3.13}$$

in the inertial range. This change in the wave number dependence is caused by the cascade rate being affected by the background magnetic field and the way in which the waves propagate along the background magnetic field. The Kolmogorov dependence is surprisingly seen more often in SW turbulence than that of Kraichnan and will therefore also be used here [*Goldstein et al.*, 1995; *Choudhuri*, 1998; *Dröge*, 2000].

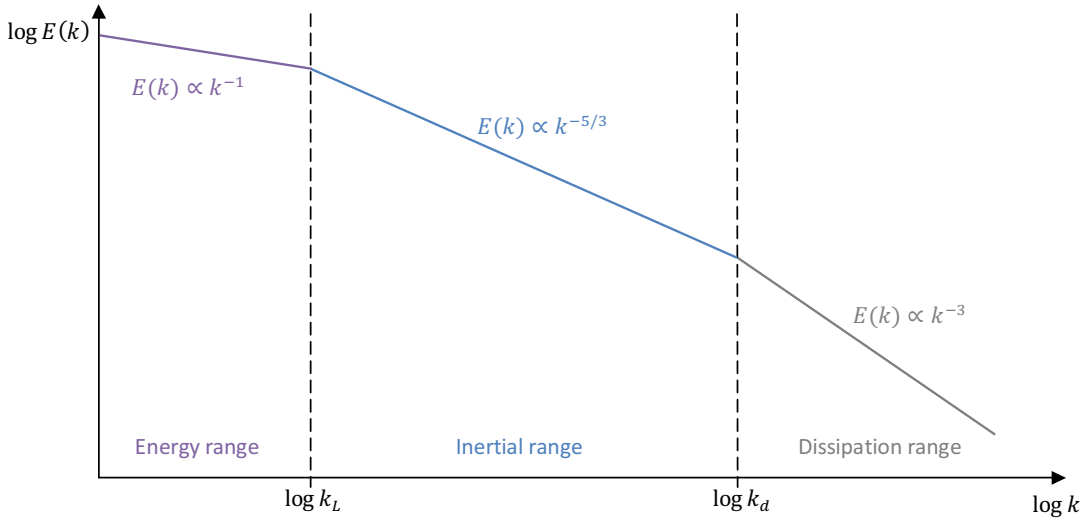

Figure 3.3: General energy spectra of slab turbulence indicating the different wave number dependencies discussed in the text. The spectra in the energy range can be flatter. The spectra in the dissipation range can be steeper and can also have more than one break or an exponential cut-off.

From this discussion it can be expected that the general energy spectrum has at least three regions, which are shown in Fig. 3.3. At small wave numbers or large wavelengths, energy is added to the turbulence and this is called the *energy range*. In the heliosphere, turbulence is generated by the expansion of the SW, fluctuations in the SW, stream instabilities and shear between fast and slow SW streams, magnetic reconnection, pickup ions, streaming energetic particles, wave excitement from wave interaction within turbulence, etc. In the energy range a $\sim k^{-1}$ or flatter spectra is normally assumed for slab turbulence (see e.g. the spectra used by *Engelbrecht and Burger* [2013] and illustrated by *Strauss et al.* [2017]). At the wave number k_L, the energy cascade sets in and the inertial range is found up to the wave number k_d where the turbulence is dissipated. The spectra has a $\sim k^{-3}$ or steeper dependence in the *dissipation range* where the energy is dissipated into the plasma [*Goldstein et al.*, 1995; *Shalchi*, 2009]. The wave number k_d is primarily dependent on the proton cyclotron frequency in the SW [*Woodham et al.*, 2018], as this is the frequency where waves will be damped by ions, but the exact dissipation process is still hotly debated. It will be seen that certain waves cannot resonate with protons and hence, the cascade of these waves will continue to the electron cyclotron frequency, where a second break might be expected in the spectra, after which the spectra becomes very steep. *Engelbrecht and Strauss* [2018] points out that the thermal motion of the SW protons will change the dispersion relations for the turbulent waves (see e.g. the dispersion relations in Chapters 4 and 12 of *Chen* [1984] and *Choudhuri* [1998], respectively), causing a complex transition in the spectrum to an electron inertial range.

Based on a general form of the second-rank correlation tensor between magnetic fluctuations of isotropic turbulence or turbulence that is axisymmetric around the background magnetic field, the turbulent fluctuations are normally decomposed further into so-called *slab* and *two-dimensional* (2D) turbulence,

$$\delta\vec{B}(s_{\parallel};\vec{s}_{\perp}) = \delta\vec{B}_{\rm slab}(s_{\parallel}) + \delta\vec{B}_{\rm 2D}(\vec{s}_{\perp}), \tag{3.14}$$

where the slab (2D) turbulence have wave vectors $k_{\parallel}$ parallel ($k_{\perp}$ perpendicular) to the background magnetic field and is only dependent on the position along (perpendicular to) the background magnetic field. 2D turbulence will mostly be neglected in this study. Notice that if the turbulence is not symmetric under reflections, then the decomposition has a third component which is imaginary, and normally neglected for simplicity, associated with the magnetic helicity of the fluctuations. Slab turbulence can be thought of as plasma waves propagating along the background magnetic field, such as Alfvén or left- and right-hand polarized waves. Similarly, 2D turbulence can be thought of as plasma waves propagating perpendicular to the background magnetic field, such as magnetosonic or ordinary and extraordinary waves. In nearly incompressible magnetohydrodynamic turbulence, 2D turbulence can be thought of as 'magnetic islands' (magnetic vortices in the plane perpendicular to the background magnetic field) [*Chen*, 1984; *Goldstein et al.*, 1995; *Shalchi*, 2009; *Karimabadi et al.*, 2013; *Zank et al.*, 2017].

Slab and 2D turbulence occur together in the heliosphere, but it is observationally difficult to resolve the 2D component, since the propagation direction of a 2D fluctuation can lie anywhere within a plane perpendicular to the HMF. *Bieber et al.* [1996] found that the SW turbulence is composed of 74% 2D and 26% slab turbulence between 0.3 and 1 AU. Due to this, a ratio of $80\%/20\%$ of 2D/slab turbulence is normally used in theories, but it is known from simulations that turbulence evolves. Since the waves move faster than the plasma outflow below the Alfvén radius, it is expected that slab turbulence in this region would be composed of waves propagating both outwards from and inwards to the Sun, with inwards propagating waves being unable to escape the Alfvén radius. Slab turbulence above the Alfvén radius is therefore composed of waves propagating outwards from the Sun, but due to the evolution of the turbulence, waves propagating towards the Sun are again encountered further out towards 1 AU [*Goldstein et al.*, 1995; *Dröge*, 2000; *Shalchi*, 2009]. All of these complications with regard to turbulence should be kept in mind for the propagation of SEPs and it is hoped that the current Parker Solar Probe and upcoming Solar Orbiter missions would shed more light on these questions and the effect thereof on SEPs.

3.2.2 Wave-particle Interactions

To understand the effect of slab turbulence on the propagation of charged particles, consider the *wave-particle interaction* between charged particles and circularly polarised Alfvén waves moving along the background magnetic field in the absence of a background electric field. In what follows it is assumed that all of space is filled with a wave field consisting of waves

with various wavelengths. Note that although there are many waves, waves with a specific wavelength will be referred to as a 'wave', while 'waves' will be used to refer to the collective spectrum of waves. Alfvén waves are used here for simplicity due to their constant phase velocity,

$$\frac{\omega}{k} = V_A, \tag{3.15}$$

where ω is the wave's angular frequency and $V_A = B_0/\sqrt{\mu_0 \rho_0}$ is the Alfvén speed, with ρ_0 the mass density of the background plasma ($V_A \approx 35$ km $\cdot$ s^{-1} at Earth). In Fig. 3.4, left- and right-hand circularly polarised waves are shown and it can be seen that the path traced out by the magnetic field vector is analogous to the path traced out by positively and negatively charged particles, respectively. Note that the polarisation is defined by the sense of rotation of the waves' magnetic field vector with respect to a point in the background magnetic field and is independent of the waves' propagation direction [*Tsurutani and Lakhina*, 1997].

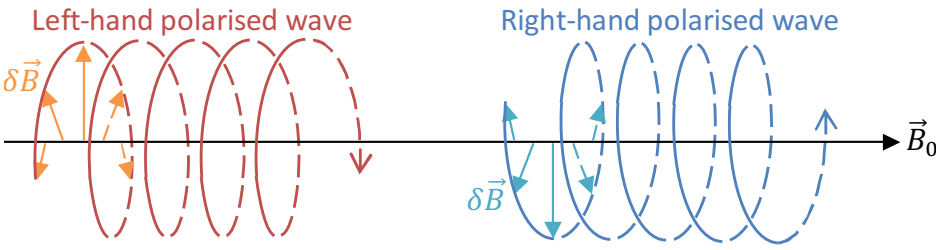

Figure 3.4: Left- and right-hand, parallel propagating, circularly polarised, electromagnetic plasma waves. This figure was adapted from *Tsurutani and Lakhina* [1997].

Resonance with Slab Turbulence

The particle will resonate with a wave if the particle and wave's magnetic field vector have the same sense of rotation and if the wave's angular frequency is equal to the particle's cyclotron frequency, or harmonics thereof, as seen in the GC reference frame,

$$\omega^* = \text{sign}(q) n \omega_c^*, \tag{3.16}$$

where * refer to that quantity in the GC frame, the wave's angular frequency is taken as positive, and $n = 0; \pm 1; \pm 2; \ldots$ indicates the harmonic of the cyclotron frequency, with the positive (negative) sign for left-(right-)handed waves. In transforming back to a stationary observer's frame, the frequency of the wave will be Doppler shifted due to the velocity of the particle relative to the wave. Hence, the *resonance condition* is given by

$$\omega - \vec{k} \cdot \vec{v} = \text{sign}(q) n \omega_c \tag{3.17a}$$

$$\omega - j k_\parallel v_\parallel = \text{sign}(q) n \omega_c, \tag{3.17b}$$

where $j = +1$ ($j = -1$) if the wave is propagating in the same (opposite) direction as the background magnetic field. The non-linearity of the dispersion relations $\omega(k)$ would generally result in more than one resonance for a specific wave mode (see e.g. *Chen* [1984] or *Choudhuri*

[1998]), but for non-dispersive Alfvén waves moving at a constant speed, the wave number with which the particle will resonate, is given by

$$k_{\parallel}^{\mathrm{res}} = \frac{\omega - \mathrm{sign}(q) n \omega_c}{j v_{\parallel}} = \frac{\mathrm{sign}(q) n}{R_L \left(V_a / v - j \mu \right)}, \tag{3.18}$$

where R_L is the *maximal Larmor radius* (with $v_\perp$ replaced by v in Eq. 3.4). The former of these two expressions shows that the particle's parallel speed Doppler shifts the wave frequency to its cyclotron frequency. This expression can also be solved for the resonant parallel velocity

$$|v_{\parallel}^{\mathrm{res}}| = V_A \left| 1 - \mathrm{sign}(q) n \frac{\omega_c}{\omega} \right|. \tag{3.19}$$

From the latter expression in Eq. 3.18 it can be interpreted that a resonance will occur if the particle's maximal Larmor radius approximately matches the wave's wavelength [*Chen*, 1984; *Tsurutani and Lakhina*, 1997; *Dröge*, 2000; *Engelbrecht and Strauss*, 2018].

The most basic, so called *Cherenkov* or *Landau resonance*, for $n = 0$, is not a resonance in the sense that the frequencies match in the GC frame, as can be seen from Eq. 3.16. In this case the particle is co-moving with the wave, according to Eq. 3.19, with the result that the wave's magnetic field vector is stationary with respect to the particle and that the particle does not experience the electric field induced by the wave. This causes a strong interaction between the particle and wave for an extended time. As illustrated in Fig. 3.6, and discussed later, the wave's magnetic field will exert a force on the particle which will change the particle's parallel and perpendicular speed. This change in the velocity components will cause a change in the resonance condition, since the particle will now move slower or faster than the wave [*Kennel and Petschek*, 1966; *Tsurutani and Lakhina*, 1997]. The resonance condition of Eq. 3.17a implies the following cases of when a particle can resonate with a wave and when it cannot:

1. A positively or negatively charged particle can resonate with a left- or right-hand polarised wave, respectively, propagating towards the particle,
2. but a positively or negatively charged particle cannot resonate with a left- or right-hand polarised wave, respectively, propagating in the same direction as the particle,
3. and a positively or negatively charged particle can resonate with a right- or left-hand polarised wave, respectively, propagating in the same direction as the particle if $|v_{\parallel}| > V_A$,
4. but a positively or negatively charged particle cannot resonate with a right- or left-hand polarised wave, respectively, propagating towards the particle.

The $|n| = 1$ resonance is called the *fundamental cyclotron resonance* and if the particle and wave move in opposite directions, it is called the *normal cyclotron resonance*. To explain the first resonance statement, consider a negative particle and right-hand polarised wave approaching each other, as illustrated in the top panel of Fig. 3.5. For all the resonances except the $n = 0$ resonance, the wave's magnetic field vector is rotating at the cyclotron frequency, or harmonics thereof, in the GC frame according to the resonance condition (Eq. 3.16), but not in the

observer's frame according to Eq. 3.17b: in the observer's frame (left panel), the particle is moving slightly slower than the wave, while both the particle and wave's magnetic field vector are rotating in the same sense, but the wave's angular frequency is less than the cyclotron frequency; transforming to the GC frame (middle panel), where the particle is only gyrating around the GC, the wave is approaching the particle 'faster' as seen by the particle, so that the particle will see the wave's magnetic field vector rotating at a faster frequency than in the observer's frame, and this frequency will be equal to the cyclotron frequency [*Tsurutani and Lakhina*, 1997].

To explain the second resonance statement, consider a negative particle and right-hand polarised wave moving in the same direction, as illustrated in the second panel from the top of Fig. 3.5. The particle is overtaking the wave and the wave's angular frequency is smaller than the cyclotron frequency. In the GC frame, the wave would approach the particle at a speed faster than the wave speed. Due to the relative motion between the wave and particle, it would seem that the wave's magnetic field vector completes more gyrations in the time it takes the particle to complete one gyration. The wave will therefore have an angular frequency equal to the cyclotron frequency, but the particle would see the magnetic field vector rotating in a left-handed manner and the wave-particle interaction cannot occur.

The third resonance statement is illustrated in the second last panel of Fig. 3.5. Consider a negative particle and left-hand polarised wave moving in the same direction. In the observer's frame, the particle is moving over the wave, while the wave's magnetic field vector is rotating in the opposite direction to the particle at a frequency slower than the cyclotron frequency. Transforming to the GC frame, the wave is approaching the particle with a speed faster than the wave speed and due to the relative motion between the wave and particle, it would seem that the wave's magnetic field vector does not complete a gyration in the time it takes the particle to complete a gyration, such that the wave's magnetic field vector rotates at the cyclotron frequency in a right-hand manner. The resonances where a positive or negative charged particle sees a right- or left-hand polarised wave as a left- or right-hand polarised wave, respectively, is called *anomalous cyclotron resonances*. Notice however, that the particle must overtake the wave for this resonance to occur and the parallel speed must therefore satisfy $|v_{\parallel}| > V_A$. This implies that if the particle's pitch-angle is close to 90° ($\mu \sim 0$), then the parallel speed would most likely not satisfy the resonance condition, which leads to a so-called *resonance gap* around $\mu = 0$ where the particle cannot experience anomalous cyclotron resonance [*Tsurutani and Lakhina*, 1997].

To explain the last resonance statement, consider a negative particle and left-hand polarised wave moving in opposite directions, as illustrated in the bottom panel of Fig. 3.5. In the observer's frame, the wave's magnetic field vector is rotating in the opposite direction to the particle at a frequency faster than the cyclotron frequency. Due to the relative motion between the particle and the wave, the particle will see the wave's magnetic field vector rotating at the cyclotron frequency, but still in the opposite sense so that the wave-particle interaction cannot

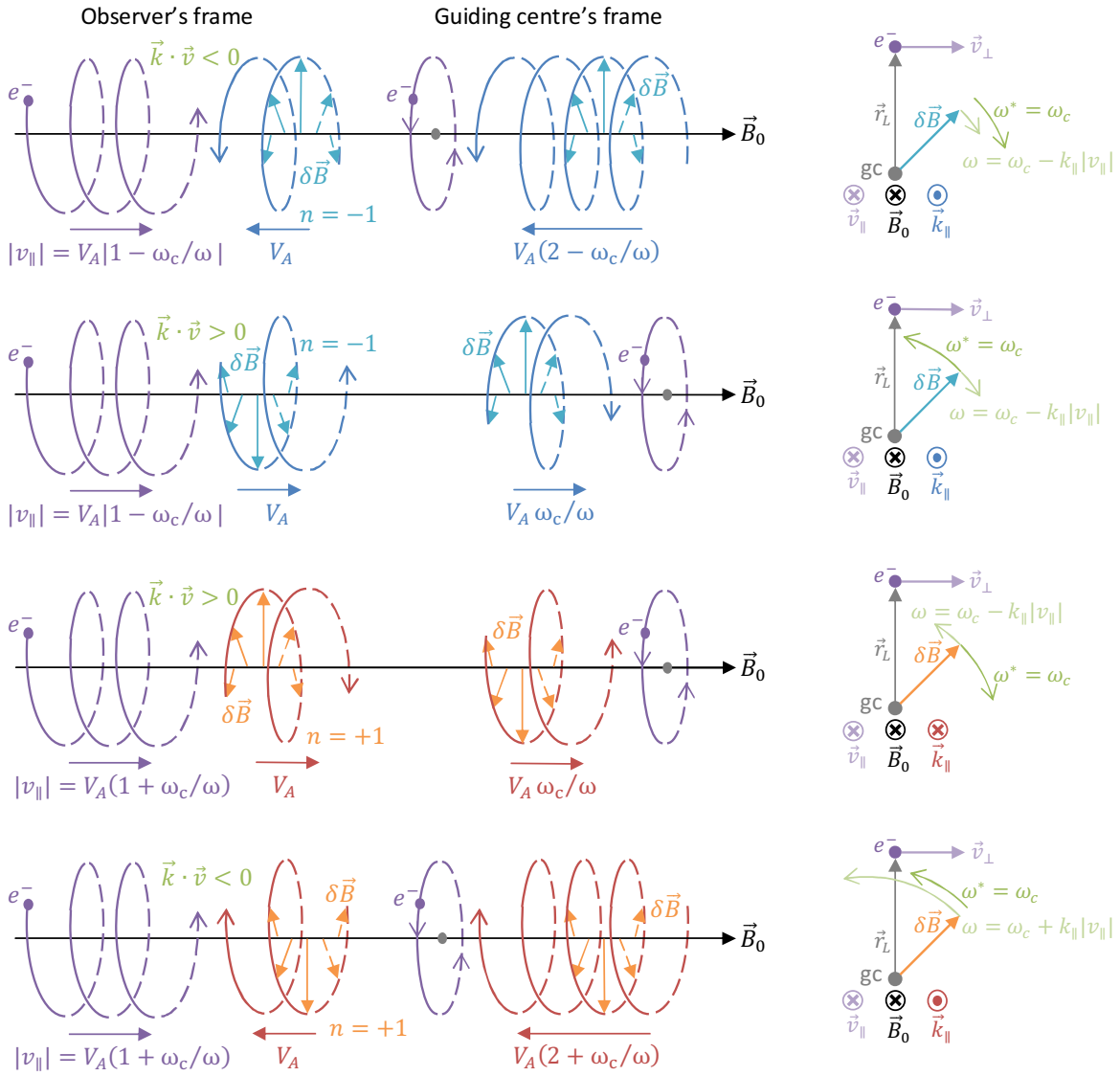

Figure 3.5: Illustration of the resonance conditions for the fundamental cyclotron resonance ($|n| = 1$). Shown are the situations for an electron interacting with a right-hand circularly polarised Alfvén wave propagating towards (*top*) and in the same direction as the electron (*second from top*), as well as interaction with a left-hand circularly polarised Alfvén wave propagating towards (*bottom*) and in the same direction as the electron (*second from bottom*). Each situation is shown in the observer's frame (*left*), guiding centre's frame (*middle*), and a face-on illustration of the electron's orbit (*right*). See the text for details.

occur. Notice that if there are waves of both polarisations moving in both directions along the background magnetic field, there should not be any resonance gap, since the particle would find some wave to interact with.

Energy Conservation in the Wave Frame, but not in the Observer's Frame

The effect of the wave-particle interaction on the particle's motion can be described using Fig. 3.6 and following a discussion similar to that of *Tsurutani and Lakhina* [1997]. Notice that the wave's magnetic field vector can be translated to the position of the particle since slab

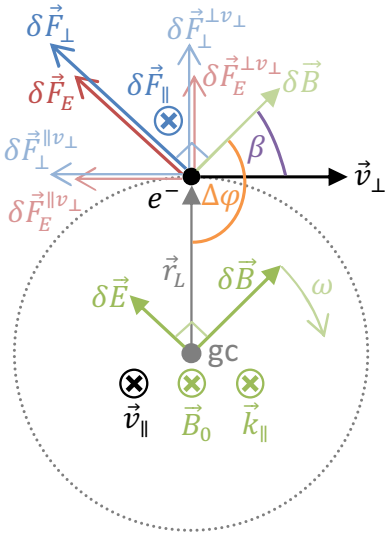

Figure 3.6: Face-on illustration of an electron's orbit and the various forces on the electron during a wave-particle interaction with a parallel propagating, right-hand circularly polarised, electromagnetic plasma wave. Notice that the charge of the particle was not considered for the directions of the forces, but is included in the equations presented in the discussion. See the text for details.

turbulence is independent of the position perpendicular to the background magnetic field. Let

$$\beta(\tau) = \arccos\left[\frac{\vec{v}_\perp(\tau)\cdot\delta\vec{B}(\tau)}{v_\perp(\tau)\delta B(\tau)}\right] \tag{3.20}$$

be the angle between $\vec{v}_\perp$ and $\delta\vec{B}$ at the time elapsed τ since the particle has started interacting with the wave. From the resonance condition it can be expected in general that $d\beta/d\tau \propto k_\parallel|v_\parallel|$ and hence, the interaction time will be short if the particle is moving fast or if the wave has a high frequency. In both these cases the wave will resonate with high harmonics of the cyclotron frequency, implying that the wave's electric and magnetic field vectors change rapidly during the interaction, yielding a faster change in the resonance condition.

The Lorentz force parallel to the background magnetic field on the particle due to the wave, in terms of the perpendicular velocity, is

$$\delta\vec{F}_\parallel = qv_\perp\delta B\sin\beta\hat{B}_0, \tag{3.21}$$

where $\hat{B}_0$ is a unit vector in the direction of the background magnetic field. From this it follows that the force exerted by the wave on the particle depends on the phase difference between the particle and wave. Let $\Delta\phi$ be the phase difference between the particle and the wave (the angle between the directional Larmor radius and the wave's magnetic field vector at the particle's position). There will be no force if the particle is $90°$ or $270°$ out of phase with the wave ($\beta = 0°$ or $\beta = 180°$) and the force will be a maximum if the particle is in phase or $180°$ out of phase ($\beta = 90°$ or $\beta = 270°$). For a positive particle, the force will be in the direction of motion, and hence the parallel speed will increase, if $90° < \Delta\phi < 270°$ ($0° < \beta < 180°$). Similarly, the force will be in the opposite direction of motion, and hence the parallel speed will decrease, if $0° < \Delta\phi < 90°$ or $270° < \Delta\phi < 360°$ ($180° < \beta < 360°$). For a negative particle, this situation

would be reversed. This situation can also be described by using the parallel velocity, in which case the Lorentz force on the particle is perpendicular to the background magnetic field,

$$\delta\vec{F}_\perp = q\vec{v}_\parallel \times \delta\vec{B}, \tag{3.22}$$

and the component of this force parallel to the perpendicular velocity is

$$\delta\vec{F}_\perp^{\parallel v_\perp} = qv_\parallel \delta B \cos\left(\frac{\pi}{2}+\beta\right)\hat{v}_\perp = -qv_\parallel \delta B \sin\beta\hat{v}_\perp, \tag{3.23}$$

where $\hat{v}_\perp$ is a unit vector in the direction of the particle's perpendicular velocity. In terms of the phase difference between the particle and the wave, the same applies to this force in regards to the zero and maximum of the force as in the previous case, just with an opposite sign in the case of a maximum. Here, however, the force is aligned with (opposite to) the perpendicular velocity, and hence the perpendicular velocity will increase (decrease), for the phase differences or values of β where the parallel speed decreases (increases).

There seems to be an exchange of energy between the parallel and perpendicular speed and it is expected that the change in parallel speed is equal to the negative change in the perpendicular speed since the magnetic field alone cannot do any work on the particle. Consider only the magnetic forces exerted on the particle by the wave, assume that the particle gains a quantum of energy $\Delta K = \hbar\omega$ from the wave during an interaction, and that the change in parallel momentum is $m\Delta v_\parallel = \hbar k_\parallel$, where $\hbar$ is Planck's constant divided by 2π. If the energy change is small compared to the particle's kinetic energy ($K = mv_\parallel^2/2 + mv_\perp^2/2$), then it would hold that

$$\begin{aligned}
\Delta K &\approx m\left(v_\parallel\Delta v_\parallel + v_\perp\Delta v_\perp\right)\\
\frac{m\Delta v_\parallel}{k_\parallel}\omega &= m\left(v_\parallel\Delta v_\parallel + v_\perp\Delta v_\perp\right)\\
0 &= m\left(v_\parallel - V_A\right)\Delta v_\parallel + mv_\perp\Delta v_\perp,
\end{aligned}$$

which gives

$$\frac{1}{2}m\left(v_\parallel - V_A\right)^2 + \frac{1}{2}mv_\perp^2 = \text{constant} \tag{3.24}$$

upon integration. This shows that the particle's energy in the *wave frame* is conserved [*Tsurutani and Lakhina*, 1997]. The wave will have an electric field $\delta\vec{E}$ in the observer's frame which is perpendicular to the wave's magnetic field vector and hence in the same direction as $\delta\vec{F}_\perp$. This will be seen in the next section where a slab model is derived and it will also be shown that the magnitude of this induced electric field is proportional to the magnitude of the fluctuating magnetic field by $\delta E = V_A\delta B$ (Eq. 3.40). Analogous to $\delta\vec{F}_\perp$, the component of the electric force parallel to the perpendicular velocity is

$$\delta\vec{F}_E^{\parallel v_\perp} = -qV_A\delta B\sin\beta\hat{v}_\perp. \tag{3.25}$$

Everything applicable to $\delta\vec{F}_\perp^{\parallel v_\perp}$ in terms of β, is also applicable to $\delta\vec{F}_E^{\parallel v_\perp}$, but unlike the magnetic forces, the electric force has no component along the background magnetic field which can cancel its energy changes. *Thus, the particle's energy is conserved in the wave frame, but not in the observer's frame.*

There exists an exchange of energy between the particle and the wave: if there are a significant number of particles gaining energy from the wave, the wave will be damped (the wave's amplitude will decrease) and this is called *Landau damping*; if there are a significant number of particles losing energy to the wave, the wave will be excited (the wave's amplitude will increase) and this is called the *Cherenkov instability* [*Tsurutani and Lakhina*, 1997]. Physically, the amplification or damping of the wave would be caused by the collective electric and magnetic field induced by the particles, being either in or out of phase, respectively, with the wave. Landau damping (The Cherenkov instability) occurs if the particles' velocity distribution is a monotonically decreasing (increasing) function of speed, such as a Maxwellian distribution (a beam of particles moving faster than the wave), having more particles moving slightly slower (faster) than the wave in comparison to particles moving slightly faster (slower) than the wave, resulting in the wave's electric field accelerating (decelerating) the slightly slower (faster) particles until they co-move with the wave [*Chen*, 1984; *Choudhuri*, 1998].

From the previous discussion, it can be written that $\Delta K/\Delta K_{\parallel} \approx \omega/k_{\parallel}v_{\parallel}^{\mathrm{res}}$, with substitution of Eq. 3.17b into this expression giving

$$\frac{\Delta K}{\Delta K_{\parallel}} = \frac{j}{1-\mathrm{sign}(q)n\omega_c/\omega}. \tag{3.26}$$

First consider the normal resonance ($|n| = 1$) for simplicity. If $\omega_c/\omega \gg 1$, then it follows from Eq. 3.19 that the particle is moving much faster than the wave and from Eq. 3.26 it follows that the change in the particle's energy is small, since $\Delta K \sim (\omega/\omega_c)\Delta K_{\parallel}$. Physically, due to the particle moving so fast relative to the wave, β is changing so quickly during the interaction that the energy lost or gained is almost immediately gained or lost again, respectively. It is said that the wave's magnetic forces dominate the electric forces and the particle does not feel the effect of the electric field. If either $\omega_c/\omega \ll 1$ or $\omega_c/\omega \approx 1$, that is when the particle is moving with the wave or the fundamental resonance occurs, respectively, then it follows from Eq. 3.26 that the change in the particle's energy might be significant. Here the electric forces dominate the magnetic forces and physically it is easy to understand this large energy change since the particle is moving approximately with the wave and the interaction occurs for a significant time [*Kennel and Petschek*, 1966; *Tsurutani and Lakhina*, 1997]. If the wave resonates with a harmonic of the cyclotron frequency ($|n| > 1$), then the qualitative discussion on the energy change for $\omega_c/\omega \gg 1$ will be unaltered, but the energy change for $\omega_c/\omega \ll 1$ or $\omega_c/\omega \approx 1$ will be smaller. Notice that if $|v_{\parallel}| \gg V_A$, then the particle's energy in the wave frame is not very different from its energy in the observer's frame, with the result that its energy will not change much when transforming between the different frames.

The Physical Effect of Wave-particle Interactions with Slab Turbulence

It was seen that the change in pitch-angle and energy is dependent on the phase between the particle and the wave. Hence, for particles interacting with waves of random phases, the pitch-angle and energy changes are a stochastic process which can be described as diffusion

processes. Combining the forces exerted on the particle by the wave (Eq. 3.21, Eq. 3.23, and Eq. 3.25), with Newton's second law, it follows that the change in the parallel and perpendicular speeds are

$$\Delta v_{\parallel} \approx \frac{\Delta\tau}{m}\delta F_{\parallel} = \mathrm{sign}(q)\omega_c \left(\frac{\delta B}{B_0}\right) v_{\perp} \sin\beta\Delta\tau \tag{3.27a}$$

$$\Delta v_{\perp} \approx \frac{\Delta\tau}{m}\left(\delta F_{\perp}^{\parallel v_{\perp}} + \delta F_{E}^{\parallel v_{\perp}}\right) = -\mathrm{sign}(q)\omega_c \left(\frac{\delta B}{B_0}\right)\left(v_{\parallel} + V_A\right)\sin\beta\Delta\tau, \tag{3.27b}$$

respectively, where $\Delta\tau$ is the short time which the particle is in resonance with the wave. Notice that if these changes were calculated in the wave frame, then the second term in $\Delta v_{\perp}$ would be absent, since there would be no induced electric field. The perpendicular magnetic (Eq. 3.28) and electric force, have components perpendicular to the perpendicular velocity

$$\delta\vec{F}_{\perp}^{\perp v_{\perp}} = q v_{\parallel}\delta B\cos\beta\hat{r}_L \tag{3.28}$$

$$\delta\vec{F}_{E}^{\perp v_{\perp}} = q V_A\delta B\cos\beta\hat{r}_L, \tag{3.29}$$

respectively, where $\hat{r}_L$ is a unit vector in the direction of the directional Larmor radius. These forces will push the particle in a direction perpendicular to the background magnetic field, causing the GC to jump to a different background magnetic field line. The change in the GC's perpendicular speed will be

$$\Delta v_{\perp}^{\mathrm{gc}} \approx \frac{\Delta\tau}{m}\left(\delta F_{\perp}^{\perp v_{\perp}} + \delta F_{E}^{\perp v_{\perp}}\right) = \mathrm{sign}(q)\omega_c \left(\frac{\delta B}{B_0}\right)\left(v_{\parallel} + V_A\right)\cos\beta\Delta\tau, \tag{3.30}$$

where the second term will be absent in the wave frame.

Assuming that the change in the speed components is small, the change in the pitch-angle during a wave-particle interaction will be, from the definition of the pitch-angle (Eq. 3.6),

$$\Delta\alpha \approx \frac{v_{\parallel}\Delta v_{\perp} - v_{\perp}\Delta v_{\parallel}}{v^2} \approx -\mathrm{sign}(q)\omega_c \left(\frac{\delta B}{B_0}\right)\left(1 + \mu\frac{V_A}{v}\right)\sin\beta\Delta\tau. \tag{3.31}$$

For a collection of fluctuations with random phases, and therefore random β, the average change in pitch-angle (or any other quantity discussed here for that matter) will be zero when averaging over β, that is $\langle\Delta\alpha\rangle_{\beta} = 0$. This is expected since the particle is interacting with random fluctuations and the probabilities of an increase or decrease of the pitch-angle are the same. For a stochastic process, the variance will generally not be zero and a measure of the amount of pitch-angle diffusion. From the $\delta B/B_0$ factor it can be seen that stronger turbulence would lead to more pitch-angle diffusion. The V_A/v term will only be present in the observer's frame and will only be significant if $v \sim V_A$, that is, if the electric forces dominate. Since SEPs are moving much faster than the Alfvén speed, it might be expected that the electric forces will not dominate. It is interesting to note that in the wave frame the pitch-angle will change independently of its value: if the particle is moving along the magnetic field ($\mu = \pm 1$), it cannot resonate with the wave since it is not gyrating around the background magnetic field; however, pitch-angle scattering can still occur since the particle will experience the fluctuating electric field. However, in the case of 90° pitch-angle in the wave frame, it is reasonable to assume

that the interaction time would be zero, as the particle is not moving over the stationary wave and is merely gyrating around the magnetic field, causing no change in the pitch-angle. This systematic, yet random, change in pitch-angle due to the interaction with turbulence is called *pitch-angle scattering*. Pitch-angle diffusion implies that the effect of turbulence on an initially anisotropic distribution of particles with pitch-angles in a preferred range, such as SEPs focused by the HMF, will therefore be to scatter the pitch-angles in the wave frame until they are isotropically distributed with pitch-angles of all values [*Kennel and Petschek*, 1966; *Tsurutani and Lakhina*, 1997; *Shalchi*, 2009].

The change in the particle's speed in the wave frame is zero due to the energy conservation (Eq. 3.24), but non-zero in the observer's frame and similar to pitch-angle scattering, turbulence will also lead to *momentum diffusion* due to the random and systematic change in the perpendicular speed caused by the fluctuating electric field. The change in the particle's speed ($v = \sqrt{v_\parallel^2 + v_\perp^2}$), using Eq. 3.27a and Eq. 3.27b, is

$$\Delta v \approx \frac{v_\parallel \Delta v_\parallel + v_\perp \Delta v_\perp}{v} = -\mathrm{sign}(q)\omega_c \left(\frac{\delta B}{B_0}\right) V_A \sqrt{1-\mu^2} \sin \beta \Delta\tau. \tag{3.32}$$

The momentum diffusion is also larger if the turbulence is strong and is dependent on the speed of the wave as it is the induced electric field which causes the change in energy, with its amplitude dependent on the wave speed. There is no momentum diffusion if $\mu = \pm 1$ because the particle does not have a perpendicular speed which the electric field can change, but it would still experience the fluctuating electric field pushing it in a direction perpendicular to the background magnetic field, causing it to gain a perpendicular speed component and start gyrating around the background magnetic field which would allow resonance to occur.

The effect of the changing pitch-angle on the particle's motion parallel to the background magnetic field, can be written, using Eq. 3.27a, as

$$\delta s_\parallel \approx \Delta v_\parallel \Delta\tau = \mathrm{sign}(q)\omega_c \left(\frac{\delta B}{B_0}\right) v \sqrt{1-\mu^2} \sin \beta (\Delta\tau)^2. \tag{3.33}$$

This term, although small due to the higher-order dependence on the interaction time, would influence the *parallel diffusion* of the particle. If the particle is moving along the background magnetic field ($\mu = \pm 1$), it seems as if the parallel motion would not be influenced, but from Eq. 3.31 it can be seen that the pitch-angle will be changed and this would influence the parallel motion during the next interaction time. If the particle is not moving along the background magnetic field ($\mu = 0$) then this term is large because there is no 'parallel momentum to suppress this perturbation'. *Pitch-angle diffusion in velocity space therefore leads to parallel spatial diffusion in configuration space* [*Shalchi*, 2009]. Similar to the discussion of parallel diffusion, the particle will also experience a stochastic motion perpendicular to the background magnetic field. The distance the GC would move perpendicular to the background magnetic field, using Eq. 3.30, would be

$$\delta s_\perp \approx \Delta v_\perp^{\mathrm{gc}} \Delta\tau \approx \mathrm{sign}(q)\omega_c \left(\frac{\delta B}{B_0}\right) (\mu v + V_A) \cos \beta (\Delta\tau)^2. \tag{3.34}$$

The second term is caused by the electric field and would cause perpendicular diffusion for all pitch-angles. The physical reason as to why the particle will not experience perpendicular diffusion in the wave frame if $\mu = 0$ will be explained now.

Field Line Random Walk

The *field line random walk* (FLRW) model is used as a conceptual appealing way of describing perpendicular diffusion. The propagating waves would perturb the background magnetic field in such a way that the field lines are systematically braided. If it is then assumed that the particle is stuck to the field line, that is, if the GC moves along this perturbed field line, it would seem that the particle moves away from the central background magnetic field line on which it started [*Jokipii*, 1973; *Shalchi*, 2009]. Although FLRW explains perpendicular diffusion in a fairly simple way, possible pitch-angle scattering and momentum diffusion might be concealed. In Fig. 3.7 different field lines, all starting close to each other, are shown for the slab turbulence model which will be derived in the next section. Since slab turbulence is only dependent on the position along the background magnetic field, all of the field lines follow the same path regardless of their starting positions perpendicular to the background magnetic field. This 'lock-step' wandering of the field lines would however cause very little perpendicular diffusion.

Notice that the particle's average parallel speed determines how fast it moves into regions of diffusing field lines. From this it is clear why Eq. 3.34 predicts no perpendicular diffusion when $\mu = 0$ in the wave frame, because the particle cannot move along the wandering magnetic field line. This simple picture of GCs following field lines can be violated by both scattering and drift effects, as the particle can decouple from the field line onto a nearby field line, although the GC would follow the field line locally over some distance. For this reason, it might be more accurate to say that the particles are confined to a *flux tube*, a cross-sectional area enclosed by the particle orbit through which the magnetic flux is constant, with the flux tubes being braided and shredded by the turbulence [*Minnie et al.*, 2009]. Another way of looking at perpendicular diffusion, is by considering the random GC drifts caused by the turbulent magnetic field (see e.g. *Strauss et al.* [2016]).

Jones et al. [1998] showed that if a general electromagnetic field is independent of at least one spatial coordinate, then a suitable gauge can be found, which is unique up to a constant in space and time, such that the magnetic vector and electric scalar potentials are also independent of this coordinate, with the implication that the particles' canonical momenta will be conserved, since the Hamiltonian is written in terms of the potentials. The particles are therefore effectively confined to a flux tube over a length scale which is in the order of the particles' instantaneous Larmor radius averaged over a gyration. The consequence of this so-called 'ignorable coordinate' is significant, as it implies that slab turbulence can only affect motion parallel to the magnetic field. FLRW is therefore imperative in accounting for perpendicular diffusion in slab turbulence, through binding of the particle to a wandering flux tube (notice that this

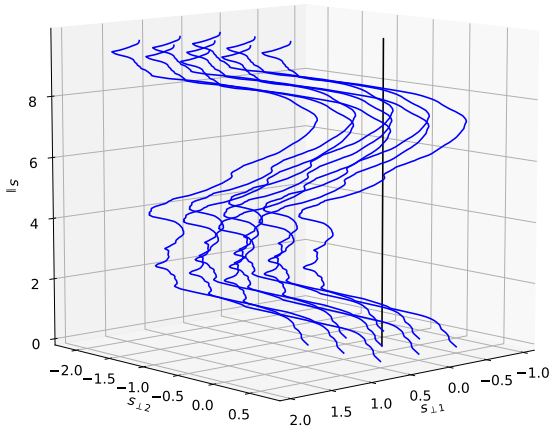

Figure 3.7: Turbulent magnetic field lines, constructed by the method in Appendix A.2.5, of the slab turbulence model derived in Section 3.2.3 at $t = 0$. A single background magnetic field line (black) is also shown. The perturbed magnetic field line could also be thought of as the path that a charged particle's guiding centre will follow if the particle is stuck to the field line.

would also explain the subdiffusive perpendicular behaviour seen in particle simulations in slab turbulence; see *Shalchi* [2009] for a review).

Stochastic Acceleration

In classical hard-sphere scattering, collisions can either be head-on or overtaking/trailing/tail-on. In a *head-on collision*, the particle and scattering centre approach each other, with the result that the particle, which is normally assumed to have a smaller momentum, will gain energy from the scattering centre. In a *trailing collision*, the particle attempts to overtake the scattering centre, with the result that the particle loses energy to the scattering centre. The concept of *stochastic acceleration* is based on the following argument: if the scattering centres have a non-zero random velocity component, then the particles will experience both head-on and trailing collisions; let $\vec{u}$ be the average velocity of the scattering centres, then the collision rate is proportional to

$$\frac{|\vec{v}-\vec{u}|}{v} = \frac{\sqrt{(\vec{v}-\vec{u})\cdot(\vec{v}-\vec{u})}}{v} = \frac{\sqrt{v^2-2\vec{v}\cdot\vec{u}+u^2}}{v} = \sqrt{1-\frac{2\vec{v}\cdot\vec{u}}{v^2}+\frac{u^2}{v^2}} \approx 1-\frac{\vec{v}\cdot\vec{u}}{v^2}$$

if it is assumed that $u \ll v$ so that $\sqrt{1-x^2} \approx 1-x^2/2$ to first order in x if $|x| \ll 1$; for a head-on collision then, $\vec{v}\cdot\vec{u} = vu\cos(180^\circ) = -vu$ and for a trailing collision, $\vec{v}\cdot\vec{u} = vu\cos(0^\circ) = vu$; from this it can be seen that the probability for a head-on collision ($\propto 1+u/v$) is larger than for a trailing collision ($\propto 1-u/v$); hence, particles will be gradually accelerated due to many small, random energy changes [*Fermi*, 1949]. The discussion of wave-particle interaction might seem to imply that the classical notion of head-on or trailing collisions and their respective energy gains or losses, are no longer valid: Eq. 3.32 states that the particle can both gain and lose energy from a single wave-particle interaction and whether the particle gains or loses energy, depends on the relative phase between the particle and the wave's magnetic field vector.

To resolve this apparent paradox, the question should be asked whether or not a single wave can be classified as a classical scattering centre? As was illustrated in Fig. 3.7, the turbulent waves perturb the background magnetic field to form complex magnetic structures which evolve in time. It is these magnetic structures which act as classical scattering centres and not the individual turbulent waves themselves. *Fermi* [1949] describes two possible scattering scenarios for the acceleration of cosmic rays. The first type of scattering is due to a magnetic mirror: in a turbulent magnetic field, the magnetic mirror, of course, would not be well-defined, but can exist and the magnetic mirror, furthermore, moves due to the evolving magnetic field; if a particle interacts with a stationary magnetic mirror, the particle's energy will not change, but if the particle is reflected by a magnetic mirror approaching (retreating from) the particle, the particle can gain (lose) energy from (to) the magnetic mirror. The second type of scattering is due to a kink/bend/turn in the magnetic field line which the particle is following: if the bend is approaching (moving in the same direction as) the particle as it is 'taking the turn', the particle can gain (lose) energy from (to) the magnetic field.

3.2.3 Slab Turbulence and Pitch-angle Scattering

The previous section established a conceptual understanding of how charged particles interact with electromagnetic plasma waves, but it did not illustrate what the actual motion of the particles would look like due to the combination of all the small interactions. In order to do this, the Newton-Lorentz equation must be solved numerically for synthetic turbulence. In no way will the model derived here be a complete turbulence model, but this simplified model should be able to capture the essence of the interaction between a single particle and turbulence. Although it seems that the particle has not yet reached diffusive behaviour in the presented simulations, the concepts and illustrations given should still give a qualitative description of the physical processes. Any turbulence model of electromagnetic waves propagating in a plasma must obey Maxwell's equations [*Chen*, 1984; *Choudhuri*, 1998; *Griffiths*, 1999]. If it is assumed, for simplicity in constructing the model, that the turbulent waves have already been set up by some process in the background plasma, then the propagation of these waves must satisfy

$$\vec{\nabla}\cdot\vec{E}=0, \qquad \vec{\nabla}\cdot\vec{B}=0, \qquad \vec{\nabla}\times\vec{E}=-\frac{\partial\vec{B}}{\partial t}, \quad \text{and} \quad \vec{\nabla}\times\vec{B}=\frac{1}{V_A^2}\frac{\partial\vec{E}}{\partial t}, \tag{3.35}$$

where the charge and current density of the background plasma have been neglected. This is justified in the assumption of non-dispersive Alfvén waves propagating with a constant speed through the background plasma.

For the remainder of this section it will be assumed that the background magnetic field is in the z-direction, that is $\vec{B}_0 = B_0\hat{z}$. A non-relativistic electron is simulated in the turbulence model using the fourth-order Runge-Kutta method, to avoid the additional calculations needed for the interpolation of the velocities (see Appendix A.2), with a time step of $\Delta t = 1\times10^{-3}$ s for $N_t = 10^5$ iterations. Unless otherwise stated, the particle was initialised at the origin with a velocity of $\vec{v}_0 = (0.5\hat{y}+0.1\hat{z})\,\mathrm{m\cdot s^{-1}}$ at $t_0 = 0$ s in a background magnetic field of $\vec{B}_0 = 1\times10^{-12}\hat{z}$

T without any background electric field. An Alfvén speed of $V_A = 0.1\ v_0$ was used, unless otherwise stated, as particles normally move much faster than the turbulence. In simulations where a wave field with only a single wavelength was simulated, the wave number could be adjusted and the wave's amplitude was scaled by a fraction β_m of the background magnetic field by $b_0 = B_0\sqrt{\beta_m/2}$ (see the next paragraph for details in this regard), to investigate the effect of changing these parameters. All quantities of interest, such as the pitch-angle or GC position, were calculated with respect to the background magnetic field, as this provides a natural and unchanging 'reference' field.

The slab model for turbulence assumes that the wave vectors are parallel to the background magnetic field and that the fluctuations are only dependent on the coordinate along the background magnetic field. The condition that the magnetic field must be divergence free,

$$0 = \vec{\nabla}\cdot\vec{B}(z) = \frac{\partial}{\partial x}\left[\delta B_x(z)\right] + \frac{\partial}{\partial y}\left[\delta B_y(z)\right] + \frac{\partial}{\partial z}\left[\delta B_z(z) + B_0\right] = \frac{\partial}{\partial z}\left[\delta B_z(z)\right],$$

implies that slab turbulence cannot have any fluctuations along the background magnetic field, so that the total magnetic field must have the form

$$\vec{B} = \delta B_x^{\text{slab}}(z;t)\hat{x} + \delta B_y^{\text{slab}}(z;t)\hat{y} + B_0\hat{z}. \tag{3.36}$$

The fluctuating components must have the general form

$$\delta B_x^{\text{slab}}(z;t) = b_0^{\text{slab}}\cos\left[k_\parallel(z - V_A t)\right] \qquad \text{and} \qquad \delta B_y^{\text{slab}}(z;t) = b_0^{\text{slab}}\sin\left[k_\parallel(z - V_A t)\right] \tag{3.37}$$

to describe a right-hand, circularly polarised, non-dispersive Alfvén wave propagating in the positive z-direction, where b_0^{slab} is the wave's amplitude. The fact that electromagnetic waves are transverse waves, with the electric and magnetic fields being mutually perpendicular and $90°$ out of phase [*Griffiths*, 1999], suggest the general form

$$\delta E_x^{\text{slab}}(z;t) = e_0^{\text{slab}}\sin\left[k_\parallel(z - V_A t)\right] \qquad \text{and} \qquad \delta E_y^{\text{slab}}(z;t) = -e_0^{\text{slab}}\cos\left[k_\parallel(z - V_A t)\right], \tag{3.38}$$

for the induced electric field, where e_0^{slab} is the wave's amplitude. Assuming that there is no background electric field, the total electric field has the form

$$\vec{E} = \delta E_x^{\text{slab}}(z;t)\hat{x} + \delta E_y^{\text{slab}}(z;t)\hat{y}. \tag{3.39}$$

Notice that a left-hand polarised wave can be set up by interchanging the sine and cosine functions in the two components of both the turbulent electric and magnetic field. Both the electric and magnetic field components satisfies their respective divergence free conditions since the components are only dependent on z. Maxwell's third and fourth equations will be satisfied if

$$e_0^{\text{slab}} = V_A b_0^{\text{slab}}. \tag{3.40}$$

It is furthermore assumed that the amplitude of the fluctuations are smaller than the background magnetic field. The strength of the turbulence would be $\delta B^2_{\text{slab}} = 2(b_0^{\text{slab}})^2$ and the amplitudes of the wave can be scaled with respect to the background magnetic field by

$$b_0^{\text{slab}} = B_0\sqrt{(0.5\ \text{m}^{-5/3})k_\parallel^{-5/3}}, \tag{3.41}$$

for a simple Komogorov inertial spectrum. The slab model can then be completed by a superposition of waves for the turbulent magnetic field,

$$\delta B_x^{\rm slab}(z;t) = \sum_i b_{0i}^{\rm slab} \cos\left[k_{\parallel i}(z - V_A t) + \phi_i\right] \tag{3.42a}$$

$$\delta B_y^{\rm slab}(z;t) = \sum_i b_{0i}^{\rm slab} \sin\left[k_{\parallel i}(z - V_A t) + \phi_i\right], \tag{3.42b}$$

and induced electric field,

$$\delta E_x^{\rm slab}(z;t) = \sum_i V_A b_{0i}^{\rm slab} \sin\left[k_{\parallel i}(z - V_A t) + \phi_i\right] \tag{3.43a}$$

$$\delta E_y^{\rm slab}(z;t) = -\sum_i V_A b_{0i}^{\rm slab} \cos\left[k_{\parallel i}(z - V_A t) + \phi_i\right], \tag{3.43b}$$

where Eq. 3.40 was substituted for the amplitude of the electric field. In the simulations 400 wavelengths are used with wave numbers between 1 and 200 m^{-1}. The spacing between wave numbers are taken as $0.5\ \mathrm{m}^{-1}$ and the amplitude of each wave is related to the wave number through Eq. 3.41. Each wave's amplitude is guaranteed to be smaller than the background magnetic field, but the superposition of these waves would occasionally result in a turbulent magnetic field which is larger than the background magnetic field. This behaviour is observed in the SW and is therefore justified. The stochastic nature of the turbulence is brought into the model by using a phase difference ϕ_i for each wave which is randomly distributed between 0 and 2π.

To build a systematic understanding of the influence of slab turbulence, first consider a magnetostatic wave field with a single wavelength and the amplitude of the turbulent field scaled to the background magnetic field by $\beta_m = 0.1$. This is a very idealised situation, but can be thought of as what an observer would experience if co-moving with the wave. The top left panel of Fig. 3.8 shows the trajectories of an electron and its GC when interacting with a long wavelength wave ($k_\parallel = 0.1\ k_\parallel^{\rm res}$, where $k_\parallel^{\rm res} \approx 1/|\mu_0| R_{L0}$ with μ_0 the initial pitch-cosine and R_{L0} the initial maximal Larmor radius). Since the magnetic field is changing slowly with position, the particle is able to follow the perturbed magnetic field line. The top right panel of Fig. 3.8 shows the interaction with a short wavelength wave ($k_\parallel = 10\ k_\parallel^{\rm res}$). Here the particle is moving so quickly over the fluctuations that it does not have time to react to the fluctuations, so that the trajectory is only slightly perturbed.

The bottom panel of Fig. 3.8 shows a resonant wave interaction ($k_\parallel = k_\parallel^{\rm res}$). Although it seems that the GC is still following the perturbed magnetic field line, the resonant interaction is clearly visible as the particle's trajectory is perturbed. The perpendicular speed changes only slightly, while the parallel speed changes more drastically, causing very large changes in the pitch-angle. The trajectory of the particle in velocity space ($v_\perp$ as a function of $v_\parallel$) is shown in Fig. 3.9. The dashed semi-circle indicates constant speed and since the trajectory lies on this semi-circle, it can be seen that the particle's energy is constant. In this graph, the pitch-angle is the angle between the positive $v_\parallel$-axis and the velocity vector. The change in pitch-angle

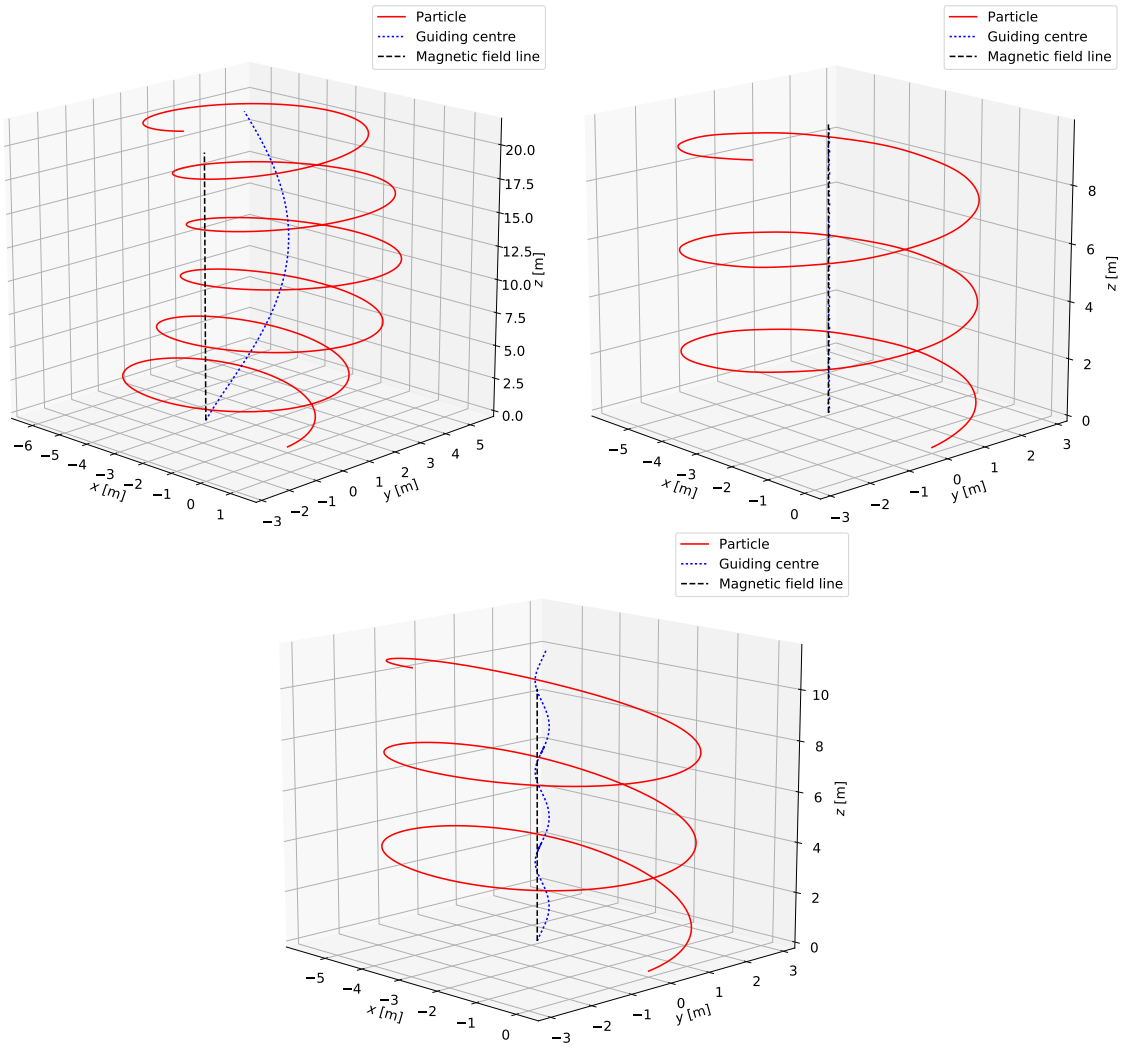

Figure 3.8: Simulation of an electron in a constant and uniform background magnetic field with a slab magnetostatic wave field having a single long (*top left*), short (*top right*), and resonant (*bottom*) wavelength. The trajectories of the particle (solid red) and its guiding centre (dotted blue; Eq. 3.5) are shown, together with a single background magnetic field line (dashed black).

can therefore be seen here as the trajectory moves on the semi-circle. In the current case of a standing wave, one would expect that the wave would have no effect on the particle if it had a $90°$ pitch-angle ($\mu = 0$), as the wave is not moving and the particle cannot move over the wave. This resonance gap at $\mu = 0$ is indeed observed if the initial parallel speed is zero ($\mu_0 = 0$).

Now that the effect of the wavelength has been established, consider a moving resonant ($k_{\parallel} = k_{\parallel}^{\mathrm{res}}$) magnetic wave with a single wavelength, but with no induced electric field, which is highly unrealistic of course. The top left panel of Fig. 3.10 shows the trajectory of an electron with initially no parallel speed ($\mu_0 = 0$) when interacting with a wave with a speed of $V_A = 0.1$ v_0. The resonance gap clearly no longer exists since the wave is now moving over the particle, which can be thought of as scattering centres colliding with the particle to set it in motion. The change in pitch-angle is very large (as expected from Eq. 3.31) and might be attributed to the fact that the particle has no initial parallel momentum. The top right panel of Fig. 3.10 shows

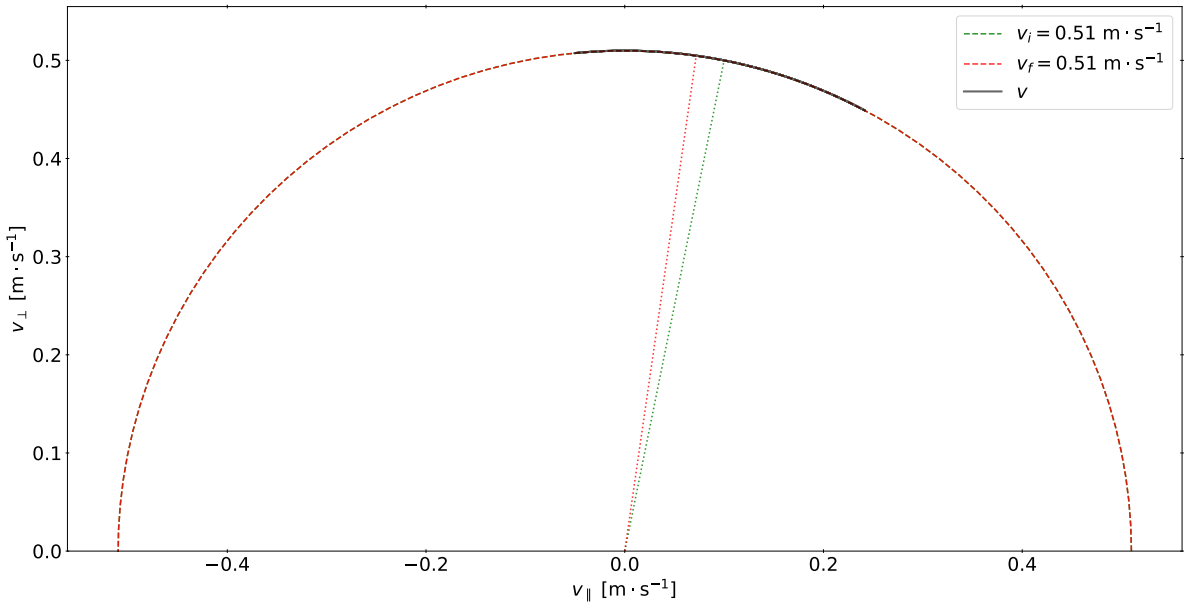

Figure 3.9: Trajectory (solid black) of the electron in the bottom panel of Fig. 3.8 in velocity space, where the perpendicular speed (Eq. 3.8) is plotted as a function of the parallel speed (Eq. 3.7). The dashed semi-circles indicate constant speed and the pitch-angle is the angle between the positive $v_\parallel$-axis and the velocity vector (dotted lines).

the interaction with a resonant wave moving at the particle's speed ($V_A = v_0$). This is the Landau or Cherenkov ($n = 0$) resonance and it can be seen that this is a very strong resonance, due to the large interaction time. Notice in both these cases that even though the trajectory of the particle itself is smooth and continuous, it seems as if the GC is bouncing between two turning points, reminiscent of classical hard-sphere collisions.

The bottom left panel of Fig. 3.10 shows an interaction with a fast moving ($V_A = 10\ v_0$) resonant wave. This is not a situation which would occur frequently, but it might be found in extreme astrophysical cases, such as relativistic shocks. The only significant results are very large changes in both the perpendicular and parallel speeds and an accompanying large change in pitch-angle. The bottom right panel of Fig. 3.10 shows an interaction with a slow moving ($V_A = 0.1\ v_0$) resonant wave. This would be the normal situation as $v \gg V_A$ for SEPs in the SW. Since the particle is moving over the wave, the GC seems to jump to different regions of the slowly propagating magnetic field line over which it is moving. Unlike the fast moving wave, the $\mu_0 = 0$ case, or the $n = 0$ resonance, the GC does not seem to experience any collisions and this might be because the interaction time is too short for significant parallel energy changes to occur. In all four of the previous cases, the particle's speed remained constant since the induced electric field has not yet been added and the magnetic field can do no work.

Now that the effect of the wave speed has been established, the induced turbulent electric field can be added to investigate its effect. The only significant change in the simulation results for all of the different cases discussed so far, is that the particle's speed is no longer constant because the electric field changes its energy. From Eq. 3.40 it is clear that a faster wave induces an

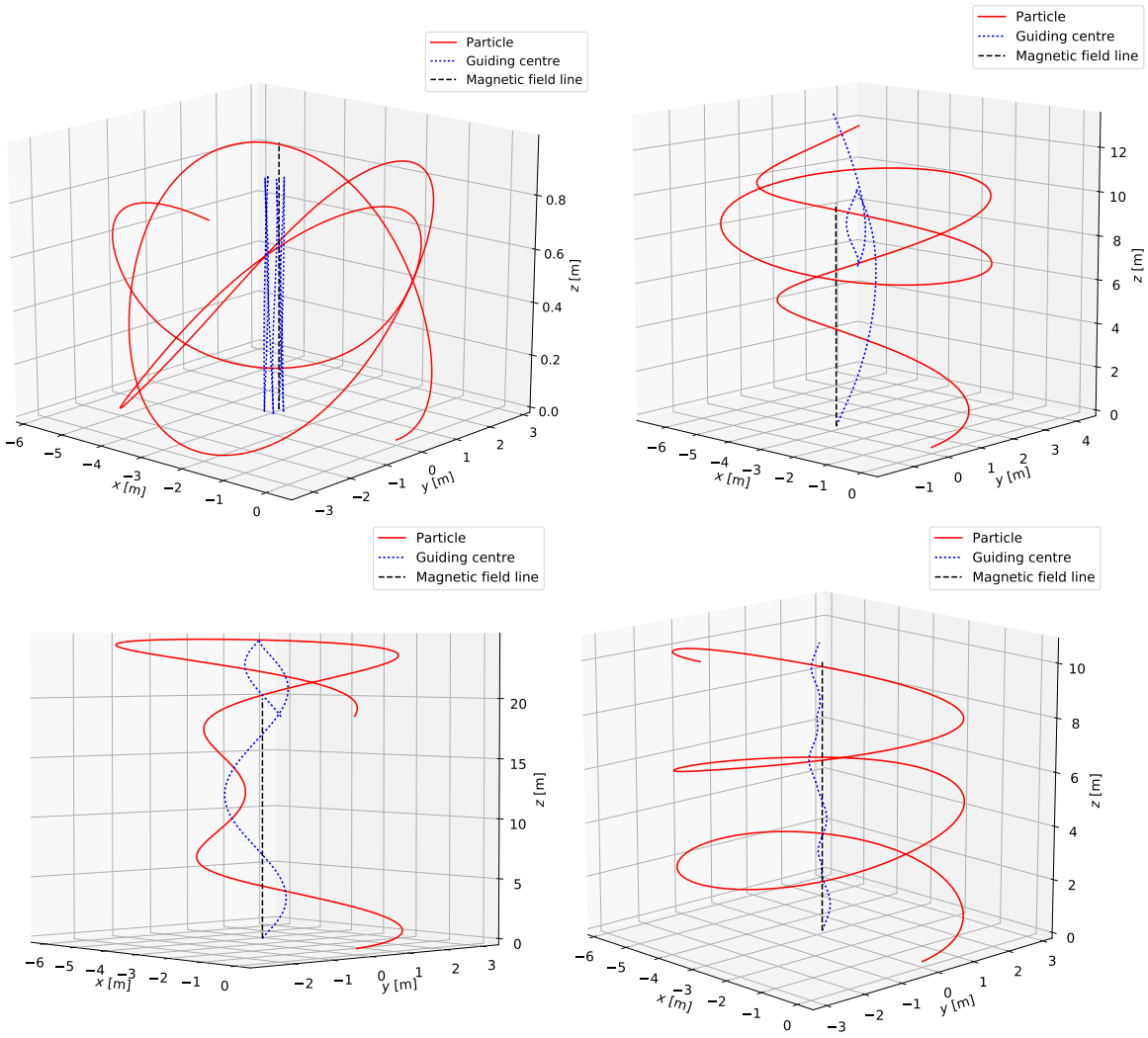

Figure 3.10: Simulation of an electron in a constant and uniform background magnetic field with a moving resonant slab magnetic wave having a single wavelength. *Top left:* The wave is moving slower than the particle's initial speed and initially the particle had no parallel speed ($90°$ pitch-angle). *Top right:* The $n = 0$ resonance where the wave speed equals the particle's initial speed. *Bottom left and right:* The wave is moving faster and slower, respectively, than the particle.

electric field with a larger amplitude. If the particle is moving faster than the wave, the energy changes are not very large, since the wave's magnetic forces are dominating. For the $n = 0$ resonance and a wave moving faster than the particle, the induced electric field's amplitude is quite significant, with the result that the change in the particle's speed is large (as implied by Eq. 3.32), because the electric forces are dominating (see the discussion of Eq. 3.26). Fig. 3.11 shows the electron's trajectory in velocity space for the $n = 0$ resonance. The dashed blue semi-circle indicates the particle's initial speed in the wave frame ($v_{pw} = \sqrt{(v_{\parallel 0} - V_A)^2 + v_{\perp 0}^2}$) and the blue dotted line is its initial velocity vector in the wave frame. This figure clearly illustrates that the particle's energy is conserved in the wave frame (Eq. 3.24) since the trajectory lies on the blue semi-circle, but that the particle's energy is continuously changing in the observer's frame.

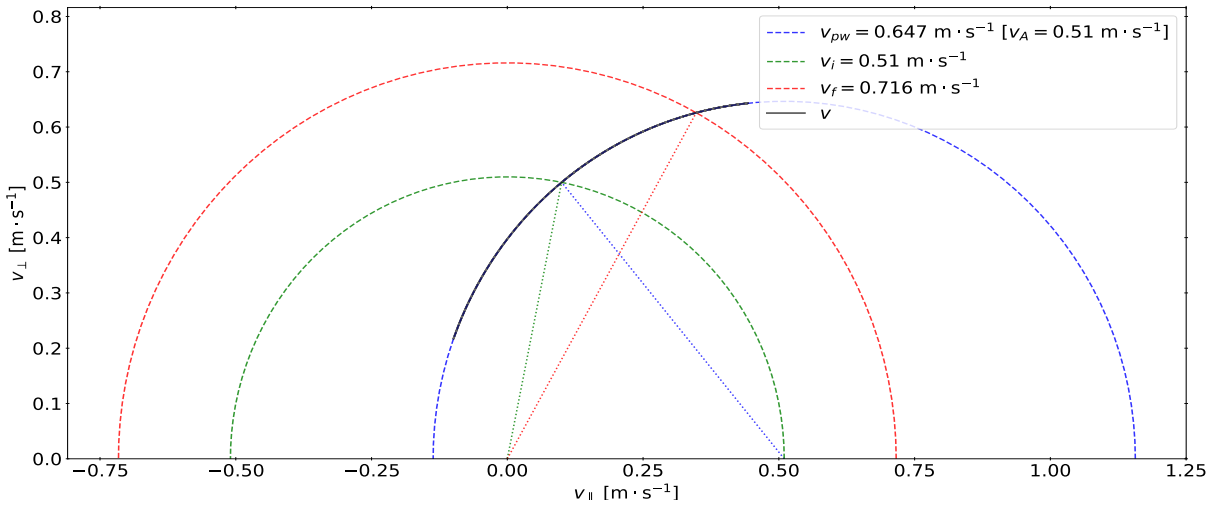

Figure 3.11: Trajectory (solid black) of the $n = 0$ resonance in velocity space. The dashed blue semi-circle indicates the particle's initial speed in the wave frame.

Having established the effect of the wave's individual characteristics on the particle's motion, the particle can be simulated in the full slab spectrum. Fig. 3.12 shows the trajectories of an electron and its GC when interacting with a spectrum of slab turbulence in the top left panel, as well as projections of the trajectories on the xy-, xz-, and yz-plane in the top right, bottom left, and bottom right panels, respectively. Although the spiral trajectory of the particle is highly perturbed, it is still smooth and continuous. The motion of the GC, however, is more irregular and reminiscent of classical hard-sphere collisions. Notice that the GC stays close to the background magnetic field line on which it started. This qualitatively different behaviour between the particle and its GC can also be seen in Fig. 3.13 where the Cartesian components of the particle's and its GC's position and velocity vectors are shown in the top and bottom panel, respectively. This behaviour is clearly seen in the velocity components: the particle's x- and y-velocity components still exhibit a fairly regular oscillation, while the z-velocity component have irregular, but still smooth and continuous features with a seemingly constant average speed; the GC's z-velocity component coincides with the particle's z-velocity component since this is the direction of the background magnetic field, but its x- and y-velocity components have discontinuous changes reminiscent of small collisions which change the velocity components discontinuously. The different behaviour of the particle and the GC can be understood if it is realized that any small changes in the particle's velocity would be amplified when 'projecting the directional Larmor radius to the distant GC'.

The fact that turbulence violates the invariance of the magnetic moment can clearly be seen in the top panel of Fig. 3.14 where the Larmor radius, magnetic moment, cyclotron frequency, and pitch-angle are shown. The cyclotron frequency stays constant, as it was calculated with respect to the background magnetic field, and both the Larmor radius and magnetic moment follow the same trend since both are dependent on the perpendicular speed. Pitch-angle scattering can also be seen, especially between ~ 20 s and ~ 40 s, where there is small stochastic

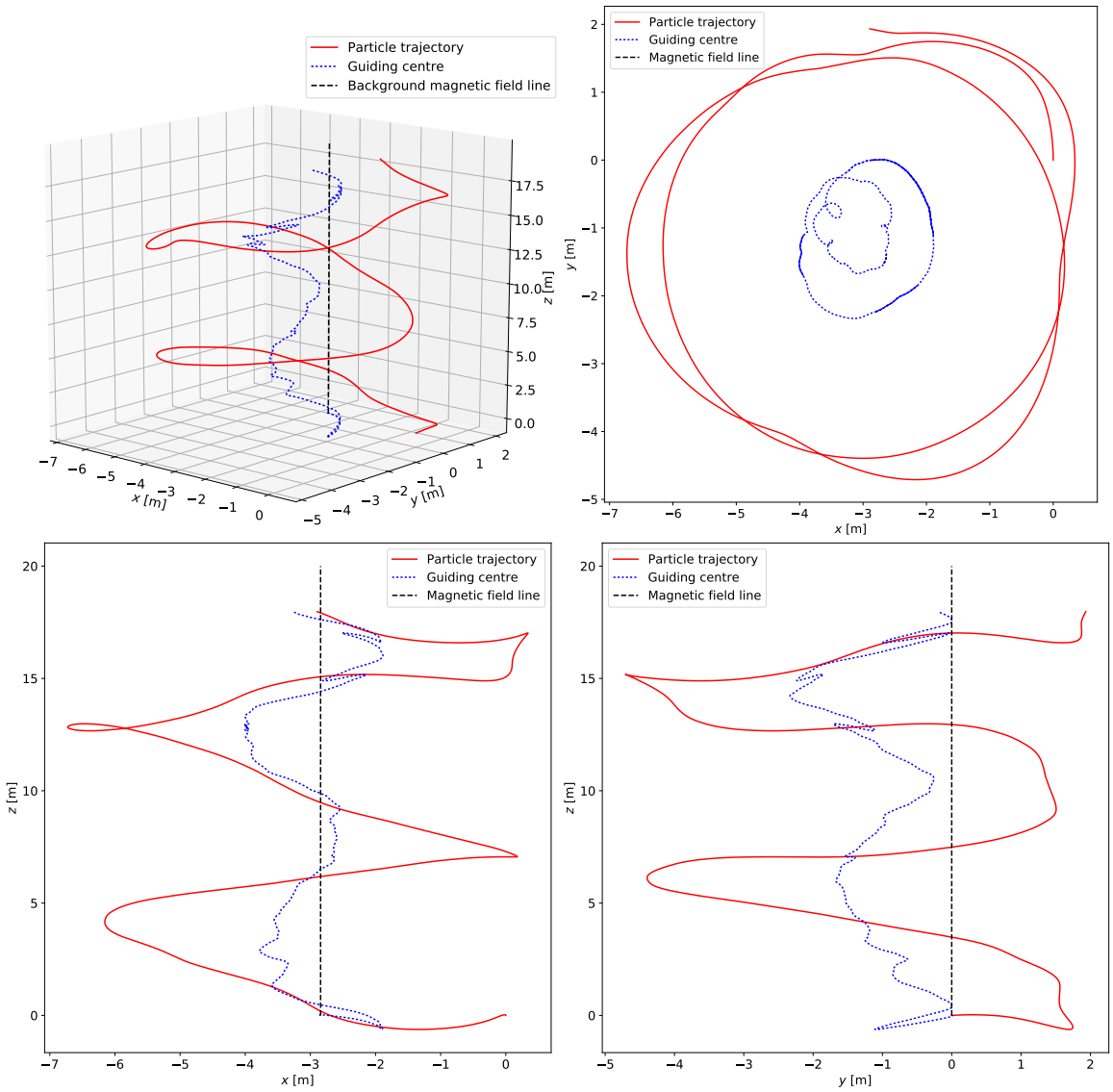

Figure 3.12: Simulation of an electron in a constant and uniform background magnetic field with a spectrum of slab turbulence. The three-dimensional view (*top left*) is projected onto the xy- (*top right*), xz- (*bottom left*), and yz-plane (*bottom right*).

changes in the pitch-angle. The bottom panel of Fig. 3.14 is an illustration of the particle's trajectory in velocity space. The single wave frame, in which scattering takes place and in which the particle's energy is conserved, is again clearly visible. Pitch-angle scattering can also be seen as the trajectory moves along the blue semi-circle of constant speed in the wave frame. Although this is the velocity space trajectory for only a single particle, the extent of the trajectory towards both 0° and 180° pitch-angles are indicative of turbulence trying to isotropise the distribution of particles (in this case a single particle) in the wave frame. Notice also that the particle's energy is continuously changing in the observer's frame.

It can again be verified that if the particle initially has no parallel speed ($\mu_0 = 0$), then it is set in motion by the turbulence and there is no resonance gap for these interactions. It can also be verified that if the particle initially has no perpendicular speed ($\mu_0 = 1$), then its pitch-

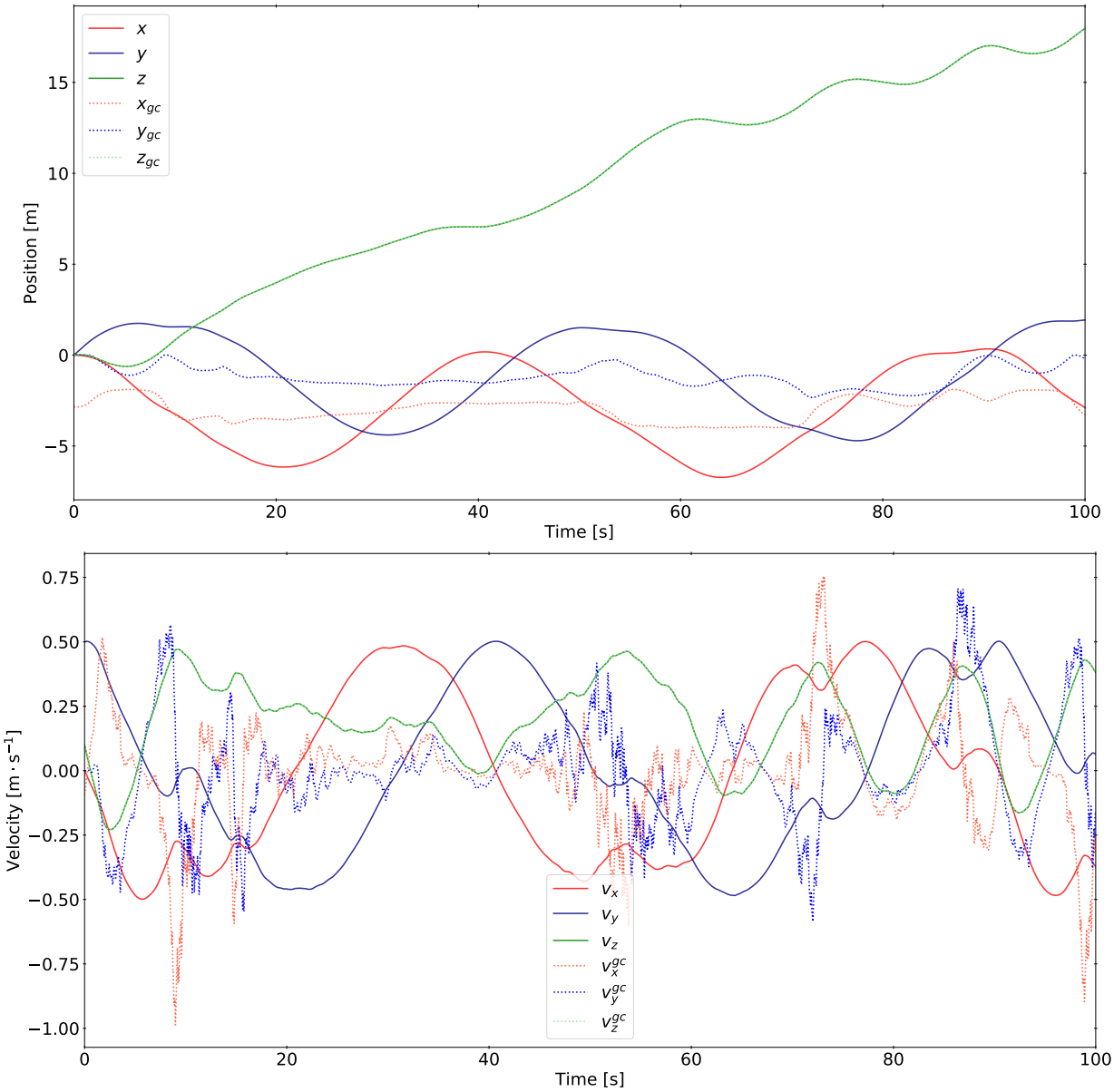

Figure 3.13: *Top:* Cartesian components of the position (solid) and guiding centre's position (dashed; Eq. 3.5) vectors for the electron in Fig. 3.12. *Bottom:* Cartesian components of the velocity (solid) and guiding centre's velocity (dashed; Eq. A.31) vectors for the electron in Fig. 3.12.

angle is changed by the electric field, as described in Section 3.2.2, with the effect that the particle develops a perpendicular velocity component and starts a perturbed gyration around the background magnetic field. If it is assumed that the GC follows the turbulent magnetic field lines, then Fig. 3.7 would suggest that the trajectory of a particle in slab turbulence would be independent of its initial x- and y-coordinates. This can indeed be verified and two particles' trajectories will be dependent on their initial position along the background magnetic field.

A last case of interest is 'isotropic' slab turbulence, where every second wave, for instance, in the spectrum propagates in the negative z-direction. The motion of the particle is much more irregular, with the GC undergoing more hard-sphere collisions, which might be attributed to

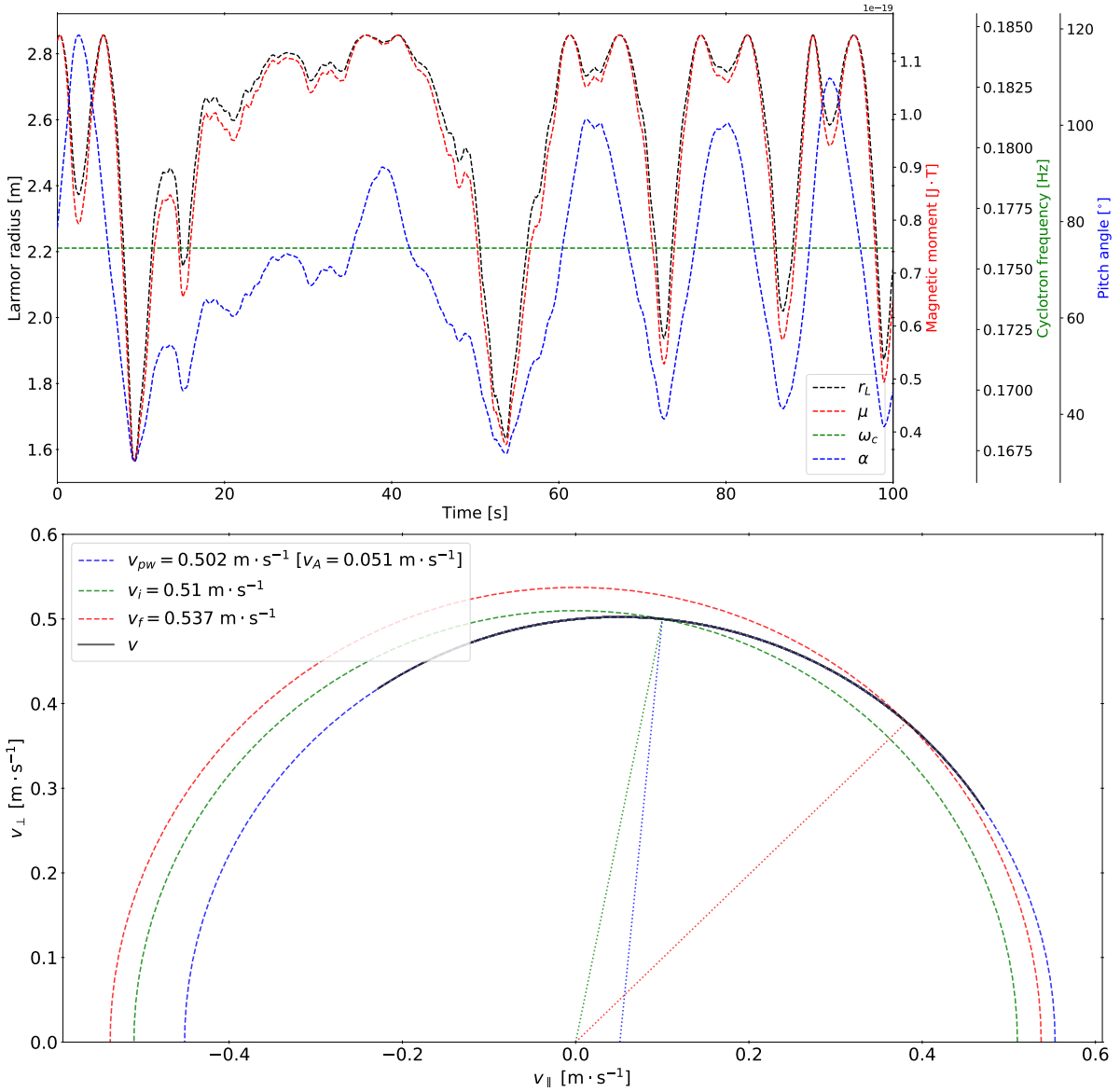

Figure 3.14: *Top:* Larmor radius (black; Eq: 3.4), magnetic moment (red; Eq. A.11), cyclotron frequency (green; Eq. 3.3), and pitch-angle (blue; Eq. 3.6) for the electron in Fig. 3.12. *Bottom:* Trajectory (solid black) of the electron in Fig. 3.12 in velocity space, similar to Fig. 3.11.

the resultant magnetic field having a more complex structure. The important result is the particle's trajectory in velocity space shown in Fig. 3.15, where the dashed blue semi-circle is the particle's initial speed in the wave frame of waves propagating in the positive z-direction. There seems to be no well-defined wave frame. It should however be realised that there is now a wave frame in both directions along the background magnetic field. The particle's energy is conserved in the wave frame in which it is interacting with turbulence, but its energy is continuously changing in the other wave frame during this interaction. The following interaction would most likely occur in the other wave frame. This results in the particle's velocity vector to 'jump' between different wave frames. A similar result will be found if all the waves are moving in the same direction, but with different speeds (for dispersive waves).

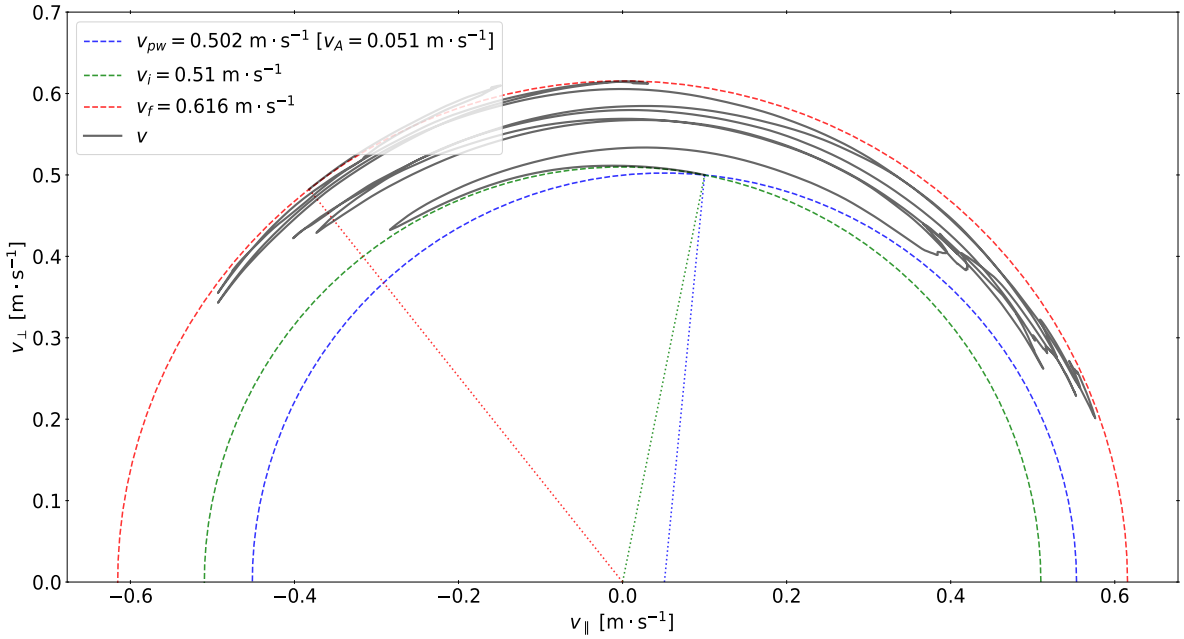

Figure 3.15: Trajectory (solid black) of an electron interacting with isotropic slab turbulence in velocity space. The dashed blue semi-circle indicates the particle's initial speed in the forward wave frame.

3.3 Summary

This chapter investigated solutions of the Newton-Lorentz equation to illustrate the motion of charged particles in various electric and magnetic fields. The following insights were gained from the analytical solutions (some of which can be found in Appendix A): in the absence of an electric field, the particle will gyrate around the magnetic field, around an imaginary point called the guiding centre (GC), while moving at a constant speed along the magnetic field; if an electric field or a non-uniform or varying magnetic field is present, the particle will experience various types of drifts, where the particle moves perpendicular to the magnetic field. A special case of interest for solar energetic particles (SEPs) is magnetic focusing, where a particle's perpendicular speed is transferred to parallel speed when entering regions of decreasing parallel magnetic field strength.

It was pointed out that magnetic fields are generally not smooth, but contain turbulence (seemingly random fluctuations superimposed on the average or background magnetic field). Special attention was given to slab turbulence, where the turbulent fluctuations are assumed to propagate along the background magnetic field and are also dependent on the position along the background magnetic field. Wave-particle interactions were discussed to illustrate when a particle will resonate with a circularly polarised wave and that the particles' energy will be conserved in the reference frame co-moving with the wave. It was seen that the turbulent wave physically exerts magnetic and electric forces on the particle which will perturb its motion.

A slab turbulence model was derived and the Newton-Lorentz equation solved numerically with the methods discussed in Appendix A. From these simulations it was seen that the clas-

sical idea of hard-sphere collisions, where particles physically collide or particles are deflected by some interaction potential between particles, cannot and should not be naively applied to charged particles interacting with turbulence. This is due to the physical interaction between charged particles and magnetic scattering centres being of a unique nature, as shown by the wave-particle interactions. It was seen that it is only when the GC is considered, that the classical scattering idea can be applied.

The general effects of slab turbulence on the motion of a charged particle can be summarised by the following characteristics: the motion of the particle itself is smooth and continuous, with a highly perturbed spiral path; the motion of the particle's GC is much more irregular and displays abrupt changes, which can be clearly seen in the GC's velocity components not being smooth and continuous; the motion of the GC is reminiscent of classical hard-sphere collisions; the GC stays close to the background magnetic field line on which it started; the pitch-angle experiences small stochastic changes; the motion of the particle parallel to the background magnetic field is influenced the most, with the largest contribution to the perturbed spiral path due to the parallel motion; the particle's energy changes continuously in the observer's frame, but is conserved in a well-defined wave frame, if such a frame can be constructed (that is, if the waves are all propagating in the same direction with the same speed).

Chapter 4

The One-dimensional Focused Transport Equation for Solar Energetic Particles

Solar energetic particles can be simulated by solving the Newton-Lorentz equation for each particle and using Maxwell's equations for the evolution of the electric and magnetic fields. This is done with particle-in-cell methods, but is not viable for a solar energetic particle event due to the extremely large number of particles involved. A macro-physical or ensemble averaged description of solar energetic particles is needed and since solar energetic particles are highly anisotropic, the *Parker* [1965] transport equation, which is used to model galactic cosmic rays, is inadequate for this purpose [*Fisk and Axford*, 1969]. The evolution of the anisotropic solar energetic particle distribution function can be described by a so called focused transport equation. Although the name "focused transport equation" might be a misnomer, as it describes the evolution of any anisotropic distribution, it is appropriate in the case of solar energetic particles since the anisotropy is caused by focusing. In this chapter, a one-dimensional focused transport equation will be derived from physical grounds following the derivation of *Ruffolo* [1995]. The derivation will begin by deriving the Fokker-Planck equation and writing it in a convenient set of coordinates, after which expressions will be derived for the various terms as applicable to the transport of solar energetic particles.

4.1 Concepts in Momentum Space

All of the concepts and processes discussed in Chapter 3 can be connected conceptually to the current chapter with the illustration given in Fig. 4.1. The particle's momentum space in a field-aligned reference frame is shown. The polar angle, the angle between the $s_{\parallel}$-axis and the momentum vector $\vec{p}$, is the pitch-angle α (Eq. 3.6). Using the definition of the pitch-cosine μ (Eq. 3.9), the particle's momentum can be decomposed into a parallel $\vec{p}_{\parallel} = p\mu\hat{s}_{\parallel}$ and perpendicular $\vec{p}_{\perp} = p\sqrt{1-\mu^2}\,(\cos\varphi\hat{s}_{\perp 1} + \sin\varphi\hat{s}_{\perp 2})$ component, similar to Eq. 3.7 and Eq. 3.8, respectively, where p is the magnitude of the momentum which can be thought of as a radius

in momentum space. The parallel momentum is the projection of the momentum vector onto the background magnetic field direction, while the perpendicular momentum is the projection of the momentum vector onto the plane perpendicular to the background magnetic field. The azimuthal angle, the angle between the $s_{\perp 1}$-axis and the perpendicular momentum, is the particle's *gyrophase* φ and its rate of change is the cyclotron frequency ω_c (Eq. 3.3). The gyration of the particle around the magnetic field causes the momentum vector to precess around the $s_{\parallel}$-axis at the cyclotron frequency.

Focusing will decrease the particle's pitch-angle, while scattering will either increase or decrease it, as indicated by the green and red arrows, respectively. As the number of particles under consideration in a real event is so large that there is, for all practical purposes, a particle in every phase of gyration, the gyrophase is neglected when describing a collection of particles and this is called a *gyrotropic* distribution of particles. This can be illustrated as a collection of particles having the same pitch-angle, but different gyrophases and is indicated by the grey circle (also referred to as a *ring-distribution*). This also represents a gyrotropic distribution of *mono-energetic* particles, since all of their momentum vectors have the same magnitude. If the particles were to have different energies and gyrophases, but the same pitch-angle, then their momentum vectors will form the shaded cone. The cone will then represent a possible *anisotropic* distribution as the particles have a preferred direction of motion along the background magnetic field. For a gyrotropic distribution of mono-energetic particles, pitch-angle scattering will cause the circle to change into a spherical shell (also referred to as a *shell-distribution*), assuming that the scattering does not change the particles' energy and that enough time has elapsed. Similarly, pitch-angle scattering will cause the cone of an anisotropic distribution to become a filled sphere. In such a case, the distribution will be called *isotropic* with particles of all energies moving in all directions.

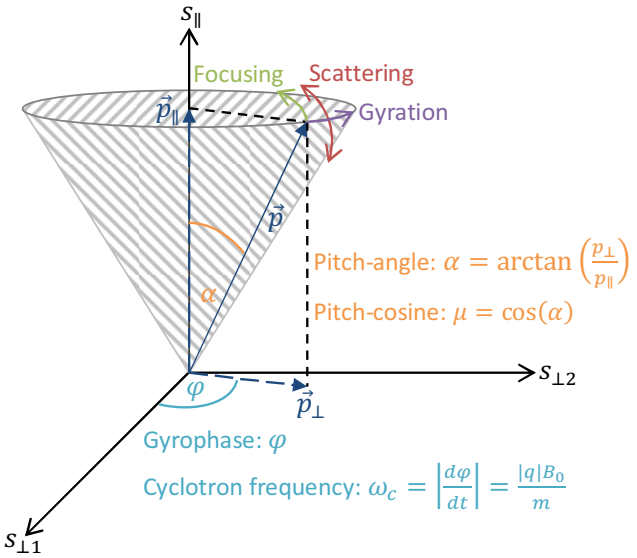

Figure 4.1: Illustration of the various processes and definitions introduced. Shown is the particle's momentum space in a field-aligned coordinate system. See the text for details.

Turbulence also changes the particles' energy, so that velocity or momentum diffusion occurs. The circle of a gyrotropic distribution of mono-energetic particles will diffuse into a doughnut (also referred to as a *'warm' ring-distribution*) and, if sufficient time has passed, into a filled sphere. Similarly, in the case of an anisotropic distribution, the cone will also diffuse into a filled sphere. In both cases, the resultant sphere will also expand or decrease in volume if the particles gain or lose energy, respectively. Turbulence can therefore drastically change the characteristics of the original particle distribution and will mostly act to isotropise an anisotropic distribution.

4.2 The Distribution Function and Fokker-Planck Equation

For a macro-physical description of solar energetic particles (SEPs), a suitable distribution function and transport equation (TPE) must be introduced. This is the aim of the current section, which will discuss various concepts applicable to the distribution function and the TPE in order to derive the focused transport equation (FTPE).

4.2.1 The Distribution Function

The *distribution function* $f(\vec{x};\vec{p};t) = dN/d^3x\,d^3p$ of a system is defined as the number density dN in a volume element $d^3x\,d^3p$ of the 6-dimensional phase-space spanned by the three physical coordinates $\vec{x}$ and momenta $\vec{p}$. The distribution function can be interpreted as the number of particles at time t having position vectors between $\vec{x}$ and $\vec{x} + d\vec{x}$ with momentum vectors between $\vec{p}$ and $\vec{p} + d\vec{p}$. Integrating the distribution function over all space and momentum would give the total number of particles in the system. By dividing the distribution function by the total number of particles, results in a probability distribution to find particles in the phase-space volume $d^3x\,d^3p$ around $(\vec{x};\vec{p})$ at time t. The distribution function can be used to give a complete description of a system's state. Under certain assumptions and conditions (see the discussions of *Mills and Sessler* [1993] and *Choudhuri* [1998]), Liouville's theorem can be applied to the distribution function, such that

$$\frac{Df}{Dt} = 0. \tag{4.1}$$

This is called the *continuous medium theorem* by *Mills and Sessler* [1993] and is a statement of the conservation of particles. The total time derivative D/Dt can be expanded by using the chain rule to yield the generalised *Boltzmann equation*

$$\frac{\partial f}{\partial t} + \vec{v}\cdot\vec{\nabla}f + \frac{d\vec{p}}{dt}\cdot\vec{\nabla}_p f = \frac{\partial f}{\partial t} + \frac{\partial}{\partial x_i}\left[\frac{dx_i}{dt}f\right] + \frac{\partial}{\partial p_i}\left[\frac{dp_i}{dt}f\right] = \left.\frac{\partial f}{\partial t}\right|_{\text{collision}}. \tag{4.2}$$

The terms on the left hand side describe temporal changes, spatial variations, and velocity changes due to forces, respectively. The right hand side includes collisions which are not included in the definition of Eq. 4.1. The vector form was rewritten in summation notation

(where repeated indexes imply summation), the velocity was brought into the spatial derivative using the fact that the position and velocity are independent of each other in the distribution function, and the force was brought into the momentum derivative using the fact that the momentum derivative of the Lorentz force is zero [*Mills and Sessler*, 1993; *Choudhuri*, 1998; *Zank*, 2014].

It was seen in Chapter 3 that the particles' energy is conserved in the wave frame and it is therefore convenient to transform to the wave frame in order to neglect momentum diffusion. Consider an observer frame, where quantities are unprimed, and a wave frame moving with respect to the observer frame, where quantities are primed. It can be proven that the phase-space volume element is invariant $d^3x\, d^3p = d^3x' d^3p'$ (see e.g. *Liboff* [1990] or *Zank* [2014]), with the implication that the distribution function would also be invariant, $f(\vec{x};\vec{p};t) = f'(\vec{x}';\vec{p}';t')$. This is expected since the distribution function is related to the particle number density which is invariant between different reference frames. Notice, however, that this result is only valid for non-relativistic transformations as the distribution function is defined at a certain time in either of the frames and the relativistic transformation of the time has not been considered. Consider now a distribution function $f^*(\vec{x};\vec{p}';t)$ in a mixed reference frame, where position and time are measured in the observer's frame and momentum in the wave frame. The momentum space volume element d^3p can be thought of as a three-dimensional surface element of a four-dimensional hypersurface in energy-momentum space and since the ratio of two parallel components of two four-vectors are Lorentz invariant, the ratio of the momentum space volume element to the total energy should be invariant $d^3p/E = d^3p'/E'$ [*Liboff*, 1990]. It can be written that $f(\vec{x};\vec{p};t)d^3x\, d^3p = Ef(\vec{x};\vec{p};t)d^3x\, d^3p/E$ and since d^3p/E is invariant, it must hold that $Ef(\vec{x};\vec{p};t)$ is then also invariant, from which it follows that

$$f(\vec{x};\vec{p};t) = \frac{E'}{E} f^*(\vec{x};\vec{p}';t) \tag{4.3}$$

for the distribution function in the mixed frame [*Forman*, 1970; *Liboff*, 1990; *Zank*, 2014]. *Zank* [2014] gives a calculation to find the general expression for $E'/E = 1/[\gamma_w(1+\vec{v}'\cdot\vec{w}/c^2)]$, where γ_w is the wave frame Lorentz factor, but for the current discussion it is sufficient to consider the ratio of Lorentz factors as an approximation. Let $\vec{w}$ be the velocity of the wave frame with respect to the observer and assume that $w \ll c$, so that a non-relativistic transformation of the particle velocity can be done between the two frames, $v_\parallel = v'_\parallel + w$ and $v_\perp = v'_\perp$, where $v_\parallel$ and $v_\perp$ are here the speed components parallel and perpendicular to $\vec{w}$, respectively. From this then

$$\frac{E'}{E} = \frac{\gamma'}{\gamma} = \frac{\sqrt{1-(v'^2+w^2+2v'_\parallel w)/c^2}}{\sqrt{1-(v'/c)^2}} \approx 1 - \frac{\vec{v}'\cdot\vec{w}}{c^2}, \tag{4.4}$$

to terms linear in w/c. For solar energetic electrons and protons, moving at speeds of $v_e \approx 0.552\, c$ and $v_p \approx 0.653\, c$, respectively, and a solar wind (SW) speed of $v_{\rm sw} \approx 0.001\, c - 0.003\, c$, it can be assumed that $E'/E \approx 1$ and this term will therefore be neglected.

The Compton-Getting Effect

The observer is actually measuring the wave or mixed distribution function in terms of its momentum coordinates $\vec{p}$ and not the co-moving momenta $\vec{p}'$. This would cause the observer to measure a distribution function which differs from the one in the wave frame. This effect, called the *Compton-Getting effect*, arises from the momentum transformation between reference frames, but can also be explained physically: for any background flow, particles will be advected by the flow; even though the distribution function might be isotropic in the flow frame, the movement of this frame past the observer would cause the observer to measure a distribution function which is anisotropic. The Compton-Getting effect can therefore be seen as a type of Doppler effect due to the relative motion between the observer and the distribution function measured by the observer [*Gleeson and Axford*, 1968; *Forman*, 1970]. When transforming the momentum, the components of the momentum perpendicular to the direction of motion will be invariant,

$$\begin{aligned} p_\perp &= p'_\perp \\ p\sqrt{1-\mu^2} &= p'\sqrt{1-\mu'^2}, \end{aligned} \tag{4.5}$$

while the momentum parallel to the direction of motion will change,

$$\begin{aligned} p_\parallel &= p'_\parallel + mw \\ p\mu &= p'\mu' + \frac{p'}{v'}w, \end{aligned} \tag{4.6}$$

where a non-relativistic transformation was made and p/v was written for the particle mass m, assumed to be invariant. The transformations then yield [*Earl*, 1984]

$$p = \sqrt{p_\perp^2 + p_\parallel^2} = p'\sqrt{1 + \left(\frac{w}{v'}\right)^2 + 2\mu'\frac{w}{v'}} \tag{4.7}$$

and

$$\mu = \frac{p_\parallel}{p} = \frac{\mu' + w/v'}{\sqrt{1 + w^2/v'^2 + 2\mu' w/v'}}. \tag{4.8}$$

Notice that an expression can be calculated for how the distribution function transforms between the observer's and wave frame with the Compton-Getting effect included (see e.g. *Gleeson and Axford* [1968] or *Forman* [1970] and *Earl* [1984] for an isotropic and anisotropic distribution, respectively), but this would not be needed for the methods employed in this research.

4.2.2 The Fokker-Planck Equation

The collision term in the Boltzmann equation (Eq. 4.2) arise from perturbed quantities when substituting the Lorentz force into the collisionless Boltzmann equation (i.e. from the *Vlasov equation*) and the general form of this term must be evaluated. Since it was seen in Chapter 3 that momentum diffusion naturally leads to spatial diffusion, only momentum diffusion will be considered. Suppose that in a time interval Δt, a particle's momenta change from $\vec{p}$ to $\vec{p}+\Delta\vec{p}$

by interactions with turbulence. Since the turbulent interactions are a stochastic process, the exact way in which the momenta would change is unknown. To take into account all of the uncertain, yet probable ways in which the momenta can change, let $\xi(\vec{p}|\Delta\vec{p})$ be the probability that the particle's momenta would change by an amount $\Delta\vec{p}$ in the time interval Δt if it has momenta $\vec{p}$. The distribution function after the time interval can be related to the distribution function before the interval by the *Chapman-Kolmogorov equation*

$$f(\vec{x};\vec{p};t) = \int f(\vec{x};\vec{p}-\Delta\vec{p};t-\Delta t)\xi(\vec{p}-\Delta\vec{p}|\Delta\vec{p})d(\Delta\vec{p}), \tag{4.9}$$

which is essentially an integral over all possible interactions which would change the momenta by $\Delta\vec{p}$ in the time interval Δt. By summing over all mutually exclusive changes, the specifics of the changes can be eliminated and only the net result can be considered. This equation describes a *Markov process* where the next state is only dependent on the current state and not the entire history of the system, that is, a system with a 'short memory'. The probability ξ is analogous to the transition probability between different states in a quantum system, where the most probable final state is dependent on the initial state integrated together with the transition probability over all possible end states [*Chandrasekhar*, 1943; *Gardiner*, 1985; *Liboff*, 1990; *Mills and Sessler*, 1993; *Zank*, 2014].

If it is assumed that the time interval Δt is small, such that the distribution function does not change significantly during this time, but not so small so that Δt is comparable to the interaction time, in which case the process would not be a pure Markov process, and that only small momenta changes contribute to the integration in Eq. 4.9, then the product of $f\xi$ can be expanded to first order in time and second order in momenta to change Eq. 4.9 to

$$\begin{aligned} f(\vec{x};\vec{p};t) \approx f(\vec{x};\vec{p};t)\int \xi(\vec{p}|\Delta\vec{p})d(\Delta\vec{p}) - \Delta t\frac{\partial f(\vec{x};\vec{p};t)}{\partial t}\int \xi(\vec{p}|\Delta\vec{p})d(\Delta\vec{p}) \\ - \frac{\partial}{\partial\vec{p}}\cdot\left[f(\vec{x};\vec{p};t)\int \Delta\vec{p}\,\xi(\vec{p}|\Delta\vec{p})d(\Delta\vec{p})\right] + \frac{1}{2}\frac{\partial^2}{\partial\vec{p}\partial\vec{p}} : \left[f(\vec{x};\vec{p};t)\int \Delta\vec{p}\Delta\vec{p}\,\xi(\vec{p}|\Delta\vec{p})d(\Delta\vec{p})\right], \end{aligned}$$

where : indicates a tensor contraction defined as $\vec{a}\vec{b} : \vec{c}\vec{d} = a_i b_j c_j d_i$. Together with the fact that ξ is a normalised probability, $\int \xi(\vec{p}|\Delta\vec{p})d(\Delta\vec{p}) = 1$, the previous expression becomes the *Fokker-Planck equation* (FPE)

$$\left.\frac{\partial f(\vec{x};\vec{p};t)}{\partial t}\right|_{\text{collision}} = -\frac{\partial}{\partial\vec{p}}\cdot\left[\left\langle\frac{\Delta\vec{p}}{\Delta t}\right\rangle f(\vec{x};\vec{p};t)\right] + \frac{1}{2}\frac{\partial^2}{\partial\vec{p}\partial\vec{p}} : \left[\left\langle\frac{\Delta\vec{p}\Delta\vec{p}}{\Delta t}\right\rangle f(\vec{x};\vec{p};t)\right], \tag{4.10}$$

where

$$\left\langle\frac{\Delta\vec{p}}{\Delta t}\right\rangle = \int\frac{\Delta\vec{p}}{\Delta t}\xi(\vec{p}|\Delta\vec{p})d(\Delta\vec{p}) \qquad \text{and} \qquad \left\langle\frac{\Delta\vec{p}\Delta\vec{p}}{\Delta t}\right\rangle = \int\frac{\Delta\vec{p}\Delta\vec{p}}{\Delta t}\xi(\vec{p}|\Delta\vec{p})d(\Delta\vec{p}) \tag{4.11}$$

are the *Fokker-Planck coefficients* [*Chandrasekhar*, 1943; *Gardiner*, 1985; *Liboff*, 1990; *Mills and Sessler*, 1993; *Zank*, 2014].

The first Fokker-Planck coefficient $\langle\Delta\vec{p}/\Delta t\rangle$ can be interpreted as a drag or friction force and is usually zero for charged particles interacting with turbulence since the particle has the same

probability of an increase than a decrease in momenta. The second Fokker-Planck coefficient $\langle \Delta\vec{p}\Delta\vec{p}/\Delta t\rangle$ is normally non-zero and can be interpreted as a diffusion tensor. The fact that diffusion is described by a tensor indicates that the diffusion is not necessarily isotropic and that the diffusion in different directions might be caused by different processes [*Chandrasekhar*, 1943; *Gardiner*, 1985; *Choudhuri*, 1998; *Liboff*, 1990; *Zank*, 2014]. The exact form of the probability ξ, and hence the Fokker-Planck coefficients, are dependent on the physical system under consideration. It is the goal of turbulent diffusion theories to find analytical expressions for the Fokker-Planck coefficients under different physical conditions (see e.g. *Shalchi* [2009] and *Zank* [2014] for different cosmic ray (CR) diffusion theories and diffusion coefficients in collisional plasmas, respectively). Notice that to illustrate the most general applicability of the FPE to stochastic systems, it can also be derived as the diffusive limit of the differential form of the Chapman-Kolomogorov equation [*Gardiner*, 1985].

Jokipii [1966] points out that the Fokker-Planck coefficients $\langle \Delta\vec{p}/\Delta t\rangle$ and $\langle \Delta\vec{p}\Delta\vec{p}/\Delta t\rangle$ must be related for pitch-angle scattering due to the following argument: given a long enough time, diffusion would cause the distribution function to become isotropic; if diffusion did not lead to isotropy, then an initially isotropic distribution could relax to an anisotropic distribution; this, however, would violate Liouville's theorem and hence, the FPE should be able to reduce to a simpler diffusion equation. Notice that the diffusive limit might not be reached by SEPs if focusing is very strong, especially pertaining to diffusion perpendicular to the heliospheric magnetic field (HMF; see e.g. discussions by *Laitinen et al.* [2013], *Dröge et al.* [2014], *Tooprakai et al.* [2016], and *Laitinen and Dalla* [2017]), but scattering would try to establish isotropy in the wave frame and hence, this should hold as an approximation.

The proof of Jokipii's statement can be formulated as in the following. Rewriting the FPE in summation notation and taking the derivatives of the products, yields

$$\left.\frac{\partial f}{\partial t}\right|_{\text{collision}} = -f\frac{\partial}{\partial p_i}\left[\left\langle\frac{\Delta p_i}{\Delta t}\right\rangle\right] - \left\langle\frac{\Delta p_i}{\Delta t}\right\rangle\frac{\partial f}{\partial p_i} + \frac{1}{2}f\frac{\partial^2}{\partial p_i\partial p_j}\left[\left\langle\frac{\Delta p_j\Delta p_i}{\Delta t}\right\rangle\right] + \frac{1}{2}\left\langle\frac{\Delta p_j\Delta p_i}{\Delta t}\right\rangle\frac{\partial^2 f}{\partial p_i\partial p_j}.$$

Isotropy implies that the distribution function would not change due to collisions ($\partial f/\partial t = 0$) and that the distribution function is independent of the momenta ($\partial f/\partial p_i = 0$), such that

$$f\frac{\partial}{\partial p_i}\left[\left\langle\frac{\Delta p_i}{\Delta t}\right\rangle\right] = \frac{1}{2}f\frac{\partial^2}{\partial p_i\partial p_j}\left[\left\langle\frac{\Delta p_j\Delta p_i}{\Delta t}\right\rangle\right] \qquad \Longrightarrow \qquad \left\langle\frac{\Delta p_i}{\Delta t}\right\rangle = \frac{1}{2}\frac{\partial}{\partial p_j}\left[\left\langle\frac{\Delta p_j\Delta p_i}{\Delta t}\right\rangle\right].$$

Substituting this back into the FPE and expanding the derivatives, gives

$$\left.\frac{\partial f(\vec{x};\vec{p};t)}{\partial t}\right|_{\text{collision}} = \frac{1}{2}\frac{\partial}{\partial p_i}\left[\left\langle\frac{\Delta p_j\Delta p_i}{\Delta t}\right\rangle\frac{\partial f}{\partial p_j}\right] = \frac{1}{2}\vec{\nabla}_p\cdot\left[\left\langle\frac{\Delta\vec{p}\Delta\vec{p}}{\Delta t}\right\rangle\cdot\vec{\nabla}_p f(\vec{x};\vec{p};t)\right] \tag{4.12}$$

and hence, information about the diffusion tensor $\langle \Delta\vec{p}\Delta\vec{p}/\Delta t\rangle$ is sufficient. By combining the FPE (Eq. 4.12) with the Boltzmann equation (Eq. 4.2),

$$\frac{\partial f}{\partial t} + \vec{\nabla}\cdot\left[\frac{d\vec{x}}{dt}f\right] + \vec{\nabla}_p\cdot\left[\frac{d\vec{p}}{dt}f\right] = \frac{1}{2}\vec{\nabla}_p\cdot\left[\left\langle\frac{\Delta\vec{p}\Delta\vec{p}}{\Delta t}\right\rangle\cdot\vec{\nabla}_p f\right], \tag{4.13}$$

gives a natural generalization of the continuous medium theorem to include diffusion in momentum space. This is an interesting result, as it implies that the distribution function is a

continuous function of its variables even though properties of its particles might change randomly due to the stochastic forces on them. Notice that an equation with the same functional form can be derived from the Vlasov equation [*Chandrasekhar*, 1943; *Gardiner*, 1985; *Liboff*, 1990; *Choudhuri*, 1998].

4.2.3 The Transport Equation for Focused Transport in One Dimension

The full derivation of the relativistic FTPE in three spatial dimensions is given in *Zank* [2014] and *Dosch and Zank* [2016] (also see *Skilling* [1975]), but the outline of a simpler derivation with only the necessary terms will be given here. The energy of charged particles interacting with magnetic turbulence will be conserved in the wave frame, if there is a single wave frame, and the particles will only experience pitch-angle scattering, assuming slab turbulence [*Skilling*, 1971; *Luhmann*, 1976; *Earl*, 1984]. It would therefore be convenient to use the distribution function in the mixed frame with the time and spatial coordinates in the observer's frame and the momentum in the wave frame. Notice that the wave frame is not necessarily an inertial reference frame, since the outflow which carries the waves might change with both time and position. This would introduce additional 'forces' on the particles when transforming to the wave frame and the temporal and spatial derivatives should also be transformed [*Zank*, 2014; *Dosch and Zank*, 2016]. To keep the calculations to a minimum, these terms will not be considered here as the constant and uniform SW will be used as a wave frame. Assuming that the wave frame is not moving relativistically, the momentum transforms as $\vec{p}' = \vec{p} - m\vec{w}$ and the momentum derivatives must be transformed as

$$\frac{\partial}{\partial p_i} = \frac{\partial p'_j}{\partial p_i}\frac{\partial}{\partial p'_j} = \frac{\partial}{\partial p_i}[p_j - mw_j]\frac{\partial}{\partial p'_j} = \delta_{ij}\frac{\partial}{\partial p'_j} = \frac{\partial}{\partial p'_i},$$

where δ_{ij} is the Kronecker delta function and it was again assumed that the mass is invariant.

For plasma with a stationary background magnetic field, it is convenient to use the magnetic field as a reference point. Assume that the magnetic field is frozen into the wave frame so that the magnetic field is parallel to the velocity vector of the wave frame (see the discussion in Section 4.3.1 for the specific application of the SW and HMF). The mixed distribution function can then be defined in a field aligned coordinate system as $f^*(s_\parallel; \vec{s}_\perp; p'_\parallel; \vec{p}'_\perp; t)ds_\parallel d^2s_\perp dp'_\parallel d^2p'_\perp$, with $d^2s_\perp = ds_{\perp 1}ds_{\perp 2}$ and $d^2p'_\perp = dp'_{\perp 1}dp'_{\perp 2}$. Since the particles' gyrating motion causes a precession of the momentum vector, a transformation from Cartesian to spherical coordinates in momentum space can be made, such that $f^*_s(s_\parallel; \vec{s}_\perp; p;' \mu'; \varphi'; t)ds_\parallel d^2s_\perp dp'd\mu'd\varphi'$. Both the gradient in configuration and momentum space should include derivatives of μ' and φ' with respect to the spatial and momentum coordinates as these coordinates would change depending on the position of a particle in a spatially varying magnetic field, with an additional derivative of p' with respect to the momentum coordinates [*Zank*, 2014; *Dosch and Zank*, 2016]. These terms, however, will also be neglected for now and considered later. Let $D_{p_ip_j} = \langle \Delta p_i \Delta p_j/\Delta t\rangle$ be the Fokker-Planck coefficients, then all the momentum diffusion coefficients in the wave frame ($D_{p'p'}$, $D_{p'\mu'}$, $D_{\mu'p'}$, $D_{p'\varphi'}$, and $D_{\varphi'p'}$) can be set equal to zero.

The dependence of the distribution function on φ' can be averaged out to yield the gyrotropic distribution function $f_g^*(s_\parallel;\vec{s}_\perp;p';\mu';t) = \int_0^{2\pi} f_s^*(s_\parallel;\vec{s}_\perp;p';\mu';\varphi';t)d\varphi'/2\pi$. Transport perpendicular to the magnetic field is ignored for simplicity by *Ruffolo* [1995] and hence the reduced distribution function is obtained by integrating over the unwanted coordinates $f_r^*(s;p';\mu';t) \propto \int\int f_g^*(s_\parallel;\vec{s}_\perp;p';\mu';t)ds_{\perp 1}ds_{\perp 2}$, where s was written for $s_\parallel$. Notice that the neglect of the perpendicular motion implies that it is assumed that there are no drifts or diffusion of the particles perpendicular to the HMF, such that particles are confined to a flux tube. It is important to realize that the neglect of perpendicular transport implies that the intensity of an SEP event would be overestimated. Applying then these momentum and coordinate transformations to the TPE (Eq. 4.13) and neglecting the derivatives with respect to the gyrophase and the perpendicular coordinates, yields

$$0 = \frac{\partial f_r^*}{\partial t} + \frac{\partial}{\partial s}\left[\frac{ds}{dt}f_r^*\right] + \frac{\partial}{\partial p'}\left[\frac{dp'}{dt}f_r^*\right] + \frac{\partial}{\partial \mu'}\left[\frac{d\mu'}{dt}f_r^*\right] - \frac{\partial}{\partial \mu'}\left[\frac{D_{\mu'\mu'}}{2}\frac{\partial f_r^*}{\partial \mu'}\right], \tag{4.14}$$

where dp'/dt is the Lorentz force experienced by the particles in the wave frame. This FTPE is appropriate for describing anisotropic distributions as it has an explicit dependence on pitch-angle. By integrating over pitch-cosine as well, a distribution function would be obtained which describes an isotropic distribution of particles, which is normally used to describe galactic cosmic rays (GCRs; see e.g. *Parker* [1965]).

4.3 The One-dimensional Focused Transport Equation of Ruffolo

The specifics of the various terms in the FTPE will be calculated in this section.

4.3.1 The Co-rotating Solar Wind Frame

Assume that the turbulent fluctuations are small, such that the average HMF is well represented by a Parker field. Although the fluctuations will move with their wave speed relative to the SW, plasma waves move much slower than the SW so that the wave frame can be approximated by the SW frame (this assumption, of course, do not hold close to the Sun). The turbulence can therefore be thought of as being frozen into the SW and momentum diffusion can then be neglected in the SW frame. From Section 2.1.3 it can be seen that an observer rotating with the Sun would see a HMF with only a radial component. In this co-rotating reference frame, the observer moves with respect to the SW and the SW must therefore be transformed into this co-rotating frame to be aligned with the HMF. The SW transformation is given by $\vec{v}_{\rm sw}^{\,c} = v_{\rm sw}^c\hat{s} = v_{\rm sw}\hat{r} - \omega_\odot(r - r_\odot)\sin\theta\hat{\phi}$, where $\hat{s}$ is a unit vector along the HMF directed away from the Sun [*Parker*, 1958], and the speed of the transformed SW is

$$v_{\rm sw}^c = v_{\rm sw}\sec\psi \tag{4.15}$$

from the geometry in Fig. 4.2 [*Ruffolo*, 1995]. In this transformation the SW is forced to be aligned with the HMF and SW effects perpendicular to the HMF are neglected. From Eq. 4.15 it

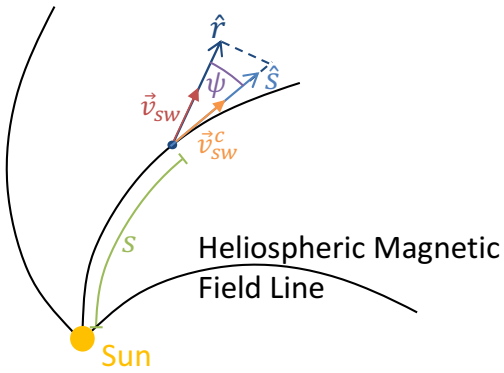

Figure 4.2: Schematic representation of a few background Parker magnetic field lines (black curves) in the equatorial plane of the inner heliosphere emanating from the Sun (orange dot), illustrating the definition of the coordinate s along the magnetic field line, the spiral angle ψ (Eq. 2.4), and the co-rotating solar wind $\vec{v}^{c}_{\rm sw}$ (Eq. 4.15) in relation to the radial direction $\hat{r}$ and radially directed solar wind $\vec{v}_{\rm sw}$. This figure was adapted from *Ruffolo* [1995].

can be seen that the SW speed in the co-rotating frame becomes infinite at large radial distances and realistic flow speeds are of course unrealistic. In reality, the HMF lies perpendicular to the SW at large radial distances, since $\psi \to 90^\circ$ when $r \to \infty$ from Eq. 2.4, and the speed of the SW parallel to the HMF should approach zero. The infinite speed is an unavoidable artefact of the transformation, but should be reasonable within a few AU from the Sun where the distribution of SEPs are studied [*Lampa*, 2011]. A non-relativistic transformation can be made of the SEPs' momenta, with the components perpendicular to the HMF being unchanged by the SW (Eq. 4.5), since it is assumed that the SW is parallel to the HMF, and $v^{c}_{\rm sw}$ substituted for the wave speed in the parallel momentum transformation of Eq. 4.6 [*Ruffolo*, 1995].

4.3.2 Energy Changes

The two major effects which cause energy changes are a decrease in the particles' velocity in the SW frame due to the interaction between focusing and pitch-angle scattering and the diverging of scattering centres [*Ruffolo*, 1995; *Webb and Gleeson*, 1979]. The deceleration is expected to be larger for slow particles as they spend more time being modulated by the various effects. Notice that although momentum diffusion was avoided by working in a mixed frame, it would still be present as a second order effect. Momentum diffusion can only be neglected if there is a single wave frame, but the SW, however, has multiple wave frames (in the current context of a field aligned SW and neglect of perpendicular transport, there would be a wave frame in both directions along the HMF; in a full three-dimensional case, there would be six different wave frames, due to the two mutually perpendicular directions). However, since the relative speed between the different wave frames is small, the fractional momentum change $\Delta p'/p'$ between the wave frames would also be small. Given that stochastic acceleration is second order in $\Delta p'/p'$ [*Fermi*, 1949], the resulting momentum diffusion can then be neglected.

Adiabatic Focusing

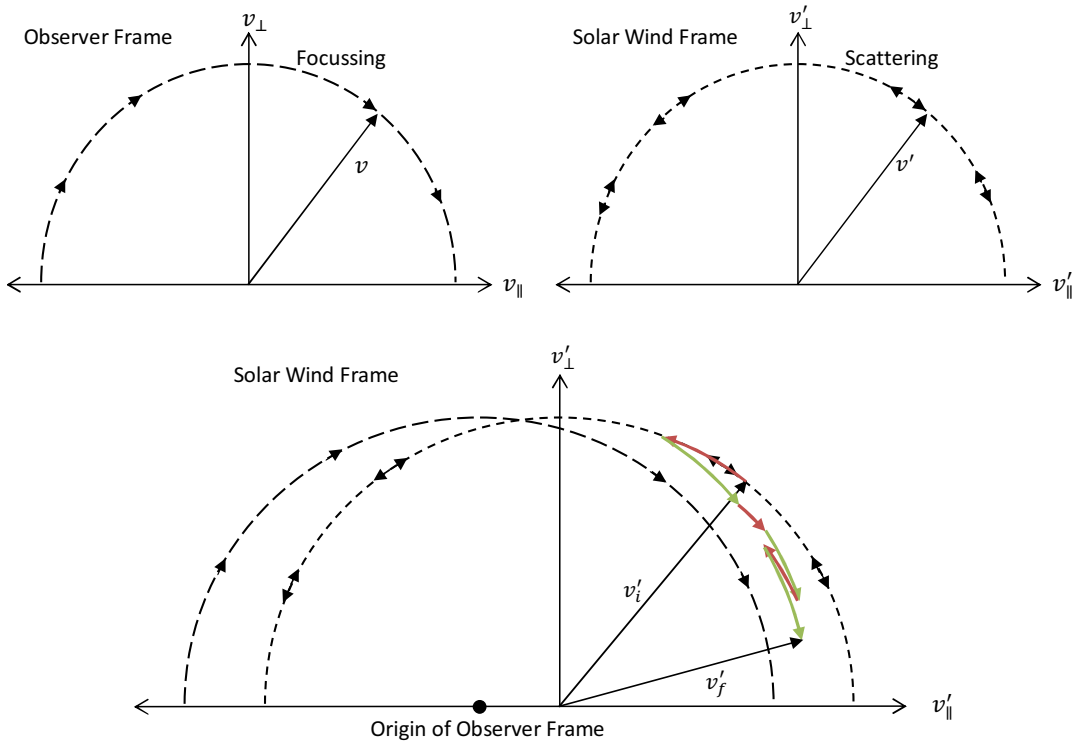

Figure 4.3: *Top panels:* Illustration of the action in velocity space of focusing in the observer frame (*left*) and pitch-angle scattering in the solar wind frame (*right*). Focusing, without the effects of scattering, acts to increase the parallel speed along semi-circles of constant speed in the observer frame, while scattering, without the effects of focusing, acts in either direction along semi-circles of constant speed in the solar wind frame. *Bottom panel:* Schematic trajectory of a solar energetic particle in velocity space, alternately undergoing scattering (indicated by red arrows) and focusing (indicated by green arrows) as viewed in the solar wind frame. The combination of the two processes leads to a systematic deceleration of the particle. This figure was adapted from *Ruffolo* [1995].

Due to the decrease of the HMF magnitude with radial distance and the turbulence in the HMF, SEPs will be focused and scattered, respectively. These two situations are illustrated in velocity space in the top panels of Fig. 4.3, where focusing (left panel) continuously increases the parallel speed in the observer frame without changing the speed in the observer frame and scattering (right panel) can either increase or decrease the parallel speed in the SW frame without changing the speed in the SW frame. When combining the two effects, the observer frame moves at a velocity $-\vec{v}^{c}_{\rm sw}$ with respect to the SW frame, as indicated by the point in the bottom panel of Fig. 4.3. Focusing moves the velocity vector to the right along semi-circles centred on the observer's frame. Scattering, however, moves the velocity vector around on semi-circles centred on the SW frame, with the result that the speed in the SW frame decreases. This energy loss is called *adiabatic focusing* and is a kinematic effect which would occur in any flow diverging from the origin. Notice that 'adiabatic' here refers to the adiabatic expansion of the SW and does not imply that the SEPs are losing energy adiabatically [*Webb and Gleeson*, 1979; *Ruffolo*, 1995; *Lampa*, 2011].

For simplicity, first consider adiabatic focusing in a radially-directed magnetic field with a radially-directed SW. The particle's speed in the SW frame change due to the change in the pitch-cosine by focusing in the observer's frame,

$$\frac{dv'}{dt} = \frac{dv'}{d\mu'}\frac{d\mu'}{dt} = \frac{dv'}{d\mu}\frac{d\mu}{d\mu'}\frac{d\mu}{dt}\frac{d\mu'}{d\mu} = \left.\frac{dv'}{d\mu}\right|_v \frac{d\mu}{dt}, \tag{4.16}$$

where focusing in the observer's frame conserves the speed. To calculate the first factor, the speed can be written similarly to Eq. 4.7 as $v' = \sqrt{v^2 + v_{\rm sw}^2 - 2\mu v v_{\rm sw}}$, from which it follows that

$$\frac{dv'}{d\mu} = -\frac{v v_{\rm sw}}{v'}. \tag{4.17}$$

The pitch-cosine changes due to the movement of the particle into different regions of the HMF, so for the last factor in Eq. 4.16

$$\frac{d\mu}{dt} = \frac{d\mu}{dB}\frac{dB}{ds}\frac{ds}{dt} = \frac{(1-\mu^2)v}{2L(s)}, \tag{4.18}$$

where $ds/dt = v_{\parallel}$, $d\mu/dB = -(1-\mu^2)/2\mu B$ from the mirroring condition (Eq. 3.10), with $B_m = B/(1-\mu^2)$ substituted, and

$$\frac{1}{L(s)} = -\frac{1}{B(s)}\frac{dB(s)}{ds} \tag{4.19}$$

is the *focusing length*. Substituting Eq. 4.17 and Eq. 4.18 into Eq. 4.16 and using $(1-\mu^2)v^2 = (1-\mu'^2)v'^2$, results in

$$\frac{dv'}{dt} = -\frac{(1-\mu'^2)v' v_{\rm sw}}{2L(s)}. \tag{4.20}$$

A relativistic approach yields a similar result in terms of momentum and hence, multiplying both sides with the mass of the particle, the adiabatic focusing term is given by [*Ruffolo*, 1995]

$$\frac{dp'}{dt} = -\frac{p'(1-\mu'^2)v_{\rm sw}}{2L(s)}. \tag{4.21}$$

Notice that for the current radial magnetic field and SW under consideration, it can be written that $v_{\rm sw}/L(s) = 2v_{\rm sw}/r$ and $\vec{\nabla}\cdot\vec{\mathrm{v}}_{sw} = 2v_{\rm sw}/r$, respectively. The adiabatic focusing term of Eq. 4.21 can therefore be written as $dp'/dt = -p'(1-\mu'^2)\vec{\nabla}\cdot\vec{v}_{\rm sw}/2$ and averaging this over pitch-cosine, yields

$$\left\langle \frac{dp'}{dt} \right\rangle_{\mu'} = -\frac{p'}{3}\vec{\nabla}\cdot\vec{v}_{\rm sw}.$$

This is the expression used in GCR studies for the adiabatic deceleration of an isotropic distribution and Eq. 4.21 is therefore the generalization of adiabatic deceleration to focused transport [*Ruffolo*, 1995; *Webb and Gleeson*, 1979]. The SW and HMF are parallel to each other in the co-rotating SW frame so that Eq. 4.21 can be used as is with $v_{\rm sw}$ replaced by $v_{\rm sw}^c$ [*Ruffolo*, 1995]:

$$\frac{dp'_{AF}}{dt} = -\frac{p'(1-\mu'^2)}{2L(s)} v_{\rm sw} \sec\psi. \tag{4.22}$$

Due to the $1/L(s)$ factor, adiabatic focusing is expected to be important close to the Sun where $L(s)$ is small.

Inverse Fermi Effect

The second mechanism responsible for energy changes is due to the divergence of the SW and is called the *inverse Fermi effect*. As the SW expands, particles scatter more frequently against receding scattering centres than approaching scattering centres, leading to a stochastic deceleration and this is called *differential advection* by *Ruffolo* [1995] (the term "differential convection" is actually used, but advection will be used here for large scale bulk flows, as convection is specifically associated with large scale motions induced by heat transfer). The deceleration can be explained as follows: as the SW expands radially, the area with scattering centres increases quadratically due to the area's dependence on radius (consider the area at r and $r+dr$, that is $4\pi(r+dr)^2 > 4\pi r^2$); for a particle between r and $r+dr$, interactions with scattering centres at r ($r+dr$) implies head-on (trailing) collisions and hence energy gains (losses); for particles propagating diffusively (equal probability moving outwards or inwards), the probability of 'hitting' a scattering centre at $r+dr$ is higher because of the larger area; the probability for trailing collisions is therefore larger than for head-on collisions and the particles lose energy on average.

The change in momentum in the SW frame due to the divergence of the SW along the HMF, can be written as

$$\left.\frac{dp'}{dt}\right|_{p'_\perp} = \frac{dp'}{dp'_\parallel}\frac{dp'_\parallel}{dt}, \tag{4.23}$$

assuming that $p'_\perp$ is constant. The first factor can be calculated from $p' = \sqrt{p'^2_\parallel + p'^2_\perp}$,

$$\frac{dp'}{dp'_\parallel} = \frac{p'_\parallel}{p'}. \tag{4.24}$$

To calculate the last factor in Eq. 4.23, consider a particle moving between point A and B on the same magnetic field line. The momentum in the SW frame at the two points are $p'_{\parallel A} = p_{\parallel A} - mv^c_{\mathrm{swA}}$ and $p'_{\parallel B} = p_{\parallel B} - mv^c_{\mathrm{swB}}$, respectively. Assuming $p_\parallel$ to be constant between the two points for simplicity, the change in momentum between the two points is then

$$\Delta p'_\parallel \approx -m\Delta v^c_{\mathrm{sw}} = -mv_{\mathrm{sw}}\frac{d}{ds}\left[\sec\psi\right]\Delta s = -mv_{\mathrm{sw}}\frac{d}{dr}\left[\sec\psi\right]\frac{dr}{ds}v_\parallel\Delta t = -p_\parallel v_{\mathrm{sw}}\frac{d}{dr}\left[\sec\psi\right]\cos\psi\Delta t,$$

where it can be seen that $dr/ds = \cos\psi$ from the geometry in Fig. 4.2. The rate of change of the parallel momentum is then

$$\frac{dp'_\parallel}{dt} = \lim_{\Delta t\to 0}\frac{\Delta p'_\parallel}{\Delta t} = -p_\parallel v_{\mathrm{sw}}\frac{d}{dr}\left[\sec\psi\right]\cos\psi. \tag{4.25}$$

Substituting Eq. 4.24 and Eq. 4.25 in Eq. 4.23 and assuming that $p'_\parallel \approx p_\parallel$, since $v^c_{\mathrm{sw}}/c \ll 1$, the change in the momentum in the SW frame is [*Lampa*, 2011; *Ruffolo*, 1995]

$$\frac{dp'_{IF}}{dt} = -p'\mu'^2 v_{\mathrm{sw}}\cos\psi\frac{d}{dr}\left[\sec\psi\right]. \tag{4.26}$$

This equation is equivalent to the full inverse Fermi effect (as derived e.g. by *Webb and Gleeson* [1979]) with the pitch-cosine dependence retained. Due to the $\cos\psi$ factor, the inverse Fermi

effect is expected to be important close to the Sun and over the poles, where $\cos\psi \approx 1$, while being small in the equatorial plane at large distances, since $\cos\psi \to 0$ as $r \to \infty$. Notice that the inverse Fermi effect cancels with the so called *betatron effect*, which is caused by the curl of the electric field on the particle's GC as the particle moves in a helical path along the HMF, in the case of isotropic GCRs, so that the adiabatic deceleration is the only energy change experienced by GCRs. However, since the perpendicular transport is neglected in this study, differential advection has an explicit influence on the energy changes of SEPs [*Ruffolo*, 1995; *Webb and Gleeson*, 1979].

4.3.3 Field-parallel Transport

The SEPs will be advected by the SW: the embedded HMF is advected outwards by the SW and since a charged particle gyrates around the HMF, the particle will also experience an outwards advection. The motion of the particle along the HMF can therefore be decomposed into the parallel speed $v'\mu'$ of the particle in the SW frame and the parallel speed of the SW frame $v_{\rm sw}^c$. This can be calculated in the observer's frame from the relativistic addition of speeds expanded to terms linear in $v_{\rm sw}^c/c$:

$$\frac{ds}{dt} = \frac{v'_\parallel + v_{\rm sw}^c}{1 + v'_\parallel v_{\rm sw}^c/c^2} \approx \mu' v' + \left[1 - \left(\frac{\mu' v'}{c}\right)^2\right] v_{\rm sw} \sec\psi. \tag{4.27}$$

The effect of advection is expected to be larger for low energy particles, as they spend more time 'stuck' to the HMF [*Ruffolo*, 1995]. It should be kept in mind that even though scattering will tend to isotropise the SEP distribution, the advection of the SEPs past an observer would cause an observed anisotropy of the distribution (Compton-Getting effect) [*Gleeson and Axford*, 1968; *Forman*, 1970].

4.3.4 Pitch-cosine Transport

It was already seen that the particle's pitch-angle is changed by focusing and the inverse Fermi effect or differential advection.

Focusing

The change in the pitch-cosine in the SW frame is

$$\frac{d\mu'}{dt} = \left.\frac{d\mu'}{d\mu}\right|_v \frac{d\mu}{dt}, \tag{4.28}$$

where focusing conserve the speed in the observer's frame. The first factor can be found from $(1-\mu^2)v^2 = (1-\mu'^2)v'^2$, such that $dv_\perp/d\mu = dv'_\perp/d\mu$ which implies $\mu v^2 = \mu' v'^2 (d\mu'/d\mu) - (1-\mu'^2)v'(dv'/d\mu)$. Together with Eq. 4.17 and the parallel velocity component of Eq. 4.27, this

becomes

$$\frac{d\mu'}{d\mu} \approx \frac{v}{v'}\left(1 - \frac{v'_{\parallel} v^c_{\rm sw}}{c^2} + \frac{\mu' v^c_{\rm sw}}{v'}\right). \tag{4.29}$$

Substituting Eq. 4.29 and Eq. 4.18 into Eq. 4.28 and using $(1-\mu^2)v^2 = (1-\mu'^2)v'^2$ again, the change in pitch-cosine due to focusing is [*Ruffolo*, 1995]

$$\frac{d\mu'_F}{dt} = \left(1 + \mu' \frac{v_{\rm sw}}{v'} \sec\psi - \mu' \frac{v' v_{\rm sw}}{c^2} \sec\psi\right) \frac{(1-\mu'^2)v'}{2L(s)}. \tag{4.30}$$

Differential Advection

The inverse Fermi effect or differential advection, also causes the pitch-cosine to change

$$\frac{d\mu'}{dt} = \frac{d\mu'}{dp'}\frac{dp'}{dt}, \tag{4.31}$$

because the loss of parallel momentum in the large number of trailing collisions, will systematically increase the pitch-angle. Since it is assumed that $p'_{\perp}$ is constant, with the definition of the perpendicular momentum in the SW frame it can be written that $0 = d[p'^2(1-\mu'^2)] = 2(1-\mu'^2)p'dp' - 2\mu' p'^2 d\mu'$, from which it follows that

$$\frac{d\mu'}{dp'} = \frac{1-\mu'^2}{\mu' p'}. \tag{4.32}$$

Substituting Eq. 4.32 and Eq. 4.26 into Eq. 4.31, the change in pitch-cosine due to differential advection is [*Ruffolo*, 1995]

$$\frac{d\mu'_{IF}}{dt} = -\mu'(1-\mu'^2) v_{\rm sw} \cos\psi \frac{d}{dr}\left[\sec\psi\right]. \tag{4.33}$$

4.3.5 The Focused Transport Equation

Substituting Eq. 4.27 for ds/dt, Eq. 4.22 and Eq. 4.26 for dp'/dt, and Eq. 4.30 and Eq. 4.33 for $d\mu'/dt$ in Eq. 4.14, and writing $f(s;p';\mu';t)$ for $f^*_r(s;p';\mu';t)$, then yields the FTPE of *Ruffolo* [1995]:

$$\begin{aligned}
\frac{\partial f}{\partial t} = & -\frac{\partial}{\partial s}\left[\mu' v' f\right] && \text{(temporal changes \& streaming)} \\
& - \frac{\partial}{\partial s}\left[\left(1 - \left[\frac{\mu' v'}{c}\right]^2\right) v^c_{\rm sw} f\right] && \text{(advection)} \\
& + \frac{\partial}{\partial p'}\left[p' v^c_{\rm sw} \frac{1-\mu'^2}{2L(s)} f\right] && \text{(adiabatic focusing)} \\
& + \frac{\partial}{\partial p'}\left[p' \mu'^2 \cos\psi \frac{dv^c_{\rm sw}}{dr} f\right] && \text{(inverse Fermi effect)} \\
& - \frac{\partial}{\partial \mu'}\left[\frac{(1-\mu'^2)v'}{2L(s)}\left(1 + \mu' \frac{v^c_{\rm sw}}{v'} - \mu' \frac{v' v^c_{\rm sw}}{c^2}\right) f\right] && \text{(focusing)} \\
& + \frac{\partial}{\partial \mu'}\left[\mu'(1-\mu'^2)\cos\psi \frac{dv^c_{\rm sw}}{dr} f\right] && \text{(differential advection)}
\end{aligned} \tag{4.34}$$

$$+\frac{\partial}{\partial\mu'}\left[\frac{D_{\mu'\mu'}(p';\mu')}{2}\frac{\partial f}{\partial\mu'}\right]. \qquad \text{(scattering)}$$

Notice that the distribution function describe the number of particles per phase-space volume in a given flux tube [*Ng and Wong*, 1979]. The FTPE derived and first applied to SEPs by *Roelof* [1969], is the same as that of *Ruffolo* [1995], but with no SW effects. It can also be shown that this FTPE is equivalent to a special case of the more general FTPE of *Skilling* [1971] with the wave frame speed set to $v_{\rm sw}^c$. This FTPE is similar to the *Parker* [1965] TPE used in GCR modulation studies when integrated over pitch-cosine. The explicit dependence on pitch-cosine, however, makes the FTPE the perfect tool to study the anisotropic particle distributions of SEPs [*Ruffolo*, 1995]. It should be noticed that the FTPE is a highly non-linear, second order, parabolic partial differential equation. The different processes' effects cannot be added linearly because each process is dependent on quantities which are affected by the other processes. The various terms affect one another and the dominating process is ultimately determined by its relative strength, that is, the effect on it by the other processes and its effect on the other processes. This non-linearity and competition between terms imply that none of the terms can be neglected to model SEPs realistically.

4.4 Summary

In this chapter the macro-physical transport of solar energetic particles was discussed. The concepts introduced in Chapter 3 were used to explain the origin of the terms appearing in the focused transport equation (FTPE). The FTPE is a special form of the general Fokker-Planck equation, which is the generalisation of Liouville's theorem to a distribution function including the effects of collisions, or in this case, pitch-angle scattering. The form of the FTPE was derived for the spatial dimension along the heliospheric magnetic field (HMF), with transport effects perpendicular to the HMF neglected. It was seen that there are three important processes entering into the FTPE, namely field parallel transport, energy losses, and pitch-angle changes. The field parallel transport is composed of the particles' motion along the HMF and the advection of particles by the solar wind (SW). The energy losses are caused by adiabatic focusing and the inverse Fermi effect, with stochastic acceleration neglected due to assumed energy conservation in the SW frame. Adiabatic focusing is caused by the interplay between focusing in the observer's frame and scattering in the SW frame, while the inverse Fermi effect is caused by trailing collisions in the diverging SW. The pitch-angle changes are caused by pitch-angle scattering, focusing, and differential advection. Pitch-angle scattering and focusing were discussed in Chapter 3, while differential advection is caused by the inverse Fermi effect.

Chapter 5

Stochastic Differential Equations

This chapter introduces stochastic differential equations to solve the focused transport equation. The chapter will begin with a discussion on stochastic differential equations and the usage thereof in solving Fokker-Planck type equations, covering a broad range of topics starting with the definition of a stochastic differential equation, the link between a stochastic differential equation and a Fokker-Planck equation, the interpretation of a stochastic differential equation based solution, constructing the distribution function from the stochastic differential equation solutions, and some boundary conditions. All of the introduced concepts will then be explained using Brownian motion in one dimension. The chapter will be concluded with a discussion of the stochastic transport model used in solving the one-dimensional focused transport equation for solar energetic particles derived in Chapter 4. Appendix B deals with the numerical solutions of stochastic differential equations and some specifics of the stochastic transport model.

5.1 Stochastic Differential Equations

Stochastic calculus is a study area with several text books dealing with its mathematical formalism and application to a variety of problems. A formal introduction to stochastic calculus is given by *Øksendal* [2000], while the introduction given by *Kloeden and Platen* [1995] focuses on numerical methods to solve stochastic differential equations (SDEs). *Gardiner* [1985] and *van Kampen* [1992] gives an introduction of stochastic calculus specifically for the fields of natural sciences, while the interested reader, who is new to the field of stochastic problems in physics, is referred to the introductory book of *Lemons* [2002]. The classical review of stochastic problems in physics is that of *Chandrasekhar* [1943], while *Strauss and Effenberger* [2017] gives a review of the application of SDEs to cosmic ray (CR) modelling with toy models to introduce the basic concepts. This section only gives the necessary details, with mathematical proofs only insofar as to illustrate an important concept.

Jokipii and Levy [1977] used a Monte Carlo simulation of galactic CRs (GCR; the diffusion was simulated using a uniformly distributed random number), while *Yamada et al.* [1998] was the

first to use SDEs in studying the modulation of GCRs. This was done for one spatial dimension and showed that the SDE approach compares well against the traditional finite difference schemes. *Zhang* [1999b] expanded the SDE approach of GCRs to three spatial dimensions, including drifts along a flat heliospheric current sheet, and showed how SDEs can be used to give additional insight into the modulation process. *Pei et al.* [2010] presented a three-dimensional, time dependent SDE approach and showed that the SDEs can be directly solved in spherical coordinates, while *MacKinnon and Craig* [1991] first applied SDEs in solving a focused transport equation (FTPE) for binary collisions of solar energetic particles (SEPs) with 'cold' hydrogen atoms in the chromosphere. *Kocharov et al.* [1998] first used Monte Carlo simulations to model SEPs, while a three-dimensional focused transport model for SEPs with and without energy losses are presented by *Qin et al.* [2006] or *Zhang et al.* [2009] and *Dröge et al.* [2010], respectively. It will be seen that solving the SDEs can be computationally expensive and these types of SDE models did not become feasible until the dawn of parallel-processing.

5.1.1 The Definition of a Stochastic Differential Equation

For the current purpose it is sufficient to define a *stochastic differential equation* (SDE) as any differential equation with the general form

$$\frac{dX(t)}{dt} = a(X;t) + b(X;t)\zeta(t) \tag{5.1}$$

in the one-dimensional case, where $X(t) = x(t)$ is the *random variable* corresponding to the physical quantity of interest x (this simple relation implies that the variable x, called a *sure* or *deterministic variable*, is changing stochastically and it is this stochastic nature which is modelled by X). Here $a(x;t)$ and $b(x;t)$ are continuous functions, with the two terms on the right hand side of the SDE referred to as the *drift* and *diffusion* terms, respectively, in SDE nomenclature (this should not be confused with the physical drift and diffusion terms present in the transport equation; TPE). The first term represent the system's deterministic behaviour, while $\zeta(t)$ represents a rapidly varying stochastic function, also referred to as the *noise* term, and describes the system's stochastic behaviour. It is required that the average of $\zeta(t)$ is zero, as any non-zero mean can be absorbed into the definition of $a(x;t)$, and it is usually assumed that $\zeta(t)$ is a Markov process with values which are independent of each other at two different times [*Gardiner*, 1985; *Kloeden and Platen*, 1995; *Øksendal*, 2000; *Strauss and Effenberger*, 2017].

In this work only SDEs of the Itô type are considered, where Eq. 5.1 can be rewritten as

$$dX(t) = a(X;t)dt + b(X;t)dW(t), \tag{5.2}$$

where $dW(t) = \zeta(t)dt$ represents the Wiener process, the integral of the stochastic function present in Eq. 5.1. The Wiener process is a time stationary, stochastic Lévy process where the time increments have a Normal/Gaussian distribution with a mean of zero and a variance of dt, that is $dW(t) = W(t) - W(t - dt) \sim \mathcal{N}(0; dt)$. By replacing $dX(t)$ with its equivalent $X(t + dt) - X(t)$, allows Eq. 5.2 to be interpreted in the following way: if the random variable

$X(t)$ is equal to the sure variable x at time t, then $X(t+dt)$ is a Normally distributed random variable with mean $x(t)+a(x;t)dt$ and variance $b^2(x;t)dt$ [*Gardiner*, 1985; *Kloeden and Platen*, 1995; *Øksendal*, 2000; *Lemons*, 2002; *Strauss and Effenberger*, 2017].

Eq. 5.1 can be integrated analytically

$$X(t) = X(t_0) + \int_{t_0}^{t} a(X;t')dt' + \int_{t_0}^{t} b(X;t')dW(t'), \tag{5.3}$$

where the first integral is a normal (Riemann or Lebesgue) integral, while the second is an Itô type stochastic integral. Notice that there are other types of SDEs in addition to those of the Itô type (e.g. the Stratonovich formulation) and that the current discussion is only applicable to Itô type SDEs. Eq. 5.2 can be generalized to a set of n-dimensional SDEs

$$dQ_i(t) = a_i(\vec{Q};t)dt + b_{ij}(\vec{Q};t)dW_j(t), \tag{5.4}$$

where $\vec{Q}$ are n generalized coordinates (which can be a mixture of spatial and momentum coordinates), $\vec{a}$ is a n-dimensional vector, b_{ij} is a $n \times n$ matrix (where summation notation is used), and $d\vec{W}(t)$ is n independent Wiener processes [*Gardiner*, 1985; *Kloeden and Platen*, 1995; *Øksendal*, 2000; *Lemons*, 2002; *Strauss and Effenberger*, 2017].

The Relation between the Fokker-Planck Equation and Stochastic Differential Equation

To establish a link between the SDE of Eq. 5.4 and the Fokker-Planck equation (FPE; Eq. 4.10), the discussion of *Gardiner* [1985] will be followed (see also the discussion in Appendix B of *Lemons* [2002]). It should be noted that since the Wiener process is Normally distributed with a variance of dt, $dW(t)$ is of order $\sqrt{dt}$. Consider an arbitrary function $g(\vec{q}(t))$, of the random variables $\vec{q}(t) = \vec{Q}(t)$, which is twice continuously differentiable. A Taylor expansion of this function's infinitesimal change to first order in dt, gives

$$\begin{aligned}
d[g(\vec{q}(t))] &= \frac{\partial g(\vec{q}(t))}{\partial q_i} dQ_i(t) + \frac{1}{2}\frac{\partial^2 g(\vec{q}(t))}{\partial q_i \partial q_j} dQ_i(t) dQ_j(t) + \cdots \\
&= \frac{\partial g(\vec{q}(t))}{\partial q_i}\left[a_i(\vec{Q};t)dt + b_{ij}(\vec{Q};t)dW_j(t)\right] + \\
&\quad \frac{1}{2}\frac{\partial^2 g(\vec{q}(t))}{\partial q_i \partial q_j}\left[a_i(\vec{Q};t)dt + b_{ij}(\vec{Q};t)dW_j(t)\right]\left[a_j(\vec{Q};t)dt + b_{ji}(\vec{Q};t)dW_i(t)\right] + \cdots \\
&\approx \left[a_i(\vec{Q};t)\frac{\partial g(\vec{q}(t))}{\partial q_i} + \frac{1}{2}C_{ij}(\vec{Q};t)\frac{\partial^2 g(\vec{q}(t))}{\partial q_i \partial q_j}\right]dt + b_{ij}(\vec{Q};t)\frac{\partial g(\vec{q}(t))}{\partial q_i} dW_j(t),
\end{aligned} \tag{5.5}$$

where $\vec{q}$ and $\vec{Q}$ was used interchangeably, Eq. 5.4 was substituted for $dQ_i(t)$, $dW_j(t)dW_i(t) \approx dt$ was used, and

$$C_{ij}(\vec{q};t) = b_{ij}(\vec{q};t)b_{ji}(\vec{q};t). \tag{5.6}$$

Eq. 5.5 is known as *Itô's formula* and is the SDE generalization of the chain rule for differentiation applicable to a change in variables and can also be viewed as the SDE governing the evolution of the function g [*Gardiner*, 1985; *Kloeden and Platen*, 1995].

Now consider the temporal evolution of the function g. The last term in Itô's formula is random due to the Wiener process and would therefore not contribute to the average value of g,

$$\left\langle \frac{d[g(\vec{q}(t))]}{dt} \right\rangle = \left\langle a_i(\vec{q};t)\frac{\partial g(\vec{q}(t))}{\partial q_i} + \frac{1}{2}C_{ij}(\vec{q};t)\frac{\partial^2 g(\vec{q}(t))}{\partial q_i \partial q_j} \right\rangle. \tag{5.7}$$

Since $\vec{q}(t)$ is a random variable, it has a conditional probability density $\rho(\vec{q};t|\vec{q}_0;t_0)$, to have a value $\vec{q}$ at time t given an initial value $\vec{q}_0$ at an earlier time t_0, such that

$$\langle g(\vec{q}(t))\rangle = \int g(\vec{q}(t))\rho(\vec{q};t|\vec{q}_0;t_0)d\vec{q} \tag{5.8}$$

and hence

$$\frac{\langle d[g(\vec{q}(t))]\rangle}{dt} = \frac{d}{dt}\int g(\vec{q}(t))\rho(\vec{q};t|\vec{q}_0;t_0)d\vec{q} = \int g(\vec{q}(t))\frac{\partial \rho(\vec{q};t|\vec{q}_0;t_0)}{\partial t}d\vec{q}, \tag{5.9}$$

since g is not explicitly time dependent. Combing these expressions, yields

$$\frac{\langle d[g(\vec{q}(t))]\rangle}{dt} = \left\langle \frac{d[g(\vec{q}(t))]}{dt} \right\rangle$$

$$\int g(\vec{q}(t))\frac{\partial \rho(\vec{q};t|\vec{q}_0;t_0)}{\partial t}d\vec{q} = \int \left[a_i(\vec{q};t)\frac{\partial g(\vec{q}(t))}{\partial q_i} + \frac{1}{2}C_{ij}(\vec{q};t)\frac{\partial^2 g(\vec{q}(t))}{\partial q_i \partial q_j}\right]\rho(\vec{q};t|\vec{q}_0;t_0)d\vec{q}$$

$$\int g(\vec{q}(t))\frac{\partial \rho(\vec{q};t|\vec{q}_0;t_0)}{\partial t}d\vec{q} = \int g(\vec{q}(t))\left\{-\frac{\partial}{\partial q_i}\left[a_i(\vec{q};t)\rho(\vec{q};t|\vec{q}_0;t_0)\right] + \frac{1}{2}\frac{\partial^2}{\partial q_i \partial q_j}\left[C_{ij}(\vec{q};t)\rho(\vec{q};t|\vec{q}_0;t_0)\right]\right\}d\vec{q},$$

where integration by parts was done in the last step and any surface terms of the form $a_i\rho g$ or $C_{ij}\rho g$ resulting from the volume integral during integration by parts was neglected due to the following argument: by deriving a differential form of the Chapman-Kolmogorov equation (which reduce to the FPE in the absence of probability gains or losses), it can be shown that the coefficients have the form $a_i(\vec{q};t) = \lim_{\Delta t\to 0}\int (q_i - q_{0i})\rho(\vec{q};t+\Delta t|\vec{q}_0;t_0)d\vec{q}$ and $b_{ij}(\vec{q};t) = \lim_{\Delta t\to 0}\int (q_i - q_{0i})(q_j - q_{0j})\rho(\vec{q};t+\Delta t|\vec{q}_0;t_0)d\vec{q}$, for small $|\vec{q} - \vec{q}_0|$ (notice that this allows the coefficients to be interpreted as the average value and variance, respectively, of the random variables [*Gardiner*, 1985; *Kloeden and Platen*, 1995]); if the process under consideration is confined to a region $\mathcal{R}$ with surface $\mathcal{S}$ in phase-space, then $\rho(\vec{q};t|\vec{q}_0;t_0) = 0$ unless both $\vec{q}$ and $\vec{q}_0 \in \mathcal{R}$, so that the conditional probability can very reasonably change discontinuously as $\vec{q}$ cross $\mathcal{S}$; it can therefore not be assumed that the derivatives of the coefficients exist on $\mathcal{S}$; the function $g(\vec{q}(t))$ should therefore be chosen such that, although arbitrary, it is non-vanishing only in an arbitrary region entirely contained in $\mathcal{R}$; the function $g(\vec{q}(t))$ is therefore zero when evaluated on the boundary surface [*Gardiner*, 1985].

Since g is an arbitrary function, it must then hold that

$$\frac{\partial \rho(\vec{q};t)}{\partial t} = -\frac{\partial}{\partial q_i}[a_i(\vec{q};t)\rho(\vec{q};t)] + \frac{1}{2}\frac{\partial^2}{\partial q_i \partial q_j}[C_{ij}(\vec{q};t)\rho(\vec{q};t)], \tag{5.10}$$

which is in the same form as the FPE (Eq. 4.10), which was derived from the Chapman-Kolmogorov equation [*Gardiner*, 1985; *Kloeden and Platen*, 1995; *Lemons*, 2002]. This is the so-called *forward Kolmogorov equation* describing the temporal evolution of the conditional probability from an initial time. Notice that a backward Kolmogorov equation also exists and that

the main difference between the two Kolmogorov equations is the formulation of the coefficients, with the result that they are not equal in general. The FPE can also contain sources or linear terms in ρ and these terms can also be incorporated into the SDE formulation (see e.g. *Kopp et al.* [2012]; *Strauss and Effenberger* [2017]). The power of SDEs therefore lies in the fact that a m-dimensional Fokker-Planck like partial differential equation can be transformed into a set of $n = m - 1$ first order SDEs for a suitable relation between the conditional probability and the quantity modelled by the FPE, with Eq. 5.6 giving the relation between the physical diffusion tensor C_{ij} used in the FPE and the stochastic diffusion matrix b_{ij} used in the SDEs. The system of SDEs in Eq. 5.4 can be integrated either forwards or backwards in time, with each approach having its relative merits and situations in which it is naturally applicable. In Appendix B.1 it will be seen that it is much simpler to solve SDEs numerically than a partial differential equation [*Gardiner*, 1985; *Kloeden and Platen*, 1995; *Kopp et al.*, 2012; *Strauss and Effenberger*, 2017].

5.1.2 Constructing the Distribution Function and Boundary Conditions

By choosing the distribution function as $f(\vec{x};\vec{p};t) \propto \rho(\vec{x};\vec{p};t|\vec{x}_0;\vec{p}_0;t_0)$, any transport equation described by a FPE can be solved by casting it into an equivalent set of SDEs. The question now is how to construct the distribution function from the SDE solutions.

The Relation between the Distribution Function and Solutions of the Stochastic Differential Equations

Webb and Gleeson [1977] showed, for steady state CR transport, that the distribution function can be constructed formally from a convolution of the boundary and initial conditions with a Green's function of the partial differential equation under consideration. Hence in general,

$$\begin{aligned} f(\vec{x};\vec{p};t) &= \iiint \left[f_b(\vec{p}';t')\delta(\vec{x}'/\vec{x}_b - 1) + f_i(\vec{x}';\vec{p}')\delta(t'/t_0 - 1) \right] G(\vec{x};\vec{p};t|\vec{x}';\vec{p}';t')d\vec{p}'d\vec{x}'dt' \\ &= \iint f_b(\vec{p}';t')G(\vec{x};\vec{p};t|\vec{x}_b;\vec{p}';t')d\vec{p}'dt' + \iint f_i(\vec{x}';\vec{p}')G(\vec{x};\vec{p};t|\vec{x}';\vec{p}';t_0)d\vec{p}'d\vec{x}', \end{aligned} \quad (5.11)$$

where $\vec{x}_b$ denotes the position of the boundary, f_b and f_i are the boundary and initial conditions, respectively, and G is a Green's function. The first set of integrals account for possible time-dependent boundary conditions specified on closed boundary surfaces, while the second set of integrals account for the possible initial spatial distribution of particles [*Zhang*, 1999a; *Pei et al.*, 2010]. Establishing a connection between the FPE and Schrödinger's equation of quantum mechanics, *Zhang* [1999a] interpreted Eq. 5.11 as a form of the Chapman-Kolmogorov equation. This is expected from the stochastic processes modelled by the FPE and implies that the Green's function is the transition probability or conditional probability density for the particles to be found at a position $\vec{x}$ with momenta $\vec{p}$ at a time t given some initial distribution of the particles at the initial time t_0 and subsequent interaction of these particles with the boundaries at $\vec{x}_b$. The SDE solutions can then be interpreted as path integrals of the FPE from which

a transition probability can be constructed and the distribution function is then basically a weighting of the initial and boundary conditions by this transition probability [*Zhang*, 1999a].

The easiest way to construct a probability density function is with a histogram by a binning procedure (see e.g. *Milstein et al.* [2004] or *Rudemo* [1982] for the use of kernel estimations). The full Green's function can therefore be approximated by a multi-dimensional histogram constructed from the SDE solutions,

$$G(x_i, y_j, z_k; p_{xl}, p_{ym}, p_{zn}; t_s) \approx \frac{N(i,j,k;l,m,n;s)}{N\Delta x_i \Delta y_j \Delta z_k \Delta p_{xl} \Delta p_{ym} \Delta p_{zn} \Delta t_s}, \tag{5.12}$$

where N is the total number of pseudo-particles (the total number of times the SDEs were solved; see the following paragraph) and $N(i,j,k;l,m,n;s)$ is the number of pseudo-particles falling into the $(i,j,k)^{\text{th}}$ spatial, $(l,m,n)^{\text{th}}$ momenta, and s^{th} temporal bin, with midpoint $(x_i, y_j, z_k; p_{xl}, p_{ym}, p_{zn}; t_s)$ and volume $\Delta x_i \Delta y_j \Delta z_k \Delta p_{xl} \Delta p_{ym} \Delta p_{zn} \Delta t_s$ (although the bin choice seems arbitrary, and will be treated as such in this work, see e.g. *Rudemo* [1982] on how to choose the bin size). Notice that this binning procedure necessarily requires a large number of pseudo-particles to be calculated in order to have suitable statistics for each bin. Eq. 5.11 in this discrete form then reads [*Zhang*, 1999b; *Strauss and Effenberger*, 2017]

$$\begin{aligned} f(\vec{x};\vec{p};t) \approx & \sum_s \sum_{(l,m,n)} f_b(p_{xl}, p_{ym}, p_{zn}; t_s) \frac{N(i,j,k;l,m,n;s)}{N} + \\ & \sum_{(i,j,k)} \sum_{(l,m,n)} f_i(x_i, y_j, z_k; p_{xl}, p_{ym}, p_{zn}) \frac{N(i,j,k;l,m,n;s)}{N}. \end{aligned} \tag{5.13}$$

Although each pseudo-particle is counted here, it should be noted that in the general case with linear and source or sink terms in the FPE, each pseudo-particle will have an amplitude (from the source or sink terms) and a weight (from the linear terms). This would change Eq. 5.13 to include an integral of the amplitudes and change the binning procedure to count the weights (see e.g. *Kopp et al.* [2012]; *Strauss and Effenberger* [2017]).

The Meaning of a Pseudo-particle

The temporal evolution of the random variables $\vec{Q}(t)$ is called the *trajectory of a pseudo-particle*. It is however important to realize that a pseudo-particle should not be thought of as a physical particle or even its guiding centre. This can be seen from the fact that the SDE is equivalent to the FPE and that the distribution function is constructed from the SDE solutions. A physical particle's trajectory is governed by the Newton-Lorentz equation, but the distribution function is a density element in phase-space of an ensemble and the FPE describe the temporal evolution of this distribution function. A pseudo-particle is therefore a mathematical realization of a particle distribution function and a more accurate term for a pseudo-particle would be *a phase-space density element*, but the term 'pseudo-particle' is widely used throughout modelling with SDEs. The FPE is the generalization of Liouville's theorem in the presence of collisions and states that the density of ensemble points is constant along the trajectory of a single member

of the ensemble. Since the SDEs are equivalent to the FPE, the distribution function remains constant along the trajectory of a pseudo-particle through phase-space and hence, a pseudo-particle is also a visualisation of Liouville's theorem. This interpretation of the pseudo-particle is of course only valid in the absence of sources or sinks [*Kopp et al.*, 2012; *Strauss and Effenberger*, 2017].

Boundary Conditions

Gardiner [1985] and *van Kampen* [1992] describe different boundary conditions, while *Strauss and Effenberger* [2017] show how the most important of these boundary conditions are handled in the SDE approach. The most important boundary condition which will be used here, is the *von Neumann boundary condition*, also known as a *reflecting boundary condition*. Mathematically this is expressed as

$$\left.\frac{df(\vec{x};\vec{p};t)}{dy}\right|_{y=y_b} = 0, \tag{5.14}$$

for some variable y on which the distribution function is dependent, where y_b is the value of y where the boundary is located. This condition is implemented in the SDE, analogous to hard sphere reflection off a planar surface, by

$$Y < y_b \quad \text{or} \quad Y > y_b \quad : \quad Y \longrightarrow 2y_b - Y, \tag{5.15}$$

where the less or greater than operation depends on the boundary being an *inner* or *outer* boundary, respectively (notice that this formulation differs from the formulation given by *Strauss and Effenberger* [2017], but that this expression is valid for any value of y_b irrespective of it being an inner or outer boundary). Another boundary condition which will be used, is the *absorbing boundary condition*, which is defined as a boundary where the distribution function is zero,

$$f(\vec{y}_b;\vec{p};t) = 0. \tag{5.16}$$

5.2 Brownian Motion

Brown [1828], a Scottish naturalist, investigated a phenomenon that was observed and described even earlier in 1785 by the Dutch biologist Jan IgenHousz. When viewed through a microscope, grains of pollen which are suspended in stationary water move around continuously and irregularly. It was initially thought that this might indicate some vitality manifestation of all life forms, but this hypothesis was abandoned after Brown had observed similar behaviour in dead material as well. *Einstein* [1905] later explained this motion using thermodynamics to prove that the random motions are due to a series of collisions between the pollen and water molecules: the molecules in any fluid move around randomly due to their thermal energy and would therefore collide with any particle suspended in the fluid; the suspended particle itself would, of course due to Newton's laws, be stationary or moving in a straight

line, if it were set in motion, until a collision occurs; if the particle, however, is small but still larger than the molecules, one would not be able to see the influence of a single collision, but the influence due to a large number of random collisions will be seen. *von Smoluchowski* [1906] derived the same explanation independently and was responsible for the systematic development and experimental verification of *Brownian motion* theory [*Gardiner*, 1985; *Lemons*, 2002].

Einstein used the Chapman-Kolmogorov equation to derive a FPE to describe Brownian motion as a diffusion process. The general *diffusion-advection equation* in one dimension is

$$\frac{\partial \rho_n(x;t)}{\partial t} = -V\frac{\partial \rho_n(x;t)}{\partial x} + D\frac{\partial^2 \rho_n(x;t)}{\partial x^2}, \tag{5.17}$$

where ρ_n is the number density of the Brownian particles and V and D is the advection speed and diffusion coefficient, respectively, assumed to be independent of position. The diffusion equation ($V = 0$) is well known in terms of the law of *Fick* [1855], which states that a density flux is caused by a gradient in the density. In the context of Brownian motion, Einstein showed that at thermal equilibrium, the diffusion coefficient is proportional to the kinetic energy of the fluid (a warmer fluid has more energy, which will cause more violent collisions) and inversely proportional to both the particle's cross sectional area (a particle with a large cross sectional area will have a larger drag force, but the cross sectional area can also be scaled to the mass of the particle and a heavy particle's inertia will oppose the collisional forces) and the fluid's viscosity (a higher viscosity will impede the motion of all particles in the fluid) [*Einstein*, 1905; *Gardiner*, 1985]. The diffusion-advection equation has an analytical solution, given by

$$\rho_n(x;t) = \frac{1}{\sqrt{4\pi D t}}\mathrm{e}^{-(x-Vt)^2/4Dt}, \tag{5.18}$$

if it is assumed that the initial density is a delta function centred on the origin at time $t = 0$, that is $\rho_n(x;t) = \delta(x)\delta(t)$, and that the density at infinity is zero, that is $\rho_n(x \to \pm\infty;t) = 0$ [*Chandrasekhar*, 1943; *Lemons*, 2002; *Strauss*, 2013].

Although Einstein and von Smoluchowski explained Brownian motion on a microscopic level, the diffusion equation describes a macroscopic quantity, namely the density. In terms of stochastic calculus, Einstein and von Smoluchowski essentially ignored Newton's second law and modelled the particle's position as a Markov process [*Lemons*, 2002]. *Langevin* [1908] (see *Lemons and Gythiel* [1997] for a translation) gave the first microscopic description of Brownian motion, which was not only more fundamental, but also easier to understand. Langevin realised that the same collisions which were responsible for the random motion of the particles, are also responsible for the drag experienced by the particles, and generalized Newton's second law of motion to

$$m\frac{d^2X}{dt^2} = -\gamma\frac{dX}{dt} + \tilde{F}(t) \quad \Longrightarrow \quad \frac{dX}{dt} = V(t) \quad \text{and} \quad m\frac{dV}{dt} = -\gamma V + \tilde{F}(t). \tag{5.19}$$

Here X and V is the particle's position and velocity, respectively, which is changing randomly, γ is the drag coefficient, and $\tilde{F}(t)$ is a random force. It was assumed that the only properties which are known about the random force, are that its magnitude is large enough to cause the

random change in the particle's position, due to the changing of the particle's velocity randomly at small velocities, and that it has no preferred direction. It was not explicitly assumed that the random force is uncorrelated at different times, but implied implicitly when the average of the force was set to zero [*Gardiner*, 1985; *Lemons and Gythiel*, 1997; *Lemons*, 2002].

Langevin wrote down the first SDE and the corresponding stochastic calculus was developed by Itô during the 1940's [*Gardiner*, 1985]. This concept and approach to Brownian motion is equivalent to the approach of Einstein and von Smoluchowski and was later expanded and developed by *Uhlenbeck and Ornstein* [1930]. By careful manipulation of the *Langevin equation* (see e.g. *Uhlenbeck and Ornstein* [1930] or *Lemons* [2002]), it is found that the motion is more complex than derived by Einstein or von Smoluchowski, but it reduces to simple diffusion if the observation time is much larger than the 'drag time': the particle's velocity follows approximately a Markov process; at very small time scales, the particle's velocity is constant, but is then damped out by the drag forces acting at slightly longer time scales; there is therefore a small correlation time over which the particle would move linearly; the observation times, however, are much larger than the correlation time, so that the velocity has increased and decreased many times; the observed displacement after many correlation times is then also a Markov process (validating the approach of Einstein and von Smoluchowski) since the position is then uncorrelated to its value during the previous observation [*van Kampen*, 1992].

To avoid the complexity of the full Langevin equation (Eq. 5.19), assume that the Brownian particles' position is indeed a Wiener process. By applying the forward Kolmogorov equation (Eq. 5.10) to the diffusion-advection equation (Eq. 5.17), the equivalent SDE has the form

$$dX(t) = V dt + \sqrt{2D} dW(t). \tag{5.20}$$

Following *Lemons* [2002], the average position and variance in position of the particles can be calculated. By taking the average of this SDE and remembering that the Wiener process is random with zero mean, $\langle dW(t) \rangle = 0$, the ordinary differential equation governing the evolution of the particles' average position $\mu_x = \langle X(t) \rangle$ is $d\mu_x/dt = V$, which upon integration gives

$$\mu_x = Vt, \tag{5.21}$$

assuming, as in Eq. 5.18, that all the particles are released at the origin as a delta injection at $t = 0$. To calculate the variance of the particles' position, $\sigma_x^2 = \left\langle X^2(t) \right\rangle - \langle X(t) \rangle^2$, an expression should be found for $\left\langle X^2(t) \right\rangle$. Per definition

$$\begin{aligned} d[X^2(t)] = X^2(t+dt) - X^2(t) &= \left[X(t) + V dt + \sqrt{2D} dW(t) \right]^2 - X^2(t) \\ &\approx 2D dW^2(t) + 2XV dt + 2X\sqrt{2D} dW(t) + 2V\sqrt{2D} dW(t) dt, \end{aligned}$$

to first order in dt. By taking the average of this and remembering that the Wiener process is random with variance dt, $\langle dW^2(t) \rangle = dt$, the ordinary differential equation governing the evolution of $\left\langle X^2(t) \right\rangle$ is $d\left\langle X^2 \right\rangle / dt = 2D + 2V \langle X \rangle$, which upon substituting the average position (Eq. 5.21) and integrating gives

$$\left\langle X^2 \right\rangle = 2Dt + V^2 t^2.$$

The variance of the particles' position is then

$$\sigma_x^2 = 2Dt. \tag{5.22}$$

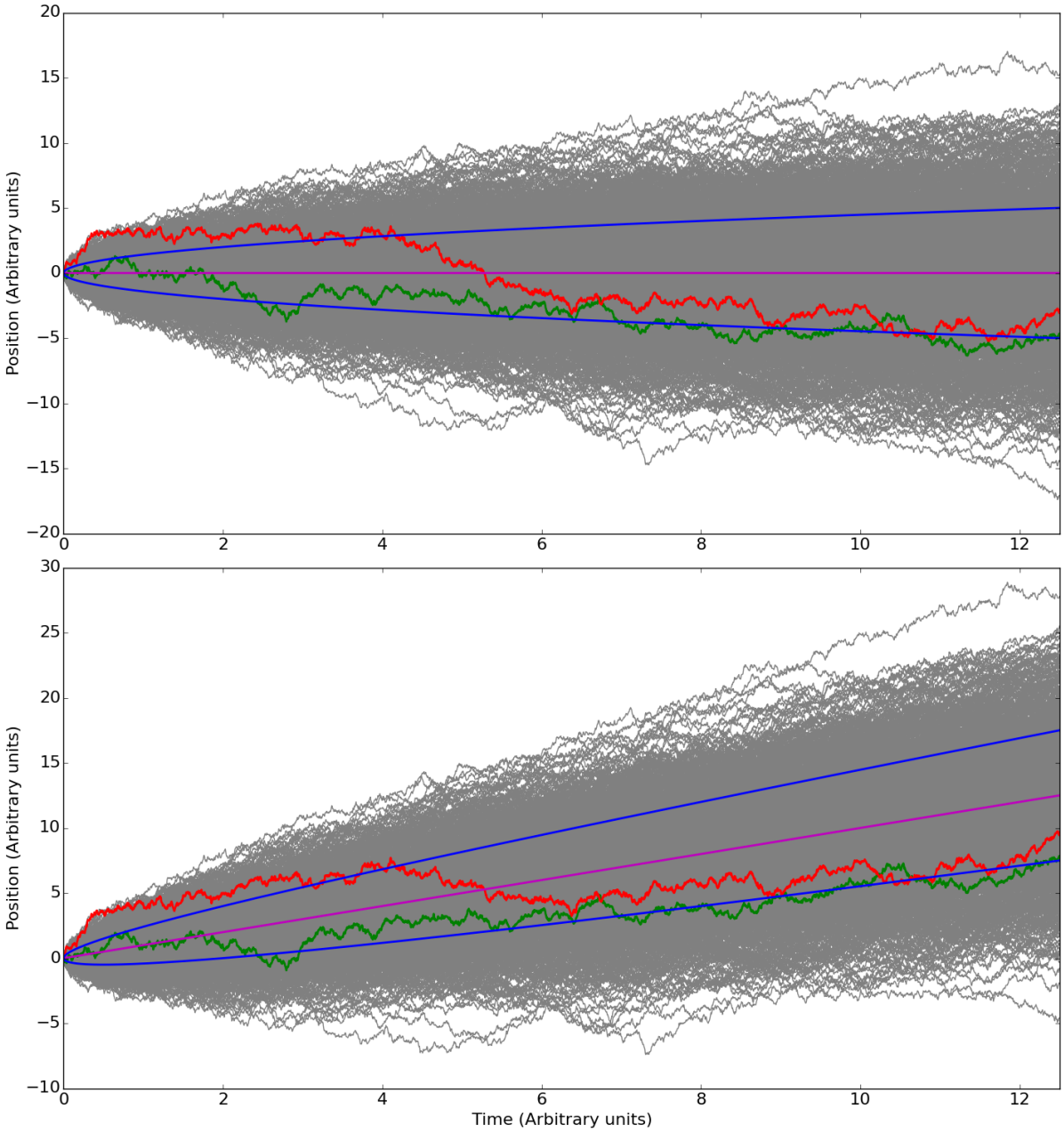

Figure 5.1: A 1000 pseudo-particle trajectories of the stochastic differential equation (Eq. 5.20) equivalent to the diffusion-advection equation (Eq. 5.17) constructed with the Euler-Maruyama method (Eq. B.4; with $\Delta t = 0.005$ and a delta injection at the origin) without (*top*; $V = 0$) and with (*bottom*; $V = 1$) advection for $D = 1$. The green and red lines illustrate the trajectories of two different pseudo-particles. The purple and blue lines show the average position (Eq. 5.21) and standard deviation (Eq. 5.22), respectively.

It was stated that each $X(t + dt)$ is Normally distributed and statistically independent of the previous $X(t)$, and the sum of the random positions $X(0), X(dt), X(2dt), \ldots X(t)$ are then also Normally distributed with mean and variance that of $X(t)$ according to the *central limit theorem*.

The analytical solution of the diffusion-advection equation (Eq. 5.18) then follows immediately from this fact with mean and variance given by Eq. 5.21 and Eq. 5.22, respectively [*Lemons*, 2002]. Fig. 5.1 show a 10^3 pseudo-particle trajectories of Eq. 5.20 constructed with the Euler-Maruyama method (Eq. B.4) using $D = 1$, $\Delta t = 0.005$, and a delta injection at the origin. The cases of no advection ($V = 0$) and with advection ($V = 1$) are shown in the top and bottom panels, respectively. The trajectory of a single pseudo-particle can be clearly seen in the green or red trajectories and it is said that the particle is performing a *random walk*. In this simple case where only the position is modelled by the SDE, the trajectories can be seen as possible paths of Brownian particles. The average position (Eq. 5.21) and its standard deviation (Eq. 5.22) is also indicated by the purple and blue lines, respectively. In the case of no advection, it should be expected that the particles' average position is zero from the fact that a particle has equal probability of moving in either of two directions, yielding no preferred direction of motion on average. It is clear that the particles are spreading out and away from the origin. It can be seen that the average position is dependent on the deterministic motion, namely the advection, while the standard deviation of the particles' position from the average is due to the stochastic motion, namely the diffusion. This might suggest a deterministic motion with small fluctuations superimposed on the deterministic motion, but *van Kampen* [1992] points out that this would only be valid if the fluctuations are small in comparison to the deterministic behaviour, if not, then the fluctuations could significantly influence the motion.

By applying Eq. 5.13 to this simple case, the normalised density can be constructed by binning the pseudo-particles' position. This is shown as the histograms in Fig. 5.2, together with the analytical solution (Eq. 5.18). The fluctuations seen in the histogram are due to the stochastic nature of the solutions and the binning procedure. The constructed histogram can be interpreted as a subset of the ensemble of all possible pseudo-particle trajectories which approximate then the true probability distribution of the system under consideration (the Gaussian function for the density in this case). The purely diffusive situation ($V = 0$) is shown in the top panel and can be physically thought of as a drop of particles released at the origin. Starting from a delta function, the density becomes Gaussian and becomes increasingly broader with time, which is a well-known characteristic of normal or Brownian diffusion. Notice that initially the particles spread out quickly, due to the large density gradient, but that the diffusion slows down as time progress since the density becomes more uniform. When advection is added, as shown in the bottom panel of Fig. 5.2 for $V = 1$, the density remains Gaussian due to the diffusion, but the density profile is advected as well. Physically this situation can be thought of as particles being released at the origin into a stream flowing in the positive x-direction. In the absence of advection, the peak density remains centred on the injection point, but if advection is present, the density remains Gaussian while the peak density is advected with the advection speed [*Lemons*, 2002]. From all the discussions given thus far, it is clear that the exact state of a stochastic process is unknown, but that the process has a certain probability distribution which is well defined and from which certain characteristic quantities can be obtained.

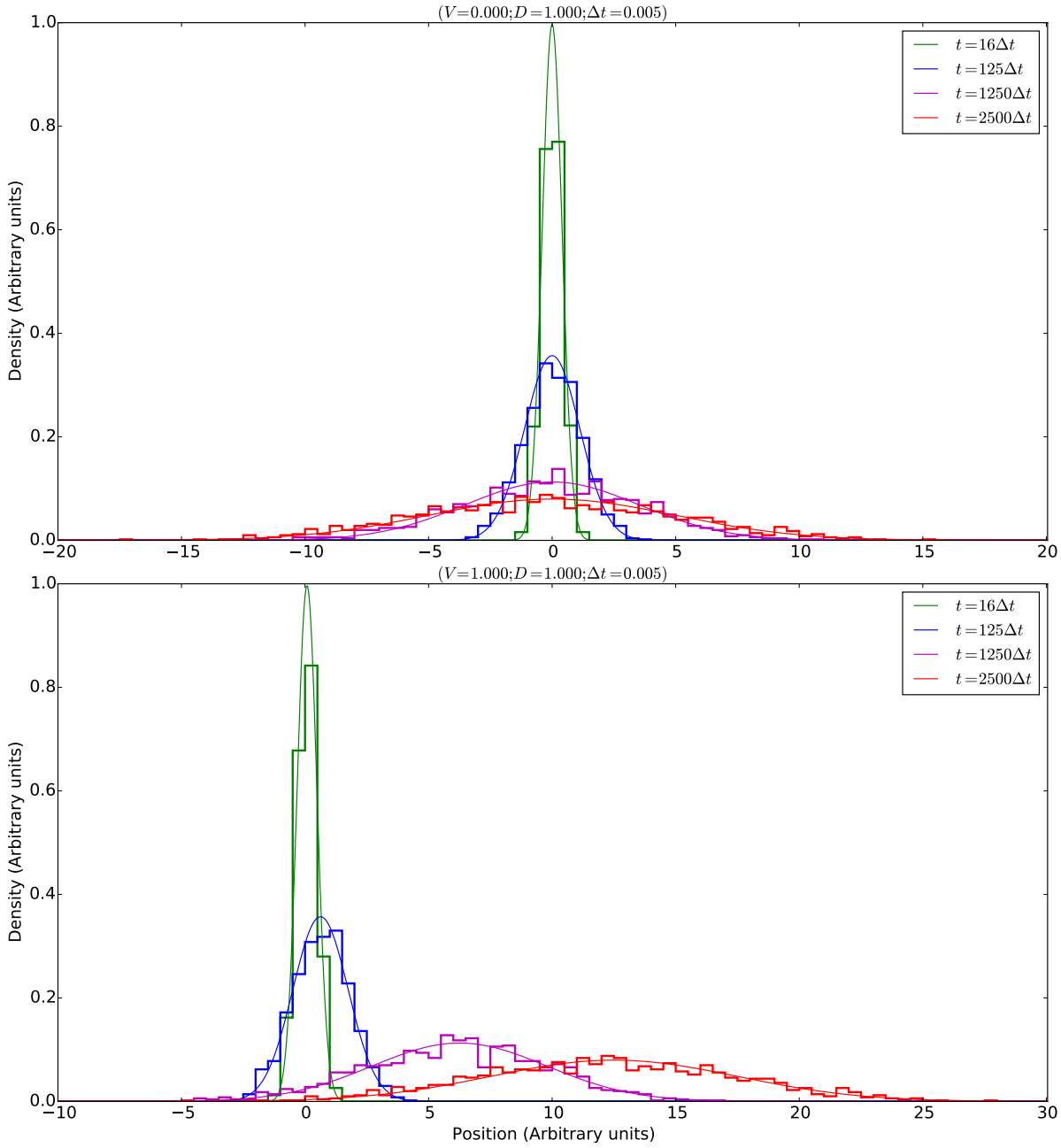

Figure 5.2: Normalised density of the pseudo-particles in Fig. 5.1 as a function of position and time without (*top*) and with (*bottom*) advection. The solid lines are the analytical solution (Eq. 5.18) and the histograms are the binned pseudo-particles.

5.3 The Stochastic Transport Model for Solar Energetic Particles

In this section the FTPE for SEPs will be cast into a set of SDEs and the stochastic transport model will be discussed in some detail. The rest of the model is discussed in Appendix B.

5.3.1 The Stochastic Differential Equations for Focused Transport

By using $\partial^2(D_{\mu\mu}f)/\partial\mu^2 = \partial[D_{\mu\mu}(\partial f/\partial\mu)+f(\partial D_{\mu\mu}/\partial\mu)]/\partial\mu$, the FTPE of *Ruffolo* [1995] (Eq. 4.34) can be written in the fully conservative form as

$$\frac{\partial f}{\partial t} = -\frac{\partial}{\partial s}\left[\frac{ds}{dt}f\right] - \frac{\partial}{\partial p'}\left[\frac{dp'}{dt}f\right] - \frac{\partial}{\partial \mu'}\left[\left(\frac{d\mu'}{dt} + \frac{1}{2}\frac{\partial D_{\mu'\mu'}}{\partial \mu'}\right)f\right] + \frac{1}{2}\frac{\partial^2}{\partial \mu'^2}\left[D_{\mu'\mu'}f\right], \tag{5.23}$$

where

$$\frac{ds}{dt} = \mu' v' + \left[1 - \left(\frac{\mu' v'}{c}\right)^2\right] v_{\rm sw}\sec\psi \tag{5.24a}$$

$$\frac{dp'}{dt} = -p' v_{\rm sw}\left[\frac{1-\mu'^2}{2L(s)}\sec\psi + \mu'^2\cos\psi\frac{d}{dr}(\sec\psi)\right] \tag{5.24b}$$

$$\frac{d\mu'}{dt} = \frac{\left(1-\mu'^2\right)v'}{2L(s)}\left(1 + \mu'\frac{v_{\rm sw}}{v'}\sec\psi - \mu'\frac{v' v_{\rm sw}}{c^2}\sec\psi\right) - \mu'\left(1-\mu'^2\right)v_{\rm sw}\cos\psi\frac{d}{dr}[\sec\psi]. \tag{5.24c}$$

This is in the correct form of the time forward Kolmogorov equation (Eq. 5.10). Let S, P, and M be the random variables corresponding to s, p', and μ', respectively, then the equivalent three, first-order SDEs are

$$dS = a_s dt \tag{5.25a}$$

$$dP = a_p dt \tag{5.25b}$$

$$dM = a_\mu dt + b_{\mu\mu} dW_\mu(t), \tag{5.25c}$$

where

$$a_s = \frac{ds}{dt} \tag{5.26a}$$

$$a_p = \frac{dp'}{dt} \tag{5.26b}$$

$$a_\mu = \frac{d\mu'}{dt} + \frac{1}{2}\frac{\partial D_{\mu'\mu'}}{\partial \mu'} \tag{5.26c}$$

are the drift coefficients,

$$b_{\mu\mu} = \sqrt{D_{\mu'\mu'}} \tag{5.27}$$

is the single diffusion coefficient associated with pitch-angle scattering, and $W_\mu(t)$ is a one-dimensional Wiener process.

5.3.2 Numerical Solution of the Stochastic Transport Model

The Euler-Maruyama scheme (Eq. B.4) for solving the set of SDEs in Eq. 5.25 is

$$S(t_k + \Delta t_k) \approx S(t_k) + a_s \Delta t_k \tag{5.28a}$$

$$P(t_k + \Delta t_k) \approx P(t_k) + a_p \Delta t_k \tag{5.28b}$$

$$M(t_k + \Delta t_k) \approx M(t_k) + a_\mu \Delta t_k + b_{\mu\mu}\Delta W_\mu, \tag{5.28c}$$

where the drift and diffusion coefficients are evaluated with $S(t_k)$, $P(t_k)$, and $M(t_k)$, and the Wiener process is given by Eq. B.5 for $n = 1$ and $j = \mu$. For the Milstein scheme (Eq. B.6), the solutions for Eq. 5.25a and Eq. 5.25b are the same as in the Euler-Maruyama scheme, with only the solution of Eq. 5.25c changing to

$$M(t_k + \Delta t_k) \approx M(t_k) + a_\mu \Delta t_k + b_{\mu\mu}\Delta W_\mu + \frac{1}{2} b_{\mu\mu}\frac{\partial b_{\mu\mu}}{\partial \mu'}\left[(\Delta W_\mu)^2 - \Delta t_k\right], \tag{5.29}$$

where the derivative is also evaluated with $S(t_k)$, $P(t_k)$, and $M(t_k)$. It seems that the Milstein scheme might not yield a great improvement in results since it is only the pitch-angle term which is affected (notice e.g. that the solutions of the Parker TPE with the Euler-Maruyama and Milstein schemes by *Wawrzynczak et al.* [2015] are indeed nearly comparable).

The second order weak Taylor scheme (Eq. B.8) is given by

$$S(t_k + \Delta t_k) \approx S(t_k) + a_s \Delta t_k + \frac{1}{2} a_s \frac{\partial a_s}{\partial s}(\Delta t_k)^2 \tag{5.30a}$$

$$P(t_k + \Delta t_k) \approx P(t_k) + a_p \Delta t_k + \frac{1}{2} a_p \frac{\partial a_p}{\partial p'}(\Delta t_k)^2 \tag{5.30b}$$

$$\begin{aligned} M(t_k + \Delta t_k) \approx\ & M(t_k) + a_\mu \Delta t_k + b_{\mu\mu}\Delta W_\mu + \frac{1}{2} b_{\mu\mu}\frac{\partial b_{\mu\mu}}{\partial \mu'}\left[(\Delta W_\mu)^2 - \Delta t_k\right] + b_{\mu\mu}\frac{\partial a_\mu}{\partial \mu'}\Delta Z_\mu \\ & + \frac{1}{2}\left(a_\mu \frac{\partial a_\mu}{\partial \mu'} + \frac{1}{2} b_{\mu\mu}^2 \frac{\partial^2 a_\mu}{\partial \mu'^2}\right)(\Delta t_k)^2 + \left(a_\mu \frac{\partial b_{\mu\mu}}{\partial \mu'} + \frac{1}{2} b_{\mu\mu}^2 \frac{\partial^2 b_{\mu\mu}}{\partial \mu'^2}\right)(\Delta W_\mu \Delta t_k - \Delta Z_\mu) \\ & + \frac{1}{2} b_{\mu\mu}\left[b_{\mu\mu}\frac{\partial^2 b_{\mu\mu}}{\partial \mu'^2} + \left(\frac{\partial b_{\mu\mu}}{\partial \mu'}\right)^2\right]\left[\frac{1}{3}(\Delta W_\mu)^2 - \Delta t_k\right]\Delta W_\mu, \end{aligned} \tag{5.30c}$$

where ΔW_μ and ΔZ_μ are given by Eq. B.9 with $n = 1$ and $j = \mu$. In addition to a constant time step, a variable time step of the form

$$\Delta t_k = \min\left\{\frac{l_s}{|a_s|}; \frac{l_p}{|a_p|}; \frac{l_\mu}{|a_\mu|}; \frac{l_\mu^2}{b_{\mu\mu}^2}\right\}, \tag{5.31}$$

will also be tested. A characteristic spatial length scale is the focusing length and hence, l_s will be some fraction of $L(s)$ to sufficiently sample the focusing effect. As there are no characteristic 'length' scales for the momentum and pitch-angle, l_p and l_μ are arbitrary.

5.3.3 The Pitch-angle Diffusion Coefficient and Some Aspects of the Stochastic Transport Model

This stochastic transport model will be benchmarked against the model of *Ruffolo* [1995] and *Dröge et al.* [2010]. *Dröge et al.* [2010] use the pitch-angle diffusion coefficient (PADC) of *Beeck and Wibberenz* [1986]

$$D_{\mu'\mu'}^{\mathrm{BW}} = D_0\left(|\mu'|^{q-1} + H\right)\left(1 - \mu'^2\right), \tag{5.32}$$

where q is the spectral index of the magnetic turbulence's inertial range and $H \in [0.05, 0.5]$ is used to give finite pitch-angle diffusion at $\mu' = 0$. With $H = 0$, Eq. 5.32 reduce to the PADC from quasi-linear theory (QLT) [*Jokipii*, 1966; *Shalchi*, 2009], which has the known problem of a

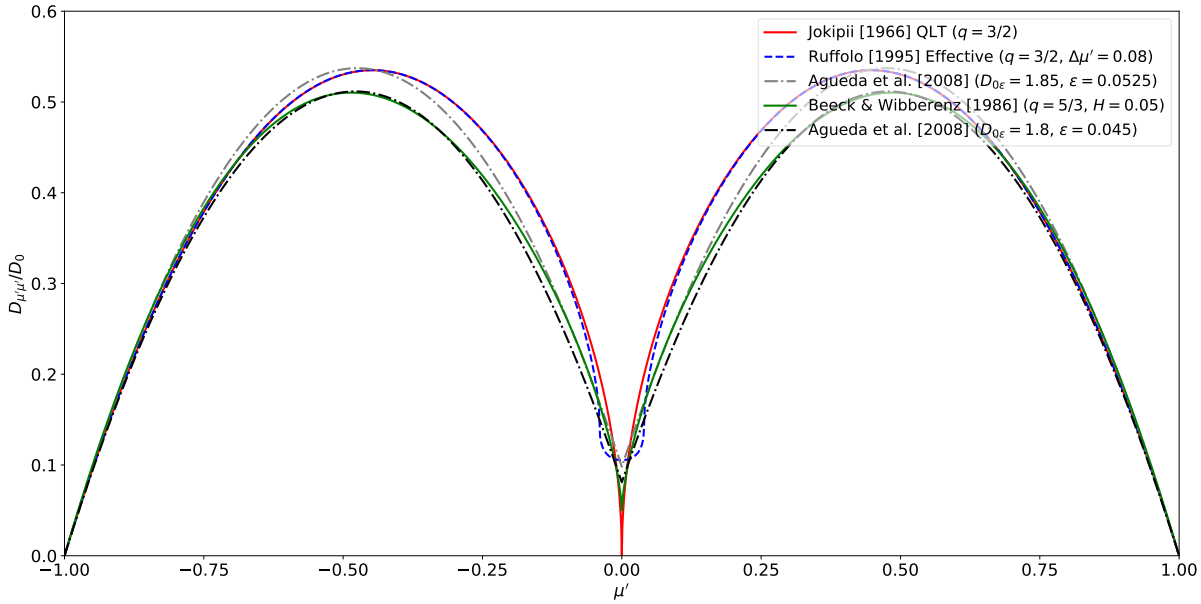

Figure 5.3: Pitch-angle diffusion coefficients of *Beeck and Wibberenz* [1986] (green; Eq. 5.32; a modification of the quasi-linear theory's result), *Agueda et al.* [2008] (black or grey dash-dotted; Eq. 5.35), and *Ruffolo* [1995] (blue dashed; Eq. 5.33). Notice the resonance gap at $\mu' = 0$ of the quasi-linear theory's pitch-angle diffusion coefficient (red; Eq. 5.32 with $H = 0$). The main difference between the forms of the pitch-angle diffusion coefficients are mainly due to the different spectra assumed for the magnetic turbulence.

resonance gap at $\mu' = 0$ (see Fig. 5.3) due to the neglect of dynamical effects. *Ruffolo* [1995] uses a Kraichnan spectrum with $q = 3/2$, while *Dröge et al.* [2010] uses a Kolmogorov spectrum with $q = 5/3$ and $H = 0.05$. To avoid the resonance gap at $\mu' = 0$, *Ruffolo* [1995] uses an effective PADC of the form

$$D^{\mathrm{eff}}_{\mu'\mu'} = D_0 \frac{1-\mu'^2}{2} \Delta\mu' \coth(I), \tag{5.33}$$

where $\Delta\mu'$ is the pitch-cosine grid spacing used in the finite difference model (used as $2/25$ by *Ruffolo* [1995]) and

$$I = \frac{\mathrm{sign}(\mu' + \Delta\mu'/2)|\mu' + \Delta\mu'/2|^{2-q} - \mathrm{sign}(\mu' - \Delta\mu'/2)|\mu' - \Delta\mu'/2|^{2-q}}{2(2-q)}. \tag{5.34}$$

These PADCs are shown in Fig. 5.3, where it can be seen that the shape of the effective PADC changes drastically around $\mu' = 0$ for large $\Delta\mu'$. As discussed in Appendix B, the infinite values of the derivatives of these PADCs around $\mu' = 0$ might be problematic. To verify the validity of the general approach applied in this study in handling these derivatives, the PADC of *Agueda et al.* [2008],

$$D^{\epsilon}_{\mu'\mu'} = D_{0\epsilon} \left(\frac{|\mu'|}{1+|\mu'|} + \epsilon \right) \left(1 - \mu'^2\right), \tag{5.35}$$

will also be used. This PADC consists of two downward opening parabolas, with finite derivatives, and ϵ parametrise the effects of both q and H. *Agueda and Vainio* [2013] investigated the values of ϵ corresponding to different values of q and H, and found that $\epsilon \approx 0.045$ for $q = 5/3$ and $H = 0.05$, while $\epsilon \approx 0.053$ for $q = 3/2$ and $H = 0$. The drawback of this PADC however,

is that it can only be used for a PADC with the form of Eq. 5.32 and not a more general form resulting from an advance diffusion theory.

D_0 in the PADC is a proportionality factor which can be calculated from the parallel mean free path (MFP) [*Hasselmann and Wibberenz*, 1970; *Shalchi*, 2009]

$$\lambda_{\parallel} = \frac{3}{8} v' \int_{-1}^{1} \frac{\left(1-\mu'^2\right)^2}{D_{\mu'\mu'}} d\mu'. \tag{5.36}$$

The *mean free path* can be generally defined as *the average distance moved by a particle before its velocity is uncorrelated with its initial velocity*, while the *parallel MFP* can be interpreted as *the average distance a particle would move in a turbulent plasma, being continuously subjected to small pitch-angle changes, before the pitch-angle is changed significantly and the particle's guiding centre reverses its direction of motion parallel to the background magnetic field*. Notice that the parallel MFP of *Ruffolo* [1995] is a factor 2 larger, and will be used as such, and that $D_{0\epsilon}$ is dependent on ϵ, since the parabolas must be scaled accordingly. This can be clearly seen by substituting Eq. 5.35 into Eq. 5.36, from which it follows that [*Agueda et al.*, 2008]

$$\begin{aligned} D_{0\epsilon} &= \frac{3v'}{4\lambda_{\parallel}} \int_0^1 \frac{(1+\mu')\left(1-\mu'^2\right)}{(1+\epsilon)\mu' + \epsilon} d\mu' \\ &= \frac{3v'}{4\lambda_{\parallel}(1+\epsilon)^4} \left[\frac{1}{6} + 2\epsilon + \frac{5}{2}\epsilon^2 + \frac{2}{3}\epsilon^3 + (1+2\epsilon) \ln\left(\frac{1+2\epsilon}{\epsilon}\right) \right]. \end{aligned} \tag{5.37}$$

By substituting Eq. 5.32 into Eq. 5.36 and comparing these two results, it is found that $D_{0\epsilon} \approx 1.8$ D_0 for $\epsilon = 0.045$ with $q = 5/3$ and $H = 0.05$, while $D_{0\epsilon} \approx 1.85\, D_0$ for $\epsilon = 0.053$ with $q = 3/2$ and $H = 0$. *Ruffolo* [1995] uses a constant parallel MFP of $\lambda_{\parallel} = 0.3$ AU, while *Dröge et al.* [2010] use a constant radial MFP of $\lambda_r = 0.3$ AU which is related to the parallel MFP by $\lambda_{\parallel} = \lambda_r / \cos^2 \psi$. Notice however that Eq. 5.36 is defined for a nearly isotropic distribution function and not an anisotropic distribution of SEPs. *Earl* [1981] showed that the MFP would change due to the focusing length, because focusing causes the distribution to have pitch-angles close to 0° ($\mu' \sim 1$) where particles would experience less scattering and hence, have a larger parallel MFP (also see the discussions of *Beeck and Wibberenz* [1986], *Qin et al.* [2005], *Litvinenko and Noble* [2013], and *Lasuik et al.* [2017], with the latter two highlighting some controversy surrounding this topic). This modification of the MFP will be discussed in Chapter 6 and due to these reasons, it might be better to specify an accurate PADC with a proportionality constant which can be explicitly calculated from solar wind properties, instead from a MFP.

The details of the stochastic transport model are discussed in Appendix B.2 and only a few important aspects will be mentioned here. The pseudo-particles will be injected as a delta function close to the Sun, with a reflecting inner boundary at the Sun, due to the mirroring effect of the heliospheric magnetic field, and an absorbing outer boundary far from the observation point. The distribution function will be constructed from a multi-dimensional histogram through a binning procedure within a spatial bin surrounding the observer. Two quantities measurable by spacecraft are the *omni-directional intensity*

$$F(s; p'; t) = \frac{1}{2} \int_{-1}^{1} f(s; p'; \mu'; t) d\mu', \tag{5.38}$$

which is essentially the distribution function without a pitch-angle dependence, and the *first order anisotropy*

$$A(s;p';t) = 3\frac{\int_{-1}^{1}\mu' f(s;p';\mu';t)d\mu'}{\int_{-1}^{1} f(s;p';\mu';t)d\mu'}, \tag{5.39}$$

which has a value of 3 (-3) if all particles are moving along (in the opposite direction of) the field and a value of zero if there are equal number of particles moving in opposite directions or if all the particles have no parallel speed. Notice that by dividing by $\int_{-1}^{1} f(s;p';\mu';t)d\mu'$, normalises the distribution function (phase-space density) to a probability and the anisotropy can be interpreted as essentially three times the average/expected pitch-cosine. Two quantities of theoretical interest is the *pitch-angle distribution* (PAD)

$$\mathrm{PAD}(s;p';\mu';t) = \frac{f(s;p';\mu';t)}{\int_{-1}^{1} f(s;p';\mu';t)d\mu'}, \tag{5.40}$$

and the *energy distribution* in terms of kinetic energy K'

$$\mathrm{ED}(s;K';\mu';t) = \frac{f(s;K';\mu';t)}{\int f(s;K';\mu';t)dK'}. \tag{5.41}$$

5.4 Summary

This chapter introduced stochastic differential equations (SDEs) as a way of solving a Fokker-Planck equation (FPE). It was seen that the forward Kolmogorov equation links the FPE to an SDE and that each m-dimensional FPE can be transformed into a set of $m-1$ first order SDEs. Appendix B discusses three methods to easily solve a set of SDEs numerically. It was seen that the distribution function can be constructed by a convolution of the boundary conditions with a probability density constructed from the SDE solution, through a multi-dimensional histogram for instance. A few important boundary conditions were discussed and it was seen that the SDE solution is a phase-space density element, which should not be viewed as a real particle or its guiding centre. The concept of an SDE was then illustrated using Brownian motion in one dimension and the focused transport equation for the propagation of solar energetic particles was written as a set of SDEs. Some aspects of this stochastic transport model were discussed, while details are given in Appendix B.

Chapter 6

The Focused Transport of Solar Energetic Particles

The stochastic transport model introduced in Chapter 5 and Appendix B was implemented in the C programming language using Message Passing Interface (MPI), to distribute the work load between parallel threads, and the GNU C compiler (`mpicc` calling `gcc`). The model was run on a computer with an Intel® Core™ i7-4790 vPro central processing unit (hyper-threaded quad-core), running at 3.6 GHz with 16 GB of memory, and 64-bit Slackware 15.0 operating system with a Linux-4.16.2 kernel. The Mersenne Twister [*Matsumoto and Nishimura*, 1998] pseudo-random number generator (PRNG) on each thread is initialised with random seeds from a file of seeds downloaded from `https://www.random.org/`.

The aim of this chapter is to verify the stochastic transport model by benchmarking against published numerical models and comparing with analytical approximations, as well as to investigate different characteristics of the focused transport of solar energetic particles. The model results will first be compared to the diffusion approximation and telegraph equation for a constant focusing length without advection or energy changes. The effect of both isotropic and anisotropic pitch-angle scattering will be compared in the absence and presence of focusing. The model results will then be compared to a few published numerical models, of both finite difference and stochastic differential equation types. This discussion will also investigate the effect of the different physical processes on the omni-directional intensity and how the three different numerical integration schemes compare to one another. A variable time step will also be implemented into the model. The energy losses and propagation times of solar energetic particles will then be investigated as an application of the model. These results will be compared with the predictions of the diffusion approximation used for cosmic rays, while an attempt will be made at deriving improved predictions from the terms in the focused transport equation. Lastly, a few observational features of solar energetic particle events will be discussed.

6.1 The Diffusion Approximation and Telegraph Equation

To test the basic stochastic transport model, the simpler focused transport equation (FTPE) of *Roelof* [1969], without advection or energy losses and with a constant focusing length

$$\frac{\partial f}{\partial t} + \frac{\partial}{\partial s}\left[\mu v f\right] + \frac{\partial}{\partial \mu}\left[\frac{(1-\mu^2)v}{2L} f\right] = \frac{\partial}{\partial \mu}\left[D_{\mu\mu}\frac{\partial f}{\partial \mu}\right], \tag{6.1}$$

will be solved first, where the prime on μ and v were neglected as there will be no transformations made between different reference frames in this section. This equation describes the evolution of the distribution function $f(s;\mu;t)$ for a constant particle speed v and the assumption of a constant focusing length is valid if $L \gg \lambda_{\parallel}$ [*Litvinenko and Schlickeiser*, 2013]. *Earl* [1981], *Beeck and Wibberenz* [1986], *Litvinenko and Noble* [2013], and *Litvinenko and Schlickeiser* [2013] give a few analytical solutions of this equation under certain assumptions to which the numerical methods can be compared (see also *Fisk and Axford* [1969]). The two equivalent stochastic differential equations (SDEs) is given by

$$dS = \mu v\, dt \tag{6.2a}$$

$$dM = \left[\frac{(1-\mu^2)v}{2L} + \frac{\partial D_{\mu\mu}}{\partial \mu}\right] dt + \sqrt{2D_{\mu\mu}}dW, \tag{6.2b}$$

where dW is a Wiener process, when applying the forward Kolmogorov equation (Eq. 5.10) [*Litvinenko and Noble*, 2013; *Effenberger and Litvinenko*, 2014]. In order to replicate the results of *Effenberger and Litvinenko* [2014], these equations were solved with the Euler-Maruyama scheme (Eq. B.4) and the distribution function, anisotropy, and pitch-angle distribution (PAD) constructed at $s_{\mathrm{obs}} = 5$ as discussed in Appendix B. A million pseudo-particles were injected at the origin with μ isotropically distributed, no spatial boundary conditions, $v = 1$, $D_0 = 0.5$, $L = 2/3$ if focusing was considered, and $\Delta t = 10^{-3}$ or $\Delta t = 10^{-4}$ for isotropic or anisotropic pitch-angle scattering, respectively.

To verify that the derivative of the pitch-angle diffusion coefficient (PADC) around $\mu = 0$ is handled correctly, the steady state PAD, $M(\mu)$, should be investigated. By neglecting the spatial dependence, Eq. 6.1 in the steady state ($\partial f/\partial t = 0$) reduce to

$$\frac{d}{d\mu}\left[\frac{(1-\mu^2)v}{2L} M(\mu)\right] = \frac{d}{d\mu}\left[D_{\mu\mu}(\mu)\frac{dM(\mu)}{d\mu}\right]. \tag{6.3}$$

Integrating this twice with respect to μ and applying the normalisation condition ($\int_{-1}^{1} M d\mu' = 1$), yields [*Earl*, 1981; *Beeck and Wibberenz*, 1986; *Agueda et al.*, 2008]

$$M(\mu) = \frac{\mathrm{e}^{G(\mu)}}{\int_{-1}^{1} \mathrm{e}^{G(\mu')} d\mu'}, \tag{6.4}$$

where

$$G(\mu) = \frac{v}{2L}\int_0^{\mu} \frac{1-\mu'^2}{D_{\mu\mu}(\mu')} d\mu'. \tag{6.5}$$

The fact that the stationary PAD is some exponential function of the pitch-cosine, illustrates that focusing causes the particles to be field aligned, with very few particles moving opposite to

the magnetic field. In the case of no focusing ($L \to \infty$), Eq. 6.3 reduce to $d[D_{\mu\mu}(dM/d\mu)]/d\mu = 0$, which yield $M(\mu) = 1/2$ upon integration and applying the reflective boundary ($dM/d\mu = 0$) and normalisation conditions. This states that the global distribution relax to isotropy, as expected for pitch-angle scattering in the absence of focusing.

If the PADC is independent of position or if one is only interested in the local properties over which $\lambda_\parallel/L$ is approximately constant, two analytical approximations are available for Eq. 6.1 with a delta injection of particles, $\delta(s)\delta(t)$, and a vanishing distribution function at infinity, $f(s \to \pm\infty; \mu; t) = 0$. In what follows, the given expressions differ from those given in some of the references due to the use of unitless variables in these references. By assuming that the distribution is nearly isotropic, the evolution of the omni-directional intensity is governed by a diffusion-advection equation (similar to Eq. 5.17 with V replaced by u) with the solution

$$F(s;t) = \frac{1}{2}\int_{-1}^{1} f(s;\mu';t)d\mu' = \frac{1}{\sqrt{4\pi\kappa_\parallel t}}\mathrm{e}^{-(s-ut)^2/4\kappa_\parallel t}, \tag{6.6}$$

where $u = \kappa_\parallel/L$ is the *coherent advection speed* caused by focusing and

$$\kappa_\parallel = \frac{1}{3}\lambda_0 v \qquad \text{or} \qquad \kappa_\parallel = Lv\frac{\int_{-1}^{1}\mu'\mathrm{e}^{G(\mu')}d\mu'}{\int_{-1}^{1}\mathrm{e}^{G(\mu')}d\mu'} \tag{6.7}$$

is the *spatial parallel diffusion coefficient* in the absence [*Litvinenko and Schlickeiser*, 2013] or presence [*Beeck and Wibberenz*, 1986] of focusing, respectively, with λ_0 the parallel mean free path (MFP) in the absence of focusing (Eq. 5.36). From the latter expression and the usual relation between the spatial diffusion coefficient and the MFP, $\lambda = 3\kappa/v$, it can be seen that the definition of the parallel MFP is modified in the presence of focusing. A known problem of the diffusion approximation is that it is too diffusive and violates causality, predicting that particles will arrive at a point before the particles could have physically propagated to that point [*Fisk and Axford*, 1969; *Litvinenko and Schlickeiser*, 2013].

As an improved approximation, the evolution of the omni-direction intensity can be modelled by the *telegraph equation*,

$$\frac{\partial F}{\partial t} + \tau\frac{\partial^2 F}{\partial t^2} = -u\frac{\partial F}{\partial s} + \kappa_\parallel\frac{\partial^2 F}{\partial s^2}, \tag{6.8}$$

where τ can be thought of as a signal propagation time (see *Malkov and Sagdeev* [2015] for a discussion on the validity of the telegraph equation). In the absence [*Litvinenko and Schlickeiser*, 2013] or presence [*Litvinenko and Noble*, 2013] of focusing

$$\tau = \int_{-1}^{1}\left[\int_0^\mu \frac{1-\mu'^2}{D_{\mu\mu}(\mu')}d\mu'\right]^2 d\mu \div \int_{-1}^{1}\frac{\left(1-\mu'^2\right)^2}{D_{\mu\mu}(\mu')}d\mu' \qquad \text{or} \qquad \tau = \frac{\kappa_\parallel - \kappa'_\parallel}{u^2}, \tag{6.9}$$

respectively, where

$$\kappa'_\parallel = \frac{v^2}{4}\int_{-1}^{1} Q(\mu')d\mu', \qquad \text{with} \qquad 0 = \frac{d}{d\mu}\left[\frac{2LD_{\mu\mu}}{(1-\mu^2)v}\left(\frac{d}{d\mu}\left[\frac{D_{\mu\mu}}{1-\mu^2}Q\right]+\mu\right)\right] - \frac{vQ}{2L} \tag{6.10}$$

and $Q(\mu = \pm 1) = 0$, which reduce to

$$\kappa'_\parallel \approx \frac{v}{3}\left\{\lambda_0 + \lambda_0\left[\frac{K(1)}{L}\right]^2 + \frac{6}{L^2}\int_{-1}^{1}\mu'\left[\frac{1}{3}K^3(\mu') - K(1)K^2(\mu')\right]d\mu'\right\} \tag{6.11}$$

in the weak focusing limit ($\lambda_0/L \ll 1$), with $K(\mu) = (v/4)\int_{-1}^{\mu}\left(1-\mu'^2\right)/D_{\mu\mu}(\mu')d\mu'$ [*Shalchi*, 2011]. The solution of the telegraph equation is

$$F(s;t) = \begin{cases} \mathrm{e}^{(s/L-t/\tau)/2}\left[I_0(z) + \frac{(1-\kappa_\parallel\tau/L^2)t}{2\tau z}I_1(z)\right]/4\sqrt{\kappa_\parallel\tau} & \text{if } |s| < t\sqrt{\kappa_\parallel/\tau} \\ \frac{1}{2}\mathrm{e}^{(s/L-t/\tau)/2} & \text{if } \quad s = \pm t\sqrt{\kappa_\parallel/\tau} \\ 0 & \text{otherwise} \end{cases}, \tag{6.12}$$

where I_0 and I_1 are modified Bessel functions of the first kind with argument

$$z = \frac{1}{2}\sqrt{\left(1-\frac{\kappa_\parallel\tau}{L^2}\right)\left(\frac{t^2}{\tau^2}-\frac{s^2}{\kappa_\parallel\tau}\right)}.$$

Notice that the signal propagation speed is $w = \sqrt{\kappa_\parallel/\tau}$ and that advection can be incorporated by adding the advection speed to u [*Litvinenko and Noble*, 2013; *Litvinenko and Schlickeiser*, 2013; *Effenberger and Litvinenko*, 2014].

The anisotropy is given by

$$A(s;t) = \frac{3\kappa_\parallel}{v}\left(\frac{1}{L}-\frac{1}{F}\frac{\partial F}{\partial s}\right) \quad \text{or} \quad A(s;t) = \frac{3\kappa_\parallel}{v}\left[\frac{1}{F}\left(\tau\frac{\partial^2 F}{\partial t\partial s}-\frac{\partial F}{\partial s}\right)+\frac{1}{L}\left(1-\frac{\tau}{F}\frac{\partial F}{\partial t}\right)\right] \tag{6.13}$$

for the diffusion approximation or telegraph equation, respectively. While this is most easily calculated numerically for the telegraph equation, the anisotropy in the diffusion approximation is $A(s;t) = 3(s/t+u)/2v$. Notice that the anisotropy of the diffusion approximation has the non-physical prediction of infinite anisotropies as $t \to 0$ due to the causality violation and that there is a persistent anisotropy at late times as $t \to \infty$ if focusing or advection is present [*Fisk and Axford*, 1969; *Litvinenko and Schlickeiser*, 2013].

6.1.1 Isotropic Scattering

The simplest case to test first, is the case of isotropic pitch-angle scattering, where $q = 1$ and $H = 0$ in the PADC of *Beeck and Wibberenz* [1986] (Eq. 5.32), such that

$$D_{\mu\mu}^{\mathrm{iso}}(\mu) = D_0\left(1-\mu^2\right) \qquad \text{and} \qquad \frac{\partial D_{\mu\mu}^{\mathrm{iso}}}{\partial\mu} = -2D_0\mu.$$

For this PADC, $\lambda_0 = v/2D_0$ (Eq. 5.36) and $G(\mu) = \mu\xi$ (Eq. 6.5) [*Beeck and Wibberenz*, 1986], where $\xi = \lambda_0/L$ is the *focusing parameter* (with a value of 0 for no focusing if $L \to \infty$). The stationary PAD (Eq. 6.4) is then given by [*Roelof*, 1969; *Litvinenko and Noble*, 2013; *Lasuik et al.*, 2017]

$$M(\mu) = \frac{\xi}{2}\mathrm{e}^{\mu\xi}\mathrm{cosech}\left(\xi\right). \tag{6.14}$$

From Eq. 6.7 it follows that $\kappa_\parallel = \lambda_0 v/3 = v^2/6D_0$ and $\kappa_\parallel = Lv\left[\coth(\xi) - 1/\xi\right] = \lambda_0 v\left[\coth(\xi)/\xi - 1/\xi^2\right]$ in the absence and presence of focusing, respectively, where the latter reduce to the former if an expansion of $\coth(\xi)$ is made for small ξ [*Beeck and Wibberenz*, 1986; *Litvinenko and Noble*, 2013; *Litvinenko and Schlickeiser*, 2013]. Furthermore, $\kappa_\parallel' = Lv\left[1-\tanh(\xi)/\xi\right]/\xi$ (Eq. 6.10)

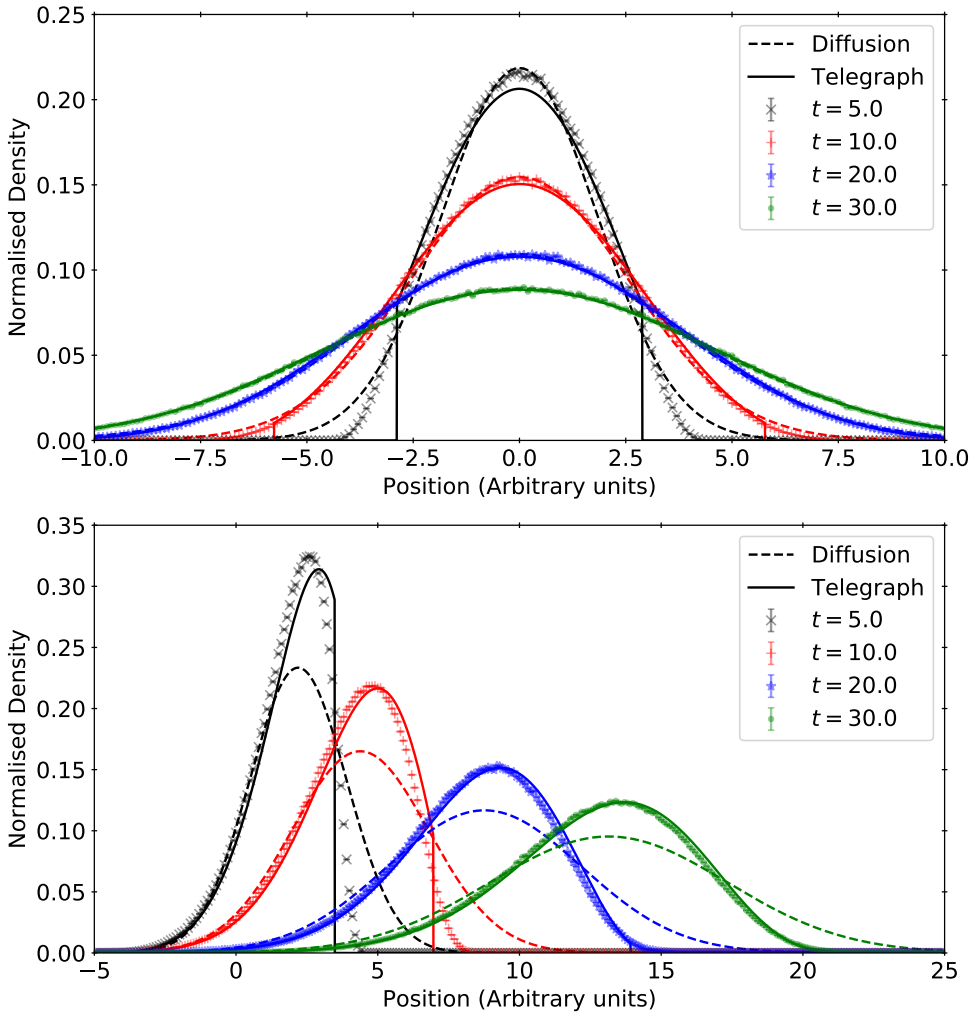

Figure 6.1: Temporal evolution of the normalised density as a function of position in the absence (*top*) and presence (*bottom*) of focusing for isotropic pitch-angle scattering. The simulation results (symbols) are compared to the diffusion approximation (dashed lines; Eq. 6.6) and telegraph equation (solid lines; Eq. 6.12).

[*Shalchi*, 2011] and hence, for the telegraph equation it holds from Eq. 6.9 that $\tau = 1/2D_0 = \lambda_0/v$ and $\tau = L\tanh(\xi)/v = \lambda_0\tanh(\xi)/v\xi$ in the absence and presence of focusing, respectively, where the latter again reduce to the former if an expansion of $\tanh(\xi)$ is made for small ξ [*Litvinenko and Noble*, 2013; *Litvinenko and Schlickeiser*, 2013].

The temporal evolution of the normalised density as a function of position is shown in Fig. 6.1, where the SDE solution is compared to the diffusion approximation and telegraph equation. In the case of no focusing (top panel), the results are comparable to the Brownian motion in Fig. 5.2, although the diffusion seems slower due to the pitch-angle dependent scattering. Both the diffusion approximation and telegraph equation is in good agreement with the SDE results at late times, while at early times the diffusion approximation is over diffusive and the telegraph equation predicts very sharp propagation fronts. If focusing is added (bottom panel), the density is no longer symmetric about the injection point due to focusing causing a

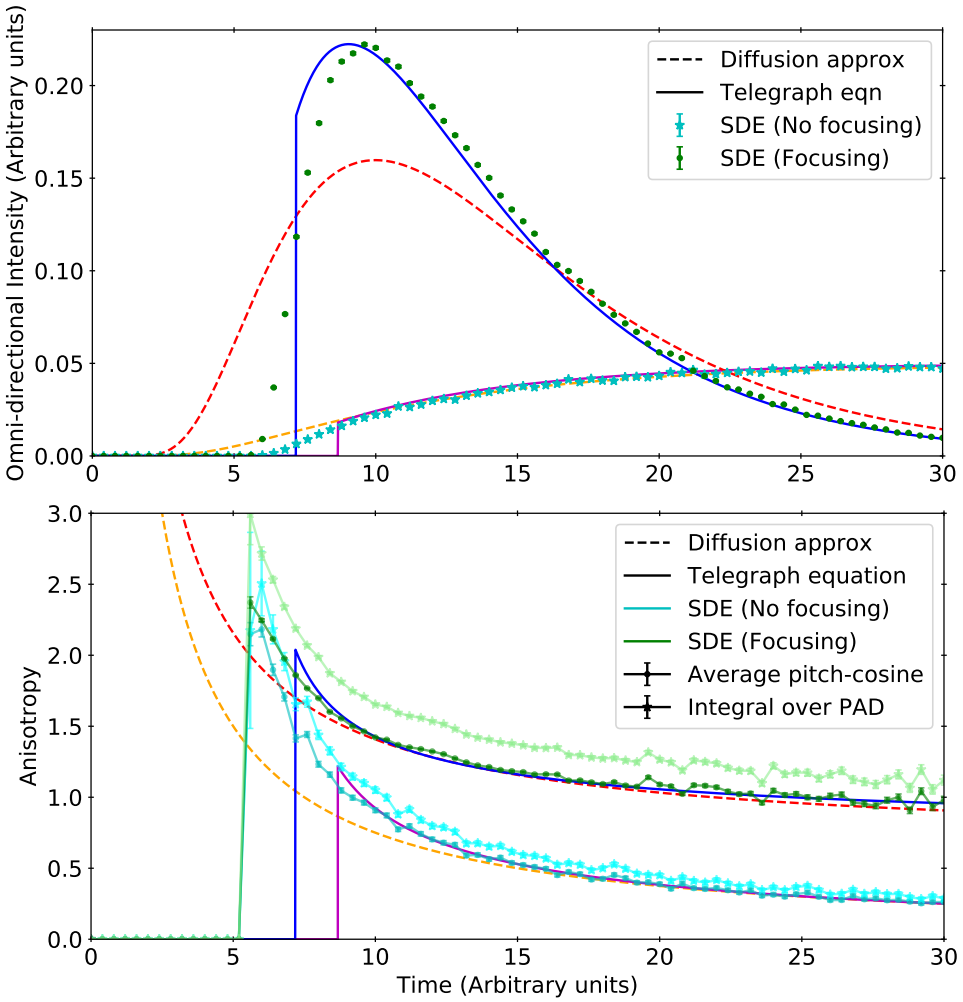

Figure 6.2: Temporal evolution of the omni-directional intensity (*top*) and anisotropy (*bottom*) at $s_{\rm obs} = 5$ in Fig. 6.1. The simulation results (symbols) in the absence (cyan) and presence (green) of focusing are compared to the diffusion approximation (dashed lines; Eq. 6.6) and telegraph equation (solid lines; Eq. 6.12).

coherent pulse to form, propagating with speed u and composed mainly of particles which have not yet undergone significant scattering. The pulse spreads out with time due to scattering, while the scattered particles, having smaller parallel speeds than the focused particles in the pulse, form a *wake* behind the pulse. The Gaussian shape of the diffusion approximation is clearly inadequate to describe the non-symmetric density, except in the wake, and the causality violation is clearly visible ahead of the pulse. The telegraph equation is better at describing the density, especially at late times, but predicts a step-like propagation front at early times since $w < v$ in these simulations [*Fisk and Axford*, 1969; *Litvinenko and Noble*, 2013; *Litvinenko and Schlickeiser*, 2013; *Effenberger and Litvinenko*, 2014].

The omni-directional intensity and anisotropy as a function of time at the observation point is shown in Fig. 6.2. In the absence of focusing, the omni-directional intensity (top panel) increases gradually as the particles diffuse to the observation point. With focusing added, the omni-directional intensity has a quick rise time up to a peak intensity, after which the flux de-

crease slowly, characteristic of impulsive solar energetic particle (SEP) events. This behaviour can be understood by looking at the lower panel of Fig. 6.1: as the pulse propagates past the observer, the event onset is seen followed by the peak intensity and the intensity decrease in the wake of the pulse, also called the *decay phase*. Although both the diffusion approximation and telegraph equation are comparable at late times, initially these two solutions are too diffusive or restrictive, respectively, and it seems as if the true solution is an interpolation between the two approximations [*Fisk and Axford*, 1969; *Earl*, 1981; *Effenberger and Litvinenko*, 2014].

The anisotropy (bottom panel in Fig. 6.2) was calculated with both methods outlined in Appendix B and although both methods follow the same trend, the anisotropy constructed by integrating the PAD (Eq. B.41; indicated by stars) is larger than the anisotropy calculated from the pseudo-particles' average pitch-cosine (Eq. B.40; indicated by dots). The latter method seems to be closer to the analytical approximations and the discrepancy might be due to a combination of the large number of pitch-cosine bins (21) and the simple summation used to approximate the integral. In both the absence and presence of focusing, the distribution is initially highly anisotropic after which it becomes more isotropic, with a more anisotropic distribution in the case of focusing. Physically this is because the first particles to arrive at the observation point are particles with small pitch-angles that have experienced little scattering, while the particles in the wake have experienced more scattering and are approaching diffusive behaviour. Notice that the larger uncertainty on the anisotropy at the event onset is due to bad statistics. As already stated, the causality violation of the diffusion approximation can be seen as infinite anisotropies before the event onset, while the diffusion approximation predicts a lower anisotropy until the distribution becomes more diffusive. The telegraph equation is generally better at predicting the anisotropy, but has a significantly delayed onset time [*Fisk and Axford*, 1969; *Effenberger and Litvinenko*, 2014].

The top panel of Fig. 6.3 shows the global PAD at $t = 30$ (constructed from all pseudo-particles irrespective of their position) and the time integrated PAD at the observation point compared to the analytical stationary solutions in both the absence and presence of focusing. The global PAD corresponds very well to the analytical solutions of the stationary PAD in both cases, while the time integrated PAD at the observation point has not yet fully reached the stationary state. Without focusing, the global distribution becomes isotropic, while focusing causes the particles to propagate predominately along the field. The effect of pitch-angle scattering, however, causes the distribution not to be beam-like with all particles having zero pitch-angles. It is interesting to note the temporal behaviour of the PAD (after taking a three point average in time and pitch-cosine to smooth out fluctuations) at the observation point in the presence of focusing, shown in the bottom panel of Fig. 6.3. The distribution is beam-like at the event onset with the PAD coinciding with the stationary solution just after the peak intensity, after which the distribution slowly approach isotropy. This seems to imply that the pulse has a quasi-stationary distribution set up by a balance between focusing and scattering, as suggested by Eq. 6.3 [*Beeck and Wibberenz*, 1986].

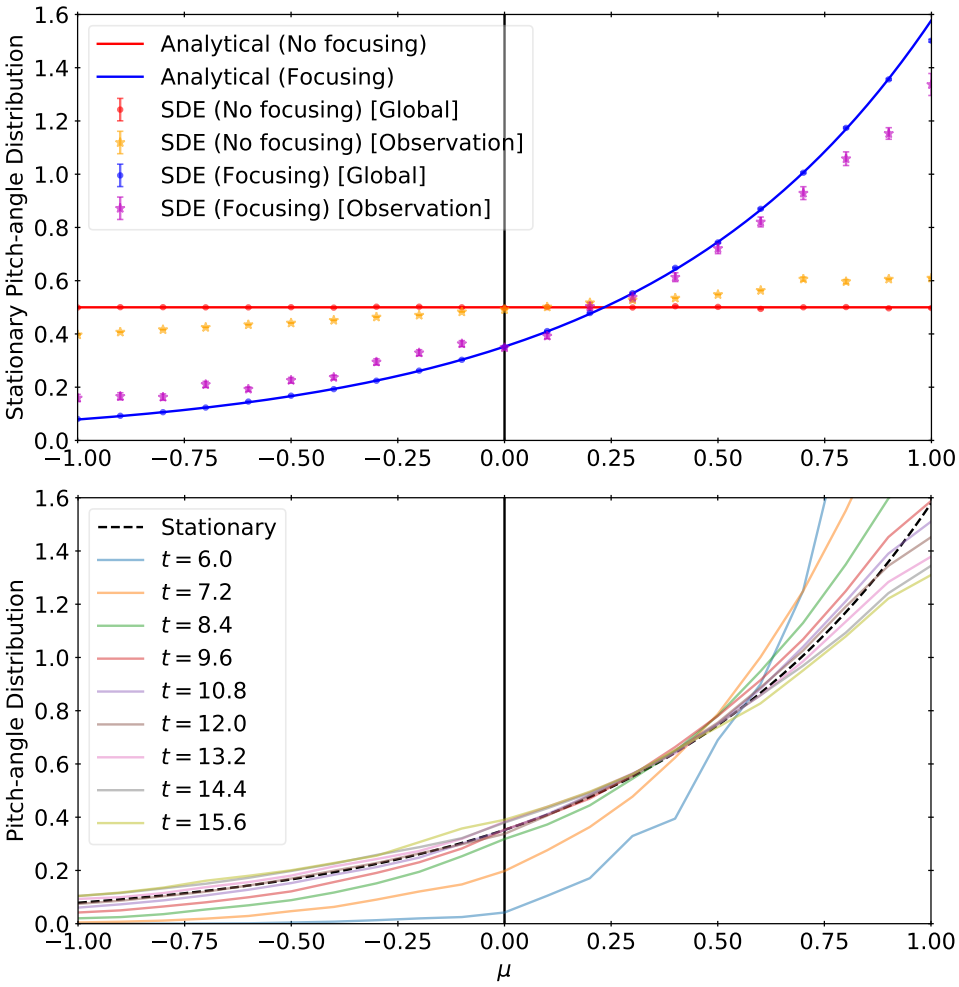

Figure 6.3: *Top:* Global pitch-angle distribution at $t = 30$ (red and blue dots) and time integrated pitch-angle distribution at $s_{\rm obs} = 5$ (orange and magenta stars) in Fig. 6.1 compared to the analytical stationary pitch-angle distribution (solid lines; Eq. 6.14 in the case of focusing), in the absence (red and orange) and presence (blue and magenta) of focusing. *Bottom:* Temporal evolution of the pitch-angle distribution in the pulse (coloured solid lines) at $s_{\rm obs} = 5$ compared to the analytical stationary pitch-angle distribution (black dashed; Eq. 6.14) in the presence of focusing. A three point average in time and pitch-cosine was taken to smooth out fluctuations.

6.1.2 Anisotropic Scattering

The next case, for which a few analytical expressions are available, especially for a Kraichnan spectrum of $q = 3/2$, and which can be used to test the way in which the PADC's derivative is handled around $\mu = 0$, is the case of anisotropic pitch-angle scattering in quasi-linear theory (QLT) [*Jokipii*, 1966], where $H = 0$ in the PADC of *Beeck and Wibberenz* [1986] (Eq. 5.32), so that

$$D_{\mu\mu}^{\rm QLT}(\mu) = D_0 \left(1-\mu^2\right) |\mu|^{q-1} \quad \text{and} \quad \frac{\partial D_{\mu\mu}^{\rm QLT}}{\partial \mu} = D_0 \text{sign}(\mu) \left[(q-1)\left(1-\mu^2\right)|\mu|^{q-2} - 2|\mu|^q\right].$$

For this PADC, $\lambda_0 = 3v/[2D_0(2-q)(4-q)]$ (Eq. 5.36) and $G(\mu) = \text{sign}(\mu)(4-q)\xi|\mu|^{2-q}/3$ (Eq. 6.5) [*Beeck and Wibberenz*, 1986]. If $q = 3/2$, the stationary PAD (Eq. 6.4) is given by

$$M^{q=3/2}(\mu) = \mathrm{e}^{\text{sign}(\mu)5\xi\sqrt{|\mu|}/6} \div \left\{\frac{24}{5\xi}\sinh\left(\frac{5}{6}\xi\right) + \frac{144}{25\xi^2}\left[1-\cosh\left(\frac{5}{6}\xi\right)\right]\right\}. \tag{6.15}$$

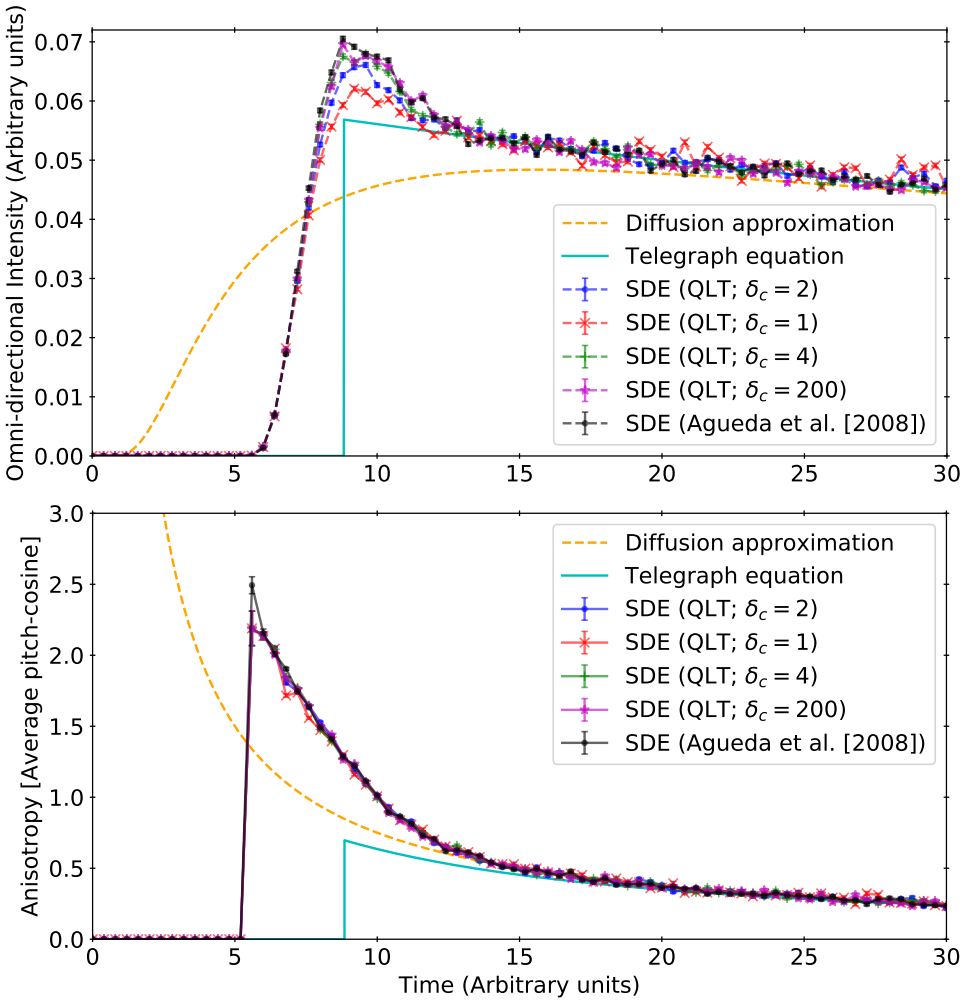

Figure 6.4: Temporal evolution of the omni-directional intensity (*top*) and anisotropy (*bottom*; Eq. B.40) at $s_{\rm obs} = 5$ in the absence of focusing for anisotropic pitch-angle scattering. See the text for details regarding the different cases.

From Eq. 6.7 it follows that $\kappa_{\parallel} = v^2/\left[2D_0(2-q)(4-q)\right]$ in the absence and $\kappa_{\parallel}^{q=3/2} = Lv\left\{\left[5\xi/6 + 36/\left(5\xi\right)\right]\cosh\left(5\xi/6\right) - \left[3 + 216/\left(25\xi^2\right)\right]\sinh\left(5\xi/6\right)\right\} \div \left\{\left(5\xi/6\right)\sinh\left(5\xi/6\right) + 1 - \cosh\left(5\xi/6\right)\right\}$ in the presence of focusing if $q = 3/2$ [*Earl*, 1981]. *Earl* [1981] give some expressions in the limit of weak and strong focusing which can be used to find approximate expressions for $M(\mu)$ and $\kappa_{\parallel}$ for an arbitrary q. For the telegraph equation it holds that $K(\mu) = (4-q)\lambda_0\left[\mathrm{sign}(\mu)|\mu|^{2-q} + 1\right]/6$, such that $\kappa_{\parallel}' \approx v\lambda_0\left[1 - 2(5-q)(4-q)^2\xi^2/27(8-3q)\right]/3$ (Eq. 6.11) and $\kappa_{\parallel}'(q = 3/2) \approx Lv\xi\left(1 - 25\xi^2/54\right)/3$ if $q = 3/2$ [*Shalchi*, 2011]. According to Eq. 6.9 it holds that $\tau = (4-q)/\left[2D_0(2-q)(5-2q)\right]$ in the absence of focusing [*Litvinenko and Noble*, 2013].

The omni-directional intensity and anisotropy as a function of time at the observation point in the absence and presence of focusing is shown in Fig. 6.4 and Fig. 6.5, respectively, for different cases which will be discussed. Without focusing, the diffusion approximation and telegraph equation seemed incapable of replicating the sharply defined coherent pulse. Strong focusing ($\xi = 3.6$) occurs for the set of parameters used here and hence, $\kappa_{\parallel}'$ calculated from Eq. 6.11 cannot be applied. The effects of anisotropic pitch-angle scattering are seen clearly

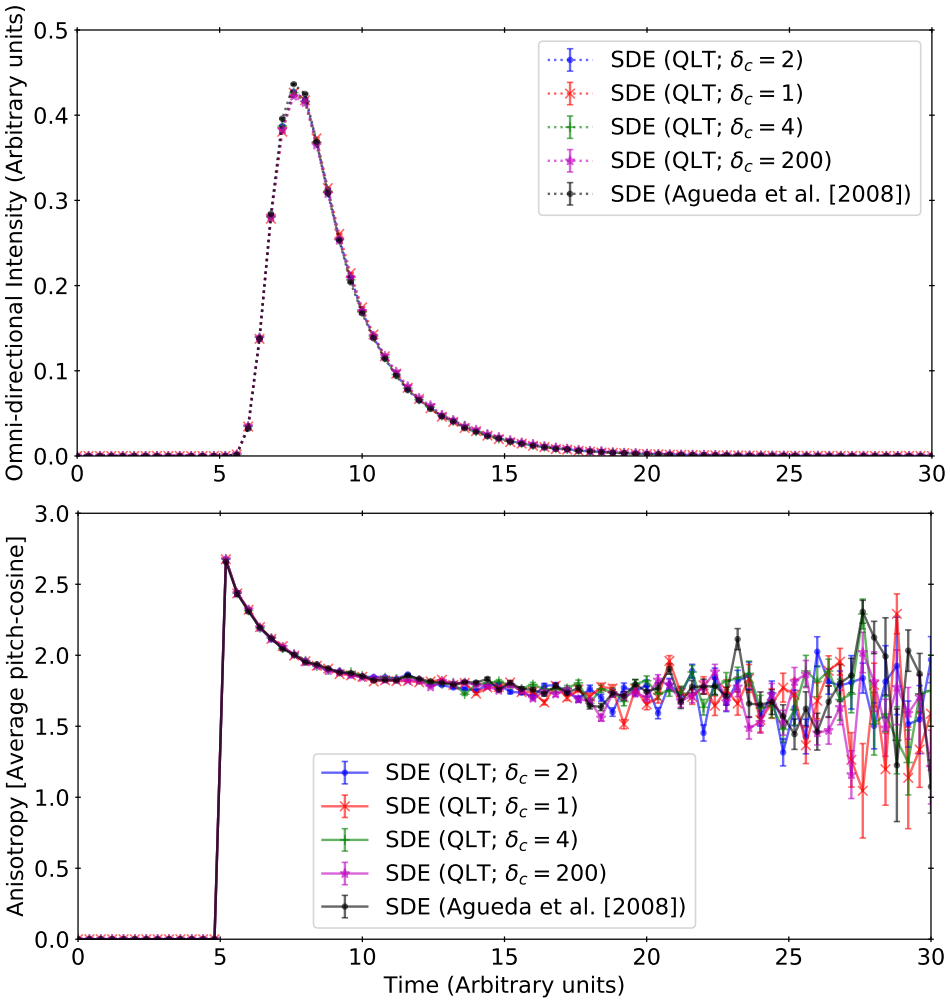

Figure 6.5: Similar to Fig. 6.4, but in the presence of focusing.

as a narrow pulse with an extended wake in the case of no focusing and a very narrow pulse when focusing is included. This behaviour is due to ineffective scattering across $\mu = 0$. In the case of no focusing, the anisotropy is almost comparable to the case of isotropic scattering, although it does not decrease as $1/t$ in the pulse's trailing edge, but rather almost linearly with time. The anisotropy in the case of focusing is much higher than for isotropic scattering, due to focusing dominating the reduced scattering. Notice that from $t \approx 20$, almost all particles have passed the observation point and that the anisotropy has very bad statistics.

The different cases indicated in Fig. 6.4 and Fig. 6.5 seek to investigate the effect of how the PADC's derivative is handled around $\mu = 0$. The derivative for the QLT PADC is cut off at different values of δ_c according to Eq. B.21: $\delta_c = 2$ as indicated in Fig. B.1 (blue), $\delta_c = 1$ for a broad region with a relatively small value of $\partial D_{\mu\mu}^{\mathrm{QLT}}/\partial\mu$ around $\mu = 0$ (red), $\delta_c = 4$ for a slightly narrower region (green), and $\delta_c = 200$ for a very narrow region with large values of $\partial D_{\mu\mu}^{\mathrm{QLT}}/\partial\mu$ around $\mu = 0$ (magenta). The results for the PADC of *Agueda et al.* [2008] is also shown in black. In general it seems that the omni-directional intensity and anisotropy are not very sensitive to the way in which the derivative is handled, especially in the wake. The most

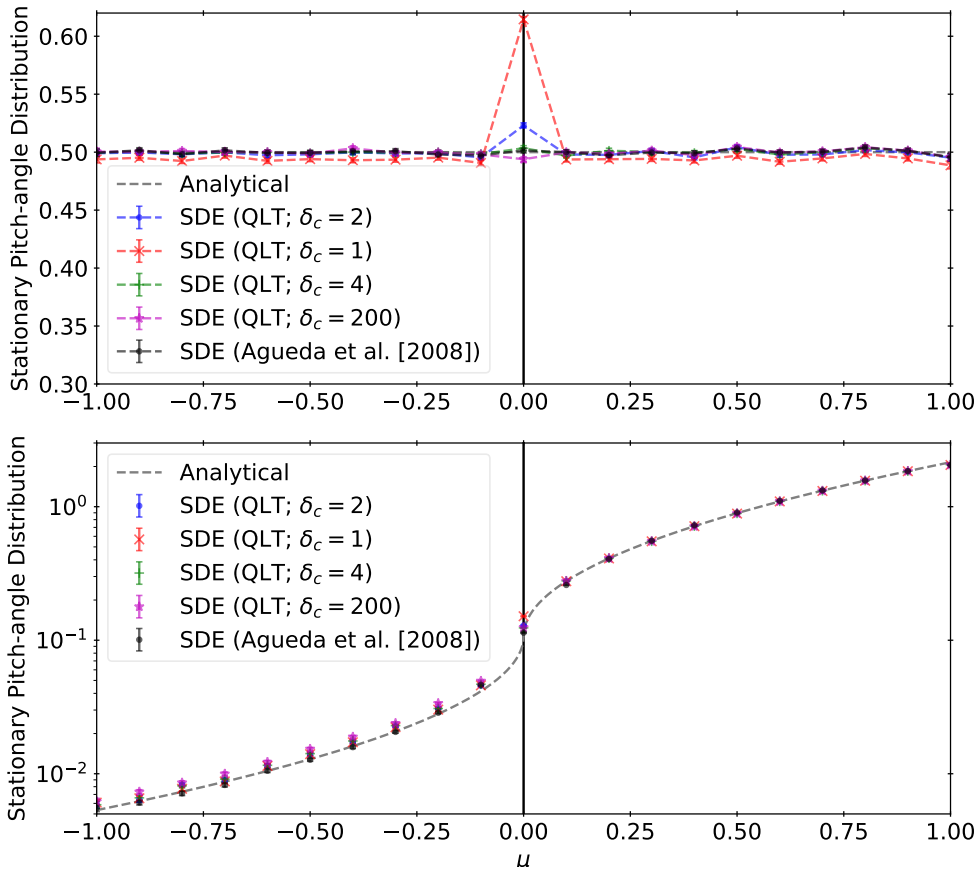

Figure 6.6: Global pitch-angle distribution at $t = 30$ in Fig. 6.4 and Fig. 6.5, compared to the analytical stationary pitch-angle distribution (solid lines; Eq. 6.15 in the case of focusing) in the absence (*top*) and presence (*bottom*) of focusing for anisotropic pitch-angle scattering.

prominent difference can be seen in the peak intensity in the case of no focusing, where the $\delta_c = 1$ case is $\sim 10\%$ lower than the $\delta_c = 200$ case. The higher peak intensity at a slightly earlier time for the PADC of *Agueda et al.* [2008] could possibly be due to effective scattering through $\mu = 0$, causing more particles that had $\mu < 0$ to have $\mu > 0$. If focusing is included, the peak intensity occurs at the same time, indicating that focusing is dominating, while the $\delta_c = 200$ case has a peak intensity which is only $\sim 1\%$ lower than that of the $\delta_c = 2$ case.

To further investigate how the PADC's derivative influences the distribution, the global PAD at $t = 30$ and the time integrated PAD at the observation point is shown in Fig. 6.6 and Fig. 6.7, respectively. Notice that a sufficiently small time step must have been used to resolve the diffusive behaviour. The anisotropic pitch-angle scattering can be seen in the PAD for focusing as a sharp decrease in crossing $\mu = 0$ from positive to negative values. In the absence of focusing, the global PAD has a peak at $\mu = 0$ for the $\delta_c = 1$ and $\delta_c = 2$ cases. This peak is also seen for the $\delta_c = 1$ case if focusing is present and indicates that the pseudo-particles are stuck around $\mu = 0$ because they are not efficiently 'advected' away from $\mu = 0$ by the derivative term. The time integrated PAD at the observation point has not yet reached a stationary state. The peak is still seen for the $\delta_c = 1$ case with no focusing, while the behaviour of the other

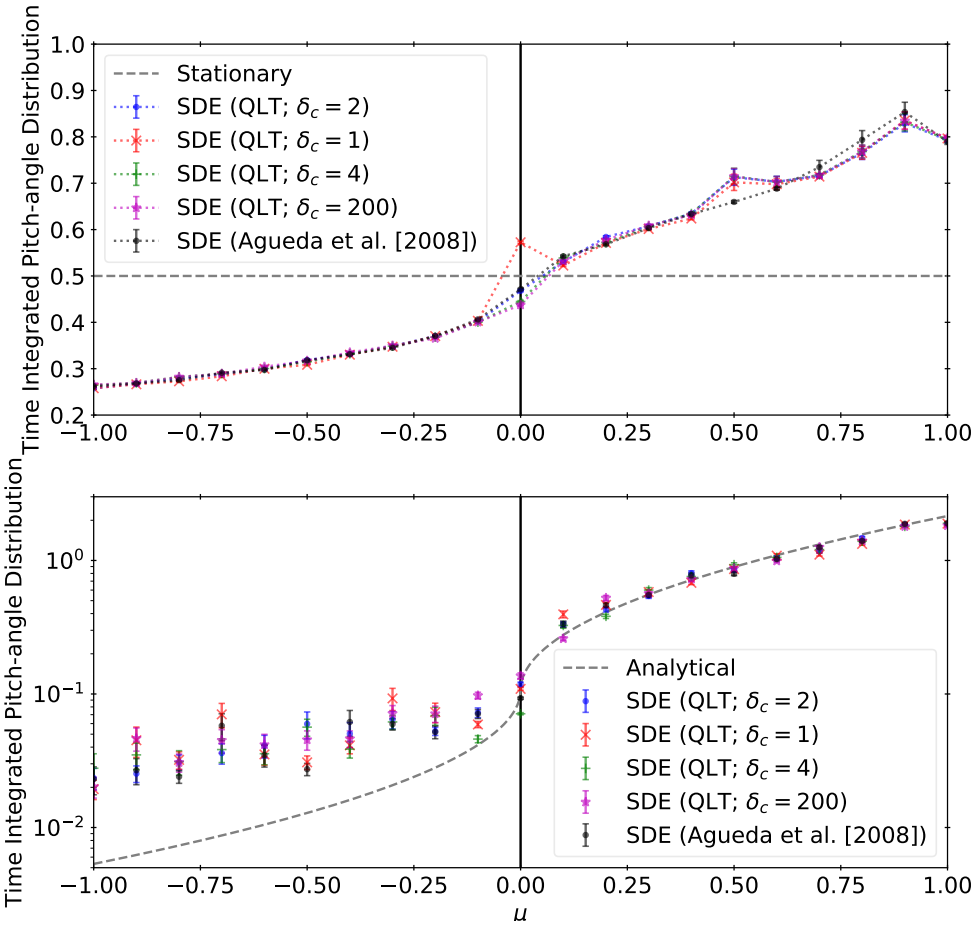

Figure 6.7: Similar to Fig. 6.6, but for the time integrated pitch-angle distribution at $s_{\mathrm{obs}} = 5$.

cases around $\mu = 0$ seem stochastic. Notice that a dip will be found at $\mu = 0$ if the derivative is too large, because particles are then efficiently advected away from $\mu = 0$, but this normally requires $\delta_c > 600$ [*private communication with N. Wijsen*].

6.2 The Effect of Advection and Energy Losses

As a first verification of the stochastic transport model's ability to model SEP events, the results of *Dröge et al.* [2010] will be replicated. Since these authors neglect solar wind (SW) advection and energy losses, the set of SDEs which must be solved is the same as Eq. 6.2 if their perpendicular transport is neglected. The simulation setup is summarised in Table 6.1 and the results of the three numerical integration schemes are shown in Fig. 6.8. The results are also compared to the finite difference (FD) models of *Strauss and Fichtner* [2015], with two spatial dimensions, and *Heita* [2018], with one spatial dimension. Notice that the stochastic fluctuations in the results of *Dröge et al.* [2010] are largely due to bad statistics at the observation point, since the pseudo-particles spread out in three dimensions, and that the anisotropy predictions of the FD models before the event onset and the oscillations, are numerical artefacts. The temporal profile of the intensity and anisotropy is expected from the results of the previous section and

Parameter		Dröge et al. [2010]	Ruffolo [1995]
Solar surface	$r_\odot$	0.005 AU	
Solar rotation rate	$\omega_\odot$	$2\pi/25$ days $= 2.66 \times 10^{-6}$ rad $\cdot$ s^{-1}	
Solar wind speed	v_{sw}	400 km $\cdot$ s^{-1}	
Particles		protons	
Constant MFP		$\lambda_r = 0.3$ AU	$\lambda_\parallel = 0.3$ AU
Inertial range index	q	$5/3$	$3/2$
Dynamical effects		$H = 0.05$	$\Delta\mu' = 2/25$
Initial kinetic energy	K_0'	4 MeV	2 MeV OR power law with $\gamma = -5$ between $2 - 4$ MeV
Number of pseudo-particles	N	10^6	10^7
Derivative cut off	δ_c	2	
Source position	r_s, s_0	0.05 AU	
Inner reflective boundary	s_i	0 AU	
Outer absorbing boundary	s_o	5 AU	
Observation point	r_{obs}	1 AU	
Time step	Δt	1×10^{-4} h	
Initial time	t_0	0 h	
Maximum simulation time	T	12 h	

Table 6.1: Parameters used in the simulations when comparing to different models.

it should be kept in mind for the remainder of the chapter that in this one-dimensional model, the observer can be thought of as co-rotating with the Sun and is therefore connected to the same magnetic field line for the entire duration of the event. If perpendicular transport was included, the intensity would decrease slightly faster, while the intensity would decrease much faster if the observer is stationary [*Zhang et al.*, 2009; *Dröge et al.*, 2010]. The results are in good agreement with both the SDE model of *Dröge et al.* [2010] and the two FD models. An earlier onset time is predicted by the two FD models as well and the three numerical integration schemes seem to be comparable. The results of the three integration schemes differ from that of *Strauss and Fichtner* [2015] and *Heita* [2018] by less than 5% and 10%, respectively, except just after the event onset where the SDE results are $\sim 40\%$ higher than that of *Heita* [2018].

The FTPE of *Ruffolo* [1995] describes different physical effects on the propagation of SEPs which have been neglected up to now. The results presented in this comparison were constructed by averaging the results of 10 simulations with 10^6 pseudo-particles per simulation and each simulation using different seed values for the PRNG. This yielded results equivalent to a single simulation with 10^7 pseudo-particles while stochastic fluctuations are averaged out, which allow for better comparison between the different integration schemes. Before discussing the comparison of the SDE scheme to the FD model of *Ruffolo* [1995], the general effect of the different physical process will be discussed. The omni-directional intensity computed with the Euler-Maruyama scheme (Eq. 5.28) is shown in the top panel of Fig. 6.9 for different physical situations and the simulation setup is also summarised in Table 6.1. Notice that the intensity is given here not in terms of time, but in terms of the distance travelled by the particles ($v't$) as this is a quantity which is comparable between situations with and without energy changes. Before the details of the different physical processes are discussed, it should be noted that SEP

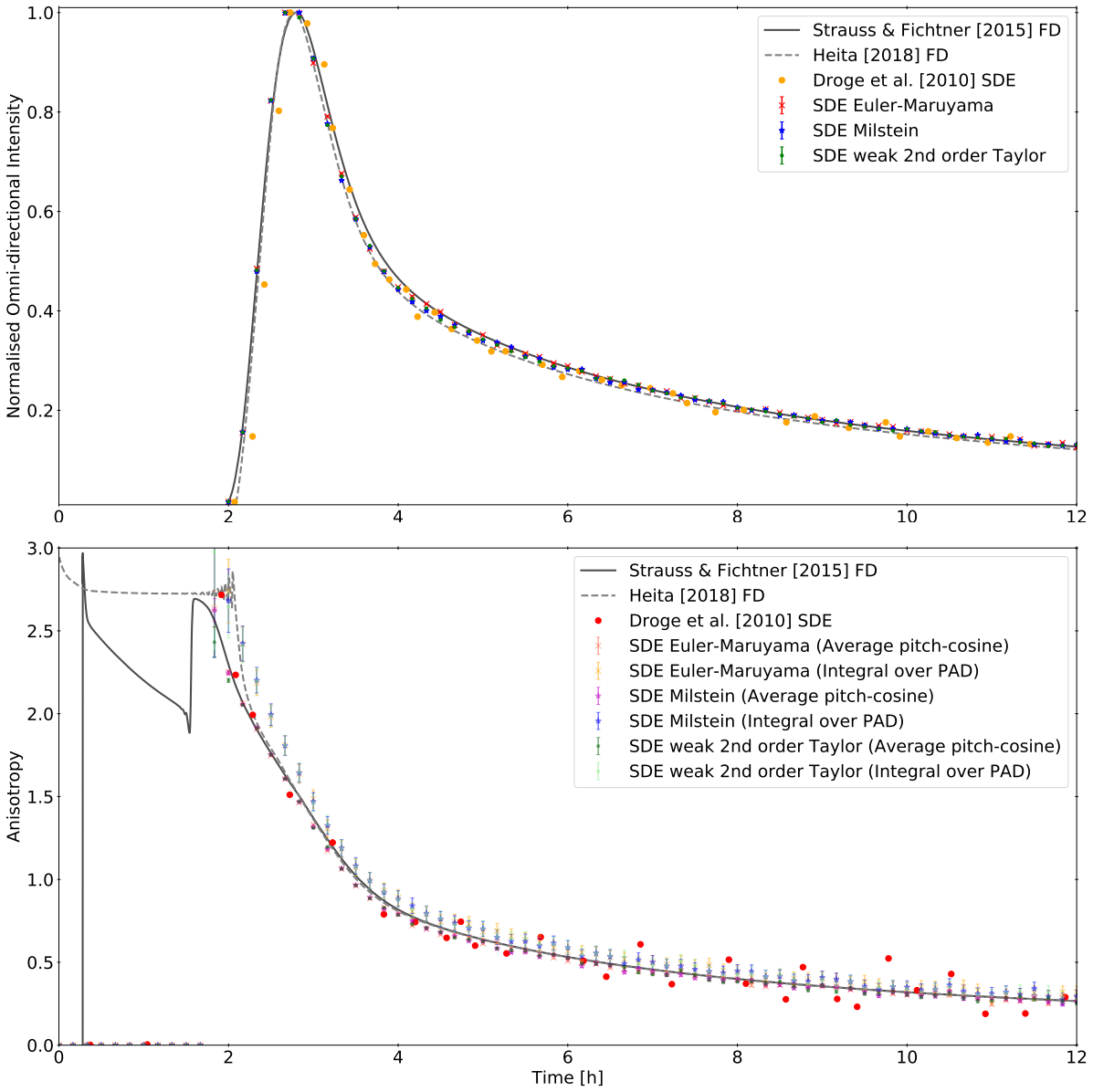

Figure 6.8: Temporal evolution of the omni-directional intensity (*top*), normalised to the peak intensity, and anisotropy (*bottom*) at Earth for 4 MeV protons in the absence of solar wind advection and energy losses. The simulation results (symbols) of the three numerical integration schemes (Eqs. 5.28-5.30), are compared to the stochastic differential equation model of *Dröge et al.* [2010] (orange or red dots) and the finite difference models of *Strauss and Fichtner* [2015] (solid black) and *Heita* [2018] (dashed grey).

transport is degenerate due to the non-linear way in which the processes affect one another. Although not investigated here, *Kocharov et al.* [1998] show e.g. that intensities with similar shapes can be obtained by using different constant parallel or radial MFPs. These authors also show the effect of the initial pitch-cosine distribution, which was also verified with the current model: if the pseudo-particles are initially anisotropically distributed (μ' uniformly distributed between $[0.9; 1]$ for instance), the event has an earlier onset compared to an isotropically distributed injection, due to less pitch-angle scattering experienced by the bulk of the distribution at these large values of μ'. The effects of energy dependent MFPs or temporal injection func-

tions are discussed by *Zhang et al.* [2009].

The black curve in the top panel of Fig. 6.9 is the situation with only focusing considered thus far. When SW advection is included while still neglecting energy losses (red curve), the particles arrive slightly earlier and the event has a higher (by $\sim 5\%$) peak intensity, while the intensity decreases slightly faster. This faster decrease in the wake, is partly due to the rarefaction caused by the increased advection due to the co-rotating SW speed which increases with distance. In the previous cases where energy changes were neglected, all of the pseudo-particles were injected and arrived at the observation point with the same momentum. In the case where energy changes are considered, the pseudo-particles are injected with momenta following a power law with a spectral index of $\gamma = -5$ ($\propto p'^{-5}$; which is slightly steep, but not unusual for SEP events [*Ruffolo*, 1995; *Tan*, 2018]) between $2 - 4$ MeV and the pseudo-particles are counted at the observation point in different momentum bins. This however, has the drawback of slightly bad statistics in a given energy channel, compared to the statistics of all particles reaching the observation point, hence the usage of 10^7 pseudo-particles. If energy losses are included while SW advection is neglected (blue curve), the particles arrive slightly later, compared to the case of only focusing, and the event has an overall lower intensity (by $\sim 20\%$). If all the physical effects are included (green curve), then compared to the case with only focusing, the particles arrive slightly earlier, due to the SW advection, while having lower (by $\sim 15\%$) intensities, due to energy losses. From this it is important to realise that if SW advection and/or energy losses are neglected in a model, the model would predict the wrong onset times and peak intensities. In particular, the onset times in different energy channels will be different since high energy particles arrive before low energy particles, an effect referred to as *velocity dispersion* [*Ruffolo*, 1995; *Kocharov et al.*, 1998; *Zhang et al.*, 2009].

The lower panel of Fig. 6.9 shows a comparison between the three different numerical integration schemes (Eqs. 5.28-5.30) and the FD model of *Ruffolo* [1995] for the case where all the physical effects are included. All three integration schemes compare well to the FD model, except for a slightly earlier onset time and higher intensities in the wake. The intensity in the wake however, is not higher than 10% and both these effects might be due to a time step which is slightly too large. In the case of only focusing and focusing with only SW advection, the Euler-Maruyama scheme deviated slightly more from the FD model compared to the other two integration schemes, while it deviated slightly less in the case of focusing with only energy losses. If all effects are included, all three integration schemes seem to behave similarly and it does not seem that a single scheme has a systematically smaller deviation from the FD model. This might indicate that the results are governed by the stochastic nature of the SDEs and that the usage of a higher order integration scheme might be redundant. Caution should be taken however, since these results are only for one spatial dimension and the different schemes might give different results in the spatially three-dimensional case where the particles must follow curved magnetic field lines. It can also be argued that if the derivatives of the PADC around $\mu' = 0$ are handled incorrectly, then this might introduce additional errors in the Milstein and

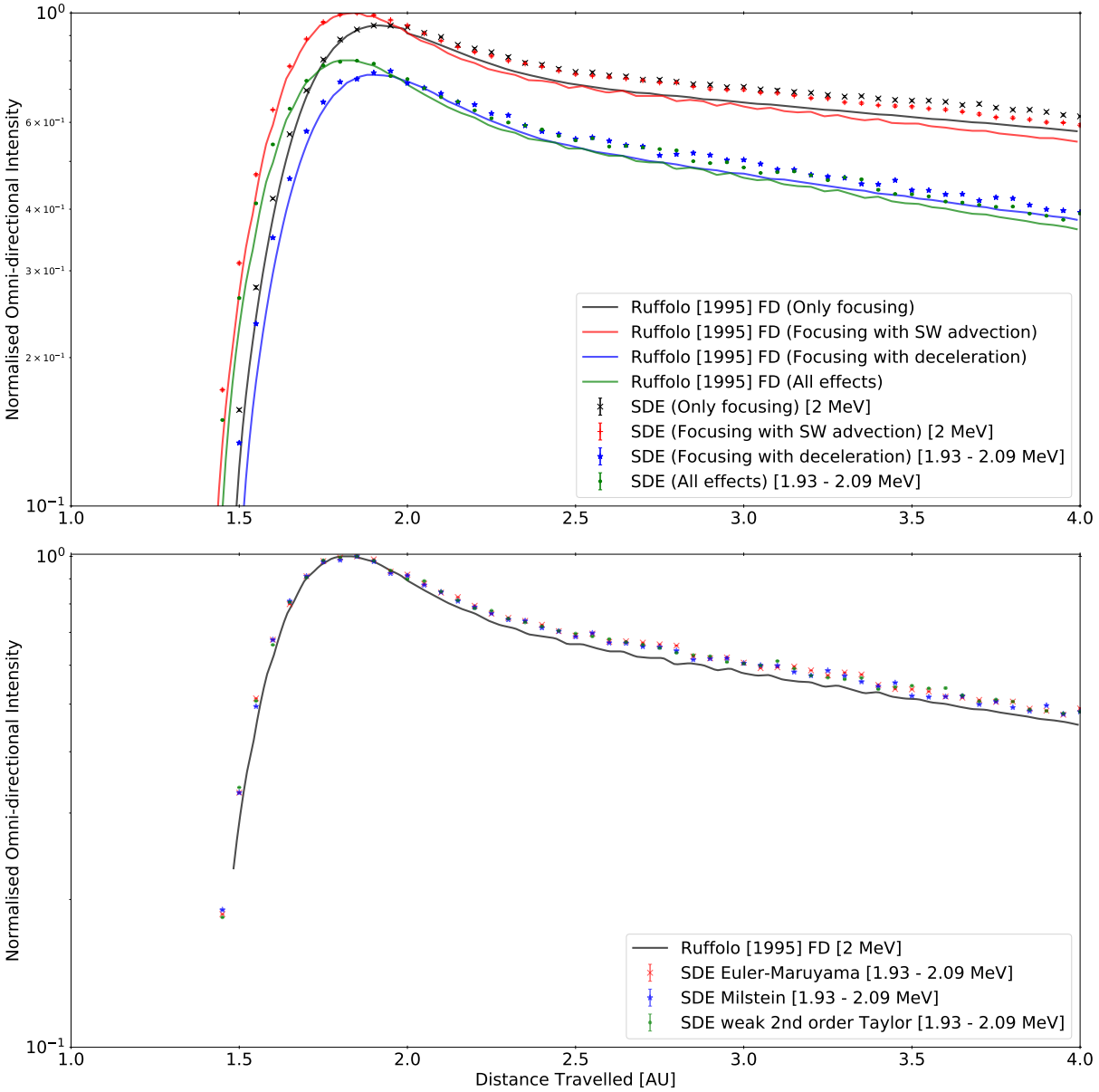

Figure 6.9: *Top:* Omni-directional intensity at Earth of 2 MeV protons, as a function of distance travelled by the protons, for different physical effects. The simulation results (symbols) of the Euler-Maruyama scheme (Eq. 5.28) are compared to the finite difference model of *Ruffolo* [1995] (solid lines). The intensities are normalised to the peak intensity of the case with focusing and solar wind advection (red). *Bottom:* Comparison of the Euler-Maruyama (red; Eq. 5.28), Milstein (blue; Eq. 5.29), and second order weak Taylor (green; Eq. 5.30) schemes to the finite difference model of *Ruffolo* [1995] (solid black) with all physical effects included (green curve in top panel).

weak second order Taylor schemes due to their additional dependence on these derivatives.

The time integrated PAD at Earth of these two comparisons are shown in Fig. 6.10, where the radial distance for the focusing length and spiral angle was chosen so that the analytical solution is comparable to the results. The radial distance which fits the results is not the Earth, as the distribution might have not yet reached the stationary state and is set up in regions close to the Sun where focusing has a larger effect. The radial distance needed to fit the global

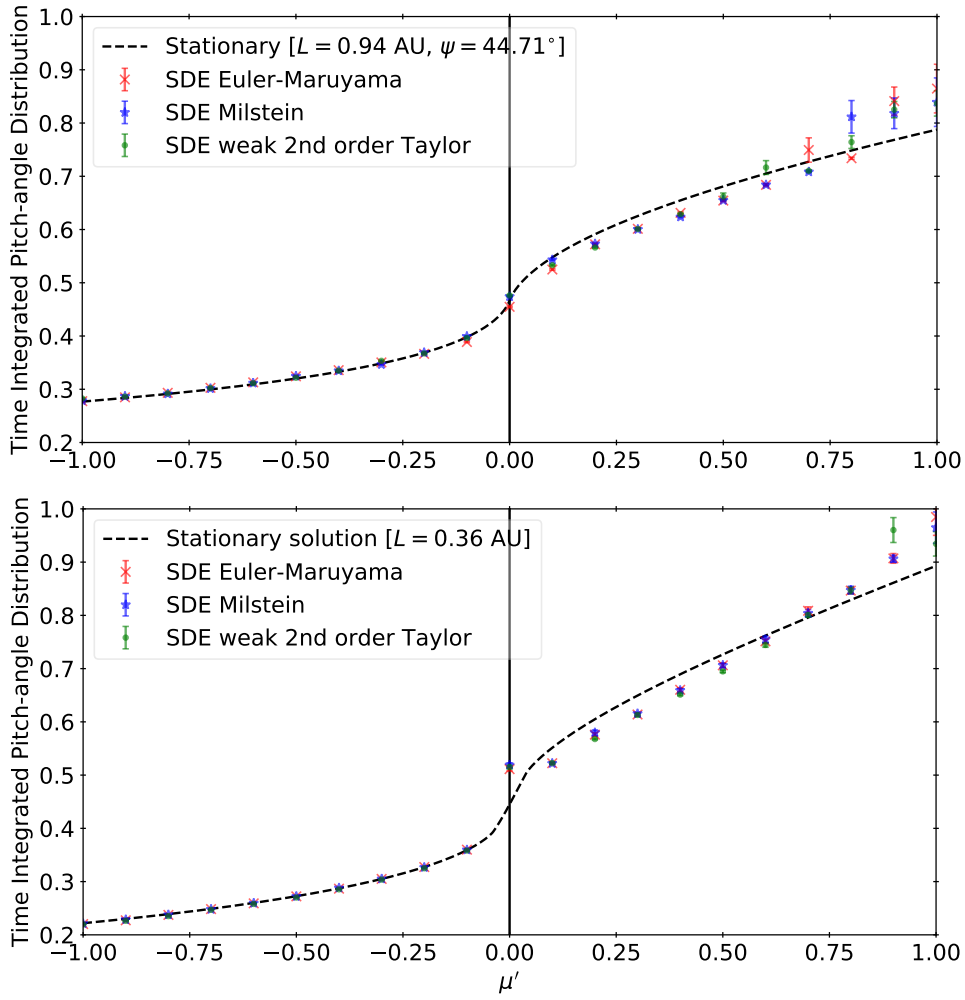

Figure 6.10: Time integrated pitch-angle distribution at Earth for Fig. 6.8 (*top*) and the lower panel of Fig. 6.9 (*bottom*) compared to the analytical stationary pitch-angle distribution (dashed black; Eq. 6.4 calculated numerically), for the three numerical integration schemes (symbols).

PAD would also differ because globally the particles have sampled a wider range of focusing lengths and experienced more scattering. The PAD for the comparison with *Dröge et al.* [2010] (top panel) is generally in good agreement with the analytical solution, except for μ' close to 1, which is also seen in the comparison with *Ruffolo* [1995] (bottom panel). These higher values could be due to the limited integration time, reflecting a larger contribution from focusing compared to scattering. If this is true, it might be expected that for longer simulation times the particles with large pitch-cosine will be moved towards smaller values by scattering and that the PAD would become stationary.

Although the PAD in the comparison with *Dröge et al.* [2010] shows no irregular behaviour around $\mu' = 0$, all of the PADs in the comparisons with *Ruffolo* [1995] show a bump at $\mu' = 0$, suggesting that the PADC derivative is not large enough, causing particles to be stuck at $\mu' = 0$. This slightly larger number of pseudo-particles around $\mu' = 0$ could also explain the higher intensities seen in the wake as these pseudo-particles do not move away form the observation

point efficiently. The fact that the peak is observed for the effective PADC of *Ruffolo* [1995] and not for the PADC of *Beeck and Wibberenz* [1986], is probably due to the different behaviour of these PADCs around $\mu' = 0$: from Fig. B.1 it can be seen that $\partial D^{\text{eff}}_{\mu'\mu'}/\partial\mu' \to \infty$ as $\mu' \to\sim 0.04$ but $\partial D^{\text{eff}}_{\mu'\mu'}/\partial\mu' \to 0$ as $\mu' \to 0$ from $\mu \approx 0.038$, implying that the pseudo-particles are not advected effectively away from $\mu' = 0$ if $\mu' \sim\in [-0.038; 0.038]$.

A variable time step (Eq. 5.31) was also implemented for the Euler-Maruyama scheme with 10^6 pseudo-particles. Although the results are not shown, the model was tested for various values of l_s, l_p, and l_μ. It seems as if $l_s = 0.001L(s)$, $l_p = 0.001p'$, and $l_\mu = 0.01$ yield satisfactory results. The time step used in the comparison with *Ruffolo* [1995] might have been slightly too large, as the event onset better coincides with the FD results if a variable time step is used. Even though the variable time step gives slightly better results, the execution time is longer and the results after the peak intensity still have fluctuations due to stochastic behaviour. The execution time is governed by the value of l_μ as diffusion is the slowest process. It can also be verified that the anisotropy calculated from the PAD is indeed comparable to the anisotropy calculated from the pseudo-particles' average pitch-cosine, if an improved integration technique, such as a composite Simpson rule (see *Press et al.* [1997] for an implementation), is used. During the event onset, however, the anisotropy calculated from the PAD predicts a maximum value of 3, which is not predicted by the other method or the FD methods.

6.3 Energy Losses, Propagation Times, and Other Observational Features

Some of the advantages of SDEs are its ability to illustrate some of the physical processes and to directly calculate propagation times and energy losses. Fig. 6.11 show the temporal evolution of the position, pitch-cosine, and kinetic energy of a single pseudo-particle in the bottom panel of Fig. 6.9 from its injection until it reaches the absorbing outer boundary or the maximum temporal integration time. The top panel is a deterministic case without any pitch-angle scattering and therefore illustrates the minimum propagation time and energy losses of a $4\ \text{MeV}$ solar energetic proton. It is clear that focusing close to the Sun causes the particle motion to become ballistic. This is expected from the focusing term $d\mu'/dt = \left(1-\mu'^2\right)v'/2L$, which yields

$$\left|\frac{\mu'(t)+1}{\mu'(t)-1}\right| = \left|\frac{\mu'_0+1}{\mu'_0-1}\right| \mathrm{e}^{v'\Delta t/L}$$

upon integration if it is assumed that L and v' is constant in time. From this $\mu'(t\to\infty) = 1$ exponentially. The particles' energy decreases quickly close to the Sun due to the short focusing length in the adiabatic focusing term, $dp'/dt \propto -p'v_{\text{sw}}\left(1-\mu'^2\right)v'/2L$ (keeping in mind that it might be unphysical to include adiabatic focusing if pitch-angle scattering is neglected). This term, however, dies out quickly as $L \to \infty$ or $\mu' \to \pm 1$, and the subsequent energy losses are due to the inverse Fermi effect. The total energy loss was small and the speed changed from $\sim 0.092\ c$ to $\sim 0.089\ c$. The distance increased almost linearly with time due to this almost

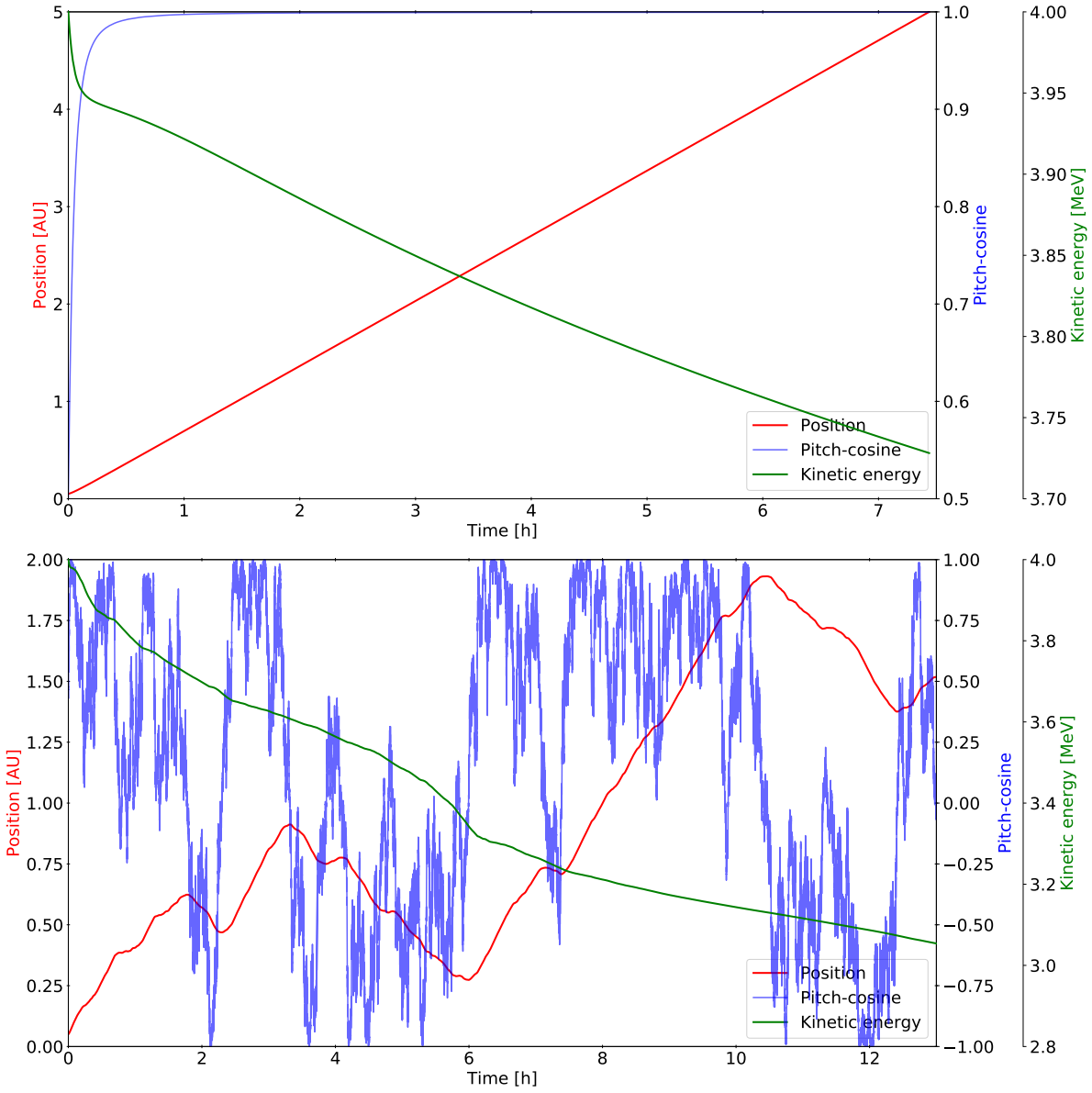

Figure 6.11: Temporal evolution of the position (red), pitch-cosine (blue), and kinetic energy (green) of a single pseudo-particle in the bottom panel of Fig. 6.9 without (*top*) and with (*bottom*) pitch-angle scattering. Notice the different ranges of the axis.

constant speed, focusing, and the increased advection due to the co-rotating SW. The pseudo-particle reached Earth in ~ 1.6 h and the outer boundary at 5 AU after ~ 7.4 h.

Pitch-angle scattering is included in the bottom panel of Fig. 6.11 and it is immediately clear that scattering drastically changes the particles' propagation. The stochastic behaviour seen in the pitch-angle is not seen in the position and kinetic energy, because there is no explicit spatial or momentum diffusion, but its influence on the position and energy is clearly visible. This is analogous to the difference between the velocity components and position of the electron in Fig. 3.13 propagating in the toy slab turbulence model: the particle's velocity components changed quickly and irregularly, while its speed and position changed smoothly. The position

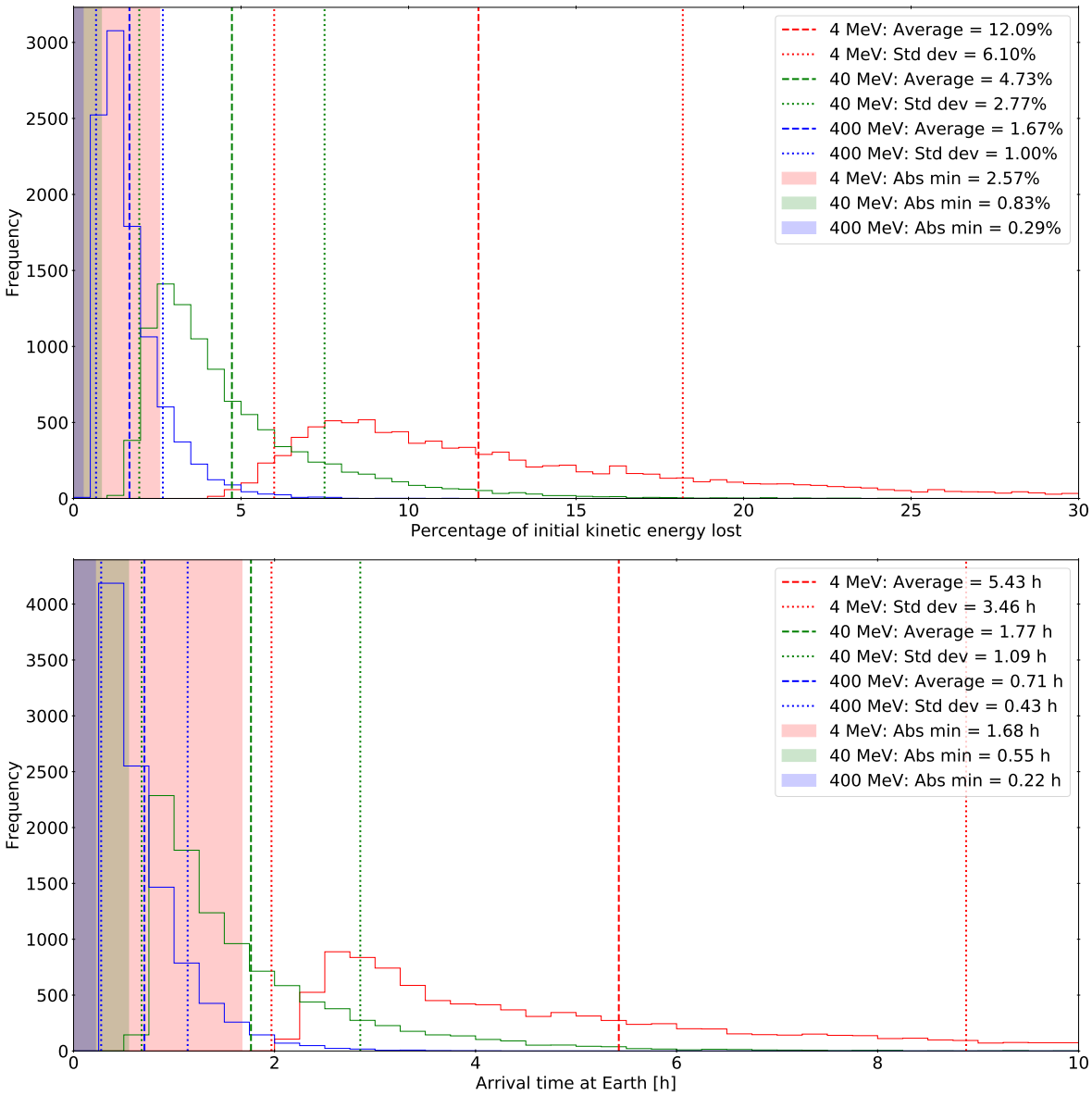

Figure 6.12: Binned percentage of initial kinetic energy lost (*top*) and arrival times (*bottom*) at Earth of 10^4 mono-energetic pseudo-particles injected at the Sun with $\mu' = 0.5$ for 4 (red), 40 (green), and 400 MeV (blue) protons. The shaded regions indicate the minimum kinetic energy that can be lost or the earliest possible arrival time if the particles were to follow a deterministic trajectory with no scattering. The legend indicate theses values, as well as the expectation value (Eq. 6.17 or 6.20) and the standard deviation from this average.

clearly decreases when $\mu' < 0$ and the position changes faster when $\mu' \to \pm 1$. The fastest energy changes occur within ~ 0.5 AU from the Sun. The energy changed by just over 1 MeV, with a $\sim 13\%$ change in speed, due to the longer residence time close to the Sun. The pseudo-particle reached Earth only after ~ 9.5 h and did not reach the outer boundary within the simulation time. From this figure it is expected that the arrival times and energy losses will have some distribution dependent on the propagation conditions.

Very little theoretical or numerical investigations have been made into the propagation times

and energy losses in focused transport and the SDE results will therefore be compared to cosmic ray (CR) diffusion approximations. In what follows, 10^4 mono-energetic pseudo-particles were injected with $\mu' = 0.5$ and integrated, using the same setup for the rest of the parameters as in the comparison with *Ruffolo* [1995], until they reached Earth for the first time. The binned percentage of initial kinetic energy lost and arrival times of these pseudo-particles are shown in Fig. 6.12. The shaded regions indicate the minimum propagation time or energy loss which the particles can experience if they were to follow a deterministic trajectory. The average and standard deviation is also indicated. Both the energy and propagation time seem to follow a Poisson distribution, as might be expected for a stochastic process, and is comparable in shape to the distributions found by *Zhang* [1999b] and *Strauss et al.* [2011] for CRs. All of these discussions also apply to electrons if it is assumed that they have similar propagation conditions.

6.3.1 Energy Losses

Parker [1965] showed that the energy loss rate of isotropic CRs is due to the adiabatic expansion of the SW,

$$\frac{dK'}{dt} = -\frac{1}{3}\Gamma' K' \vec{\nabla} \cdot \vec{v}_{\rm sw} = -\frac{1}{3}\Gamma' K' \frac{1}{r^2}\frac{\partial}{\partial r}\left[r^2 v_{\rm sw}\right] = -\frac{2}{3}\Gamma' K' \frac{v_{\rm sw}}{r}, \tag{6.16}$$

where $\Gamma' = (K' + 2E_0)/(K' + E_0)$, with E_0 the particle's rest mass energy (for relativistic particles $\Gamma' \to 1$ if $K' \gg E_0$ and $\Gamma' \to 2$ if $K' \ll E_0$ for non-relativistic particles, so SEPs would have $1 < \Gamma' < 2$) [*Strauss et al.*, 2011]. It was already stated in Section 4.3.2 that the adiabatic focusing term reduce to this adiabatic deceleration when averaged over pitch-cosine. The change in energy is therefore directly proportional to the particle's energy and the SW speed, and inversely proportional to its radial position. Although the energy loss is complicated by its energy dependence, this equation describes the basic behaviour of the energy in Fig. 6.11. The largest contribution to the energy losses is the particle's position through the $1/r$ dependence since the radial distance changes by a factor of ~ 100 from the injection site to the outer boundary. The co-rotating SW might change by a factor of ~ 3, but this would also be the change in transitions from very slow to very fast radially directed SW. The energy change by a factor of ~ 2 and its influence is comparable to that of the SW. Physically this weak dependence of the energy loss on energy is due to the fact that a higher energy particle would propagate quickly away from the Sun where energy losses are smaller.

The expected kinetic energy that SEPs will have at the observation point, can be defined as

$$\left\langle K' \right\rangle = \frac{\int_0^{K'_0} \tilde{K}' f(s; \tilde{K}'; \mu'; t) d\tilde{K}'}{\int_0^{K'_0} f(s; \tilde{K}'; \mu'; t) d\tilde{K}'} \approx \frac{1}{N}\sum_i K'_i N_i, \tag{6.17}$$

where the integration is only up to the initial kinetic energy since only energy losses are considered. The latter expression approximates the weighted average by counting the number of pseudo-particles N_i in an energy bin with midpoint K'_i. The radial part of the Parker transport

equation for the CR distribution function $U(r; K'; t)$ in a spherically symmetric heliosphere, is

$$\frac{\partial U}{\partial t} + \frac{v_{\rm sw}}{r^2}\frac{\partial}{\partial r}\left[r^2 U\right] - \frac{2v_{\rm sw}}{3r}\frac{\partial}{\partial K'}\left[\Gamma' K' U\right] = \frac{1}{r^2}\frac{\partial}{\partial r}\left[r^2 \kappa_{rr}\frac{\partial U}{\partial r}\right],$$

where $\kappa_{rr} = \lambda_r v'/3$ is the radial diffusion coefficient assumed to be independent of position and time [*Parker*, 1965; *Strauss et al.*, 2011]. *Parker* [1965] solved this equation in the steady state, neglecting advection and the energy dependence of Γ' and κ_{rr}, with an absorbing outer boundary at infinity and mono-energetic particles being injected at the Sun at a steady rate. In the diffusive limit, the expected energy of SEPs is then

$$\left\langle K' \right\rangle \approx K'_0 \sqrt{\frac{8}{3}\Gamma' \frac{v_{\rm sw} r}{\kappa_{rr}}} K_1\left(\sqrt{\frac{8}{3}\Gamma' \frac{v_{\rm sw} r}{\kappa_{rr}}}\right), \tag{6.18}$$

where K_1 is a modified Bessel function of the second kind. Since $K_1(z)$ is approximately an exponentially decaying function of z, particles will reach a point further away from the Sun with lower energies on average. From the $1/\sqrt{\kappa_{rr}}$ factor it can be seen that higher energy particles, with a larger MFP and hence diffusion coefficient, will experience less energy loss on average than low energy particles [*Parker*, 1965].

It is clear from the binned kinetic energy upon arrival at Earth in the top panel of Fig. 6.12 that high energy particles lose less energy than low energy particles, since the low energy particles are subject to more modulation. Models neglecting energy losses might therefore be valid for high energy particles but not for low energy particles. It is also clear that the most probable energy (the midpoint of the bin with the largest bin count) with which the particles would arrive, given a specific initial energy, is slightly higher than the expected value due to the distribution's long tail, with these two values being close for high energy particles [*Strauss et al.*, 2011]. The top panel of Fig. 6.13 shows the fractional kinetic energy loss upon arrival at Earth as a function of the initial energy. The maximum energy which a particle can have if it followed a deterministic trajectory and the minimum energy resulting from the simulations are also indicated by the red and black squares, respectively, where it should be kept in mind that the minimum energy is not an absolute value and would depend on the trajectory of the particle. A particle will reach Earth with an energy between these two points, with some expected energy (green circle) and the most probable energy (magenta triangle) falling within the distribution's standard deviation from the expected value.

The expected energy upon arrival of Eq. 6.18 is indicated in the top panel of Fig. 6.13 by the blue shaded region, where the top and bottom of this region correspond to relativistic and non-relativistic particles, respectively. Notice that the simulations used a constant parallel MFP whereas Eq. 6.18 assumes a constant radial MFP. The local radial MFP at Earth of $\lambda_r = 0.15$ AU was therefore used to calculate κ_{rr}. It is clear that the diffusion approximation overestimates the energy losses since it does not take the focusing effect into consideration, while a slightly better prediction can be found by using $\lambda_r = 0.3$ AU. The pseudo-particles that experienced the most energy losses are closer to this region as they experienced more scattering and are therefore closer to diffusive behaviour. As a possible better approximation for the energy losses,

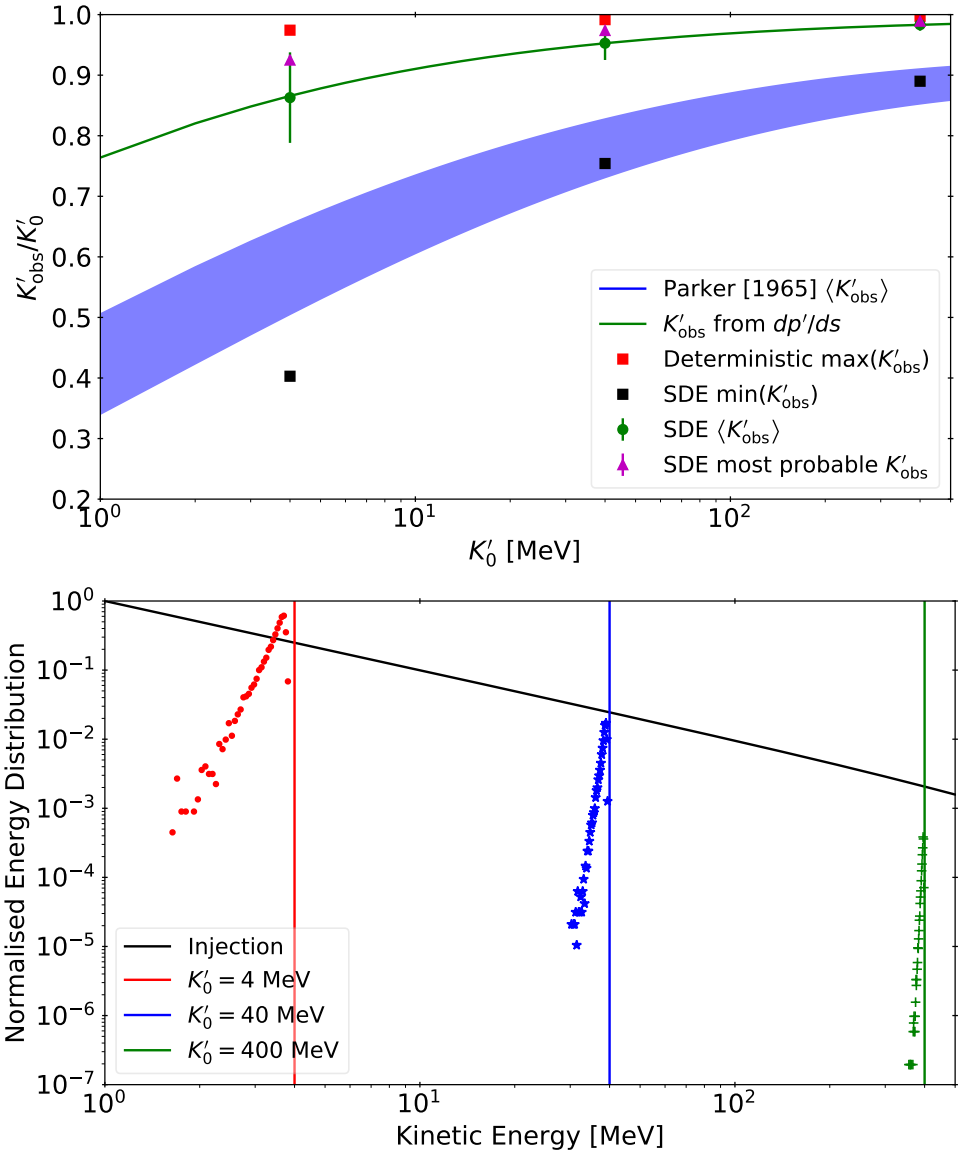

Figure 6.13: *Top:* Kinetic energy upon arrival at Earth as a function of initial injection energy. Symbols indicate the simulation results of the mono-energetic injections in Fig. 6.12 for the maximum energy if the particles were to experience no scattering (red squares), the minimum energy that occurred (black squares), the expected energy with the standard deviation (green circles), and the most probable energy (magenta triangles). Also indicated are the predicted average values from the diffusion approximation (shaded blue region; Eq. 6.18) and terms in the focused transport equation (green line; Eq. 6.19). *Bottom:* Energy distribution (symbols) upon arrival at Earth of the mono-energetic injections in Fig. 6.12 normalised to an injection spectrum with a spectral index of $\gamma = -2$ (black line).

consider the deceleration term in the FTPE. An expression for the momentum as a function of position along the magnetic field line can be constructed by dividing Eq. 5.24b by Eq. 5.24a, while scattering and focusing can be incorporated by weighting each of these equations by the stationary PAD (Eq. 6.4) using the local focusing length at each position. Transforming the integral over arc length to radial position, by using $dr/ds = \cos\psi$, then yields

$$\langle p'(r)\rangle \approx p'_0 \exp\left[-\int_{r_0}^{r} \zeta(r')\sec\psi(r')dr'\right], \tag{6.19}$$

where

$$\zeta(r) = \frac{v_{\rm sw}\int_{-1}^{1} M(\mu';r)\left\{\left(1-\mu'^2\right)\sec\psi(r)/2L(r) + \mu'^2\cos\psi(r)\left[d\sec\psi(r)/dr\right]\right\}d\mu'}{\int_{-1}^{1} M(\mu';r')\left\{\mu' v_0' + \left[1-(\mu' v_0'/c)^2\right]v_{\rm sw}\sec\psi(r)\right\}d\mu'},$$

which should be integrated numerically. This is indicated by the green line in the top panel of Fig. 6.13 and it is clear that this expression gives a much better approximation for the energy losses, with a small underestimation due to the use of the initial speed.

The energy spectrum of an SEP event has not yet been considered and it might be expected that the spectrum would steepen/soften at an observation point due to the energy losses. This is illustrated in the bottom panel of Fig. 6.13 where the energy distribution of the pseudo-particles upon arrival at Earth for the delta injection energy is normalised to a spectrum with a spectral index of $\gamma = -2$. It is evident that the spectrum steepens/softens as particles are decelerated and 'advected' in momentum space from high to low energies, so that the number of high (low) energy particles decrease (increase). The evolution of the energy spectrum can therefore be seen as the contribution of a lot of mono-energetic injections and their subsequent evolution into some distribution [*Strauss et al.*, 2011]. Remember that the spectrum could develop a break due to different processes (see e.g. the discussion in Section 2.2.3).

6.3.2 Propagation Times

The expected propagation time, from the injection to the observation point, can be defined as

$$\langle\tau\rangle = \frac{\int_0^\infty \tau f(s;p';\mu';\tau)d\tau}{\int_0^\infty f(s;p';\mu';\tau)d\tau} \approx \frac{1}{N}\sum_k \tau_k N_k, \tag{6.20}$$

where N_k is the number of pseudo-particles in a temporal bin with mid-point τ_k. *Parker* [1965] investigated the probability $\rho(r;t)$ to find CRs at radius r and time t in a spherically symmetric heliosphere. Neglecting energy losses and advection, the isotropic probability is then governed by

$$\frac{\partial\rho}{\partial t} = \frac{1}{r^2}\frac{\partial}{\partial r}\left[r^2\kappa_{rr}\frac{\partial\rho}{\partial r}\right].$$

With an absorbing outer boundary at R and particles being injected at $r_0 \to 0$ close to the Sun at $t = 0$, the solution of this equation is

$$\rho(r;t) = \frac{1}{2\pi R r_0 r}\sum_{n=1}^{\infty}\sin\left(\frac{n\pi r_0}{R}\right)\sin\left(\frac{n\pi r}{R}\right)\mathrm{e}^{-n^2\pi^2\kappa_{rr}t/R^2}. \tag{6.21}$$

The expected propagation time then has the simple relation

$$\langle\tau_{\rm d}\rangle = \frac{R^2}{\pi^2\kappa_{rr}}\sum_{n=1}^{\infty}\frac{1}{n^2} = \frac{r^2}{6\kappa_{rr}}, \tag{6.22}$$

where R was replaced by r in the last step since the derivation assumed CRs diffusing from R to the origin and the situation should be symmetric for SEPs diffusing from the origin to

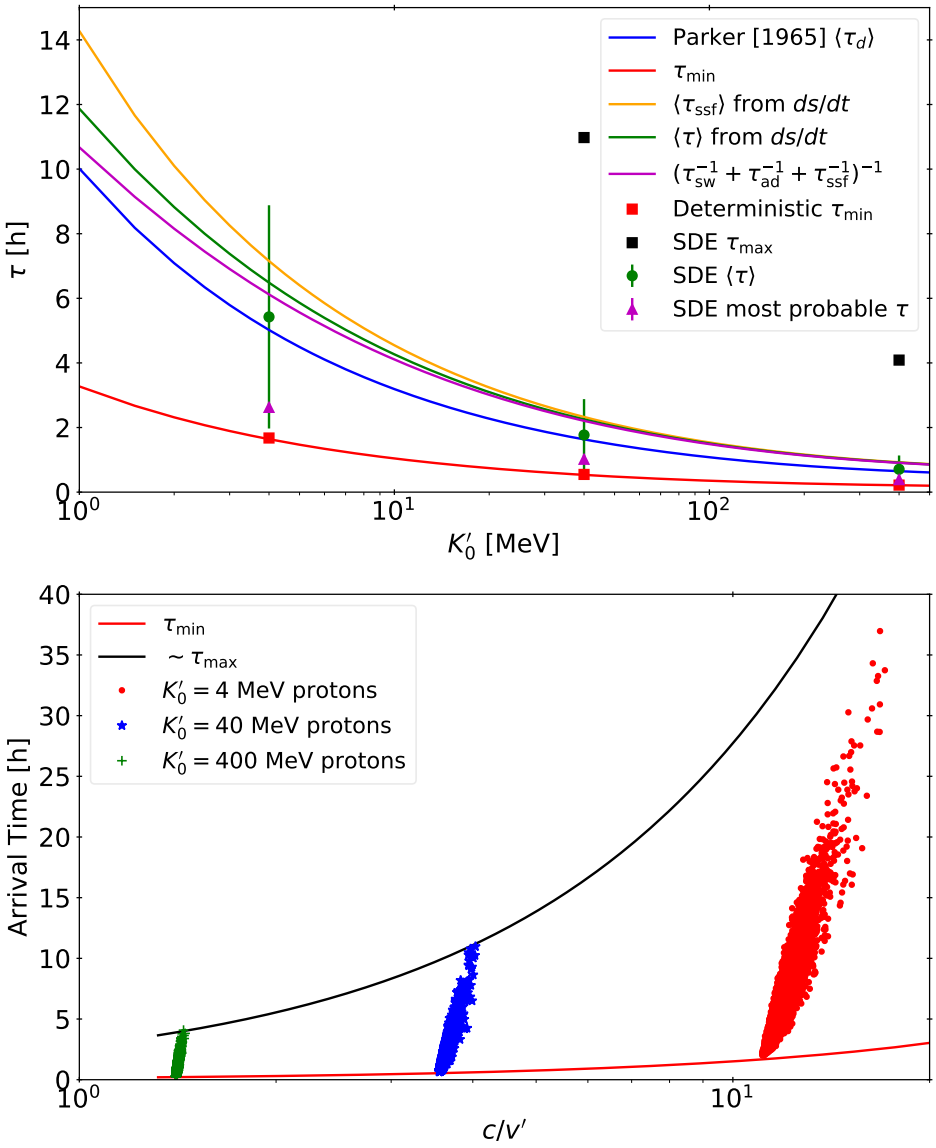

Figure 6.14: *Top:* Similar to the top panel of Fig. 6.13 but for the propagation or arrival times. The shortest possible arrival time is indicated by the red line, while the magenta line indicates an addition of the different time scales affecting the propagation time (Eq. 6.24). Also indicated are the predicted average values from the diffusion approximation (blue line; Eq. 6.22) and terms in the focused transport equation (orange and green; Eq. 6.23). *Bottom:* Arrival time as a function of the inverse of the particle speed (symbols) at Earth of the mono-energetic injections in Fig. 6.12. The red line indicates the earliest arrival time if the particles were to move with a constant speed along the magnetic field line, while the black line indicates a possible upper bound on the latest arrival times.

r. This expression predicts that the average propagation time will be four times longer if the observation point's radial distance is doubled and from the $1/\kappa_{rr}$ factor it can be seen that higher energy particles will reach a point faster on average than low energy particles [*Parker*, 1965; *Strauss et al.*, 2011].

It is clear from the binned arrival time at Earth in the bottom panel of Fig. 6.12 that high energy particles arrive earlier than low energy particles. This is expected, but it should be noted that

there might be a delay in the release of high energy particles at the solar flare since it might take longer to accelerate particles to these energies, or low energy particles might arrive 'early' as high energy particles are decelerated by wave-generation [*Kontar and Reid*, 2009; *Wang et al.*, 2016]. The most probable arrival time, given a specific initial energy, is also slightly earlier than the expected value, with these two values being close for high energy particles. The top panel of Fig. 6.14 show the propagation time as a function of the initial energy, similar to the top panel of Fig. 6.13. The shortest possible propagation time would be if the particles were to experience no scattering while moving with a constant speed along the magnetic field line. This time will be $\tau_{\min} = \Delta s/v_0'$ and is indicated by the red line. The expected propagation time of Eq. 6.22 is indicated by the blue line. It is surprising that the diffusion approximation is quite close to the computed values, and even underestimates the propagation time, given that focusing is not considered. In CR studies this can be viewed as a *diffusion time*, although it does not seem to really correspond here to diffusive behaviour. Perhaps the infinite signal propagation speed in the diffusion approximation fortuitously cancels with the late arrival time of the diffusive particles to yield a good approximation of the expected arrival time. Notice that there are different time scales all contributing to the average propagation time: the SW *advection time* is $\langle \tau_{\rm sw} \rangle = \Delta r/v_{\rm sw} \approx 4.3$ days, while Eq. 6.16 suggest an *adiabatic deceleration time* of $\langle \tau_{\rm ad} \rangle = 3\Delta r/2\Gamma' v_{\rm sw} \approx 6.5/\Gamma'$ days at 1 AU. This adiabatic deceleration time might be shorter in an SEP event due to the spectrum with more low energy particles experiencing more energy losses [*Ruffolo*, 1995; *Strauss et al.*, 2011].

In view of the success of Eq. 6.19 in predicting the energy losses, an approximation for the arrival time might be constructed from Eq. 5.24a. By integrating Eq. 5.24a over the PAD and again changing the integration over arc length to an integral over radial distance, yields

$$\langle \tau(r) \rangle \approx \int_{r_0}^{r} \frac{\sec\psi(r')}{\int_{-1}^{1} M(\mu';r') \left\{ \mu' v_0' + \left[1 - (\mu' v_0'/c)^2 \right] v_{\rm sw} \sec\psi(r') \right\} d\mu'} dr', \tag{6.23}$$

where this reduces to an expression for only streaming, scattering, and focusing ($\langle \tau_{\rm ssf} \rangle$) if $v_{\rm sw} = 0$. This is indicated by the green and orange lines, respectively, in the top panel of Fig. 6.14, but these expressions overestimate the arrival time. It is clear that SW advection shortens the propagation time when comparing the green and orange lines, while these predicted propagation times will increase if Eq. 6.19 is used to calculate $v'(r)$, since slower particles will take longer to reach Earth. In general the different time scales can be added,

$$\langle \tau \rangle \approx \frac{1}{1/\langle \tau_{\rm ssf} \rangle + 1/\langle \tau_{\rm sw} \rangle + 1/\langle \tau_{\rm ad} \rangle}, \tag{6.24}$$

if the non-linear effects between the different physical processes are neglected [*Ruffolo*, 1995; *Strauss et al.*, 2011]. This is indicated by the purple line and gives a slightly better prediction at low energies than Eq. 6.23.

The bottom panel of Fig. 6.14 shows the arrival time of each pseudo-particle as a function of the inverse of its speed upon arrival at Earth. Notice that the slope of a line passing through the origin on this graph represents a distance. The minimum propagation time of a particle

if it experienced no scattering, while moving an arc length distance of 1.14 AU exactly along the magnetic field line, is indicated by the red line. From this it seems that the onset time is $\sim 1.08 - 1.1$ times this minimum propagation time. The black line indicates an approximate upper limit on the propagation times and suggest that these particles travelled a distance of ~ 20 AU.

6.3.3 Observational Features

Fig. 6.15 shows the temporal evolution of the omni-directional intensity at Earth for protons as would typically be measured by spacecraft. The simulation used the same setup as in the comparison with *Dröge et al.* [2010], but with a spectrum with spectral index $\gamma = -3$, solar wind advection and energy losses included, as well as a variable time step. The intensities of two detectors, with 45° opening angles, looking towards the Sun and perpendicular to the equatorial plane are shown by the black dashed and dotted lines, respectively. This clearly shows that the first particles to arrive are focused and streaming away from the Sun. Particles whose pitch-angle has been increased by scattering, have smaller parallel speeds and arrive later in the event. The coloured lines show the intensities detected in different energy channels. The purple, red, green, and orange lines illustrate the concept of velocity dispersion where high energy particles arrive earlier than low energy particles. The low energy particles have higher peak intensities because there are more low energy particles in the spectrum than high energy particles. The behaviour of the blue and brown lines are partly due to the limited injection spectrum: the high energy particles just below the upper injection limit decay fast because they stream away quickly from the observation point and there is not an appreciable amount of high energy particles that can be decelerated into this energy range; the low energy particles below the lower injection limit have a delayed onset since higher energy particles must first be decelerated into this energy range.

The temporal evolution of the PAD in both the SW and observer's frame is shown in Fig. 6.16 as polar plots and is comparable to the polar plots of *Ruffolo* [1995]. The different times indicated correspond with the pulse's leading edge, the peak intensity, the pulse's trailing edge and the wake. In these plots the Sun in located towards the left such that particles moving away from the Sun are directed to the right, while 90° and 270° are perpendicular to the equatorial plane. Notice that the bins are not equally spaced in pitch-angle because in the model they are equally spaced in pitch-cosine and that different scales are used for the different times. These plots clearly show the focused distribution of the first particles to arrive which are streaming away from the Sun. The effect of pitch-angle scattering can be seen in the wake as the distribution becomes more isotropic, but there are still more particles moving away from the Sun than towards it due to anisotropic scattering. The Compton-Getting effect (see Section 4.2.1) [*Gleeson and Axford*, 1968; *Forman*, 1970] can also be seen as the number of particles moving away from (towards) the Sun is slightly more (less) in the observer's frame compared to the SW frame.

The top panel of Fig. 6.17 shows the global and time integrated energy distribution at Earth for

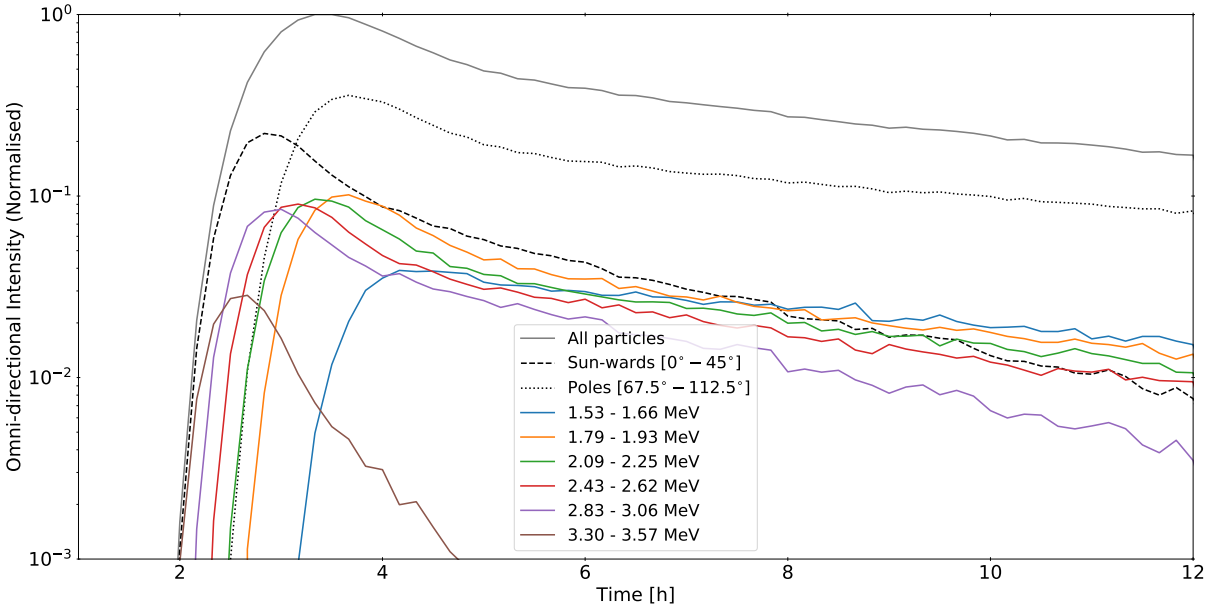

Figure 6.15: Omni-directional intensity at Earth for protons as would typically be measured by spacecraft. Intensities are shown for different energy channels (coloured lines) as well as two detectors, with $45°$ opening angles, looking towards the Sun (black dashed) and perpendicular to the equatorial plane (black dotted). The intensities are normalised to the peak intensity of all particles detected (solid grey).

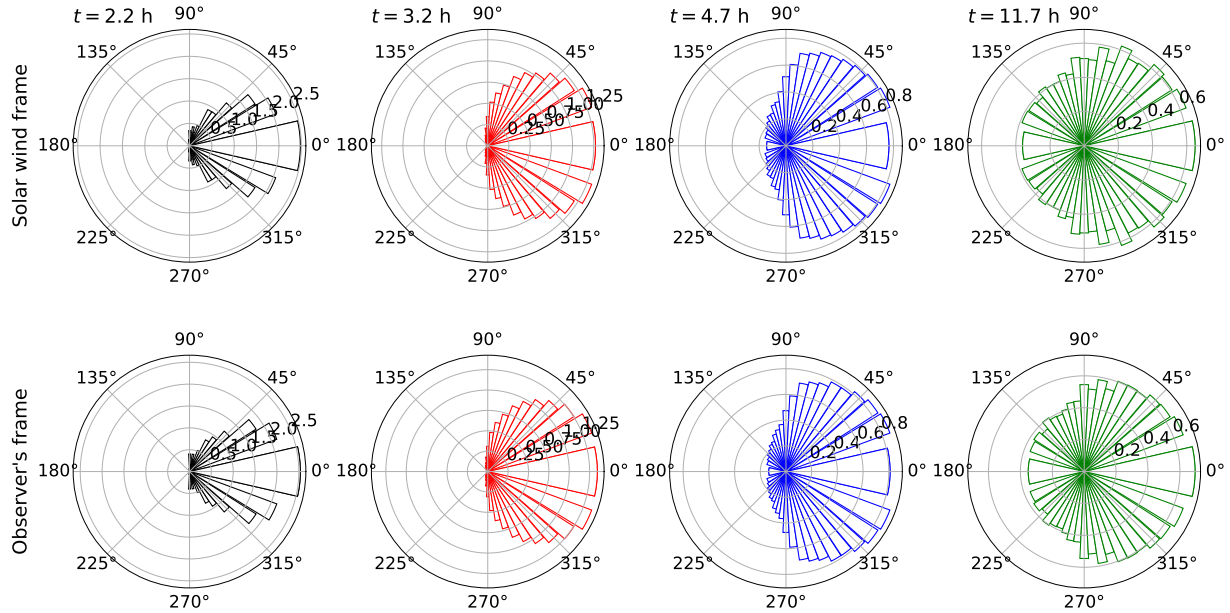

Figure 6.16: Temporal evolution of the pitch-angle distribution in Fig. 6.15 in the solar wind (*top*) and observer's (*bottom*) frame. Notice the different scales used at different times.

the Euler-Maruyama scheme in the bottom panel of Fig. 6.9 with both a constant and variable time step. The fact that the constant time step was not small enough can be seen here when comparing the time integrated energy distributions. In the stationary state it seems as if the distribution is simply shifted to lower energies and broadened due to deceleration, but that the distribution's spectral index does not change. The global distribution is shifted towards lower energies compared to the time integrated distribution at the observation point, because on a

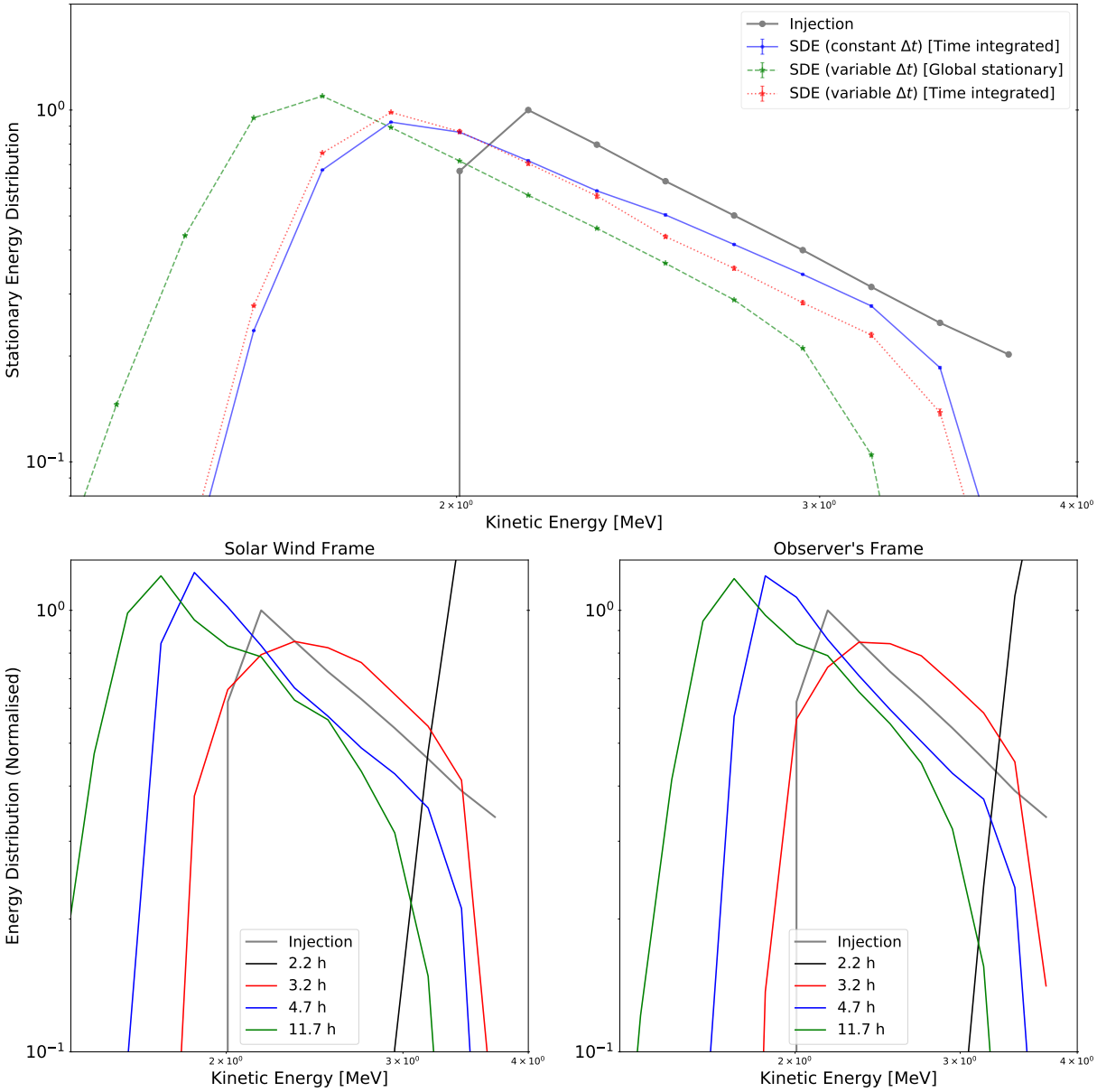

Figure 6.17: *Top:* Global stationary and time integrated energy distribution at Earth for the Euler-Maruyama scheme in the bottom panel of Fig. 6.9. The injection spectrum is shown by the grey line and the distributions are normalised to the peak of the injection spectrum. *Bottom:* Temporal evolution of the energy distribution in Fig. 6.15 in the solar wind (*left*) and observer's (*right*) frame.

global scale the particles have experienced more energy losses. For longer simulation times it might be expected that the time integrated distribution at the observation point would approach the global distribution as decelerated particles propagate back to the observation point. It should be kept in mind that the energy lost by the SEPs is dumped into the background SW plasma, but that the energy density in an SEP event is not high enough to noticeably heat the SW plasma [*Parker*, 1965].

The temporal evolution of the energy distribution in both the SW and observer's frame of Fig. 6.15 is shown in the bottom panels of Fig. 6.17. Velocity dispersion is also visible here as

the high energy particles arrive first, almost as a delta function, followed by the low energy particles, showing a clearer spectrum. The exponential cut-off at high energies is due to the deceleration of high energy particles in the limited injection spectrum and the propagation of these particles away from the observation point. Deceleration and the late arrival of particles are further visible as the spectrum shifts to lower energies with time. A clear steepening of the spectra is unfortunately not visible in this limited injection spectrum, but would be visible over a broader energy range [*private communication with N. Wijsen*]. The Compton-Getting effect is again visible as the spectrum is shifted to slightly higher energies in the observer's frame compared to the SW frame.

6.4 Summary

This chapter verified the stochastic transport model introduced in Chapter 5 and Appendix B by comparing it to published numerical models and analytical approximations. The model was first compared to the diffusion approximation and telegraph equation for a constant focusing length without advection or energy losses. The model was able to replicate the results of *Effenberger and Litvinenko* [2014] for isotropic pitch-angle scattering in both the presence and absence of focusing, while the results seemed reasonable for anisotropic scattering as well. The anisotropy calculated from the average of the pseudo-particles' pitch-cosine seemed to be more accurate than the anisotropy calculated by integrating the pitch-angle distribution (PAD), although the two methods are comparable and the latter method could be improved numerically. The ad hoc way in which the pitch-angle diffusion coefficient's (PADC) derivative is handled around zero pitch-cosine seem valid, but the PAD should be investigated to make sure that it is not cut off at too small or too large values. If the derivative is too small (large), a peak (dip) develops in the PAD around zero pitch-cosine.

The stochastic transport model was compared to the finite difference models of *Ruffolo* [1995], *Strauss and Fichtner* [2015], and *Heita* [2018], as well as the stochastic differential equation (SDE) model of *Dröge et al.* [2010]. These comparisons showed that the model is able to simulate the transport of solar energetic particles (SEPs) and that the different physical processes are handled correctly. In the comparison with *Ruffolo* [1995], the omni-directional intensity had slightly earlier onset times and higher fluxes during the decay phase. This was due to a too large time step and the behaviour of the effective PADC's derivative, respectively. It was seen that a higher order numerical integration scheme does not yield any improvement in the results, as the results are governed by the stochastic nature of the SDEs, and that the Euler-Maruyama scheme is sufficient in this model with one spatial dimension. Furthermore, additional errors might be introduced into the higher order schemes if the derivatives of the PADC around zero pitch-cosine are handled incorrectly. It was also seen that a variable time step can be used to ensure that the time step is small enough but not too small.

The different characteristics of focused transport were also investigated. It was seen in general

that focusing causes a coherent pulse of focused particles to propagate away from the injection point into regions of weaker magnetic fields. Pitch-angle scattering broadens the coherent pulse and causes an extended wake behind the pulse composed of particles closer to diffusive behaviour. Both the diffusion approximation and telegraph equation are comparable in the wake, but the diffusion approximation underestimates both the onset time and peak intensity of the event. Although the telegraph equation is better at modelling the omni-directional intensity, its solution to obeying causality is to simply limit the distribution based on the signal propagation speed. This, however, causes delayed onset times, unrealistically sharp propagation fronts which is not smeared out due to scattering, and require two delta functions in order to conserve particles [*Malkov and Sagdeev*, 2015]. These two approximations also seem incapable of replicating the narrow coherent pulse of anisotropic pitch-angle scattering.

The effect of solar wind (SW) advection on the omni-directional intensity of SEPs is to quicken the onset time and increase the peak intensity. Energy losses, in contrast, have the effect of later onset times, lower peak intensities, and a faster decay phase. It was seen that the fastest energy changes occur close to the Sun and that the particles' position has the greatest influence on the energy loss rate, even though the loss rate is dependent on the energy and SW speed. Both the energy distribution upon arrival at Earth and the arrival times of SEPs injected with a single energy, follow a Poisson distribution, which is narrower for high energy particles. The expected kinetic energy upon arrival and the expected propagation times were compared to the diffusion approximation of *Parker* [1965] for isotropic cosmic rays. The diffusion approximation underestimates the average kinetic energy, but gives a surprisingly good estimate for the average propagation times. An accurate approximation of the average energy was constructed from the terms in the focused transport equation, while this approach unfortunately overestimates the average propagation time. This approach first weighs the transport terms by the stationary PAD at each position, to include the balancing between focusing and scattering, before integrating over radial distance.

It was also seen that the first particles to arrive at an observation point are high energy particles with small pitch-angles streaming away from the Sun. Lower energy particles arrive later with higher peak intensities, due to more low energy particles in the spectrum, and larger pitch-angles, since they experienced more pitch-angle scattering. The pitch-angle and energy distribution is shifted slightly to smaller pitch-angles and higher energies, respectively, in the observer's frame, compared to the SW frame, due to the Compton-Getting effect. The similarities between the coherent pulse's PAD at the observation point and the stationary PAD, suggest that the pulse is in a quasi-stationary state set up by the balance between focusing and scattering. It was also seen that the global and time integrated energy distribution at the observation point is broadened and shifted to lower energies due to the energy losses, while retaining the initial spectral index. The temporal evolution of the energy distribution at the observation point would show a steepening/softening of the spectrum due to energy losses.

Chapter 7

Summary and Conclusions

This research summarised the fundamental physics underlying the propagation of solar energetic particles (SEPs) and introduced a numerical code, with one spatial dimension and energy losses, to model an SEP event using stochastic differential equations (SDEs).

Chapter 2 introduced the dynamic nature of the Sun, which leads to periodicities in various observables of the Sun on various time scales, and to the violent and energetic events of solar flares and coronal mass ejections (CMEs). Energetic charged particles, called solar energetic particles (SEPs), are produced by these transient events and are observed both in situ and remotely in various ways. The focus fell on impulsive SEP events which are caused by solar flares, observed as a quick increase in energetic particle fluxes, followed by a decrease lasting several hours. These events are characterized by directional particles streaming away from the Sun, steep spectra, and elemental abundances typical of the corona, with enhancements in $^3\mathrm{He}$, highly ionized heavy ions, and electrons. These SEPs propagate in the Sun's solar wind (SW), a radially outflowing plasma with speeds varying between $\sim 400 - 800\ \mathrm{km \cdot s^{-1}}$, and magnetic field frozen into the SW and carried away from the Sun to form the heliospheric magnetic field (HMF), forming Archimedean spirals which lie on cones of constant latitude in the *Parker* [1958] model.

Chapter 3 investigated solutions of the Newton-Lorentz equation to illustrate the motion of charged particles in various electric and magnetic fields. Some basic analytical solutions (some of which can be found in **Appendix A**) were investigated, showing that the particle would follow a smooth trajectory while gyrating around an imaginary point called the guiding centre (GC). SEPs experience magnetic focusing, where their perpendicular speed is transferred to parallel speed when entering regions of decreasing parallel magnetic field strength. As magnetic fields are generally not smooth, an introduction to turbulence was given with an emphasis on slab turbulence, where the turbulent fluctuations are assumed to propagate and is dependent on the position along the background magnetic field. Wave-particle interactions were discussed to illustrate the effect of the magnetic and electric forces exerted on the particle by the turbulent field and numerical schemes (which are introduced in **Appendix A**) were used to simulate an electron propagating in a slab turbulence model. The classical idea of

hard-sphere collisions should not be naively applied to charged particles interacting with turbulence: the classical scattering idea may apply only when the GC is considered and this is due to the physical interaction between charged particles and magnetic scattering centres being of a unique nature.

The general effects of slab turbulence on the motion of a charged particle can be summarised by the following characteristics: the motion of the particle itself is smooth and continuous, with a highly perturbed spiral path; the motion of the particle's GC is much more irregular and displays abrupt changes, which can be clearly seen in the GC's velocity components; the motion of the GC is reminiscent of classical hard-sphere collisions; the GC stays close to the background magnetic field line on which it started; the particle's pitch-angle experiences small stochastic changes; the motion of the particle parallel to the background magnetic field is influenced the most; the particle's energy changes continuously in the observer's frame, but is conserved in a well-defined wave frame, if such a frame can be constructed (that is, if the waves are propagating in the same direction with the same speed).

Chapter 4 discussed the macro-physical transport of SEPs by using the concepts introduced in Chapter 3 to explain the origin of the terms appearing in the focused transport equation (FTPE). The FTPE of *Ruffolo* [1995] was derived for the spatial dimension along the HMF, with transport effects perpendicular to the HMF neglected. There are three important processes entering into the FTPE, namely field parallel transport, energy losses, and pitch-angle changes. The field parallel transport is composed of the particles' motion along the HMF and the advection of particles by the SW. The energy losses are caused by adiabatic focusing and the inverse Fermi effect, with stochastic acceleration neglected due to assumed energy conservation in the SW frame. Adiabatic focusing is caused by the interplay between focusing in the observer's frame and scattering in the SW frame, while the inverse Fermi effect is caused by trailing collisions in the diverging SW. The pitch-angle changes are caused by pitch-angle scattering, focusing, and differential advection, with the latter being caused by the inverse Fermi effect.

In order to solve the FTPE, **Chapter 5** introduced stochastic differential equations (SDEs). Each m-dimensional Fokker-Planck type equation can be transformed into a set of $m - 1$ first order SDEs and the distribution function can be constructed by a convolution of the boundary conditions with a probability density constructed from the SDE solution. The SDE solution, called a pseudo-particle, is a phase-space density element, which should not be viewed as a real particle or its GC. The concept of an SDE was then illustrated using Brownian motion in one dimension and the FTPE for the propagation of SEPs was written as a set of SDEs. Some aspects of this stochastic transport model were discussed, while details were given in **Appendix B**, which also discussed three methods to solve a set of SDEs numerically.

Lastly, **Chapter 6** verified the stochastic transport model by comparing it to published numerical models and analytical approximations. The model could solve the FTPE for a constant focusing length without advection or energy losses for isotropic and anisotropic pitch-angle scattering in both the presence and absence of focusing. Comparisons to the finite difference

models of *Ruffolo* [1995], *Strauss and Fichtner* [2015], and *Heita* [2018], as well as the SDE model of *Dröge et al.* [2010], showed that the model is able to simulate the transport of SEPs and that the different physical processes are handled correctly. It seems that higher order numerical integration schemes do not yield any improvements in the results, as the results are governed by the stochastic nature of the SDEs. The Euler-Maruyama scheme is sufficient in this model with one spatial dimension and a variable time step can be used to ensure that the time step is small enough, but not too small. The anisotropy can be either calculated from the average of the pseudo-particles' pitch-cosine or by integrating the pitch-angle distribution (PAD). Both methods are comparable, although they disagree during the event onset and the former method is more accurate if a simple numerical integral is used for the latter. It was proposed, ad hoc, to cut off the derivative of the pitch-angle diffusion coefficient, which have infinite values around 90° pitch-angles (zero pitch-cosine), if it is too large. This approach seems valid, but the PAD should be investigated to make sure that the derivative is not cut off at too small or too large values, in which case a peak or dip would develop, respectively, around zero pitch-cosine.

The different characteristics of focused transport were also investigated. Focusing causes a coherent pulse of particles to propagate away from the injection point into regions of weaker magnetic fields. Pitch-angle scattering broadens the coherent pulse and causes an extended wake behind the pulse composed of particles closer to diffusive behaviour. Both the diffusion approximation and telegraph equation are comparable in the wake, but the diffusion approximation underestimates both the onset time and peak intensity of the event, while the telegraph equation has delayed onset times and unrealistically sharp propagation fronts. Both approximations also seem incapable of replicating the narrow pulse of anisotropic pitch-angle scattering. The effect of SW advection on SEP intensities is to quicken the onset time and increase the peak intensity. Energy losses, in contrast, have the effect of later onset times, lower peak intensities, and a faster decay phase. Neglecting these processes would therefore predict incorrect event onset times and peak intensities. The first particles to arrive at an observation point are high energy particles with small pitch-angles streaming away from the Sun. Lower energy particles arrive later with higher peak intensities, due to more low energy particles in the spectrum, and larger pitch-angles, since they experienced more pitch-angle scattering. The pitch-angle and energy distribution is shifted slightly to smaller pitch-angles and higher energies, respectively, in the observer's frame, compared to the SW frame, due to the Compton-Getting effect.

The similarities between the coherent pulse's PAD at the observation point and the stationary PAD, suggest that the pulse is in a quasi-stationary state set up by the balance between focusing and scattering. The global and time integrated energy distributions at the observation point are broadened and shifted to lower energies due to the energy losses, while retaining the initial spectral index. The temporal evolution of the energy distribution at the observation point would show a steepening of the spectrum due to energy losses. The fastest energy changes occur close to the Sun and the particles' position has the greatest influence on the energy loss

rate, even though the loss rate is dependent on the particles' energy and SW speed. For a mono-energetic injection of SEPs, both the energy distribution upon arrival at Earth and arrival times follow a Poisson distribution, which is narrower for high energy particles. The diffusion approximation of *Parker* [1965] for isotropic cosmic rays underestimates the average kinetic energy upon arrival, but gives a surprisingly good estimate for the average propagation times. An accurate approximation of the average energy was constructed from the terms in the FTPE, by weighing the transport terms with the stationary PAD at each position before integrating over position, while this approach unfortunately overestimates the average propagation time.

Avenues of further research related to this study are:

- Investigating the micro-physics of charged particles propagating in 2D and composite slab-2D turbulence.
- Exploring the FTPE's form in three spatial dimensions with transport perpendicular to the HMF.
- Extending the stochastic transport model to include three spatial dimensions in order to predict the correct radial, longitudinal, and latitudinal distribution of an SEP event.
- Investigating the solutions of different numerical integration schemes for the SDEs in three spatial dimensions.
- Using pitch-angle and perpendicular diffusion coefficients, with a plausibly correct pitch-angle dependence, which are described in terms of SW quantities in order to avoid calculating the scattering amplitude from a predefined mean free path, as its definition is altered in the presence of focusing.
- Using more accurate descriptions of the SW and HMF in the stochastic transport model.
- Including diffusive shock acceleration in the stochastic transport model in order to model gradual SEP events caused by CMEs.
- Investigating the scaling during parallel processing and improving the numerical efficiency of the stochastic transport model.

Appendix A

Analytical and Numerical Solutions of the Newton-Lorentz Equation

This appendix deals mainly with the numerical schemes used to solve the Newton-Lorentz equation. The appendix begins with the analytical solution of the Newton-Lorentz equation for a constant and uniform electric and magnetic field, as this will be used to test the numerical schemes, and a discussion on magnetic mirroring, as this is important in understanding the concept of magnetic focusing. The discussion of the numerical solution of the Newton-Lorentz equation will focus on the implementation of three methods, the *Boris* [1970], *Vay* [2008], and Runge-Kutta methods, as well as a discussion on how to calculate various quantities of interest from the results of these methods. In addition, the discussion also shows how to construct electric or magnetic field lines and how the different methods compare in terms of numerical stability and convergence.

Section A.2 was presented as a poster (`https://doi.org/10.6084/m9.figshare.5818119.v1`) at the 2017 Centre for High Performance Computing's (CHPC) National Conference in Pretoria, South Africa.

A.1 Some Analytical Solutions of the Newton-Lorentz Equation

A.1.1 A Constant and Uniform Electric and Magnetic Field

The most basic solution of the Newton-Lorentz equation (Eq. 3.1) is found when the particle is moving in a constant and uniform electric and magnetic field. Consider a charged particle with initial position $\vec{r}_0 = x_0\hat{x} + y_0\hat{y} + z_0\hat{z}$ and velocity $\vec{v}_0 = v_{0x}\hat{x} + v_{0y}\hat{y} + v_{0z}\hat{z}$ at time t_0 in a constant and uniform electric $\vec{E}_0$ and magnetic $\vec{B}_0$ field. The non-relativistic Newton-Lorentz equation can be solved analytically in this case for the position $\vec{r}(t) = x(t)\hat{x} + y(t)\hat{y} + z(t)\hat{z}$ and velocity $\vec{v}(t) = v_x(t)\hat{x} + v_y(t)\hat{y} + v_z(t)\hat{z}$ as a function of time (see problems 7.17 and 7.18 of *de Lange and Pierrus* [2010]). Integrating the non-relativistic Newton-Lorentz equation once

with respect to time, yields

$$\int_{t_0}^{t} \frac{d\vec{v}}{dt} dt = \int_{t_0}^{t} \frac{q}{m} \left(\vec{E}_0 + \frac{d\vec{r}}{dt} \times \vec{B}_0 \right) dt$$
$$\vec{v}(t) - \vec{v}_0 = \frac{q}{m} \left[(t - t_0)\vec{E}_0 + (\vec{r}(t) - \vec{r}_0) \times \vec{B}_0 \right],$$

and calculating the vector product, the components of the velocity can be written as

$$\frac{dx}{dt} = v_{0x} + \frac{q}{m} \left[(t - t_0)E_{0x} + (y - y_0)B_{0z} - (z - z_0)B_{0y} \right]$$
$$\frac{dy}{dt} = v_{0y} + \frac{q}{m} \left[(t - t_0)E_{0y} + (z - z_0)B_{0x} - (x - x_0)B_{0z} \right]$$
$$\frac{dz}{dt} = v_{0z} + \frac{q}{m} \left[(t - t_0)E_{0z} + (x - x_0)B_{0y} - (y - y_0)B_{0x} \right].$$

To simplify these equations, assume that the magnetic field is along the z-axis, such that $\vec{B}_0 = B_0\hat{z}$. The z-velocity component is then simply

$$v_z(t) = v_{0z} + \frac{q}{m}(t - t_0)E_{0z} \tag{A.1}$$

and integrating this once with respect to time yields the z-coordinate as

$$\int_{t_0}^{t} \frac{dz}{dt} dt = \int_{t_0}^{t} \left[v_{0z} + \frac{q}{m}(t - t_0)E_{0z} \right] dt$$
$$z(t) = z_0 + \left(v_{0z} - \frac{qt_0E_{0z}}{m} \right)(t - t_0) + \frac{qE_{0z}}{2m}(t - t_0)^2. \tag{A.2}$$

Let $\omega_c = |q|B_0/m$ be the cyclotron frequency (Eq. 3.3), then differentiate the x- and y-velocity components with respect to time, to give

$$\frac{d^2x}{dt^2} = \frac{q}{m} \left(E_{0x} + B_0 \frac{dy}{dt} \right) = \frac{q}{m} E_{0x} + \text{sign}(q)\omega_c \frac{dy}{dt}$$
$$\frac{d^2y}{dt^2} = \frac{q}{m} \left(E_{0y} - B_0 \frac{dx}{dt} \right) = \frac{q}{m} E_{0y} - \text{sign}(q)\omega_c \frac{dx}{dt},$$

and substitute the y- and x-velocity components, respectively, back to obtain the two uncoupled, second order differential equations

$$\frac{d^2x}{dt^2} + \omega_c^2 x = \frac{q}{m} E_{0x} + \text{sign}(q)\omega_c \left[v_{0y} + \frac{q}{m}(t - t_0)E_{0y} \right] + \omega_c^2 x_0$$
$$\frac{d^2y}{dt^2} + \omega_c^2 y = \frac{q}{m} E_{0y} - \text{sign}(q)\omega_c \left[v_{0x} + \frac{q}{m}(t - t_0)E_{0x} \right] + \omega_c^2 y_0,$$

where it should be remembered that $\text{sign}^2(q) = 1$. These second order differential equations describe a harmonic motion with the general solution $C_1 \cos(\omega_c t) + C_2 \sin(\omega_c t) + C_3 t + C_4$. The coefficients C_3 and C_4 can be found by adding the general solution, multiplied by ω_c^2, to the second time derivative of the general solution and comparing this with the second order differential equation. The coefficients C_1 and C_2 can then be found by applying the initial conditions to the general solution. Doing this, it can be found that the x- and y-coordinates are given by

$$x(t) = C_{1x} \cos(\omega_c t) + C_{2x} \sin(\omega_c t) + C_{3x} t + C_{4x} \tag{A.3}$$
$$y(t) = C_{1y} \cos(\omega_c t) + C_{2y} \sin(\omega_c t) + C_{3y} t + C_{4y}, \tag{A.4}$$

where

$$C_{1x} = \frac{x_0 - (v_{0x} - C_{3x})\tan(\omega_c t_0)/\omega_c - C_{3x}t_0 - C_{4x}}{\cos(\omega_c t_0) + \sin(\omega_c t_0)\tan(\omega_c t_0)} \tag{A.5a}$$

$$C_{2x} = \frac{v_{0x} - C_{3x}}{\omega_c \cos(\omega_c t_0)} + C_{1x}\tan(\omega_c t_0) \tag{A.5b}$$

$$C_{3x} = \frac{E_{0y}}{B_0} \tag{A.5c}$$

$$C_{4x} = x_0 - \frac{E_{0y}}{B_0}t_0 + \frac{\mathrm{sign}(q)}{\omega_c}\left(v_{0y} + \frac{E_{0x}}{B_0}\right) \tag{A.5d}$$

and

$$C_{1y} = \frac{y_0 - (v_{0y} - C_{3y})\tan(\omega_c t_0)/\omega_c - C_{3y}t_0 - C_{4y}}{\cos(\omega_c t_0) + \sin(\omega_c t_0)\tan(\omega_c t_0)} \tag{A.6a}$$

$$C_{2y} = \frac{v_{0y} - C_{3y}}{\omega_c \cos(\omega_c t_0)} + C_{1y}\tan(\omega_c t_0) \tag{A.6b}$$

$$C_{3y} = -\frac{E_{0x}}{B_0} \tag{A.6c}$$

$$C_{4y} = y_0 + \frac{E_{0x}}{B_0}t_0 - \frac{\mathrm{sign}(q)}{\omega_c}\left(v_{0x} + \frac{E_{0y}}{B_0}\right). \tag{A.6d}$$

Differentiating the x- and y-coordinates with respect to time, yields the x- and y-velocity components as

$$v_x(t) = -\omega_c C_{1x}\sin(\omega_c t) + \omega_c C_{2x}\cos(\omega_c t) + C_{3x} \tag{A.7}$$

$$v_y(t) = -\omega_c C_{1y}\sin(\omega_c t) + \omega_c C_{2y}\cos(\omega_c t) + C_{3y}. \tag{A.8}$$

From Eq. A.1 it can be seen that the particle will move at a constant speed along the magnetic field unless the electric field has a component along the magnetic field. The oscillating terms in Eqs. A.7 and A.8 are due to the gyration of the particle around the magnetic field and the C_3 term are due to the electric field drift if the electric field has a component perpendicular to the magnetic field.

Now consider the position of the guiding centre (GC) calculated from Eq. 3.5. The two vector products are $(\vec{B}_0 \times \vec{v})/B_0 = -v_y\hat{x} + v_x\hat{y}$ and $[\vec{B}_0 \times (\vec{E}_0 \times \vec{B}_0)]/B_0^2 = E_{0x}\hat{x} + E_{0y}\hat{y}$, such that the position of the GC will be

$$x_{\mathrm{gc}}(t) = x(t) + \frac{\mathrm{sign}(q)}{\omega_c}v_y(t) + \frac{\mathrm{sign}(q)}{\omega_c}\frac{E_{0x}}{B_0} \tag{A.9a}$$

$$y_{\mathrm{gc}}(t) = y(t) - \frac{\mathrm{sign}(q)}{\omega_c}v_x(t) + \frac{\mathrm{sign}(q)}{\omega_c}\frac{E_{0y}}{B_0} \tag{A.9b}$$

$$z_{\mathrm{gc}}(t) = z(t), \tag{A.9c}$$

with velocity components

$$v_x^{\mathrm{gc}}(t) = v_x(t) + \frac{\mathrm{sign}(q)}{\omega_c}\frac{dv_y}{dt} \tag{A.10a}$$

$$v_y^{\mathrm{gc}}(t) = v_y(t) - \frac{\mathrm{sign}(q)}{\omega_c}\frac{dv_x}{dt} \tag{A.10b}$$

$$v_z^{\mathrm{gc}}(t) = v_z(t). \tag{A.10c}$$

By substituting Eqs. A.3-A.4 and Eqs. A.7-A.8, the coefficients of the sine and cosine terms should be zero under most circumstances, since these terms are associated with the gyration of the particle around the GC. The electric field drift is then seen in the C_3 term in Eq. A.10a and Eq. A.10b as a constant velocity of the GC perpendicular to both the electric and magnetic field. From Eq. A.9c and Eq. A.10c it can be seen that the GC will move along the magnetic field in the same way as the particle would.

From this example it can be seen that it is cumbersome to solve the Newton-Lorentz equation analytically even for a relatively simple scenario. However, it is handy to have such an analytical solution to compare to numerical simulations. If the particle's speed does not change during its motion, as would be the case if there is no electric field, γ can be taken out of the time derivative of the relativistic Newton-Lorentz equation. The solution will be the same as for the non-relativistic case, only now with the cyclotron frequency given by $\omega_c = (|q|B_0)/(\gamma m)$ (see problem 15.15 of *de Lange and Pierrus* [2010]). According to electrodynamics, an accelerated charged particle radiates and in the case where the particle is undergoing gyrations, this is called *cyclotron* or *synchrotron radiation*, depending on whether the particle's motion is non-relativistic or relativistic, respectively. The power radiated is given by (see problem 10.16 of *Griffiths* [1999])

$$P = \frac{2q^4 B^2 \gamma^2 v^2 \sin^2 \alpha}{3m^2 c^3},$$

and the change in kinetic energy ΔK over a gyration, assuming the speed not to change during the gyration, is just the power multiplied by the period,

$$\Delta K \approx -P\frac{2\pi}{\omega_c} = -\frac{2q^4 B^2 \gamma^2 v^2 \sin^2 \alpha}{3m^2 c^3}\frac{2\pi\gamma m}{|q|B} = -\frac{2\pi |q^3| B \gamma^3 v^2}{3mc^3},$$

where an average was performed over all pitch-angles. For a $100\ \mathrm{keV}$ electron moving in the heliospheric magnetic field with strength $B \approx 15\ \mu\mathrm{T}$ at the Sun, its change in kinetic energy is $\Delta K_e \approx -2.5\times10^{-40}$ J $\approx -1.6\times10^{-21}$ eV and for a $300\ \mathrm{MeV}$ proton, this is $\Delta K_p \approx -2.5\times10^{-43}$ J $\approx -1.6\times10^{-24}$ eV. Notice for interest that in solar flares, the energy losses are only $\sim 10^3$ times larger for the strong magnetic field of $\sim 15\ \mathrm{mT}$ [*Benz*, 2008; *Shibata and Magara*, 2011] and that the synchrotron radiation observed in flares are mostly due to the high density of electrons. It is therefore justified to neglect the energy loss through cyclotron or synchrotron radiation, as long as the Lorentz factor is close to unity and the particle do not make a very large number of gyrations (also see problem 7.21 of *de Lange and Pierrus* [2010]).

A.1.2 Magnetic Mirroring

The analytical expression for the gradient drift is dependent on a vector product between the magnetic field and its gradient ($\vec{B} \times \vec{\nabla} B$) and does not describe the drift of the GC due to a gradient along the magnetic field. To illustrate the effect of this gradient, consider a magnetic field pointed primarily in the z-direction, with its magnitude also varying in the z-direction, and let it be axisymmetric, such that cylindrical coordinates can be used, with $B_\phi = 0$ and

$\partial B/\partial\phi = 0$. If the magnitude of the magnetic field changes along the z-direction, then the magnetic field will converge and diverge from the z-axis in the radial direction and hence, the magnetic field can be written as $\vec{B} = B_r\hat{r} + B_z\hat{z}$. The radial component can be obtained from the fact that the magnetic field should be divergence free,

$$0 = \vec{\nabla}\cdot\vec{B} = \frac{1}{r}\frac{\partial}{\partial r}[rB_r] + \frac{\partial B_z}{\partial z}.$$

If $\partial B_z/\partial z$ is given on the z-axis at $r = 0$ and does not vary much with r, then it can be approximated that

$$\int_0^r \frac{\partial}{\partial r}[rB_r]dr = -\int_0^r r\frac{\partial B_z}{\partial z}dr \qquad \Longrightarrow \qquad B_r \approx -\frac{1}{2}r\left[\frac{\partial B_z}{\partial z}\right]_{r=0},$$

where $B_r = 0$ at $r = 0$, as it should. The components of the non-relativistic Newton-Lorentz equation in the absence of an electric field are then

$$\frac{dv_r}{dt} = \frac{q}{m}v_\phi B_z, \qquad \frac{dv_\phi}{dt} = \frac{q}{m}\left(v_z B_r - v_r B_z\right), \qquad \text{and} \qquad \frac{dv_z}{dt} = -\frac{q}{m}v_\phi B_r.$$

The r-component and the second term of the ϕ-component simply give rise to the gyration of the particle around the magnetic field. The first term of the ϕ-component is zero on the axis, but non-zero away from the axis. This causes a drift in the radial direction, since it will change the ϕ-velocity component, which will in turn change the r-velocity component. This drift, however, merely causes the GC to follow the magnetic field lines as they converge and diverge from the z-axis. For simplicity, consider a particle with its GC on the z-axis, such that $v_r = 0$ and v_ϕ is constant during a gyration. Depending on the sign of the charge, it holds that $v_\phi = -\text{sign}(q)v_\perp$, while the particle gyrates at the Larmor radius (Eq. 3.4). Together with the expression for B_r, the z-component of the Lorentz-force can be written as

$$F_z \approx -q\left[-\text{sign}(q)v_\perp\right]\left[-\frac{1}{2}r_L\frac{\partial B_z}{\partial z}\right] = -\frac{mv_\perp^2}{2B}\frac{\partial B_z}{\partial z} = -M\frac{\partial B_z}{\partial z},$$

where

$$M = \frac{mv_\perp^2}{2B}. \tag{A.11}$$

Writing this in terms of the Larmor radius and cyclotron frequency, gives $M = mv_\perp^2/2B = q\omega_c v_\perp^2/2\omega_c^2 = (q\omega_c/2\pi)\pi r_L^2$. The $q\omega_c/2\pi$ and πr_L^2 factors can be interpreted as the current due to and the area enclosed by the gyrating charge, respectively. Hence, M is defined as the particle's *magnetic moment*. Since the magnetic field is primarily along the z-axis, the force parallel to the magnetic field can be written in general as

$$\vec{F}_\parallel = -M\frac{\partial B}{\partial\vec{s}} = -M\vec{\nabla}_\parallel B, \tag{A.12}$$

where $d\vec{s}$ is a line segment parallel to the magnetic field and $\vec{\nabla}_\parallel$ denotes the gradient along the magnetic field [*Chen*, 1984; *Choudhuri*, 1998].

To understand the effect of this parallel force on the particle, consider the parallel component of the Newton-Lorentz equation multiplied by $v_\parallel$ on the left and its equivalent ds/dt on the right:

$$mv_\parallel\frac{dv_\parallel}{dt} = -M\frac{\partial B}{\partial s}\frac{ds}{dt} \qquad \Longrightarrow \qquad \frac{d}{dt}\left[\frac{1}{2}mv_\parallel^2\right] = -M\frac{dB}{dt}.$$

Notice that since the magnetic field is time independent, dB/dt here is the variation of B as seen by the particle. The particle's energy must be conserved, therefore

$$0 = \frac{d}{dt}\left[\frac{1}{2}mv_{\parallel}^2 + \frac{1}{2}mv_{\perp}^2\right] = -M\frac{dB}{dt} + \frac{d}{dt}\left[MB\right] = B\frac{dM}{dt},$$

which shows that the magnetic moment is invariant or a constant, if the magnetic field does not change rapidly over a gyration. This implies that the particle's perpendicular speed must increase when entering a region with a stronger magnetic field, but the conservation of kinetic energy then requires that its parallel speed must decrease. Therefore, as the particle moves into regions with a stronger parallel magnetic field, its parallel speed will be transferred to perpendicular speed until the perpendicular speed is equal to its total speed. At this point the particle cannot penetrate further into regions with an even stronger magnetic field and its motion is reversed. This is called *magnetic mirroring*, but a particle is not always mirrored. A particle moving along the magnetic field, for instance, has no magnetic moment and does not experience the parallel force. Particles with pitch-angles smaller than a critical angle α_m can therefore be expected to penetrate a region with a maximum magnetic field B_m. If the perpendicular speed of the particle is initially $v_{\perp} = v\sin\alpha_m$ in a region of magnetic field strength B and since $v_{\perp} = v$ at the mirror point, by the conservation of energy, it follows then from the invariance of the magnetic moment that [*Chen*, 1984; *Choudhuri*, 1998]

$$\frac{v_{\perp}^2}{B} = \frac{v^2}{B_m} \qquad \Longrightarrow \qquad \sin^2\alpha_m = \frac{B}{B_m}. \tag{A.13}$$

A.2 Numerical Solutions of the Newton-Lorentz Equation

It becomes increasingly difficult to solve the Newton-Lorentz equation analytically for complicated electric and magnetic fields. In this section three numerical schemes for solving the Newton-Lorentz equation will be discussed. The methods of *Boris* [1970] and *Vay* [2008] will be discussed alongside a fourth-order Runge-Kutta scheme. This will be followed by a discussion on calculating various quantities of interest from the simulations results, as well as how to construct electric or magnetic field lines. Since these numerical schemes are used to simulate the motion of particles in turbulent electric and magnetic fields, these numerical schemes will focus rather on accuracy instead of computational speed, with which the section will be concluded. Since the vector product is easily calculated in Cartesian coordinates and due to the difficulty of finding a symmetry axis for a general magnetic field, the Newton-Lorentz equation is most easily solved in Cartesian coordinates. The numerical solution to the relativistic case will be presented for completeness, while the schemes are easily simplified to the non-relativistic case.

The Newton-Lorentz equation (Eq. 3.1) can be rewritten into the equations of motion

$$\frac{d\vec{r}(t)}{dt} = \vec{v}(t) \tag{A.14a}$$

$$m\frac{d\vec{u}(t)}{dt} = q\left[\vec{E}\left(\vec{r}(t);t\right) + \vec{v}(t) \times \vec{B}\left(\vec{r}(t);t\right)\right], \tag{A.14b}$$

where $\vec{u}(t) = \gamma(t)\vec{v}(t)$. The basis of any finite difference scheme is to calculate the position and velocities at later times from the initial position and velocity, with the time being discretely spaced by a time step Δt. The position can be calculated by a time-centred approximation of Eq. A.14a

$$\frac{\vec{r}_{n+1/2} - \vec{r}_{n-1/2}}{\Delta t} \approx \vec{v}_n \qquad \Longrightarrow \qquad \vec{r}_{n+1/2} = \vec{r}_{n-1/2} + \vec{v}_n \Delta t, \tag{A.15}$$

where a subscript n denotes that quantity at time $t_n = t_0 + n\Delta t$, with t_0 the initial time and $n = 0; 1; 2; \ldots$, and it should be remembered that

$$\vec{v}_n = \frac{\vec{u}_n}{\gamma_n}. \tag{A.16}$$

A.2.1 The Boris Method

Boris [1970] suggested a decoupling of the electric and magnetic field to solve Eq. A.14b, by first applying the electric field experienced during the first half time step, then applying the rotation of the velocity vector by the magnetic field, and lastly applying the electric field experienced during the second half time step:

$$\vec{u}_- = \vec{u}_{n-1} + \frac{q\Delta t}{2m}\vec{E}(\vec{r}_{n-1/2}; t_{n-1/2}) \tag{A.17a}$$

$$\vec{u}_{n-1/2} = \vec{u}_- + f_1\left[\vec{u}_- \times \vec{B}(\vec{r}_{n-1/2}; t_{n-1/2})\right] \tag{A.17b}$$

$$\vec{u}_+ = \vec{u}_- + f_2\left[\vec{u}_{n-1/2} \times \vec{B}(\vec{r}_{n-1/2}; t_{n-1/2})\right] \tag{A.17c}$$

$$\vec{u}_n = \vec{u}_+ + \frac{q\Delta t}{2m}\vec{E}(\vec{r}_{n-1/2}; t_{n-1/2}), \tag{A.17d}$$

with

$$f_1 = \frac{1}{B(\vec{r}_{n-1/2}; t_{n-1/2})} \tan\left[\frac{qB(\vec{r}_{n-1/2}; t_{n-1/2})\Delta t}{2m\gamma_-}\right] \tag{A.18a}$$

$$f_2 = \frac{2f_1}{1 + \left[f_1 B(\vec{r}_{n-1/2}; t_{n-1/2})\right]^2} \tag{A.18b}$$

and

$$\gamma_n = \sqrt{1 + \left(\frac{u_n}{c}\right)^2} \tag{A.19}$$

defined differently than the Lorentz-factor of Eq. 3.2.

The Boris method is a popular choice for particle-in-cell codes due to its simplicity and speed. It can be noted that to save time on evaluating the tangent function, Eqs. A.17b-A.17c and Eqs. A.18a-A.18b are normally simplified to

$$\vec{u}_{n-1/2} = \vec{u}_- + \vec{u}_- \times \vec{f}_1 \qquad \text{and} \qquad \vec{u}_+ = \vec{u}_- + \vec{u}_{n-1/2} \times \vec{f}_2 \tag{A.20}$$

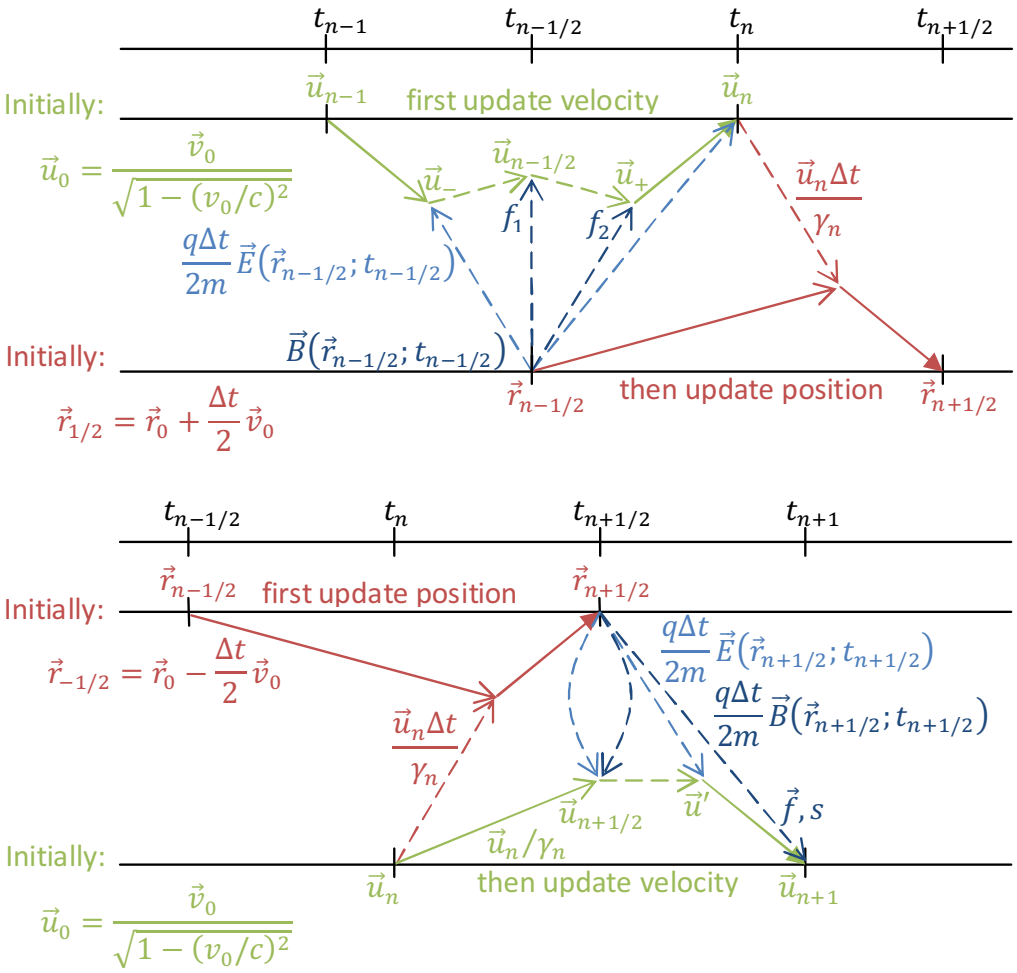

Figure A.1: Schematic representation of the method of *Boris* [1970] (*top*) and *Vay* [2008] (*bottom*). The spatial and velocity coordinates are illustrated in red and green, respectively, while calculations with the electric and magnetic fields are illustrated in light and dark blue, respectively.

and

$$\vec{f}_1 \approx \frac{q\Delta t}{2m\gamma_-}\vec{B}(\vec{r}_{n-1/2}; t_{n-1/2}) \quad \text{and} \quad \vec{f}_2 = \frac{2\vec{f}_1}{1+f_1^2}, \tag{A.21}$$

respectively, since $\tan\theta \approx \theta$ to first order in θ if $|\theta| \ll 1$, as should hold for a small time step [*Birdsall and Langdon*, 1991]. This algorithm is illustrated in the top panel of Fig. A.1, from which it can be seen that care should be taken with the initial conditions. Given the initial position $\vec{r}_0$ and velocity $\vec{v}_0$, then initially

$$\vec{u}_0 = \frac{\vec{v}_0}{\sqrt{1-(v_0/c)^2}}. \tag{A.22}$$

From Eq. A.15 and Eqs. A.17a-A.18b it can be seen that the position is needed at half time steps, so initially a half time step must be taken forward in the position using the initial velocity, $\vec{r}_{1/2} = \vec{r}_0 + \vec{v}_0\Delta t/2$. The velocity can then be updated and the new velocity can be used to subsequently update the position.

A.2.2 The Vay Method

Vay [2008] argues that the Boris method is invalid for the case where the mutual contributions of the electric and magnetic field cancel, such that the particle experience no Lorentz force, and that this causes the particle to have the wrong gyrophase when doing the calculations in different inertial frames. The Vay method does not decouple the electric and magnetic field when solving Eq. A.14b, but rather applies both the electric and magnetic field during the first half time step, while applying the electric field and a rotation of the velocity vector during the second half time step:

$$\vec{u}_{n+1/2} = \vec{u}_n + \frac{q\Delta t}{2m}\left[\vec{E}(\vec{r}_{n+1/2}; t_{n+1/2}) + \vec{v}_n \times \vec{B}(\vec{r}_{n+1/2}; t_{n+1/2})\right] \tag{A.23a}$$

$$\vec{u}' = \vec{u}_{n+1/2} + \frac{q\Delta t}{2m}\vec{E}(\vec{r}_{n+1/2}; t_{n+1/2}) \tag{A.23b}$$

$$\vec{u}_{n+1} = s\left[\vec{u}' + (\vec{u}' \cdot \vec{f})\vec{f} + \vec{u}' \times \vec{f}\right], \tag{A.23c}$$

where

$$\vec{b} = \frac{q\Delta t}{2m}\vec{B}(\vec{r}_{n+1/2}; t_{n+1/2}), \qquad \vec{f} = \frac{\vec{b}}{\gamma_{n+1}}, \qquad s = \frac{1}{1+f^2}, \tag{A.24}$$

and

$$\gamma_{n+1} = \sqrt{\frac{\sigma + \sqrt{\sigma^2 + 4(b^2 + u_*^2)}}{2}}, \qquad u_* = \frac{\vec{u}' \cdot \vec{b}}{c},$$
$$\gamma_* = \sqrt{1 + \left(\frac{u'}{c}\right)^2} \qquad \text{and} \qquad \sigma = \gamma_*^2 - b^2, \tag{A.25}$$

with $\vec{v}_n$ still given by Eq. A.16. This algorithm is illustrated in the bottom panel of Fig. A.1, from which it can be seen that care should also be taken with the initial conditions. Given the initial position $\vec{r}_0$ and velocity $\vec{v}_0$, then $\vec{u}_0$ is still given by Eq. A.22. Since $\vec{r}_{n+1/2}$ is needed to update the velocity, the position must be updated first, using Eq. A.15, before updating the velocity. Therefore, initially a half time step must be taken backward in the position using the initial velocity, $\vec{r}_{-1/2} = \vec{r}_0 - \vec{v}_0\Delta t/2$, after which the position can then be subsequently updated followed by the velocity.

A.2.3 The Runge-Kutta Method

A potential drawback of the Boris and Vay methods when calculating quantities of interest, as will be seen in the next paragraph, is the fact that the position and velocity are not calculated at the same time instant. It is also convenient to have a trusted numerical scheme to test other numerical schemes against if there is no analytical solution to compare the results with. The fourth-order Runge-Kutta scheme is widely used in solving systems of complex differential equations due to its high accuracy, but it is not as fast as the Boris and Vay methods due to both its accuracy and generality. The Runge-Kutta scheme for solving the set of differential

equations

$$\frac{d\vec{w}(t)}{dt} = \vec{f}(t; \vec{w}(t))$$

of the unknown functions $\vec{w}(t)$, with $\vec{w}(t) = [x(t)\ \ y(t)\ \ z(t)\ \ v_x(t)\ \ v_y(t)\ \ v_z(t)]^T$ in this case, is

$$\vec{w}_{n+1} = \vec{w}_n + \frac{\Delta t}{6}\left(\vec{k}_1 + 2\vec{k}_2 + 2\vec{k}_3 + \vec{k}_4\right), \tag{A.26}$$

with [*Press et al.*, 1997]

$$\vec{k}_1 = \vec{f}\,(t_n; \vec{w}_n) \tag{A.27a}$$

$$\vec{k}_2 = \vec{f}\left(t_{n+1/2}; \vec{w}_n + \vec{k}_1\frac{\Delta t}{2}\right) \tag{A.27b}$$

$$\vec{k}_3 = \vec{f}\left(t_{n+1/2}; \vec{w}_n + \vec{k}_2\frac{\Delta t}{2}\right) \tag{A.27c}$$

$$\vec{k}_4 = \vec{f}\left(t_{n+1}; \vec{w}_n + \vec{k}_3\Delta t\right). \tag{A.27d}$$

Notice that since the position and velocity are calculated at the same time instance, no special care has to be taken with the initial conditions.

Eq. A.14b should be rewritten in terms of the time derivative of only $\vec{v}$ and not $\vec{u}$, which can be done with a few mathematical manipulations of special relativity (see problems 12.36 and 12.40 of *Griffiths* [1999]). Remembering that $v^2 = \vec{v}\cdot\vec{v}$ and taking special care of the Lorentz factor's time derivative, the time derivative of the momenta can be written as

$$\frac{d}{dt}\left[\frac{m\vec{v}}{\sqrt{1-(v/c)^2}}\right] = \frac{m}{\sqrt{1-(v/c)^2}}\left[\frac{d\vec{v}}{dt} + \frac{\vec{v}}{c^2-v^2}\vec{v}\cdot\frac{d\vec{v}}{dt}\right]$$

so that Newton's second law reads

$$\frac{d\vec{v}}{dt} + \frac{\vec{v}}{c^2-v^2}\vec{v}\cdot\frac{d\vec{v}}{dt} = \frac{q}{\gamma m}\left[\vec{E} + \vec{v}\times\vec{B}\right]. \tag{A.28}$$

By taking the scalar product on both sides of this expression with the velocity, the magnetic force can be eliminated, since it is perpendicular to the velocity, and after solving for the second term on the left-hand-side of Eq. A.28, by multiplying again on both sides with $\vec{v}/c^2$, it can be shown that

$$\vec{v}\cdot\frac{d\vec{v}}{dt} + \frac{\vec{v}\cdot\vec{v}}{c^2-v^2}\vec{v}\cdot\frac{d\vec{v}}{dt} = \frac{q}{\gamma m}\vec{v}\cdot\vec{E} + 0$$

$$\frac{\vec{v}}{c^2-v^2}\vec{v}\cdot\frac{d\vec{v}}{dt} = \frac{q}{\gamma m c^2}(\vec{v}\cdot\vec{E})\vec{v}.$$

This can be thought of as the Lorentz factor's rate of change due to the electric field in terms of the velocity. Substituting this back into Eq. A.28, yields the desired form of Eq. A.14b

$$\frac{d\vec{v}}{dt} = \frac{q}{\gamma m}\left[\vec{E} + \vec{v}\times\vec{B} - \frac{\vec{v}\cdot\vec{E}}{c^2}\vec{v}\right]. \tag{A.29}$$

The functions $\vec{f}$ describing the differential equations in the relativistic case, are then

$$\vec{f}(t;\vec{w}(t)) = \begin{bmatrix} v_x(t) \\ v_y(t) \\ v_z(t) \\ \frac{q}{\gamma m}\left\{E_x(\vec{r};t) + v_y(t)B_z(\vec{r};t) - v_z(t)B_y(\vec{r};t) - [\vec{v}(t)\cdot\vec{E}(\vec{r};t)]v_x(t)/c^2\right\} \\ \frac{q}{\gamma m}\left\{E_y(\vec{r};t) + v_z(t)B_x(\vec{r};t) - v_x(t)B_z(\vec{r};t) - [\vec{v}(t)\cdot\vec{E}(\vec{r};t)]v_y(t)/c^2\right\} \\ \frac{q}{\gamma m}\left\{E_z(\vec{r};t) + v_x(t)B_y(\vec{r};t) - v_y(t)B_x(\vec{r};t) - [\vec{v}(t)\cdot\vec{E}(\vec{r};t)]v_z(t)/c^2\right\} \end{bmatrix}, \quad \text{(A.30)}$$

where γ is given here by Eq. 3.2.

A.2.4 Analysing the Numerical Results

If the particle's position, velocity, and Lorentz factor, as well as the electric and magnetic field experienced by the particle, are saved at each time instance, then the temporal evolution of any quantity of interest about the particle can be calculated. The position of the GC can be calculated by applying Eq. 3.5 and it is easiest to numerically differentiate the GC position to calculate its velocity (notice that its velocity can be calculated by adding all the various drifts, as is done by *Northrop* [1961] or *Burger et al.* [1985], but these expressions require the spatial and/or temporal derivatives of the electric and magnetic field, which is not generally available for arbitrary electric and magnetic fields). A time-centred derivative can be used

$$\vec{v}_n^{\,\mathrm{gc}} \approx \frac{\vec{r}_{n+1}^{\,\mathrm{gc}} - \vec{r}_{n-1}^{\,\mathrm{gc}}}{2\Delta t} \qquad \text{for } n = 1; 2; \ldots; N_t - 1, \quad \text{(A.31)}$$

with

$$\vec{v}_0^{\,\mathrm{gc}} \approx \frac{\vec{r}_1^{\,\mathrm{gc}} - \vec{r}_0^{\,\mathrm{gc}}}{\Delta t} \qquad \text{and} \qquad \vec{v}_{N_t}^{\,\mathrm{gc}} \approx \frac{\vec{r}_{N_t}^{\,\mathrm{gc}} - \vec{r}_{N_t-1}^{\,\mathrm{gc}}}{\Delta t},$$

where N_t is the number of integration steps and the latter expressions should be used for the initial and final velocity, respectively. Since the Boris (Vay) method initially takes a half time step forward (backward) in the position, $n \to n + 1/2$ ($n \to n - 1/2$) should then be used. If the time step is small, this approximation of the GC velocity gives a smooth and relatively accurate result. Notice however, that the GC velocity is somewhat unphysical since the GC is not a physical particle which is moving. The pitch-angle can be calculated using the first expression of Eq. 3.6, while the parallel and perpendicular speeds can be calculated with Eq. 3.7 and Eq. 3.8, respectively. The cyclotron frequency, Larmor radius, and magnetic moment can be calculated with Eq. 3.3, Eq. 3.4, and Eq. A.11, respectively.

Using the Runge-Kutta method presents no difficulty in calculating the various quantities, since the position and velocity are calculated at the same time instance, but the position and velocity are calculated with a difference of half a time step in the Boris and Vay methods. Since the electric and magnetic fields coincide with the positions and an approximation was already made for the initial position, it follows naturally that the velocity should be interpolated to also coincide with the position. If the time step is small, then a linear interpolation should be

sufficient. Since the Boris method initially takes a half time step forward in the position, the velocities can be interpolated by

$$\vec{v}_{n+1/2} \approx \frac{\vec{v}_n + \vec{v}_{n+1}}{2} \qquad \text{for } n = 0; 1; \ldots; N_t$$

and an additional velocity $\vec{v}_{N_t+1}$ should be calculated using $\vec{r}_{N_t+1/2}$, $\vec{v}_{N_t}$, $\vec{E}(\vec{r}_{N_t+1/2}; t_{N_t+1/2})$, and $\vec{B}(\vec{r}_{N_t+1/2}; t_{N_t+1/2})$ before calculating the new final velocity $\vec{v}_{N_t+1/2}$. Since the Vay method initially takes a half time step backward in the position, the velocities can be interpolated by

$$\vec{v}_{n-1/2} \approx \frac{\vec{v}_{n-1} + \vec{v}_n}{2} \qquad \text{for } n = 0; 2; \ldots; N_t$$

and an additional velocity $\vec{v}_{-1}$ should be calculated using $\vec{r}_{-1/2}$, $\vec{v}_0$, $\vec{E}(\vec{r}_{-1/2}; t_{-1/2})$, and $\vec{B}(\vec{r}_{-1/2}; t_{-1/2})$ before calculating the new initial velocity $\vec{v}_{-1/2}$. The additional velocity $\vec{v}_{-1}$ can be calculated using $-\Delta t$ since all three numerical methods can be used in both a time forward or backward sense. The Lorentz factor of these interpolated velocities should then be computed using Eq. 3.2.

A.2.5 Visualising Electric and Magnetic Field Lines

When working with electric or magnetic fields, it is sometimes necessary to visualise the field lines. To find a field line of any vectorfield $\vec{F} = F_x\hat{x} + F_y\hat{y} + F_z\hat{z}$, construct a line element $d\vec{s} = dx\,\hat{x} + dy\,\hat{y} + dz\,\hat{z}$ parallel to the field by setting the vector product between the vectorfield and line element equal to zero,

$$\vec{0} = d\vec{s} \times \vec{F} = (F_z dy - F_y dz)\hat{x} + (F_x dz - F_z dx)\hat{y} + (F_y dx - F_x dy)\hat{z}.$$

Assuming that the background or main part of the vectorfield is in the z-direction, then the two differential equations

$$\frac{dx}{dz} = \frac{F_x}{F_z} \qquad \text{and} \qquad \frac{dy}{dz} = \frac{F_y}{F_z}, \tag{A.32}$$

resulting from the x- and y-component of the vector product, can be solved (with the fourth-order Runge-Kutta method, for instance, if a numerical solution is needed) to parametrise the field line as a function of z.

A.2.6 Stability and Convergence of the Numerical Methods

The accuracy of numerical methods should be tested to ensure that the simulation results are reliable. Boris shows that his method has second order accuracy, while the Runge-Kutta method has fourth order accuracy [*Press et al.*, 1997]. No explicit calculation is given for the order of accuracy by Vay, but it might be expected to also have second order accuracy. The results of a second or fourth order method become four or sixteen times more accurate, respectively, when the time step is halved. Using a smaller time step will therefore yield more accurate results, but will also require longer execution times, and a balance must be found

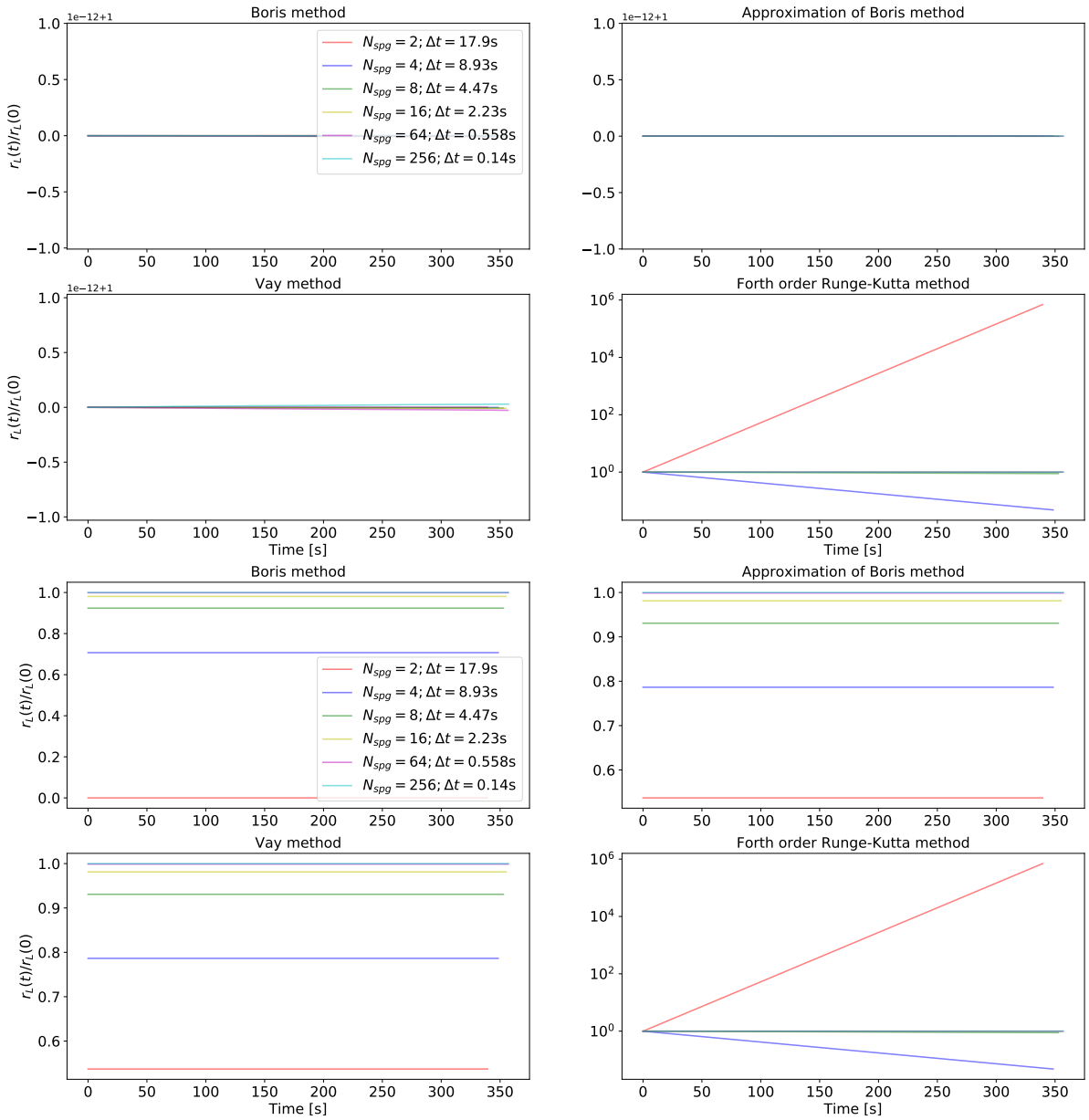

Figure A.2: Ratio of the Larmor radius $r_L(t)$ to the initial Larmor radius $r_L(0)$ as a function of time for the numerical methods discussed in the text for different numbers of steps per gyration N_{spg} using uninterpolated (*top four panels*) and interpolated (*bottom four panels*) velocities for the Boris and Vay method. Notice that the ratio for the Boris and Vay methods in the top four panels are one with deviations occurring at the computer's floating point accuracy.

between these two factors. The three methods were implemented in the Python programming language, making use of the `numpy` package, and in what follows, a non-relativistic electron was simulated in the absence of an electric field and in a constant and uniform magnetic field $\vec{B} = 1\hat{z}$ nT. The electron was initialized at time $t_0 = 0$ s with a velocity $\vec{v}_0 = (1\hat{x} + 0.1\hat{z})$ m $\cdot$ s^{-1} at the origin. The path of the electron was integrated for 10 gyrations ($N_t = \mathrm{int}(20\pi/\omega_c\Delta t)$) with all three the numerical methods, including the approximation of the Boris method, for $N_{\mathrm{spg}} = 2^i$ steps per gyration, with $i = 0; 1; \cdots; 20$, that is with time steps $\Delta t = 2\pi/\omega_c N_{\mathrm{spg}}$. For each of these simulations the Larmor radius, deviation between the final numerical and

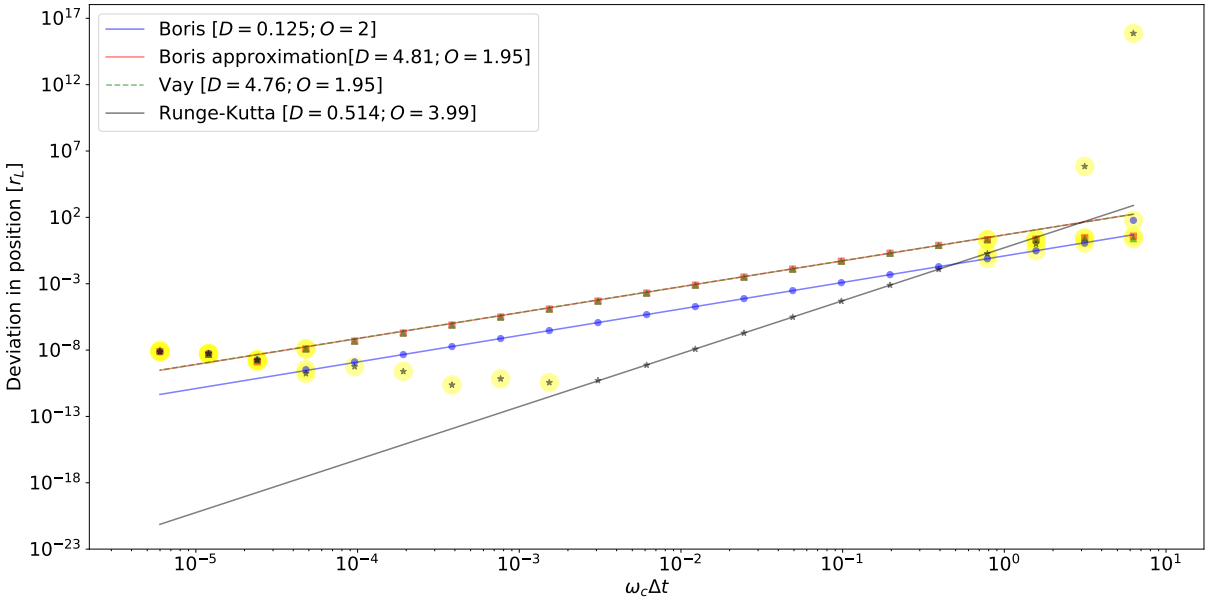

Figure A.3: Deviation between the numerical and analytical end position, in units of the initial Larmor radius, as a function of the time step multiplied by the cyclotron frequency, for the numerical methods discussed in the text. Indicated in the legend are the results of a function fit which give the order of accuracy O of the numerical method. The yellow encircled points were not used in fitting this function.

analytical position, and execution time were calculated and recorded.

The top four panels of Fig. A.2 show the ratio of the Larmor radius $r_L(t)$ to the initial Larmor radius $r_L(0)$ as a function of time for the four numerical methods for different numbers of steps per gyration. These are the Larmor radii calculated without the velocity interpolation for the Boris and Vay methods (as the particle moves in a constant and uniform magnetic field, the magnetic field calculated at the different time instances, will be the same). It can be seen that the Larmor radius stays constant with time, as might be expected from second order schemes, except for large time steps in the case of the Runge-Kutta method. The Boris and Vay methods are explicitly designed to integrate the Newton-Lorentz equation and aim to keep the Larmor radius constant for all time steps. There is a very small change in the Larmor radius for large (surprisingly small) time steps of the Boris (Vay) method. These changes are however not significant as they are on the computer's floating point accuracy. The Larmor radius stays generally constant independent of the time step and this implies that the numerical methods do not numerically change the particle's energy. The bottom four panels of Fig. A.2 show the ratio of the Larmor radii using interpolated velocities for the Boris and Vay methods. For large time steps the Larmor radius is smaller than the true Larmor radius, but rapidly converges to the correct value if the time step is made smaller. The smaller Larmor radii for large time steps are due to a partial cancellation of the velocity vectors when the interpolation is done. For the Boris method with two steps per gyration, it can be seen that the method gives the correct phase of the velocity, as the two velocity vectors cancel exactly when doing the interpolation to yield a zero Larmor radius (remembering that the Larmor radius is dependent on the perpendicular speed). The approximation of the Boris method and the Vay method behaves

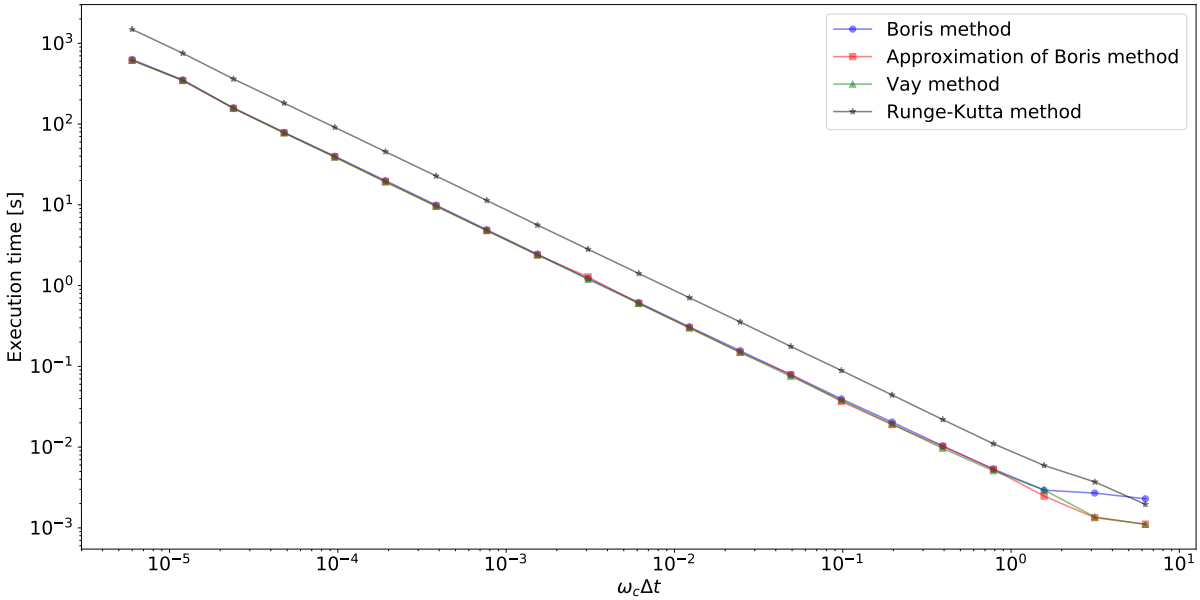

Figure A.4: Execution time as a function of the time step, multiplied by the cyclotron frequency, for the numerical methods discussed in the text.

similarly.

Fig. A.3 shows the deviation between the numerical and analytical (Eqs. A.2-A.4) end position in units of the Larmor radius, as a function of the time step multiplied by the cyclotron frequency, for the four numerical methods. By fitting the function

$$\frac{|\vec{r}_{N_t}^{\,\mathrm{anl}} - \vec{r}_{N_t}^{\,\mathrm{num}}|}{r_L(0)} = D\,(\omega_c \Delta t)^O \tag{A.33}$$

to these data points, the order of convergence O of the method can be calculated, where D is a constant [*Schutte*, 2016]. The function was fitted only through the data points lying in a straight line (the data points not encircled in yellow). The Boris and Vay method, including the approximation of the Boris method, has a second order accuracy and the Runge-Kutta method has a fourth order accuracy, as expected. Again, the approximation of the Boris method and the Vay method behaves in a similar manner, with the full Boris method having a slightly better accuracy and the Runge-Kutta method being the most accurate if at least sixteen steps are taken per gyration. The approximation of the Boris method, the Vay, and the Runge-Kutta methods do not converge with second or fourth order, respectively, if less than eight steps per gyration are taken. If more than $2^{17} = 131072$ steps are taken per gyration for the Boris and Vay methods, or more than $2^{11} = 2048$ steps for the Runge-Kutta method, the accuracy is limited by the computer's floating point accuracy and deviations in the solution are caused by round-off errors.

Fig. A.4 shows the execution time as a function of the time step, multiplied by the cyclotron frequency, for the four numerical methods. It can be seen that the Runge-Kutta method is slower than the other two methods, which is due to the generic way in which the method was implemented and the fact that the method evaluates the electric and magnetic fields four times

per integration step, where the other methods evaluate the fields only once per integration step. The additional execution time in evaluating the tangent function of the full Boris method is only evident at large time steps and the platform specific implementation thereof does not seem to add additional execution time. It might be suggested that sixteen steps per gyration give a reasonable balance between execution time and accuracy for the full Boris method, while this could also be used for the approximation of the Boris method and the Vay method at the cost of slightly less accurate results. By using eight steps per gyration, the Runge-Kutta method would yield an accuracy comparable to the full Boris method, with sixteen steps per gyration, at about the same computational cost.

Appendix B

Numerical Solutions of Stochastic Differential Equations and Specifics of the Stochastic Transport Model

In this appendix the numerical solution of stochastic differential equations will be presented together with some specifics of the stochastic transport model introduced in Chapter 5. The former section will discuss the advantage and stability conditions of numerical schemes to solve stochastic differential equations in general, as well as the concept of a variable time step for the numerical schemes. Three numerical schemes, of increasing accuracy, will be introduced to solve stochastic differential equations.

B.1 Numerical Solutions of Stochastic Differential Equations

As with deterministic differential equations, analytical solutions for stochastic differential equations (SDEs) are only available in a few scenarios (see e.g. *Gardiner* [1985] or *Kloeden and Platen* [1995]) and Eq. 5.3 is therefore usually integrated numerically. It was already mentioned that *Kloeden and Platen* [1995] discuss a wide range of numerical schemes for solving SDEs. Notice that there exists higher-order, implicit and explicit, predictor-corrector, and two-step schemes of various orders in addition to the three numerical schemes which will be presented here. The former schemes, however, become very involved, which could make them error prone in their implementation, and it is hoped that the relatively simple implementation of the schemes presented here would be less error prone while still being accurate. An application of these three schemes in solving the Parker transport equation (TPE) can be found in *Wawrzynczak et al.* [2015].

B.1.1 The Advantage and Conditions of Numerical Schemes

A major advantage of numerical schemes in solving SDEs, is that they are unconditionally stable, in stark contrast with finite difference (FD) schemes, where the stability of the numerical

solution is dependent on a specific relation between the temporal and spatial step sizes. The only practical conditions which apply to these numerical schemes, is that the drift and diffusion coefficients should be bounded, to ensure that the propagation of an initial error would not grow, and that the time step should be chosen appropriately, as it governs the size of structures which can be sampled. The unconditional stability also allows the numerical schemes to handle large gradients and the calculations to be done with more numerical dimensions than the FD schemes, which are usually restricted to four numerical dimensions. Caution, however, should be taken as this unconditional stability allows for the calculation of solutions which might not be physical [*Kloeden and Platen*, 1995; *Strauss and Effenberger*, 2017].

A *strong* solution of an SDE can be described as the exact solution of the SDE for a certain realization of initial conditions and the Wiener process. As the Wiener process is a stochastic process, each realization thereof would yield a strong solution differing from all the other solutions even for the same initial conditions. Although a strong solution could potentially illustrate some interesting behaviour of the underlying physical processes, a single strong solution is not of interest for measurable quantities as there are an infinite number of strong solutions all contributing to the behaviour of the measurable quantities. A *weak* solution of an SDE can be described as a solution of the SDE for an arbitrary Wiener process following the same probability distribution as the strong solution. This implies that a strong solution can be used as a weak solution (i.e. the average value of x can be calculated from the strong solution X), but a weak solution is not a strong solution. Since the exact realizations of the Wiener process are unknown, the drift and diffusion coefficients are specified together with the initial conditions and the Wiener process left unspecified. Making use of a single realization of the Wiener process then, or a collection of realizations, suitable averages, standard deviations, or other statistical quantities of interest can be calculated from these solutions [*Kloeden and Platen*, 1995; *Øksendal*, 2000].

The SDE must be solved a large number of times to get good statistics (see Section 5.1.2). As the solutions are independent of each other, the calculations can be performed in parallel, resulting in a significant reduction of computational time (see *Dunzlaff et al.* [2015] for an SDE implementation on graphical processing units in solving the Parker TPE). Since solutions are calculated at a number of discrete phase-space positions, not on a grid as in FD models, and appropriate averages or quantities can be calculated in place, the SDE scheme saves computational memory as no unnecessary information is stored. A strong solution can also be used to illustrate or visualise some of the behaviour of the underlying physical processes (see e.g. *Strauss and Effenberger* [2017] on how strong solutions can be used to illustrate the drift effects experienced by galactic cosmic rays).

Similar to deterministic differential equations, the existence and uniqueness of SDE solutions are dependent on certain conditions. The first condition is that the initial values should have a finite average and should be independent of the Wiener process. For simplicity in notation, the following conditions will be given here only for the one-dimensional case. If a solution of

the SDE is needed over the time interval $[t_0, T]$ and it is known that the solutions should fall in the realistic spatial interval $[x_1, x_2]$, then the following conditions apply:

- *Lipschitz condition:* there exist a real positive number K_L such that

$$|a(x;t) - a(y;t)| + |b(x;t) - b(y;t)| \leq K_L|x - y| \tag{B.1}$$

  for all x and $y \in [x_1, x_2]$ and all $t \in [t_0, T]$.

- *Spatial growth condition:* there exist a real positive number K_S for a given order δ such that

$$|a(x;t)|^\delta + |b(x;t)|^\delta \leq K_S^\delta(1 + |x|^\delta) \tag{B.2}$$

  for all $x \in [x_1, x_2]$ and all $t \in [t_0, T]$.

- *Temporal growth condition:* there exist a real positive number K_T such that

$$|a(x;t) - a(x;s)| + |b(x;t) - b(x;s)| \leq K_T(1 + |x|)\sqrt{|t - s|} \tag{B.3}$$

  for all $x \in [x_1, x_2]$ and all t and $s \in [t_0, T]$.

Furthermore, all the coefficients K_i, for $i = L; S; T$, must be independent of the time step used in the numerical solution. The Lipschitz condition can be interpreted as a smoothness condition and is important for higher order numerical schemes, which use the derivatives of the coefficients, to ensure that the derivatives do not become infinite. If the Lipschitz condition is satisfied, there exists a strong solution for the SDE which is unique for the given initial conditions and Wiener process. Even though the solution exists and is unique, it does not guarantee that the solution is well behaved globally: if the growth conditions are violated then the solution might become infinite in a finite time or an initial or numerical error could grow to large values [*Gardiner*, 1985; *Kloeden and Platen*, 1995].

B.1.2 The Euler-Maruyama Scheme

SDEs can be solved numerically in a similar time discrete way as deterministic differential equations, although care should be taken when considering the stochastic term. The natural extension of the Euler scheme to SDEs is given by the *Euler-Maruyama scheme*. If the random variables' initial value $\vec{Q}_0 = \vec{q}(t_0)$ at the initial time t_0 is specified, then its value at a later time can be calculated iteratively by

$$Q_i(t_k + \Delta t_k) \approx Q_i(t_k) + a_i(\vec{Q}(t_k); t_k)\Delta t_k + b_{ij}(\vec{Q}(t_k); t_k)\Delta W_j(t_k; \Delta t_k), \tag{B.4}$$

where Δt_k is the time step of the k^{th} iteration and $t_k = t_0 + k\Delta t_k$ for $k = 0; 1; 2; \ldots$, until a spatial or temporal integration boundary is reached. This scheme is equivalent to the Euler scheme if $b_{ij} = 0$ and is generally a good scheme for nearly constant or slowly varying coefficients. This scheme converges to the strong solution with order 0.5 if the coefficients satisfy

the Lipschitz condition and linear ($\delta = 1$) growth conditions. It has a first order weak convergence if the coefficients satisfy bounded growth conditions and are four times continuously differentiable [*Kloeden and Platen*, 1995].

By using the fact that $\mathcal{N}(0; dt)$ has the same distribution as $\mathcal{N}(0; 1)\sqrt{dt}$, the discrete version of the Wiener process can be written as

$$\Delta W_j(t_k; \Delta t_k) = \sqrt{\Delta t_k}\Lambda_j(t_k), \tag{B.5}$$

where $\Lambda_j(t_k) \sim \mathcal{N}(0; 1)$ are n independent, Gaussian distributed pseudo-random numbers (PRNs) [*Kloeden and Platen*, 1995]. The validity of using terms of order 1 and 0.5 in Δt together in an equation might seem questionable from a deterministic point of view, since $\sqrt{\Delta t} \gg \Delta t$ for small Δt, but the Normally distributed PRN with which $\sqrt{\Delta t}$ is multiplied, reduce its value to be of first order [*van Kampen*, 1992; *Lemons*, 2002]. Notice that since weak solutions only have to follow the same distribution as strong solutions, the discrete Wiener process can be replaced by other random variables $\Delta\hat{W}_j(t_k; \Delta t_k)$ with similar moment properties, such as a two-point distributed random variable with equal probabilities of obtaining $\Delta\hat{W}_j(t_k; \Delta t_k) = \pm\sqrt{\Delta t_k}$ [*Kloeden and Platen*, 1995]. To ensure true stochastic nature of the solution, it is important that the PRNs are independent of each other. In this work the 'high-level' Mersenne Twister pseudo-random number generator (PRNG) of *Matsumoto and Nishimura* [1998] will be used, due to its large cycling period of $2^{19937} - 1$ [*Brugger et al.*, 2014], to generate two uniformly distributed PRNs on the interval $[0, 1)$ which are then converted with the Box-Muller transformation [*Box and Muller*, 1958] to two Gaussian distributed PRNs (see *Press et al.* [1997] for an implementation).

B.1.3 The Milstein Scheme

Higher order schemes can be constructed by truncating the stochastic Taylor expansion of Eq. 5.3. The *Milstein scheme* solves the SDEs of Eq. 5.4 through

$$\begin{aligned} Q_i(t_k + \Delta t_k) \approx Q_i(t_k) + a_i(\vec{Q}(t_k); t_k)\Delta t_k + b_{ij}(\vec{Q}(t_k); t_k)\Delta W_j(t_k; \Delta t_k) \\ + \frac{1}{2} b_{ij}(\vec{Q}(t_k); t_k)\frac{\partial b_{ij}(\vec{Q}(t_k); t_k)}{\partial q_i}\left([\Delta W_j(t_k; \Delta t_k)]^2 - \Delta t_k\right), \end{aligned} \tag{B.6}$$

where all symbols are as defined in the Euler-Maruyama scheme. If $\partial b_{ij}/\partial q_i = 0$, then this would be the same as the Euler-Maruyama scheme. This scheme has a first order strong convergence if the coefficients are twice continuously differentiable and if $\vec{a}$, $\vec{a}'$, b_{ij}, b'_{ij}, and b''_{ij} all satisfy the Lipschitz and linear growth conditions, where

$$\vec{a}' = \frac{\partial a_i(\vec{q}; t)}{\partial q_i}, \qquad \vec{b}' = \frac{\partial b_{ij}(\vec{q}; t)}{\partial q_i}, \qquad \text{and} \qquad \vec{b}'' = \frac{\partial^2 b_{ij}(\vec{q}; t)}{\partial q_i^2}. \tag{B.7}$$

No explicit statement of the Milstein scheme for weak solutions is given by *Kloeden and Platen* [1995], but it might be expected that it would have an order 1.5 weak convergence.

B.1.4 The Order 1.5 Strong / 2 Weak Taylor Scheme

The previous numerical scheme is already lengthy and the current scheme reduces to a second order deterministic Taylor scheme if $b_{ij} = 0$ (notice that *Wawrzynczak et al.* [2015] refer to this scheme incorrectly as a Runge-Kutta scheme). Using the notation introduced in Eq. B.7, together with $\vec{a}'' = \partial^2 a_i(\vec{q};t)/\partial q_i^2$, and abbreviating $g = g(\vec{q}(t);t)$ for any function g, together with $\Delta W = \Delta W(t;\Delta t)$, the SDEs can be solved by

$$\begin{aligned} Q_i(t_k+\Delta t_k) \approx Q_i(t_k) &+ a_i\Delta t_k + b_{ij}\Delta W_j + \frac{1}{2}b_{ij}b'_{ij}\left[(\Delta W_j)^2 - \Delta t_k\right] + a'_i b_{ij}\Delta Z_j \\ &+ \frac{1}{2}(\Delta t_k)^2\left(a_i a'_i + \frac{1}{2}b_{ij}^2 a''_i\right) + \left(a_i b'_{ij} + \frac{1}{2}b_{ij}^2 b''_{ij}\right)(\Delta W_j \Delta t_k - \Delta Z_j) \\ &+ \frac{1}{2}b_{ij}\left[b_{ij}b''_{ij} + \left(b'_{ij}\right)^2\right]\left[\frac{1}{3}(\Delta W_j)^2 - \Delta t_k\right]\Delta W_j, \end{aligned} \tag{B.8}$$

where

$$\begin{aligned} \Delta W_j(t_k;\Delta t_k) &= \sqrt{\Delta t_k}\Lambda_j^{(1)}(t_k) \\ \Delta Z_j(t_k;\Delta t_k) &= \frac{1}{2}(\Delta t_k)^{3/2}\left[\Lambda_j^{(1)}(t_k) + \frac{1}{\sqrt{3}}\Lambda_j^{(2)}(t_k)\right] \end{aligned} \tag{B.9}$$

with $\Lambda_j^{(1)}(t_k)$ and $\Lambda_j^{(2)}(t_k)$ two, n independent, Gaussian distributed PRNs. Notice that the terms in the last line of Eq. B.8 are usually not included for weak solutions and that ΔW_j and ΔZ_j can again be simplified for weak solutions, with $\Delta\hat{Z}_j(t_k;\Delta t_k) = \Delta\hat{W}_j(t_k;\Delta t_k)\Delta t_k/2$ and a three-point distributed random variable with equal probabilities of $1/6$ to obtain $\Delta\hat{W}_j(t_k;\Delta t_k) = \pm\sqrt{3\Delta t_k}$ and a probability of $2/3$ to obtain $\Delta\hat{W}_j(t_k;\Delta t_k) = 0$. This scheme has a 1.5 strong order of convergence if the coefficients are three times continuously differentiable and if all the coefficients and their derivatives appearing in Eq. B.8 satisfy the Lipschitz and linear growth conditions. This scheme has a second order weak convergence if the coefficients are six times continuously differentiable with all these derivatives uniformly bounded and if all products of the diffusion coefficients satisfy a linear growth condition [*Kloeden and Platen*, 1995].

B.1.5 A Variable Time Step

In FD schemes the spatial grid is chosen such that it is some fraction of a characteristic length scale which should be resolved and the time step is then chosen appropriately according to some stability criteria. Although SDEs are stable, the time step should still be chosen sufficiently small in order to resolve the diffusive behaviour, which is normally slower than the deterministic behaviour. In a realistic system where the drift and diffusion coefficients are spatially non-uniform or time dependent, it might be difficult to choose an appropriate time step. In order to avoid a too large or too small time step, which would yield inaccurate results or long execution times, respectively, a variable time step can be used which changes at each iteration to sufficiently sample some length scale l_i of the general coordinates $\vec{Q}$, which is normally

chosen as a fraction of the characteristic length scales L_i ($l_i \ll L_i$). The first order moment of the SDEs (Eq. 5.4), is

$$\langle dQ_i(t) \rangle = \left\langle a_i(\vec{Q};t)dt + b_{ij}(\vec{Q};t)dW_j(t) \right\rangle = \left\langle a_i(\vec{Q};t)dt \right\rangle, \tag{B.10}$$

since the Wiener process is stochastic with zero mean, and the second order moment to first order in dt, is

$$\begin{aligned} \left\langle dQ_i^2(t) \right\rangle &= \left\langle a_i^2(\vec{Q};t)dt^2 + b_{ij}^2(\vec{Q};t)dW_j^2(t) + 2a_i(\vec{Q};t)b_{ij}(\vec{Q};t)dW_j(t)dt \right\rangle \\ &\approx \left\langle b_{ij}^2(\vec{Q};t)dt \right\rangle, \end{aligned} \tag{B.11}$$

since the Wiener process is stochastic with variance dt. These two moments imply that if a length scale l_i should be sampled, then the time step should be chosen such that [*Strauss and Effenberger*, 2017]

$$\Delta t_k(\vec{Q}(t_k);t_k) = \min\left\{ \frac{l_i(\vec{Q}(t_k);t_k)}{|a_i(\vec{Q}(t_k);t_k)|}; \frac{l_i^2(\vec{Q}(t_k);t_k)}{b_{ij}^2(\vec{Q}(t_k);t_k)} \right\}. \tag{B.12}$$

B.2 Specifics of the Stochastic Transport Model

This section discusses various quantities needed in the stochastic transport model presented in Chapter 5.

B.2.1 Derivatives of the Drift and Diffusion Coefficients

The derivatives of the coefficients needed in the Milstein and second order weak Taylor scheme are given here. Using Eq. 4.27, the derivative of a_s is

$$\frac{\partial a_s}{\partial s} = \left[1 - \left(\frac{\mu' v'}{c}\right)^2\right] v_{\mathrm{sw}} \cos\psi \frac{d}{dr}[\sec\psi], \tag{B.13}$$

where it should be remembered that the spatial and velocity/momentum components are independent of each other in the distribution function and that $dr/ds = \cos\psi$ from the geometry in Fig. 4.2. Using Eq. 5.24b, the derivative of a_p is

$$\frac{\partial a_p}{\partial p'} = -v_{\mathrm{sw}} \left[\frac{1-\mu'^2}{2L(s)} \sec\psi + \mu'^2 \cos\psi \frac{d}{dr}(\sec\psi)\right]. \tag{B.14}$$

Using Eq. 5.24c the derivatives of a_μ are

$$\begin{aligned} \frac{\partial a_\mu}{\partial \mu'} &= \frac{1-\mu'^2}{2L(s)} \left[1 - \left(\frac{v'}{c}\right)^2\right] v_{\mathrm{sw}} \sec\psi - \frac{\mu' v'}{L(s)} \left(1 + \mu' \frac{v_{\mathrm{sw}}}{v'} \sec\psi - \mu' \frac{v' v_{\mathrm{sw}}}{c^2} \sec\psi\right) \\ &\quad - \left(1 - 3\mu'^2\right) v_{\mathrm{sw}} \cos\psi \frac{d}{dr}(\sec\psi) + \frac{1}{2} \frac{\partial^2 D_{\mu'\mu'}}{\partial \mu'^2} \end{aligned} \tag{B.15a}$$

$$\begin{aligned} \frac{\partial^2 a_\mu}{\partial \mu'^2} &= 6\mu' v_{\mathrm{sw}} \cos\psi \frac{d}{dr}[\sec\psi] - \frac{2\mu'}{L(s)} \left[1 - \left(\frac{v'}{c}\right)^2\right] v_{\mathrm{sw}} \sec\psi + \frac{1}{2} \frac{\partial^3 D_{\mu'\mu'}}{\partial \mu'^3} \\ &\quad - \frac{v'}{L(s)} \left(1 + \mu' \frac{v_{\mathrm{sw}}}{v'} \sec\psi - \mu' \frac{v' v_{\mathrm{sw}}}{c^2} \sec\psi\right), \end{aligned} \tag{B.15b}$$

and the derivatives of b_μ from Eq. 5.27 are

$$\frac{\partial b_{\mu\mu}}{\partial \mu'} = \frac{1}{2\sqrt{D_{\mu'\mu'}}} \frac{\partial D_{\mu'\mu'}}{\partial \mu'} \tag{B.16a}$$

$$\frac{\partial^2 b_{\mu\mu}}{\partial \mu'^2} = \frac{1}{2\sqrt{D_{\mu'\mu'}}} \frac{\partial^2 D_{\mu'\mu'}}{\partial \mu'^2} - \frac{1}{4\sqrt{D^3_{\mu'\mu'}}} \left(\frac{\partial D_{\mu'\mu'}}{\partial \mu'} \right)^2 . \tag{B.16b}$$

B.2.2 Derivatives of the Pitch-angle Diffusion Coefficient

The derivatives of the pitch-angle diffusion coefficient (PADC) of *Beeck and Wibberenz* [1986] (Eq. 5.32) are

$$\frac{\partial D^{\mathrm{BW}}_{\mu'\mu'}}{\partial \mu'} = D_0 \left[\mathrm{sign}(\mu')(q-1)|\mu'|^{q-2} \left(1-\mu'^2\right) - 2\mu'(|\mu'|^{q-1} + H) \right] \tag{B.17a}$$

$$\frac{\partial^2 D^{\mathrm{BW}}_{\mu'\mu'}}{\partial \mu'^2} = D_0 \left[(q-1)(q-2)|\mu'|^{q-3} \left(1-\mu'^2\right) - 4(q-1)|\mu'|^{q-1} - 2(|\mu'|^{q-1} + H) \right] \tag{B.17b}$$

$$\frac{\partial^3 D^{\mathrm{BW}}_{\mu'\mu'}}{\partial \mu'^3} = D_0 \mathrm{sign}(\mu')(q-1) \left[(q-2)(q-3)|\mu'|^{q-4} \left(1-\mu'^2\right) - 6(q-1)|\mu'|^{q-2} \right] , \tag{B.17c}$$

and the derivatives of the effective PADC of *Ruffolo* [1995] (Eq. 5.33) are

$$\frac{\partial D^{\mathrm{eff}}_{\mu'\mu'}}{\partial \mu'} = -D_0 \mu' \Delta\mu' \coth(I) - D_0 \frac{1-\mu'^2}{2} \Delta\mu' \mathrm{cosech}^2(I) I', \tag{B.18a}$$

$$\begin{aligned} \frac{\partial^2 D^{\mathrm{eff}}_{\mu'\mu'}}{\partial \mu'^2} = & -D_0 \Delta\mu' \coth(I) + D_0 \Delta\mu' \mathrm{cosech}^2(I) I' \left[2\mu' + \left(1-\mu'^2\right) \coth(I) I' \right] \\ & - D_0 \frac{1-\mu'^2}{2} \Delta\mu' \mathrm{cosech}^2(I) I'' \end{aligned} \tag{B.18b}$$

$$\begin{aligned} \frac{\partial^3 D^{\mathrm{eff}}_{\mu'\mu'}}{\partial \mu'^3} = & \, 3D_0 \Delta\mu' \mathrm{cosech}^2(I) I' - 6D_0 \mu' \Delta\mu' \mathrm{cosech}^2(I) \coth(I) I'^2 \\ & - D_0 \left(1-\mu'^2\right) \Delta\mu' \mathrm{cosech}^2(I) I'^3 \left[\mathrm{cosech}^2(I) + 2\coth^2(I) \right] + 3D_0 \mu' \Delta\mu' \mathrm{cosech}^2(I) I'' \\ & + 3D_0 \left(1-\mu'^2\right) \Delta\mu' \mathrm{cosech}^2(I) \coth(I) I' I'' - D_0 \frac{1-\mu'^2}{2} \Delta\mu' \mathrm{cosech}^2(I) I''', \end{aligned} \tag{B.18c}$$

where

$$I' = \frac{|\mu' + \Delta\mu'/2|^{1-q} - |\mu' - \Delta\mu'/2|^{1-q}}{2} \tag{B.19a}$$

$$I'' = (1-q) \frac{\mathrm{sign}(\mu' + \Delta\mu'/2)|\mu' + \Delta\mu'/2|^{-q} - \mathrm{sign}(\mu' - \Delta\mu'/2)|\mu' - \Delta\mu'/2|^{-q}}{2} \tag{B.19b}$$

$$I''' = (1-q)q \frac{|\mu' - \Delta\mu'/2|^{-q-1} - |\mu' + \Delta\mu'/2|^{-q-1}}{2}. \tag{B.19c}$$

The derivatives of the PADC of *Agueda et al.* [2008] (Eq. 5.35) are

$$\frac{\partial D^{\epsilon}_{\mu'\mu'}}{\partial \mu'} = D_{0\epsilon} \left[\mathrm{sign}(\mu') \frac{1-\mu'^2}{(1+|\mu'|)^2} - 2\mu' \left(\frac{|\mu'|}{1+|\mu'|} + \epsilon \right) \right] \tag{B.20a}$$

$$\frac{\partial^2 D^{\epsilon}_{\mu'\mu'}}{\partial \mu'^2} = -2D_{0\epsilon}(\epsilon + 1) \tag{B.20b}$$

$$\frac{\partial^3 D^{\epsilon}_{\mu'\mu'}}{\partial \mu'^3} = 0, \tag{B.20c}$$

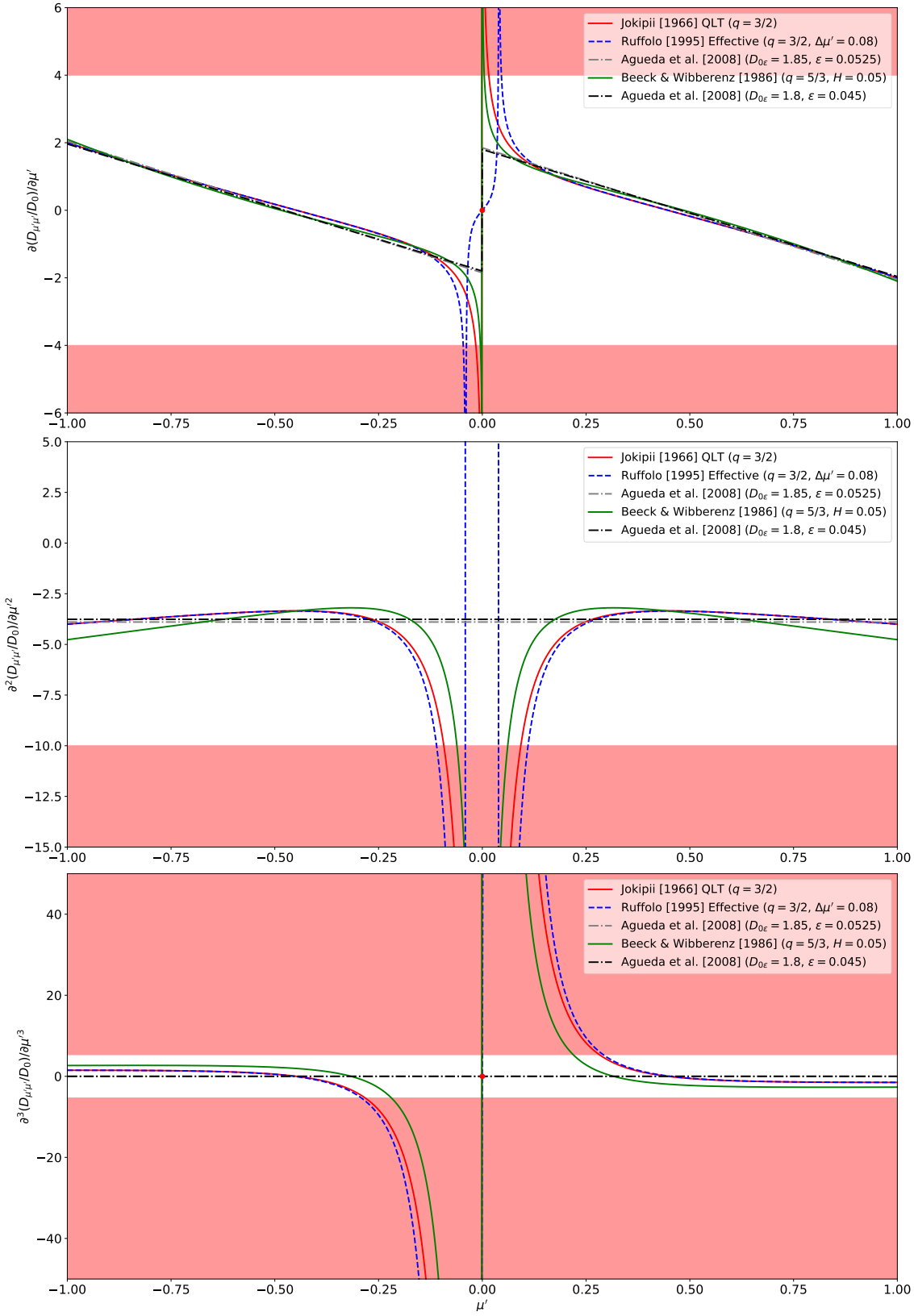

Figure B.1: First (*top*), second (*middle*), and third (*bottom*) derivatives of the pitch-angle diffusion coefficients shown Fig. 5.3. The red bands indicate the limits of Eq. B.21 for $\delta_c = 2$, while the red dot indicates the condition of Eq. B.22.

where the first derivative is zero for $\mu' = 0$ if $\mathrm{sign}(0) = 0$.

The derivatives of the different PADC are shown in Fig. B.1. With all of the terms from the following paragraph it can be verified that most of the drift coefficients together with their derivatives are well behaved so that they are Lipschitz continuous and linearly bounded in growth. The only exception is a_μ and its derivatives and the derivatives of $b_{\mu\mu}$ in μ', due to the infinite values assumed by the derivatives of the PADC around $\mu' = 0$. This should be kept in mind as it might cause very large changes in the pitch-cosine when it is close to zero. Hence, the derivatives of the PADC around $\mu' = 0$ will be limited to

$$\begin{aligned}
\delta_c \left.\frac{\partial D_{\mu'\mu'}}{\partial \mu'}\right|_{\mu'=+1} &\leq \frac{\partial D_{\mu'\mu'}}{\partial \mu'} \leq \delta_c \left.\frac{\partial D_{\mu'\mu'}}{\partial \mu'}\right|_{\mu'=-1} \\
\delta_c \left.\frac{\partial^2 D_{\mu'\mu'}}{\partial \mu'^2}\right|_{\mu'=1} &\leq \frac{\partial^2 D_{\mu'\mu'}}{\partial \mu'^2} \leq -\delta_c \left.\frac{\partial^2 D_{\mu'\mu'}}{\partial \mu'^2}\right|_{\mu'=1}, \\
\delta_c \left.\frac{\partial^3 D_{\mu'\mu'}}{\partial \mu'^3}\right|_{\mu'=+1} &\leq \frac{\partial^3 D_{\mu'\mu'}}{\partial \mu'^3} \leq \delta_c \left.\frac{\partial^3 D_{\mu'\mu'}}{\partial \mu'^3}\right|_{\mu'=-1}
\end{aligned} \tag{B.21}$$

for some number δ_c, with the additional condition that

$$\left.\frac{\partial D_{\mu'\mu'}}{\partial \mu'}\right|_{\mu'=0} = \left.\frac{\partial^3 D_{\mu'\mu'}}{\partial \mu'^3}\right|_{\mu'=0} = 0, \tag{B.22}$$

in order to prevent the pitch-cosine from changing so much that it would jump too far out of its allowed range of $[-1, 1]$. These limits are approximately indicated by the red bands in Fig. B.1 and are checked each time the PADC and its derivatives are calculated to set their values to the limiting values if the values are outside the allowed range. Another possible way to handle the derivatives, which will avoid both a plateau and very large values around zero pitch-cosine, would be to use a linear extrapolation of the derivative from the cut-off point. This method, however, will not be investigated.

B.2.3 Arc and Focusing Length

The arc length of the *Parker* [1958] magnetic field line can be calculated as

$$s = \int \sqrt{1 + \tan^2 \psi} dr.$$

From the definition of the spiral angle (Eq. 2.4) it follows that $dr = v_{\mathrm{sw}} d(\tan\psi)/(\omega_\odot \sin\theta)$ and with this change in variables, the previous equation can be integrated analytically to give

$$s = \frac{v_{\mathrm{sw}}}{2\omega_\odot \sin\theta} \left[\tan\psi \sec\psi + \mathrm{arcsinh}\left(\tan\psi\right)\right], \tag{B.23}$$

where the integration constant must be zero to satisfy the condition $s(r_\odot) = 0$ [*Lampa*, 2011]. The spiral angle and arc length are shown in the top left and right panels of Fig. B.2, respectively, and has values of $\psi = 44.71°$ and $s = 1.139$ AU, respectively, at Earth. As s is calculated in the SDEs, this equation must be solved numerically (e.g. with Newton's root finding

method; see *Press et al.* [1997] for an implementation) to find $\psi(s)$ which must be used in evaluating the various drift coefficients. Using the magnitude of the Parker heliospheric magnetic field (HMF; Eq. 2.7), the focusing length can be calculated as

$$\frac{1}{L(s)} = \left(\frac{2}{r_\odot + v_{\rm sw} \tan\psi/\omega_\odot \sin\theta} - \frac{\omega_\odot \sin\theta}{v_{\rm sw}} \sin\psi \cos\psi \right) \cos\psi, \tag{B.24}$$

where Eq. 2.4 was used to eliminate r. The focusing length is shown in the middle left panel of Fig. B.2 and it can be seen that focusing will have the largest effect within the first ~ 1 AU from the Sun as the focusing length at Earth is ~ 0.936 AU. The 'divergence of the co-rotating solar wind (SW) along the magnetic field line' is given by

$$v_{\rm sw} \cos\psi \frac{d}{dr}[\sec\psi] = \omega_\odot \sin\theta \sin\psi \cos\psi. \tag{B.25}$$

The co-rotating SW speed (Eq. 4.15) and this co-rotating SW divergence is illustrated in the middle right and bottom panels of Fig. B.2, respectively. At Earth, $v_{\rm sw}^c = 562.8\ {\rm km \cdot s^{-1}}$, which clearly illustrates that the co-rotating SW may only be used within ~ 2 AU. From the radial profile of the SW divergence, it can be seen that the inverse Fermi effect and differential advection will have the largest effect between $\sim 0.5 - 2$ AU.

B.2.4 Initial and Boundary Conditions

In the code, quantities are measured in units which are best suited to the problem, that is astronomical unit (AU) for distance, hour (h) for time, and mega-electron volt (MeV) for energy. Either a mono-energetic (p_0') delta function or spectrum (power law distributed between p_l and p_u with spectral index $\gamma < 0$) injection of N pseudo-particles with isotropically distributed (uniformly distributed between -1 and 1) pitch-cosines at the source surface ($r_s = 0.05$ AU $\implies s_0 \approx 0.05$ AU) will be used

$$I_0(s; p'; \mu'; t) = N\delta(t/t_0 - 1)\delta(s/s_0 - 1)(\mu' \sim \mathcal{U}[-1,1]) \begin{cases} \delta(p'/p_0' - 1) \\ \frac{\gamma+1}{p_u^{\gamma+1} - p_l^{\gamma+1}} p'^{\gamma} \end{cases}. \tag{B.26}$$

The integration will be performed for a time T much longer than the arrival time of the first particles at the observation point. An absorbing boundary condition will be assumed at a position $s_o \approx 5$ AU much larger than the observation point,

$$f(s_o; p'; \mu'; t) = 0, \tag{B.27}$$

since the probability for the particles to return to the observation point from this point will be small (due to both focusing and the outwards advection by the SW), and a reflecting inner boundary condition at $s_i = 0$ AU will be assumed, such that

$$\left.\frac{\partial f}{\partial s}\right|_{s=s_i} = 0. \tag{B.28}$$

The latter boundary condition is motivated by the mirroring effect of the HMF and in addition to the spatial inner reflecting boundary condition, it should be remembered that the mirroring

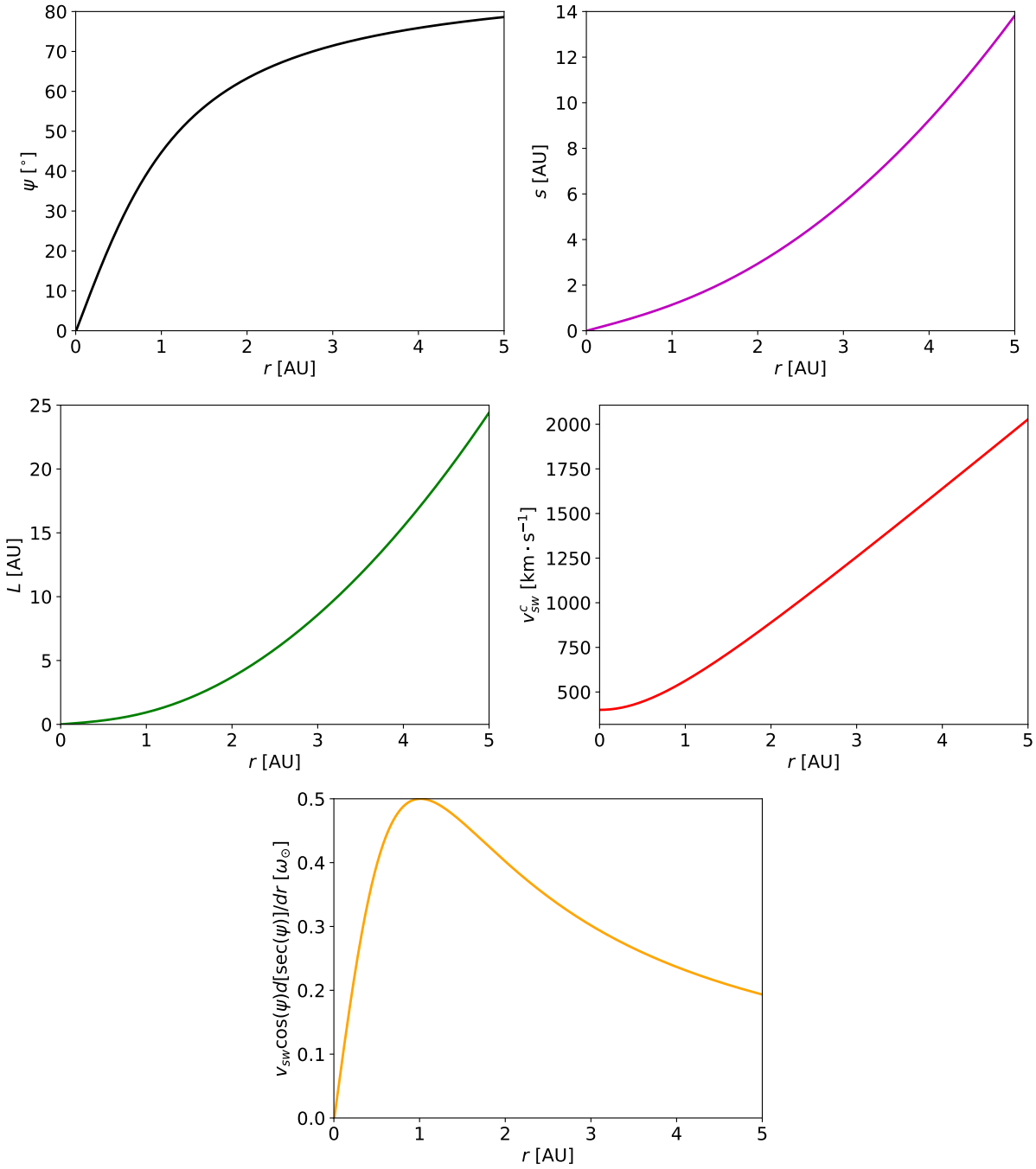

Figure B.2: Spiral angle (Eq. 2.4; *top left*), magnetic field line length (Eq. B.23; *top right*), and focusing length (Eq. B.24; *middle left*) of the *Parker* [1958] heliospheric magnetic field in the equatorial plane ($\sin\theta = 1$) as a function of heliocentric radius. Co-rotating solar wind speed (Eq. 4.15; *middle right*) used by *Ruffolo* [1995] and 'divergence of the co-rotating solar wind along the heliospheric magnetic field line' (Eq. B.25; *bottom*) in the equatorial plane as a function of heliocentric radius.

is accompanied by the reversal of the particles' motion, such that

$$S < s_i \; : \begin{cases} S & \longrightarrow & 2s_i - S \\ M & \longrightarrow & |M| \end{cases} . \tag{B.29}$$

Since μ' must be in the range $[-1, 1]$, a von Neumann boundary condition must also be applied such that

$$\left.\frac{\partial f}{\partial \mu'}\right|_{\mu'=\pm 1} = 0, \tag{B.30}$$

which implies

$$\begin{aligned} M < -1 \ &: \ M \ \longrightarrow \ -2 - M \\ M > 1 \ \ &: \ M \ \longrightarrow \ 2 - M, \end{aligned} \tag{B.31}$$

and this is motivated by the periodic behaviour of the pitch-angle itself.

B.2.5 Constructing the Distribution Function

Green's theorem (Eq. 5.11) for focused transport in one spatial dimension, is

$$\begin{aligned} f(s; p'; \mu'; t) = \int_{t_0}^{t} \int_{s_i}^{s_o} \int_{p'}^{p'_0} \int_{-1}^{1} \big[& f_b^{\mathrm{in}}(\tilde{p}'; \tilde{\mu}'; \tilde{t}) \delta(\tilde{s}/s_i - 1) + f_b^{\mathrm{out}}(\tilde{p}'; \tilde{\mu}'; \tilde{t}) \delta(\tilde{s}/s_o - 1) \\ & + f_i(\tilde{s}; \tilde{p}'; \tilde{\mu}') \delta(\tilde{t}/t_0 - 1) \big] \, G(s; p'; \mu'; t | \tilde{s}; \tilde{p}'; \tilde{\mu}'; \tilde{t}) d\tilde{\mu}' d\tilde{p}' d\tilde{s} d\tilde{t}, \end{aligned} \tag{B.32}$$

where f_b^{in} and f_b^{out} are the inner and outer boundary conditions, respectively. Consider the simplified initial condition $f_i(s; p'; \mu') = f_0 \delta(s/s_0 - 1) \delta(p'/p'_0 - 1) \delta(\mu'/\mu'_0 - 1)$, where f_0 is an arbitrary phase-space density, and an absorbing outer boundary $f_b^{\mathrm{out}}(p'; \mu'; t) = 0$. It is difficult to write down an explicit form for the inner reflective boundary condition, because particles can reach the boundary with any momentum and any pitch-cosine at any time with the particles' pitch-angle being reversed, with $f_b^{\mathrm{in}} G$ being approximately constant at s_i according to Eq. 5.14. Eq. B.32 can therefore be written as

$$f(s; p'; \mu'; t) = f_0 G(s; p'; \mu'; t | s_0; p'_0; \mu'_0; t_0) \equiv f_0 G(s; p'; \mu'; t) \approx \frac{f_0 N(m; i; l; k)}{N \Delta s_m \Delta p'_i \Delta \mu'_l \Delta t_k}, \tag{B.33}$$

where $N(m; i; l; k)$ is the number of pseudo-particles in the m^{th} spatial, i^{th} momentum, l^{th} pitch-cosine, and k^{th} temporal bin with midpoint $(s_m; p'_i; \mu'_l; t_k)$ and volume $\Delta s_m \Delta p'_i \Delta \mu'_l \Delta t_k$. Notice that $G(s; p'; \mu'; t)$ represents the probability distribution to reach the phase-space point $(s; p'; \mu'; t)$ from the injection point s_0 at initial time t_0 with initial momentum p'_0 and initial pitch-cosine μ'_0 regardless of the phase-space trajectory taken to reach this point.

B.2.6 Observable Quantities

In discrete form, together with Eq. B.33, the omni-directional intensity (Eq. 5.38) is

$$F(s_m; p'_i; t_k) \approx \frac{1}{2} \sum_l \frac{f_0 N(m; i; l; k)}{N \Delta s_m \Delta p'_i \Delta t_k}, \tag{B.34}$$

and at an observation point s_{obs} it is therefore proportional to the number of pseudo-particles N_k within a spatial bin around the observation point and the k^{th} temporal bin,

$$F(s_{\mathrm{obs}}; t_k) \propto \left. \frac{N_k}{N \Delta t_k} \right|_{\substack{S \in s_{\mathrm{obs}} \pm v' \Delta t/2 \\ t \in t_k \pm \Delta t_k/2}} . \tag{B.35}$$

In order to count all pseudo-particles passing the observation point, the minimum spatial bin size should be equal to the distance $v'\Delta t$ a particle would travel in the integration time step Δt and is therefore energy dependent [*Kocharov et al.*, 1998]. Notice that the omni-directional intensity can be constructed for either all particles, regardless of their momentum/pitch-angle, in which another integration should be done over momentum in the former case, or for specific momentum/pitch-angle bins, in which only a partial integration should be done over pitch-angle in the latter case.

The pitch-angle distribution (PAD; Eq. 5.40) in discrete form is

$$\mathrm{PAD}(s_m; p'_i; \mu'_l; t_k) = \frac{f_0 N(m;i;l;k)}{N\Delta s_m \Delta p'_i \Delta \mu'_l \Delta t_k} \div \sum_l \frac{f_0 N(m;i;l;k)}{N\Delta s_m \Delta p'_i \Delta t_k} = \frac{N(m;i;l;k)}{N(m;i;k)\Delta \mu'_l}, \tag{B.36}$$

where $N(m;i;k) = \sum_l N(m;i;l;k)$, and at the observation point

$$\mathrm{PAD}(s_{\mathrm{obs}}; p'_i; \mu'_l; t_k) \propto \left. \frac{N_{lk}}{N_k \Delta \mu'_l} \right|_{\substack{M \in \mu'_l \pm \Delta\mu'_l/2 \\ S \in s_{\mathrm{obs}} \pm v'\Delta t/2 \\ t \in t_k \pm \Delta t_k/2}}, \tag{B.37}$$

where N_{lk} is the number of pseudo-particles in the spatial bin around the observation point, the l^{th} pitch-cosine bin, and the k^{th} temporal bin. Similar to the PAD, the energy distribution (Eq. 5.41) in discrete form is

$$\mathrm{ED}(s_m; K'_i; \mu'_l; t_k) = \frac{f_0 N(m;i;l;k)}{N\Delta s_m \Delta K'_i \Delta \mu' \Delta t_k} \div \sum_i \frac{f_0 N(m;i;l;k)}{N\Delta s_m \Delta \mu'_l \Delta t_k} = \frac{N(m;i;l;k)}{N(m;l;k)\Delta K'}, \tag{B.38}$$

or at the observation point

$$\mathrm{ED}(s_{\mathrm{obs}}; K'_i; \mu'_l; t_k) \propto \left. \frac{N_{ik}}{N_k \Delta K'_i} \right|_{\substack{K' \in K'_i \pm \Delta K'_i/2 \\ S \in s_{\mathrm{obs}} \pm v'\Delta t/2 \\ t \in t_k \pm \Delta t_k/2}}, \tag{B.39}$$

where N_{ik} is the number of pseudo-particles in the spatial bin around the observation point, the i^{th} kinetic energy bin, with midpoint K'_i and bin size $\Delta K'_i$, and the k^{th} temporal bin. It should be kept in mind that these pitch-angle and momentum distributions are in the SW frame and that the quantities should be transformed to the observer's frame using Eq. 4.7 and Eq. 4.8 before binning if the distributions are to be calculated in the observer's frame.

The anisotropy (Eq. 5.39) can be calculated from the average pitch-cosine value of the pseudo-particles passing the observation point,

$$A^{\langle M \rangle}(s_{\mathrm{obs}}; t_k) \approx \frac{3}{N_k} \sum_{j=1}^{N_k} M_{jk} \pm 3 \left. \sqrt{\frac{1}{N_k} \left[\frac{1}{N_k} \sum_{j=1}^{N_k} M_{jk}^2 - \left(\frac{1}{N_k} \sum_{j=1}^{N_k} M_{jk} \right)^2 \right]} \right|_{\substack{S \in s_{\mathrm{obs}} \pm v'\Delta t/2 \\ t \in t_k \pm \Delta t_k/2}}, \tag{B.40}$$

where M_{jk} is the pitch-cosine of the j^{th} pseudo-particle in the spatial bin around the observation point in the k^{th} temporal bin. The estimate for the uncertainty in this calculated anisotropy is just the standard deviation of the pseudo-particles' pitch-cosines from the average value. A

second method to calculate the anisotropy follows from the definition of the anisotropy as an integration over the PAD

$$A^{\langle \mathrm{PAD} \rangle}(s_{\mathrm{obs}}; p'_i; t_k) \approx 3 \sum_l \mu'_l \frac{f_0 N(m;i;l;k)}{N \Delta s_m \Delta p'_i \Delta t_k} \div \sum_l \frac{f_0 N(m;i;l;k)}{N \Delta s_m \Delta p'_i \Delta t_k}$$
$$= 3 \sum_l \mu'_l \frac{N(m;i;l;k)}{N(m;i;k)\Delta \mu'_l} \Delta \mu'_l = 3 \sum_l \mu'_l \mathrm{PAD}(s_{\mathrm{obs}}; p'_i; \mu'_l; t_k) \Delta \mu'_l. \quad \text{(B.41)}$$

Some estimate can be made about the error of the discussed quantities. Consider, in general, the sum S_k of a number of samples N_k, with weights W_j, out of a total of N samples being counted in a bin k. During the binning procedure there are two sources of uncertainty: the first is due to the number of samples falling into each bin (the more samples, the better the statistics) and the second is the typical weights of the samples falling in the bin (the standard deviation of the weights in the sample). Now, it holds that

$$S_k = \sum_{j=1}^{N_k} W_j = \sum_{j=1}^{N} W_j$$

because the definition of the weights can be modified such that it is zero if the samples do not fall in the bin (N weights are being counted of which only N_k are non-zero). The uncertainty on S_k is then simply the standard deviation,

$$\delta S_k = \sqrt{\sum_{j=1}^{N} W_j^2 - \frac{1}{N} \left(\sum_{j=1}^{N} W_j \right)^2}, \quad \text{(B.42)}$$

of the weights [*Bohm and Zech*, 2010; *Turner*, 2017]. In the simple case where all the weights are unity, this reduce to [*Turner*, 2017]

$$\delta S_k \approx \sqrt{N_k \left(1 - \frac{N_k}{N} \right)}, \quad \text{(B.43)}$$

and the error of SDEs normally has a $1/\sqrt{N}$ dependence [*Milstein et al.*, 2004]. When calculating the anisotropy from the PAD (Eq. B.41), the uncertainty is just the sum of the uncertainties of the bins being added, multiplied by a constant, such that

$$\delta A^{\langle \mathrm{PAD} \rangle}(s_{\mathrm{obs}}; t_k) = 3 \sqrt{\sum_l \left[\mu'_l \delta \mathrm{PAD}(s_{\mathrm{obs}}; p'_i; \mu'_l; t_k) \Delta \mu'_l \right]^2}, \quad \text{(B.44)}$$

where $\delta \mathrm{PAD}(s_{\mathrm{obs}}; p'_i; \mu'_l; t_k)$ is the uncertainty of the l^{th} PAD bin.

Bibliography

Agueda, N., and R. Vainio, On the parametrization of the energetic-particle pitch-angle diffusion coefficient, *Journal of Space Weather and Space Climate*, *3*, A10, 2013.

Agueda, N., R. Vainio, D. Lario, and B. Sanahuja, Injection and interplanetary transport of near-relativistic electrons: modeling the impulsive event on 2000 May 1, *Astrophysical Journal*, *675*, 1601–1613, 2008.

Balogh, A., and L. J. Lanzerotti, The heliosphere: its origin and exploration, in *The heliosphere through the solar activity cycle*, edited by A. Balogh, L. J. Lanzerotti, and S. T. Suess, pp. 1–20, Springer-Praxis, Chichester, UK, 2008.

Balogh, A., L. J. Lanzerotti, and S. T. Suess (Eds.), *The heliosphere through the solar activity cycle*, Springer-Praxis, Chichester, UK, 2008.

Beeck, J., and G. Wibberenz, Pitch angle distributions of solar energetic particles and the local scattering properties of the interplanetary medium, *Astrophysical Journal*, *311*, 437–450, 1986.

Benz, A. O., Flare observations, *Living Reviews in Solar Physics*, *5*, 2008.

Bieber, J. W., W. Wanner, and W. H. Matthaeus, Dominant two-dimensional solar wind turbulence with implications for cosmic ray transport, *Journal of Geophysical Research*, *101*(A2), 2511–2522, 1996.

Biermann, L., Solar corpuscular radiation and the interplanetary gas, *The Observatory*, *77*, 109–110, 1957.

Birdsall, C. K., and A. B. Langdon, *Plasma physics via computer simulation*, Adam Hilger, Bristol, UK, 1991.

Bohm, G., and G. Zech, *Introduction to statistics and data analysis for physicists*, Verlag Deutsches Elektronen-Synchrotron, 2010.

Boris, J. P., Relativistic plasma simulation: optimization of a hybrid code, in *Proceedings of the Forth Conference on the Numerical Simulations of Plasmas*, edited by J. P. Boris and R. A. Shanny, 4, pp. 3–67, Naval Research Laboratory, Washington, D.C., 1970.

Box, G. E. P., and M. E. Muller, A note on the generation of normal deviates, *Annals of Mathematical Statistics*, *21*, 455–456, 1958.

Brown, F. R. S., A brief account of microscopical observations made in the months of June, July, and August 1827, on the particles contained in the pollen of plants; and on the general existence of active molecules in organic and inorganic bodies, *Philosophical Magazine and Annals of Philosophy Series 2*, *4*(21), 121–173, 1828.

Brugger, C., S. Weithoffer, C. de Schryver, U. Wasenmüller, and N. Wehn, On parallel random number generation for accelerating simulations of communication systems, *Advances in Radio Science*, *12*, 75–81, 2014.

Burger, R. A., H. Moraal, and G. M. Webb, Drift theory of charged particles in electric and magnetic fields, *Astrophysics and Space Science*, *116*, 107–129, 1985.

Cane, H. V., R. E. McGuire, and T. T. von Rosenvinge, Two classes of solar energetic particle events associated with impulsive and long-duration soft X-ray flares, *Astrophysical Journal*, *301*, 448–459, 1986.

Carrington, R. C., Description of a singular appearance seen in the Sun on September 1, 1859, *Monthly Notices of the Royal Astronomical Society*, *20*, 13–15, 1859.

Chandrasekhar, S., Stochastic problems in physics and astronomy, *Reviews of Modern Physics*, *15*(1), 1–89, 1943.

Chen, F. F., *Introduction to plasma physics and controlled fusion*, vol. 1, second ed., Plenum, NY, 1984.

Chen, P. F., Coronal mass ejections: models and their observational basis, *Living Reviews in Solar Physics*, *8*, 2011.

Chhiber, R., A. Usmanov, W. H. Matthaeus, and M. L. Goldstein, Contextual predictions for Parker Solar Probe I: critical surfaces and regions, *arXiv:1806.00570*, 2018.

Choudhuri, A. R., *The physics of fluids and plasmas: an introduction for astrophysicists*, Cambridge University Press, UK, 1998.

Cliver, E. W., S. W. Kahler, and P. S. McIntosh, Solar proton flares with weak impulsive phases, *Astrophysical Journal*, *264*, 699–707, 1983.

Cook, W. R., E. C. Stone, and R. E. Vogt, Elemental composition of solar energetic particles, *Astrophysical Journal*, *279*, 827–838, 1984.

Cranmer, S. R., S. E. Gibson, and P. Riley, Origins of the ambient solar wind: implications for space weather, *Space Science Reviews*, *212*, 1345–1384, 2017.

Dalla, S., M. S. Marsh, J. Kelley, and T. Laitinen, Solar energetic particle drifts in the Parker spiral, *Journal of Geophysical Research: Space Science*, *118*, 5979–5985, 2013.

de Lange, O. L., and J. Pierrus, *Solved problems in classical mechanics: analytical and numerical solutions with comments*, Oxford University Press, Oxford, UK, 2010.

Dosch, A., and G. P. Zank, *Transport processes in space physics and astrophysics: problems and solutions*, Springer, Heidelberg, Germany, 2016.

Dresing, N., The longitudinal distribution of energetic particles in the inner heliosphere: multi-point observations with STEREO, Ph.D. thesis, Christian-Albrechts-Universität, Kiel, 2014.

Dresing, N., R. Gómez-Herrero, A. Klassen, B. Heber, Y. Kartavykh, and W. Dröge, The large longitudinal spread of solar energetic particles during the 17 January 2010 solar event, *Solar Physics*, *281*, 281–300, 2012.

Dröge, W., Particle scattering by magnetic fields, *Space Science Reviews*, *93*, 121–151, 2000.

Dröge, W., Y. Y. Kartavykh, B. Klecker, and G. A. Kovaltsov, Anisotropic three-dimensional focused transport of solar energetic particles in the inner heliosphere, *Astrophysical Journal*, *709*, 912–919, 2010.

Dröge, W., Y. Y. Kartavykh, N. Dresing, B. Heber, and A. Klassen, Wide longitudinal distribution of interplanetary electrons following the 7 February 2010 solar event: observations and transport modeling, *Journal of Geophysical Research: Space Physics*, *119*, 6074–6094, 2014.

Dunzlaff, P., R. D. Strauss, and M. S. Potgieter, Solving Parker's transport equation with stochastic differential equations on GPUs, *Computer Physics Communications*, *192*, 156–165, 2015.

Earl, J. A., Analytical description of charged particle transport along arbitrary guiding field configurations, *Astrophysical Journal*, *251*, 739–755, 1981.

Earl, J. A., The effect of convection upon charged particle transport in random magnetic fields, *Astrophysical Journal*, *278*, 825–840, 1984.

Effenberger, F., and Y. E. Litvinenko, The diffusion approximation versus the telegraph equation for modeling solar energetic particle transport with adiabatic focusing I: isotropic pitch-angle scattering, *Astrophysical Journal*, *783*, 15–21, 2014.

Einstein, A., über die von der molekular-kinetischen Theorie der Wärme geforderte Bewegung von in ruhenden Flüssigkeiten suspendierten Teilchen, *Annalen der Physik*, *17*, 549–560, 1905.

Engelbrecht, N. E., and R. A. Burger, An ab initio model for cosmic-ray modulation, *Astrophysical Journal*, *772*, 46–58, 2013.

Engelbrecht, N. E., and R. D. Strauss, A tractable estimate for the dissipation range onset wavenumber throughout the heliosphere, *Astrophysical Journal*, *856*, 159–175, 2018.

Fermi, E., On the origin of the cosmic radiation, *Physical Review*, *75*(8), 1169–1174, 1949.

Fick, A., Ueber Diffusion, *Annalen der Physik*, *170*(1), 59–86, 1855.

Fisk, L. A., and W. I. Axford, Anisotropies of solar cosmic rays, *Solar Physics*, *7*, 486–498, 1969.

Forbush, S. E., Three unusual cosmic-ray increases possibly due to charged particles from the Sun, *Physical Review Letters*, *70*, 71, 1946.

Forman, M. A., The Compton-Getting effect for cosmic-ray particles and photons and the Lorentz-invariance of distribution functions, *Planetary and Space Science*, *18*, 25–31, 1970.

Gardiner, C. W., *Handbook of stochastic methods: for physics, chemistry and the natural sciences*, second ed., Springer-Verlag, Berlin, 1985.

Gleeson, L. J., and W. I. Axford, The Compton-Getting effect, *Astrophysics and Space Science*, *2*, 431–437, 1968.

Goldstein, M. L., D. A. Roberts, and W. H. Matthaeus, Magnetohydrodynamic turbulence in the solar wind, *Annual Reviews of Astronomy and Astrophysics*, *33*, 283–325, 1995.

Gosling, J. T., The solar flare myth, *Journal of Geophysical Research*, *98*, 18,937–18,949, 1993.

Griffiths, D. J., *Introduction to electrodynamics*, third ed., Prentice Hall, Upper Saddle River, New Jersey, 1999.

Hasselmann, K., and G. Wibberenz, A note on the parallel diffusion coefficient, *Astrophysical Journal*, *162*, 1049–1051, 1970.

Hathaway, D. H., The solar cycle, *Living Reviews in Solar Physics*, *7*, 2010.

Hathaway, D. H., and S. T. Suess, Solar cycle 23, in *The heliosphere through the solar activity cycle*, edited by A. Balogh, L. J. Lanzerotti, and S. T. Suess, pp. 21–39, Springer-Praxis, Chichester, UK, 2008.

Heita, P., Numerical investigation of solar energetic particle transport between the Sun, Earth, and Mars, Master's thesis, North-West University, South Africa, 2018.

Hodgson, R., On a curious appearance seen in the Sun, *Monthly Notices of the Royal Astronomical Society*, *20*, 15–16, 1859.

Hsieh, K. C., and J. A. Simpson, The relative abundances and energy spectra of ^{3}He and ^{4}He from solar flares, *Astrophysical Journal*, *162*, L191–L196, 1970.

Hudson, H. S., Solar flares: no "myth", *EOS, Transactions American Geophysical Union*, *76*(41), 1995.

Iroshnikov, P. S., Turbulence of a conducting fluid in a strong magnetic field, *Soviet Astronomy - AJ*, *7*(40), 566–571, 1964.

Jokipii, J. R., Cosmic-ray propagation I: charged particles in a random magnetic field, *Astrophysical Journal*, *146*(2), 480–487, 1966.

Jokipii, J. R., The rate of separation of magnetic lines of force in a random magnetic field, *Astrophysical Journal*, *183*, 1029–1036, 1973.

Jokipii, J. R., and E. H. Levy, Effects of particle drifts on the solar modulation of galactic cosmic rays, *Astrophysical Journal*, *213*, L85–L88, 1977.

Jokipii, J. R., and E. H. Levy, Electric field effect on galactic cosmic rays at the heliosphere boundary, in *International Cosmic Ray Conference*, vol. 3, pp. 52–56, 1979.

Jones, F. C., J. R. Jokipii, and M. G. Baring, Charged-particle motion in electromagnetic fields having at least one ignorable spatial coordinate, *Astrophysical Journal*, *509*, 238–243, 1998.

Karimabadi, H., et al., Coherent structures, intermittent turbulence, and dissipation in high-temperature plasmas, *Physics of Plasmas*, *20*, 012,303, 2013.

Kennel, C. F., and H. E. Petschek, Limit on stably trapped particle fluxes, *Journal of Geophysical Research*, *71*(1), 1–28, 1966.

Klein, K. L., and S. Dalla, Acceleration and propagation of solar energetic particles, *Space Science Reviews*, *212*, 1107–1136, 2017.

Kloeden, P. E., and E. Platen, *Numerical solution of stochastic differential equations*, second ed., Springer-Verlag, Berlin, 1995.

Kocharov, L., R. Vainio, G. A. Kovaltsov, and J. Torsti, Adiabatic deceleration of solar energetic particles as deduced from Monte Carlo simulations of interplanetary transport, *Solar Physics*, *182*, 195–215, 1998.

Kolmogorov, A. N., The local structure of turbulence in incompressible viscous fluids for very large Reynolds numbers *(in Russian)*, *Akademiia Nauk SSSR Doklady*, *30*, 301–305, 1941.

Kolmogorov, A. N., The local structure of turbulence in incompressible viscous fluids for very large Reynolds numbers, *Proceedings of the Royal Society of London*, *434*, 9–13, 1991.

Kontar, E. P., and H. A. S. Reid, Onsets and spectra of impulsive solar energetic electron events observed near the Earth, *Astrophysical Journal*, *695*, L140–L144, 2009.

Kopp, Q., I. Büsching, R. D. Strauss, and M. S. Potgieter, A stochastic differential equation code for multidimensional Fokker-Planck type problems, *Computer Physics Communications*, *183*, 530–542, 2012.

Kraichnan, R. H., Inertial-range spectrum of hydromagnetic turbulence, *Physics of Fluids*, *8*, 1385–1387, 1965.

Krüger, A., *Introduction to solar radio astronomy and radio physics*, D. Reidel Publishing, Dordrecht, Holland, 1979.

Laitinen, T., and S. Dalla, Energetic particle transport across the mean magnetic field: before diffusion, *Astrophysical Journal*, *834*, 127–136, 2017.

Laitinen, T., S. Dalla, and M. S. Marsh, Energetic particle cross-field propagation early in a solar event, *Astrophysical Journal Letters*, *773*, L29–L34, 2013.

Lampa, F., Modeling solar cosmic ray transport within the ecliptic plane, Ph.D. thesis, Universität Osnabrück, 2011.

Langevin, P., Sur la théorie du mouvement Brownien, *Comptes rendus Académie des Sciences*, *146*, 530–533, 1908.

Langner, U. W., Effects of termination shock acceleration on cosmic rays in the heliosphere, Ph.D. thesis, Potchefstroomse Universiteit vir Christelike Hoër Onderwys, South Africa, 2004.

Lario, D., A. Aran, R. Gómez-Herrero, N. Dresing, B. Heber, G. C. Ho, R. B. Decker, and E. C. Roelof, Longitudinal and radial dependence of solar energetic particle peak intensities: STEREO, ACE, SOHO, GOES, and MESSENGER observations, *Astrophysical Journal*, *767*, 41–59, 2013.

Lasuik, J., J. D. Fiege, and A. Shalchi, Numerical analysis of the Fokker-Planck equation with adiabatic focusing: realistic pitch-angle scattering, *Advances in Space Research*, *59*, 722–735, 2017.

Lemons, D. S., *An introduction to stochastic processes in physics*, Johns Hopkins University, Baltimore, USA, 2002.

Lemons, D. S., and A. Gythiel, Paul Langevin's 1908 paper "on the theory of Brownian motion" ["sur la théorie du mouvement Brownien," C. R. Acad. Sci. (Paris) 146, 530–533 (1908)], *American Journal of Physics*, *65*, 1079–1081, 1997.

Liboff, R. L., *Kinetic theory: classical, quantum, and relativistic descriptions*, Prentice Hall, New Jersey, USA, 1990.

Litvinenko, Y. E., and P. L. Noble, A numerical study of diffusive cosmic-ray transport with adiabatic focusing, *Astrophysical Journal*, *765*, 31–38, 2013.

Litvinenko, Y. E., and R. Schlickeiser, The telegraph equation for cosmic-ray transport with weak adiabatic focusing, *Astronomy & Astrophysics*, *554*, A59, 2013.

Luhmann, J. G., A quasi-linear kinetic equation for cosmic rays in the interplanetary medium, *Journal of Geophysical Research*, *81*(13), 2089–2093, 1976.

Luhn, A., B. Klecker, D. Hovestadt, and E. Möbius, The mean ionic charge of silicon in ^{3}He-rich solar flares, *Astrophysical Journal*, *317*, 951–955, 1987.

MacKinnon, A. I., and I. J. D. Craig, Stochastic simulation of fast particle diffusive transport, *Astronomy & Astrophysics*, *251*, 693–699, 1991.

Malkov, M. A., and R. Z. Sagdeev, Cosmic ray transport with magnetic focusing and the "telegraph" model, *Astrophysical Journal*, *808*, 157–158, 2015.

Marsch, E., Kinetic physics of the solar corona and solar wind, *Living Reviews in Solar Physics*, *3*, 2006.

Matsumoto, M., and T. Nishimura, Mersenne Twister: a 623-dimensionally equidistributed uniform pseudo-random number generator, *ACM Transactions on Modeling and Computer Simulation*, *8*(1), 3–30, 1998.

Mewaldt, R. A., Solar energetic particle composition, energy spectra, and space weather, *Space Science Reviews*, *124*, 303–316, 2006.

Miller, J. A., Controversy over "Solar Flare Myth" explored, *EOS, Transactions American Geophysical Union*, *76*(41), 401–412, 1995.

Miller, J. A., and D. A. Roberts, Stochastic proton acceleration by cascading Alfvén waves in impulsive solar flares, *Astrophysical Journal*, *452*, 912–932, 1995.

Miller, J. A., and A. F. Viñas, Ion acceleration and abundance enhancements by electron beam instabilities in impulsive solar flares, *Astrophysical Journal*, *412*, 386–400, 1993.

Miller, J. A., T. N. LaRosa, and R. L. Moore, Stochastic electron acceleration by cascading fast mode waves in impulsive solar flares, *Astrophysical Journal*, *461*, 445–464, 1996.

Miller, J. A., P. J. Cargill, A. G. Emslie, G. D. Holman, B. R. Dennis, T. N. LaRosa, R. M. Winglee, S. G. Benka, and S. Tsuneta, Critical issues for understanding particle acceleration in impulsive solar flares, *Journal of Geophysical Research*, *102*(A7), 14,631–14,659, 1997.

Mills, R. L., and A. M. Sessler, Liouville's theorem and phase-space cooling, in *Montreux Proceedings, CERN Report*, vol. 94-03, p. 4, 1993.

Milstein, G. N., J. G. M. Schoenmakers, and V. Spokoiny, Transition density estimation for stochastic differential equations via forward-reverse representations, *Bernoulli*, *10*(2), 281–312, 2004.

Minnie, J., W. H. Matthaeus, J. W. Bieber, D. Ruffolo, and R. A. Burger, When do particles follow field lines?, *Journal of Geophysical Research*, *114*, A01,102, 2009.

Moeketsi, D. M., M. S. Potgieter, S. E. S. Ferreira, B. Heber, H. Fichtner, and V. K. Heinze, The heliospheric modulation of 3-10 MeV electrons: modeling of changes in the solar wind speed in relation to perpendicular polar diffusion, *Advances in Space Research*, *35*, 597–604, 2005.

Ng, C. K., and K. Wong, Solar particle propagation under the influence of pitch-angle diffusion and collimation in the interplanetary magnetic field, in *16th International Cosmic Ray Conference*, vol. 5, edited by S. Miyake, pp. 252–257, Institute for Cosmic Ray Research, University of Tokyo, 1979.

Northrop, T. G., The guiding center approximation to charged particle motion, *Annals of Physics*, *15*, 79–101, 1961.

Øksendal, B., *Stochastic differential equations: an introduction with applications*, fifth ed., Springer-Verlag, Berlin, 2000.

Owens, M. J., and R. J. Forsyth, The heliospheric magnetic field, *Living Reviews in Solar Physics*, *10*, 2013.

Pallavicini, R., S. Serio, and G. S. Vaiana, A survey of soft X-ray limb flare images: the relation between their structure in the corona and other physical parameters, *Astrophysical Journal*, *216*, 108–122, 1977.

Parker, E. N., The formation of sunspots from the solar toroidal field, *Astrophysical Journal*, *121*, 491–507, 1955.

Parker, E. N., Dynamics of the interplanetary gas and magnetic fields, *Astrophysical Journal*, *128*, 664–676, 1958.

Parker, E. N., The passage of energetic charged particles through interplanetary space, *Planetary and Space Science*, *13*, 9–49, 1965.

Pei, C., J. W. Bieber, R. A. Burger, and J. Clem, A general time-dependent stochastic method for solving Parker's transport equation in spherical coordinates, *Journal of Geophysical Research*, *115*, A12,107–A12,119, 2010.

Press, W. H., S. A. Teukolsky, W. T. Vetterling, and B. P. Flannery, *Numerical recipes in C: the art of scientific computing*, second ed., Cambridge University, Cambridge, 1997.

Qin, G., M. Zhang, J. R. Dwyer, H. K. Rassoul, and G. M. Mason, The model dependence of solar energetic particle mean free paths under weak scattering, *Astrophysical Journal*, *627*, 562–566, 2005.

Qin, G., M. Zhang, and J. R. Dwyer, Effect of adiabatic cooling on the fitted parallel mean free path of solar energetic particles, *Journal of Geophysical Research*, *111*, A08,101, 2006.

Reames, D. V., The dark side of the Solar Flare Myth, *EOS, Transactions American Geophysical Union*, *76*(41), 1995.

Reames, D. V., Particle acceleration at the Sun and in the heliosphere, *Space Science Reviews*, *90*, 413–491, 1999.

Reames, D. V., The two sources of solar energetic particles, *Space Science Reviews*, *175*, 53–92, 2013.

Reames, D. V., *Solar energetic particles*, Springer-Verlag, Berlin, 2017.

Reames, D. V., and R. G. Stone, The identification of solar ^{3}He-rich events and the study of particle acceleration at the Sun, *Astrophysical Journal*, *308*, 902–911, 1986.

Reames, D. V., J. P. Meyer, and T. T. von Rosenvinge, Energetic-particle abundances in impulsive solar flare events, *Astrophysical Journal Supplement Series*, *90*, 649–667, 1994.

Roelof, E. C., Propagation of solar cosmic rays in the interplanetary magnetic field, in *Lectures in high-energy astrophysics*, edited by H. Ögelman and J. R. Wayland, pp. 111–136, NASA, Washington, D.C., 1969.

Rudemo, M., Empirical choice of histograms and kernel density estimators, *Scandinavian Journal of Statistics*, *9*(2), 65–78, 1982.

Ruffolo, D., Effect of adiabatic deceleration on the focused transport of solar cosmic rays, *Astrophysical Journal*, *442*, 861–874, 1995.

Ryan, J. M., J. A. Lockwood, and H. Debrunner, Solar energetic particles, *Space Science Reviews*, *93*, 35–53, 2000.

Schutte, H. M., Particle push comparisons, Hons.B.Sc. mini-dissertation, Potchefstroom Campus of the North-West University, South Africa, 2016.

Shalchi, A., *Nonlinear cosmic ray diffusion theories*, Springer-Verlag, Berlin, 2009.

Shalchi, A., Improved analytical description of parallel diffusion with adiabatic focusing, *Astrophysical Journal*, *728*, 113–119, 2011.

Sheeley, N. R., et al., Measurements of flow speeds in the corona between 2 and 30 $R_{\odot}$, *Astrophysical Journal*, *484*, 472–478, 1997.

Shibata, K., and T. Magara, Solar flares: magnetohydrodynamic processes, *Living Reviews in Solar Physics*, *8*, 2011.

Skilling, J., Cosmic rays in the galaxy: convection or diffusion?, *Astrophysical Journal*, *170*, 265–273, 1971.

Skilling, J., Cosmic ray streaming I: effect of Alfvén waves on particles, *Monthly Notices of the Royal Astronomical Society*, *172*, 557–566, 1975.

Smith, E. J., The global heliospheric magnetic field, in *The heliosphere through the solar activity cycle*, edited by A. Balogh, L. J. Lanzerotti, and S. T. Suess, pp. 79–150, Springer-Praxis, Chichester, UK, 2008.

Strauss, R. D., Modelling of cosmic rays in the heliosphere by stochastic processes, Ph.D. thesis, Potchefstroom Campus of the North-West University, South Africa, 2013.

Strauss, R. D., and F. Effenberger, A hitch-hiker's guide to stochastic differential equations: solution methods for energetic particle transport in space physics and astrophysics, *Space Science Reviews*, *212*, 151–192, 2017.

Strauss, R. D., and H. Fichtner, On aspects pertaining to the perpendicular diffusion of solar energetic particles, *Astrophysical Journal*, *801*, 29–38, 2015.

Strauss, R. D., M. S. Potgieter, A. Kopp, and I. Büsching, On the propagation times and energy losses of cosmic rays in the heliosphere, *Journal of Geophysical Research*, *116*, A12,105–A12,117, 2011.

Strauss, R. D., J. A. le Roux, N. E. Engelbrecht, D. Ruffolo, and P. Duzlaff, Non-axisymmetric perpendicular diffusion of charged particles and their transport across tangential magnetic discontinuities, *Astrophysical Journal*, *825*, 43–57, 2016.

Strauss, R. D., N. Dresing, and N. E. Engelbrecht, Perpendicular diffusion of solar energetic particles: model results and implications for electrons, *Astrophysical Journal*, *837*, 43–60, 2017.

Tan, L. C., Electron spectral breaking caused by magnetic reconnection in impulsive flare events, *Astrophysical Journal*, *858*, 25, 2018.

Tandberg-Hanssen, E., and A. G. Emslie, *The physics of solar flares*, Cambridge University, Great Britain, 1988.

Temerin, M., and I. Roth, The production of ^{3}He and heavy ion enrichments in ^{3}He-rich flares by electromagnetic hydrogen cyclotron waves, *Astrophysical Journal*, *391*, L105–L108, 1992.

Tooprakai, P., A. Seripienlert, D. Ruffolo, P. Chuychai, and W. H. Matthaeus, Simulations of lateral transport and dropout structure of energetic particles from impulsive solar flares, *Astrophysical Journal*, *831*, 195–207, 2016.

Tsurutani, B. T., and G. S. Lakhina, Some basic concepts of wave-particle interactions in collisionless plasmas, *Reviews of Geophysics*, *35*(4), 491–502, 1997.

Turner, C., Histogram errors, `https://suchideas.com/articles/maths/applied/histogram-errors/`, (Date accessed: 2018-08-21), 2017.

Tylka, A. J., New insights on solar energetic particles from Wind and ACE, *Journal of Geophysical Research*, *106*(A11), 25,333–25,352, 2001.

Uhlenbeck, G. E., and L. S. Ornstein, On the theory of Brownian motion, *Physical Review*, *36*, 823–841, 1930.

Usoskin, I. G., The history of solar activity over millennia, *Living Reviews in Solar Physics*, *10*, 2013.

van Kampen, N. G., *Stochastic processes in physics and chemistry*, second ed., Elsevier Science B.V., Amsterdam, 1992.

Vay, J. L., Simulation of beams or plasmas crossing at relativistic velocity, *Physics of Plasmas*, *15*, 056,701, 2008.

von Smoluchowski, M., Zur kinetischen Theorie der Brownschen Molekularbewegung und der Suspensionen, *Annalen der Physik*, *326*(14), 756–780, 1906.

von Steiger, R., The solar wind throughout the solar cycle, in *The heliosphere through the solar activity cycle*, edited by A. Balogh, L. J. Lanzerotti, and S. T. Suess, pp. 41–78, Springer-Praxis, Chichester, UK, 2008.

Wang, L., S. Krucker, G. M. Mason, R. P. Lin, and G. Li, The injection of ten electron/^{3}He-rich SEP events, *Astronomy & Astrophysics*, *585*, A119, 2016.

Wawrzynczak, A., R. Modzelewska, and M. Kluczek, Numerical methods for solution of the stochastic differential equations equivalent to the non-stationary Parkers transport equation, in *Proceedings of the 4th International Conference on Mathematical Modeling in Physical Sciences*, vol. 633, Journal of Physics: Conference Series, 2015.

Webb, D. F., and T. A. Howard, Coronal mass ejections: observations, *Living Reviews in Solar Physics*, *9*, 2012.

Webb, G. M., and L. J. Gleeson, Green's theorem and Green's function for the steady-state cosmic-ray equation of transport, *Astrophysics and Space Science*, *50*, 205–223, 1977.

Webb, G. M., and L. J. Gleeson, On the equation of transport for cosmic-ray particles in the interplanetary region, *Astrophysics and Space Science*, *60*, 335–351, 1979.

Wild, J. P., S. F. Smerd, and A. A. Weiss, Solar bursts, *Annual Review of Astronomy and Astrophysics*, *1*, 291–366, 1963.

Woodham, L. D., R. T. Wicks, D. Verscharen, and C. J. Owen, The role of proton cyclotron resonance as a dissipation mechanism in solar wind turbulence: a statistical study at ion-kinetic scales, *Astrophysical Journal*, *856*, 49–65, 2018.

Yamada, Y., S. Yanagita, and T. Yoshida, A stochastic view of the solar modulation phenomena of cosmic rays, *Geophysical Review Letters*, *25*, 2353–2356, 1998.

Zank, G. P., *Transport processes in space physics and astrophysics*, Springer, Heidelberg, Germany, 2014.

Zank, G. P., L. Adhikari, P. Hunana, D. Shiota, R. Bruno, and D. Telloni, Theory and transport of nearly incompressible magnetohydrodynamic turbulence, *Astrophysical Journal*, *835*, 147–177, 2017.

Zhang, M., A path integral approach to the theory of heliospheric cosmic-ray modulation, *Astrophysical Journal*, *510*, 715–725, 1999a.

Zhang, M., A Markov stochastic process theory of cosmic-ray modulation, *Astrophysical Journal*, *513*, 409–420, 1999b.

Zhang, M., G. Qin, and H. Rassoul, Propagation of solar energetic particles in three-dimensional interplanetary magnetic fields, *Astrophysical Journal*, *692*, 109–132, 2009.

Acknowledgements

Above all, I would like to thank my heavenly Father and Saviour, Jesus Christ, for blessing me with health and the mental ability to study and understand not only physics but also computer science and mathematics. I would also like to thank the following persons and institutions for support:

- Dr. R. DT. Strauss, my supervisor, for his excellent guidance, explanations, and discussions throughout this project, as well as for his interest in my well-being.
- Prof. M. S. Potgieter, Prof. R. A. Burger, and Dr. N. E. Engelbrecht for introducing me to heliospheric physics, transport theory, plasma physics, and turbulence, taking an interest in my academic work, and learning me how to think critically as a physicist.
- N. Wijsen for interesting and helpful discussions on the pitch-angle diffusion coefficient and other related topics.
- The National Astrophysics and Space Science Program (NASSP), the Centre for Space Research (CSR), and the North-West University (NWU) for financial and infrastructure support throughout my studies.
- My parents and family for their on-going support in whatever I pursue and for their interest in my research.
- Colleagues for interesting research discussions and fun-filled conferences.
- Friends for putting a smile on my face when most needed.
- Mrs. M. P. Sieberhagen, Mr. L. Fransman, Mrs. E. van Rooyen, and Mrs. L. van Wyk for their help with administration, as well as Mr. M. Holleran for his help with computer related problems.
- Ms. L. du Toit for the language editing of this dissertation.

Jacobus Petrus van den Berg
Centre for Space Research, North-West University,
November 2018.